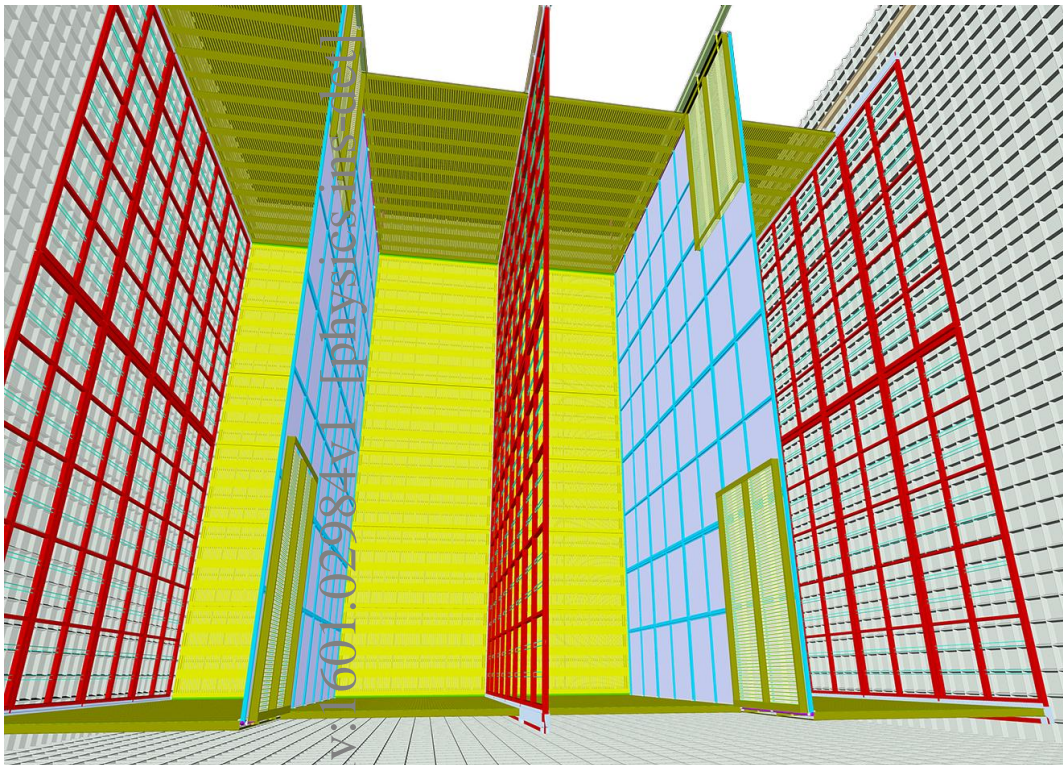# Long-Baseline Neutrino Facility (LBNF) and Deep Underground Neutrino Experiment (DUNE)

Conceptual Design Report

Volume 4: The DUNE Detectors at LBNF

January 13, 2016

DUNE DEEP UNDERGROUND NEUTRINO EXPERIMENT

The DUNE Collaboration

R. Acciarri[43], M. A. Acero[10], M. Adamowski[43], C. Adams[144], P. Adamson[43], S. Adhikari[77], Z. Ahmad[135],
C. H. Albright[43], T. Alion[120], E. Amador[131], J. Anderson[8], K. Anderson[43], C. Andreopoulos[76], M. Andrews[43],
R. Andrews[43], I. Anghel[62], J. d. Anjos[99], A. Ankowski[137], M. Antonello[72], A. Aranda Fernandez[31], A. Ariga[13],
T. Ariga[13], D. Aristizabal[75], E. Arrieta-Diaz[87], K. Aryal[131], J. Asaadi[129], D. Asner[103], M. S. Athar[6], M. Auger[13],
A. Aurisano[29], V. Aushev[68], D. Autiero[63], M. Avila[131], J. J. Back[139], X. Bai[122], B. Baibussinov[106], M. Baird[61],
B. Balantekin[142], B. Baller[43], P. Ballett[41], B. Bambah[52], M. Bansal[107], S. Bansal[107], G. J. Barker[139],
W. A. Barletta[83], G. Barr[102], N. Barros[109], L. Bartoszek[78], A. Bashyal[131], M. Bass[102], F. Bay[133], J. Beacom[100],
B. R. Behera[107], G. Bellettini[110], V. Bellini[26], O. Beltramello[16], P. A. Benetti[108], A. Bercellie[114], M. Bergevin[19],
E. Berman[43], H. Berns[20], R. Bernstein[43], S. Bertolucci[16], B. Bhandari[49], V. Bhatnagar[107], B. Bhuyan[60], J. Bian[90],
K. Biery[43], M. Bishai[15], T. Blackburn[128], A. Blake[73], F. d. M. Blaszczyk[14], E. Blaufuss[82], B. Bleakley[124],
E. Blucher[28], V. Bocean[43], F. Boffelli[108], J. Boissevain[78], S. Bolognesi[117], T. Bolton[65], M. Bonesini[89], T. Boone[33],
C. Booth[118], S. Bordoni[53], M. Borysova[68], B. Bourguille[53], S. B. Boyd[139], D. Brailsford[73], A. Brandt[131],
J. Bremer[16], S. Brice[43], C. Bromberg[87], G. Brooijmans[34], G. Brown[131], R. Brown[15], G. Brunetti[43], X. Bu[43],
N. Buchanan[33], H. Budd[114], B. Bugg[130], P. Calafiura[74], E. Calligarich[108], E. Calvo[17], L. Camilleri[34],
M. Campanelli[77], C. Cantini[147], B. Carls[43], R. Carr[34], M. Cascella[77], C. Castromonte[44], E. Catano Mur[62],
F. Cavanna[43], S. Centro[106], A. Cervera Villanueva[136], V. B. Chandratre[12], A. Chatterjee[131], S. Chattopadhyay[43],
S. Chattopadhyay[135], L. Chaussard[63], S. Chembra[52], H. Chen[15], K. Chen[15], M. Chen[21], D. Cherdack[33], C. Chi[34],
S. Childress[43], S. Choubey[47], B. C. Choudhary[38], G. Christodoulou[76], C. Christofferson[122], E. Church[103],
D. Cianci[81], D. Cline[21], T. Coan[125], A. Cocco[93], J. Coelho[134], P. Cole[58], G. Collin[83], J. M. Conrad[83],
M. Convery[115], R. Corey[122], L. Corwin[122], J. Cranshaw[8], P. Crivelli[147], D. Cronin-Hennessy[90], A. Curioni[89],
J. Cushing[28], D. L. Adams[15], D. Dale[58], S. R. Das[60], T. Davenne[116], G. S. Davies[61], J. Davies[128], J. Dawson[2],
K. De[131], A. de Gouvea[97], J. K. de Jong[102], P. de Jong[92], P. De Lurgio[8], M. Decowski[92], A. Delbart[117],
C. Densham[116], R. Dharmapalan[8], N. Dhingra[107], S. Di Luise[147], M. Diamantopoulou[9], J. S. Diaz[61],
G. Diaz Bautista[114], M. Diwan[15], Z. Djurcic[8], J. Dolph[15], G. Drake[8], D. Duchesneau[71], M. Duvernois[142],
H. Duyang[120], D. A. Dwyer[74], S. Dye[48], S. Dytman[111], B. Eberly[115], R. Edgecock[50], D. Edmunds[87], S. Elliott[78],
M. Elnimr[21], S. Emery[117], E. Endress[105], S. Eno[82], A. Ereditato[13], C. O. Escobar[43], J. Evans[81], A. Falcone[108],
L. Falk[128], A. Farbin[131], C. Farnese[106], Y. Farzan[57], A. Fava[106], L. Favilli[18], J. Felde[82], J. Felix[46], S. Fernandes[4],
L. Fields[43], A. Finch[73], M. Fitton[116], B. Fleming[144], T. Forest[58], J. Fowler[40], W. Fox[61], J. Fried[15], A. Friedland[78],
S. Fuess[43], B. Fujikawa[74], A. Gago[105], H. Gallagher[134], S. Galymov[63], T. Gamble[118], R. Gandhi[47],
D. Garcia-Gamez[81], S. Gardiner[20], G. Garvey[78], V. M. Gehman[74], A. Gendotti[147], G. d. Geronimo[15], C. Ghag[77],
P. Ghoshal[47], D. Gibin[106], I. Gil-Botella[17], R. Gill[15], D. Girardelli[25], A. Giri[55], S. Glavin[109], D. Goeldi[13],
S. Golapinni[65], M. Gold[96], R. A. Gomes[44], J. J. Gomez Cadenas[136], M. C. Goodman[8], D. Gorbunov[56],
S. Goswami[47], N. Graf[111], N. Graf[115], M. Graham[115], E. Gramelini[144], R. Gran[91], C. Grant[20], N. Grant[139],
V. Greco[26], H. Greenlee[43], L. Greenler[142], C. Greenley[79], M. Groh[29], S. Grullon[109], T. Grundy[73], K. Grzelak[138],
E. Guardincerri[78], V. Guarino[8], E. Guarnaccia[137], G. P. Guedes[42], R. Guenette[102], A. Guglielmi[106], A. T. Habig[91],
R. W. Hackenburg[15], A. Hackenburg[144], H. Hadavand[131], R. Haenni[13], A. Hahn[43], M. D. Haigh[139], T. Haines[78],
T. Hamernik[43], T. Handler[130], S. Hans[15], D. Harris[43], J. Hartnell[128], T. Hasegawa[67], R. Hatcher[43],
A. Hatzikoutelis[130], S. Hays[43], E. Hazen[14], M. Headley[123], A. Heavey[43], K. Heeger[144], J. Heise[123], K. Hennessy[76],
J. Hewes[81], A. Higuera[49], T. Hill[58], A. Himmel[43], M. Hogan[33], P. Holanda[25], A. Holin[77], W. Honey[73],
S. Horikawa[147], G. Horton-Smith[65], B. Howard[61], J. Howell[43], P. Hurh[43], J. Huston[87], J. Hylen[43], R. Imlay[79],
J. Insler[79], G. Introzzi[108], D. Ioanisyan[145], A. Ioannisian[145], K. Iwamoto[114], A. Izmaylov[136], C. Jackson[131],
D. E. Jaffe[15], C. James[43], E. James[43], F. Jediny[36], C. Jen[137], A. Jhingan[107], S. Jiménez[17], J. H. Jo[127],
M. Johnson[43], R. Johnson[29], J. Johnstone[43], B. J. Jones[83], J. Joshi[15], H. Jostlein[43], C. K. Jung[127], T. Junk[43],
A. Kaboth[59], R. Kadel[74], T. Kafka[134], L. Kalousis[137], Y. Kamyshkov[130], G. Karagiorgi[81], D. Karasavvas[9],
Y. Karyotakis[71], A. Kaur[107], P. Kaur[107], B. Kayser[43], N. Kazaryan[145], E. Kearns[14], P. Keener[109], S. Kemboi[131],
E. Kemp[25], S. H. Kettell[15], M. Khabibullin[56], M. Khandaker[58], A. Khotjantsev[56], B. Kirby[15], M. Kirby[43],
J. Klein[109], T. Kobilarcik[43], S. Kohn[19], G. Koizumi[43], A. Kopylov[56], M. Kordosky[141], L. Kormos[73], U. Kose[16],
A. Kostelecky[61], M. Kramer[19], I. Kreslo[13], R. Kriske[90], W. Kropp[21], Y. Kudenko[56], V. A. Kudryavtsev[118],
S. Kulagin[56], A. Kumar[107], G. Kumar[69], J. Kumar[48], L. Kumar[107], T. Kutter[79], A. Laminack[4], K. Lande[109],
C. Lane[39], K. Lang[132], F. Lanni[15], J. Learned[48], P. Lebrun[43], D. Lee[78], H. Lee[114], K. Lee[21], W. M. Lee[43],
M. A. Leigui de Oliveira[1], Q. Li[43], S. Li[15], S. Li[100], X. Li[127], Y. Li[15], Z. Li[40], J. Libo[120], C. S. Lin[74], S. Lin[33],
J. Ling[15], J. Link[137], Z. Liptak[32], D. Lissauer[15], L. Littenberg[15], B. Littlejohn[54], Q. Liu[78], T. Liu[125], S. Lockwitz[43],
N. Lockyer[43], T. Loew[74], M. Lokajicek[3], K. Long[59], M. D. L. Lopes[43], J. P. Lopez[32], J. Losecco[98], W. Louis[78],

J. Lowery[61], M. Luethi[13], K. Luk[19], B. Lundberg[43], T. Lundin[43], X. Luo[144], T. Lux[53], J. Lykken[43],
A. A. Machado[72], J. R. Macier[43], S. Magill[8], G. Mahler[15], K. Mahn[87], M. Malek[59], S. Malhotra[12], D. Malon[8],
F. Mammoliti[26], S. Mancina[8], S. K. Mandal[38], S. Mandodi[52], S. L. Manly[114], A. Mann[134], A. Marchionni[43],
W. Marciano[15], C. Mariani[137], J. Maricic[48], A. Marino[32], M. Marshak[90], C. Marshall[114], J. Marshall[24],
J. Marteau[63], J. Martin-Albo[102], D. Martinez[54], S. Matsuno[48], J. Matthews[79], C. Mauger[78], K. Mavrokoridis[76],
D. Mayilyan[145], E. Mazzucato[117], N. McCauley[76], E. McCluskey[43], N. McConkey[118], K. McDonald[112],
K. S. McFarland[114], A. M. McGowan[114], C. McGrew[127], R. McKeown[141], D. McNulty[58], R. McTaggart[124],
A. Mefodiev[56], M. Mehrian[33], P. Mehta[95], D. Mei[121], O. Mena[136], S. Menary[146], H. Mendez[85], A. Menegolli[108],
G. Meng[106], Y. Meng[21], H. Merritt[59], D. Mertins[4], M. Messier[61], W. Metcalf[79], M. Mewes[61], H. Meyer[140],
T. Miao[43], R. Milincic[48], W. Miller[90], G. Mills[78], O. Mineev[56], O. Miranda[30], C. S. Mishra[43], S. R. Mishra[120],
B. Mitrica[51], D. Mladenov[16], I. Mocioiu[104], R. Mohanta[52], N. Mokhov[43], C. Montanari[16], D. Montanari[43],
J. Moon[83], M. Mooney[15], C. Moore[43], J. Morfin[43], B. Morgan[139], C. Morris[49], W. Morse[15], Z. Moss[83], C. Mossey[43],
C. A. Moura[1], J. Mousseau[86], L. Mualem[23], M. Muether[140], S. Mufson[61], S. Murphy[147], J. Musser[61], R. Musser[131],
Y. Nakajima[74], D. Naples[111], J. Navarro[10], D. Navas[17], J. Nelson[141], M. Nessi[16], M. Newcomer[109], Y. Ng[131],
R. Nichol[77], T. C. Nicholls[116], K. Nikolics[147], E. Niner[61], B. Norris[43], F. Noto[16], P. Novakova[15], P. Novella[136],
J. Nowak[73], M. S. Nunes[25], H. O'Keeffe[73], R. Oldeman[24], R. Oliveira[25], T. Olson[134], Y. Onishchuk[68], J. Osta[43],
T. Ovsjannikova[56], B. Page[87], S. Pakvasa[48], S. Pal[118], O. Palamara[43], A. Palazzo[84], J. Paley[43], C. Palomares[17],
E. Pantic[20], V. Paolone[111], V. Papadimitriou[43], J. Park[137], S. Parke[43], Z. Parsa[15], S. Pascoli[41], R. Patterson[23],
S. Patton[74], T. Patzak[2], B. Paulos[142], L. Paulucci[1], Z. Pavlovic[43], G. Pawloski[90], S. Peeters[128], E. Pennacchio[63],
A. Perch[77], G. N. Perdue[43], L. Periale[147], J. D. Perkin[118], H. Pessard[71], G. Petrillo[43], R. Petti[120], A. Petukhov[122],
F. Pietropaolo[106], R. Plunkett[43], S. Pordes[43], M. Potekhin[15], R. Potenza[26], B. Potukuchi[64], N. Poudyal[121],
O. Prokofiev[43], N. Pruthi[107], P. Przewlocki[94], D. Pushka[43], X. Qian[15], J. L. Raaf[43], R. Raboanary[7], V. Radeka[15],
A. Radovic[141], G. Raffelt[84], I. Rakhno[43], H. T. Rakotondramanana[7], L. Rakotondravohitra[7], Y. A. Ramachers[139],
R. Rameika[43], J. Ramsey[78], A. Rappoldi[108], G. Raselli[108], P. Ratoff[73], B. Rebel[43], C. Regenfus[147],
J. Reichenbacher[122], D. Reitzner[43], A. Remoto[71], A. Renshaw[49], S. Rescia[15], M. Richardson[118], K. Rielage[78],
K. Riesselmann[43], M. Robinson[118], L. Rochester[115], O. B. Rodrigues[25], P. Rodrigues[114], B. Roe[86], M. Rosen[48],
R. M. Roser[43], M. Ross-Lonergan[41], M. Rossella[108], A. Rubbia[147], C. Rubbia[45], R. Rucinski[43],
C. Rudolph von Rohr[13], B. Russell[144], D. Ruterbories[114], R. Saakyan[77], N. Sahu[55], P. Sala[88], N. Samios[15],
F. Sanchez[53], M. Sanchez[62], B. Sands[112], S. Santana[85], R. Santorelli[17], G. Santucci[127], N. Saoulidou[9],
A. Scaramelli[88], H. Schellman[101], P. Schlabach[43], R. Schmitt[43], D. Schmitz[28], J. Schneps[134], K. Scholberg[40],
A. Schukraft[43], J. Schwehr[33], E. Segreto[72], S. Seibert[109], J. A. Sepulveda-Quiroz[62], F. Sergiampietri[147],
L. Sexton-Kennedy[43], D. Sgalaberna[147], M. Shaevitz[34], J. Shahi[107], S. Shahsavarani[131], P. Shanahan[43],
S. U. Shankar[47], R. Sharma[15], R. K. Sharma[113], T. Shaw[43], R. Shrock[127], I. Shyrma[68], N. Simos[15], G. Sinev[40],
I. Singh[107], J. Singh[107], J. Singh[80], V. Singh[11], G. Sinnis[78], W. Sippach[34], D. Smargianaki[16], M. Smy[21],
E. Snider[43], P. Snopok[54], J. Sobczyk[143], H. Sobel[21], M. Soderberg[129], N. Solomey[140], W. Sondheim[78], M. Sorel[136],
A. Sousa[29], K. Soustruznik[27], J. Spitz[83], J. Spitz[86], N. J. Spooner[118], M. Stancari[43], I. Stancu[4], D. Stefan[16],
H. M. Steiner[74], J. Stewart[15], J. Stock[122], S. Stoica[51], J. Stone[14], J. Strait[43], M. Strait[28], T. Strauss[43],
S. Striganov[43], R. Sulej[94], G. Sullivan[82], Y. Sun[48], L. Suter[8], C. M. Sutera[26], R. Svoboda[20], B. Szczerbinska[37],
A. Szelc[81], S. Söldner-Rembold[81], R. Talaga[8], M. Tamsett[128], S. Tariq[43], E. Tatar[58], R. Tayloe[61], C. Taylor[78],
D. Taylor[123], K. Terao[34], M. Thiesse[118], J. Thomas[77], L. F. Thompson[118], M. Thomson[24], C. Thorn[15],
M. Thorpe[116], X. Tian[120], D. Tiedt[122], S. C. Timm[43], A. Tonazzo[2], T. Tope[43], A. Topkar[12], F. R. Torres[25],
M. Torti[108], M. Tortola[136], F. Tortorici[26], M. Toups[83], C. Touramanis[76], M. Tripathi[20], I. Tropin[43], Y. Tsai[115],
K. V. Tsang[74], R. Tsenov[119], S. Tufanli[144], C. Tull[74], J. Turner[41], M. Tzanov[79], E. Tziaferi[9], Y. Uchida[59],
J. Urheim[61], T. Usher[115], M. Vagins[66], P. Vahle[141], G. A. Valdiviesso[5], L. Valerio[43], Z. Vallari[127], J. Valle[136],
R. Van Berg[109], R. Van de Water[78], P. Van Gemmeren[8], F. Varanini[106], G. Varner[48], G. Vasseur[117], K. Vaziri[43],
G. Velev[43], S. Ventura[106], A. Verdugo[17], T. Viant[147], T. V. Vieira[25], C. Vignoli[72], C. Vilela[127], B. Viren[15],
T. Vrba[36], T. Wachala[70], D. Wahl[142], M. Wallbank[118], N. Walsh[20], B. Wang[125], H. Wang[22], L. Wang[121],
T. Wang[41], T.K. Warburton[118], D. Warner[33], M. Wascko[59], D. Waters[77], T. B. Watson[131], A. Weber[116],
M. Weber[13], W. Wei[121], A. Weinstein[62], D. Wells[122], D. Wenman[142], M. Wetstein[62], A. White[131], L. Whitehead[49],
D. Whittington[61], M. Wilking[127], J. Willhite[43], P. Wilson[43], R. J. Wilson[33], L. Winslow[83], P. Wittich[35],
S. Wojcicki[126], H. H. Wong[19], K. Wood[120], E. Worcester[15], M. Worcester[15], S. Wu[147], T. Xin[62], C. Yanagisawa[127],
S. Yang[29], T. Yang[43], K. Yarritu[78], J. Ye[125], M. Yeh[15], N. Yershov[56], K. Yonehara[43], B. Yu[15], J. Yu[131],
J. Zalesak[3], A. Zalewska[70], B. Zamorano[128], L. Zang[118], A. Zani[108], A. Zani[16], G. Zavala[46], G. Zeller[43],
C. Zhang[15], C. Zhang[121], E. D. Zimmerman[32], M. Zito[117], and R. Zwaska[43]

[1]*ABC Federal University, Santo André –SP, 09210-580, Brazil*
[2]*APC-Paris, Batiment Condorcet; 10, rue Alice Domon et L'eonie Duquet; F-75205 Paris CEDEX 13, France*
[3]*Institute of Physics ASCR, v. v. i. , Na Slovance 2; 182 21 Praha 8, Czech Republic*
[4]*Univ. of Alabama (Tuscaloosa), Tuscaloosa, AL 35487-0324, USA*

^{5} *Univ. Federal de Alfenas em Poços de Caldas, 11999, CEP 37715-900 Poços de Caldas-MG, Brazil*

^{6} *Aligarh Muslim University, Department of Physics Aligarh-202002, India*

^{7} *Antananarivo, Présidence de l'Université d'Antananarivo: BP 566, Antananarivo 101, Madagascar*

^{8} *Argonne National Lab., Argonne, IL 60439, USA*

^{9} *University of Athens, University Campus, Zografou GR 157 84 Greece, Greece*

^{10} *Universidad del Atlantico, Km 7 antigua vi a Puerto Colombia, Barranquilla, Colombia*

^{11} *Banaras Hindu University, Dept. of Physics, Varanasi UP 221005, India*

^{12} *Bhabha Atmoic Research Center, Trombay, Mumbai, India*

^{13} *Univ. of Bern, Lab for High Energy Physics; Sidlerstrasse 5; CH-3012 Bern, Switzerland*

^{14} *Boston University, Boston, MA 02215, USA*

^{15} *Brookhaven National Lab., Upton, NY 11973-5000, USA*

^{16} *CERN, European Organization for Nuclear Research European Laboratory for Particle Physics; 1211 Gen'eve 23, Switzerland*

^{17} *CIEMAT, División de Física de Partículas; Avenida Complutense 40; E-28040 Madrid, Spain*

^{18} *CNR Pisa, 1, 56124 Pisa PI, Italy*

^{19} *University of California at Berkeley, #7300; Berkeley, CA 94720-7300, USA*

^{20} *Univ. of California (Davis), Davis, CA 95616, USA*

^{21} *Univ. of California (Irvine), Irvine, CA 92697-4575, USA*

^{22} *Univ. of California (Los Angeles), Los Angeles, CA 90095-1547, USA*

^{23} *California Inst. of Tech., MC 356-48; Pasadena, CA 91125, USA*

^{24} *Univ. of Cambridge, JJ Thomson Avenue, Cambridge CB3 0HE, UK*

^{25} *Univ. de Campinas, Av. Sérgio Buarque de Holanda, 777 CEP 13083-859 Campinas-SP, Brazil*

^{26} *Univ. di Catania, Via Santa Sofia, I-95123 Catania, Italy*

^{27} *Institute of Particle and Nuclear Physics of the Faculty of Mathematics and Physics of the Charles University in Prague, V Holešovičkách 747/2; 180 00 Praha 8-Libeň, Czech Republic*

^{28} *Univ. of Chicago, Chicago, IL 60637-1434, USA*

^{29} *Univ. of Cincinnati, Cincinnati, OH 45221-0011, USA*

^{30} *Cinvestav, 07360 Ciudad de México, D.F., Mexico*

^{31} *Universidad de Colima, Facultad de Ciencias Bernal Diaz del Castillo 340 Colonia Villa San Sebastian Colima, Colima, Mexico*

^{32} *Univ. of Colorado, Boulder, CO 80309, USA*

^{33} *Colorado State University, Fort Collins, CO 80523, USA*

^{34} *Columbia University, New York, NY 10027, USA*

^{35} *Cornell Univ., Laboratory for Elementary-Particle Physics; Newman Lab; Ithaca, NY 14853–5001, USA*

^{36} *Czech Technical University in Prague, Brehova 7; 115 19 Praha 1, Czech Republic*

^{37} *Dakota State University, Madison, SD 57042, USA*

^{38} *Univ. of Delhi, Department of Physics and Astrophysics, Delhi 110007, India*

^{39} *Drexel University, Philadelphia, PA 19104, USA*

^{40} *Duke University, Durham, NC 27706, USA*

^{41} *Univ. of Durham, Institute for Particle Physics Phenomenology; Dept. of Physics, Ogden Centre for Fund. Physics; South Road; Durham DH1 3LE, UK*

^{42} *Univ. Estadual de Feira de Santana, S/N;44036-900, Feira de Santana-BA, Brazil*

^{43} *Fermi National Accelerator Lab, Batavia, IL 60510-0500, USA*

^{44} *Univ. Federal de Goias, Goiania, GO, Brazil*

^{45} *Gran Sasso Science Institute, 7, L'Aquila, Italy*

^{46} *Universidad de Guanajuato, Gto., C.P.37000, Mexico*

^{47} *Harish-Chandra Research Institute, Jhunsi, Allahabad 211 019, India*

^{48} *Univ. of Hawaii, Honolulu, HI 96822-2219, USA*

^{49} *Univ. of Houston, Houston, TX 77204, USA*

^{50} *Huddersfield, Huddersfield, West Yorkshire HD1 3DH, UK*

^{51} *Horia Hulubei National Institute of Physiscs and Nuclear Engineering, Horia Hulubei National Institute of Physiscs and Nuclear Engineering, Bucharest-Magurele, Romania*

^{52} *University of Hyderabad, Gachibowli, Hyderabad - 500 046, India*

^{53} *Institut de Física d'Altes Energies (IFAE); Campus Universitat Autonoma de Barcelona , E-08193 Cerdanyola del Valles (Barcelona), Spain*

^{54} *Illinois Institute of Technology , Room 182LS; Chicago, IL 60616, USA*

^{55} *IIT Hyderabad, Kandi, Hyderabad - 502205, India*

^{56} *Institute for Nuclear Research of the Russian Academy of Sciences (INR RAS), 60th October Anniversary Prosp. 7a Moscow, Russia 117312, Russia*

3

[57]Institute for Research in Fundamental Sciences (IPM), Tehran, Iran. Postal code: 19538-33511 PO Box: 19395-5531, Iran

[58]Idaho State University, Department of Physics 921 South 8th Ave. Stop 8106 Pocatello, ID 83209-8106, USA

[59]Imperial College of Science Tech. & Medicine, Blackett Lab.; Prince Consort Road; London SW7 2BZ, UK

[60]Indian Institute of Technology Guwahati, Guwahati, 781 039, India

[61]Indiana University, Bloomington, IN 47405-7105, USA

[62]Iowa State University, Ames, IA 50011, USA

[63]Institut de Physique Nucleaire de Lyon (IPNL), Rue E. Fermi 4 69622 Villeurbanne, France

[64]University of Jammu, Physics Department, JAMMU-180006, India

[65]Kansas State University, Manhattan, KS 66506, USA

[66]Kavli IPMU, Univ. of Tokyo, Kashiwa Shi, Chiba 277-8568, Japan

[67]KEK, High Energy Accelerator Research Organization 1–1 Oho, Tsukuba-shi; Ibaraki-ken 305-0801, Japan

[68]KYIV National University, Department of Nuclear Physics, 64, 01601 Kyiv, Ukraine

[69]Koneru Lakshmaiah, , India

[70]Krakow, , Poland

[71]Lab. d'Annecy-le-Vieux de Phys. des Particules, BP 110; F-74941 Annecy-le-Vieux CEDEX, France

[72]Laboratori Nazionali del Gran Sasso, I-67010 Assergi, AQ, Italy

[73]Lancaster University, Bailrigg, Lancaster LA1 4YB, UK

[74]Lawrence Berkeley National Lab., Berkeley, CA 94720-8153, USA

[75]Université de Liège, Bat B5, Sart Tilman B-4000, Belgium

[76]Univ. of Liverpool, L69 7ZE, Liverpool, UK

[77]University College London, London, WC1E 6BT, UK

[78]Los Alamos National Laboratory, Los Alamos, NM 87545, USA

[79]Louisiana State University, Baton Rouge, LA 70803-4001, USA

[80]University of Lucknow, Department of Physics Lucknow 226007 Uttar Pradesh, India

[81]Univ. of Manchester, Oxford Road, Manchester M13 9PL, UK

[82]Univ. of Maryland, College Park, MD 20742-4111, USA

[83]Massachusetts Institute of Technology, Cambridge, MA 02139-4307, USA

[84]Max Planck MPP, Max-Planck-Institut fuer Physik (Werner-Heisenberg-Institut) Foehringer Ring 6 80805 Muenchen, Germany

[85]Univ. of Puerto Rico, Box 9016; Mayaguez, PR 00681-9000, USA

[86]University of Michigan, 450 Church Street Ann Arbor, Michigan 48109-1040, USA

[87]Michigan State University, East Lansing, MI 48824, USA

[88]Univ. di Milano, INFN Sezione di Milano, I-20133 Milano, Italy

[89]INFN Sezione di Milano Bicocca, Piazza della Scienza 3, 20126 Milano, Italy

[90]Univ. of Minnesota, Minneapolis, MN 55455, USA

[91]Univ. of Minnesota (Duluth), Duluth, MN 55812, USA

[92]NIKHEF, Science Park, Amsterdam, Netherlands

[93]Istituto Nazionale di Fisica Nucleare - Sezione di Napoli, Complesso Universitario di Monte S. Angelo, I-80126 Napoli, Italy

[94]National Centre for Nuclear Research, A. Soltana 7, 05 400 Otwock, Poland

[95]Jawaharlal Nehru University, New Delhi 110067, INDIA, India

[96]Univ. of New Mexico, MSC07 4220; Albuquerque, NM 87131, USA

[97]Northwestern University, Evanston, Il 60208, USA

[98]Univ. of Notre Dame, Notre Dame, IN 46556-5670, USA

[99]Observatorio Nacional, , Brazil

[100]Ohio State Univ., Dept. of Physics; 191 W. Woodruff Ave.; Columbus, OH 43210, USA

[101]Oregon State University, Dept. of Physics; 301 Weniger Hall; Corvallis, OR 97331–6507, USA

[102]Univ. of Oxford, Oxford, OX1 3RH, UK

[103]Pacific Northwest National Lab, , USA

[104]Pennsylvania State University, PMB 264; University Park, PA 16802-6300, USA

[105]PUCP, Av. Universitaria 1801, Lima, Peru

[106]Univ. of Padova, Dip. Fisica e Astronomia G. Galilei and INFN Sezione di Padova, I-35131 Padova, Italy

[107]Panjab University, Chandigarh, 160014 U.T., India

[108]Univ. of Pavia, INFN Sezione di Pavia, I-27100 Pavia, Italy

[109]Univ. of Pennsylvania, Philadelphia, PA 19104-6396, USA

[110]Univ. di Pisa, Theor. Division; Largo B. Pontecorvo 3, Ed. B-C; I-56127 Pisa, Italy

[111]Univ. of Pittsburgh, Pittsburgh, PA 15260, USA

[112]Princeton University, Princeton, New Jersey 08544-0708, USA

[113] *Punjab Agri. University, Centre for High Energy Physics; Lahore - 54590, India*

[114] *Univ. of Rochester, Rochester, NY 14627-0171, USA*

[115] *SLAC National Acceleratory Laboratory, Menlo Park, CA 94025, USA*

[116] *STFC Rutherford Appleton Laboratory, Harwell Oxford, Didcot OX11 0QX, UK*

[117] *CEA/Saclay, IPhT; Inst. de Physique Theorique; Orme des Merisiers, Point Courrier 136; F-91191 Gif-sur-Yvette CEDE, France*

[118] *Univ. of Sheffield, Sheffield, S3 7RH, UK*

[119] *Univ. of Sofia, Atomic Physics Dept., Faculty of Physics; 5 James Bourchier Blvd.; BG-1164 Sofia, Bulgaria*

[120] *Univ. of South Carolina, Columbia, SC 29208, USA*

[121] *Univ. of South Dakota, Vermillion, SD 57069, USA*

[122] *South Dakota School of Mines and Technology, Rapid City, SD 57701, USA*

[123] *South Dakota Science And Technology Authority, Lead, SD 57754, USA*

[124] *South Dakota State University, Brookings, SD 57007, USA*

[125] *Southern Methodist University, Dallas, TX 75275, USA*

[126] *Stanford University, Varian Physics Bldg.; 382 Via Pueblo Mall; Stanford, CA 94305–4060, USA*

[127] *Stony Brook University, Nucleon Decay and Neutrino Physics Group Department of Physics and Astronomy Stony Brook University Stony Brook, NY 11794-3800, USA*

[128] *Univ. of Sussex, Brighton, BN1 9RH, UK*

[129] *Syracuse University, Syracuse, NY 13244-1130, USA*

[130] *Univ. of Tennessee at Knoxville, Knoxville, TN, USA*

[131] *Univ. of Texas (Arlington), Arlington, TX 76019, USA*

[132] *Univ. of Texas (Austin), Austin, TX 78712-0264, USA*

[133] *TUBITAK Space Technologies Research Institute , TR-06800, Ankara, Turkey*

[134] *Tufts University, Medford, MA 02155, USA*

[135] *Variable Energy Cyclotron Centr, 1/AF, Bidhannagar Kolkata - 700 064 West Bengal, India*

[136] *Instituto de Fisica Corpuscular, C/Catedratico Jose Beltran, 2 E-46980 Paterna (Valencia), Spain*

[137] *Virginia Tech., Blacksburg, VA 24061-0435, USA*

[138] *Univ. of Warsaw, Faculty of Physics ul. Pasteura 5 02-093 Warsaw, Poland*

[139] *Univ. of Warwick, Coventry CV4 7AL, UK*

[140] *Wichita State University, Physics Division 1845 Fairmount St. Wichita, KS 67260-0032, USA*

[141] *College of William and Mary, Williamsburg, VA 23187-8795, USA*

[142] *Univ. of Wisconsin, Madison, WI 53706, USA*

[143] *Wroclaw University, Plac Maxa Borna 9, 50-204 Wroclaw, Poland*

[144] *Yale University, New Haven, CT 06520, USA*

[145] *Yerevan Institute for Theoretical Physics and Modeling, Halabian Str. 34; Yerevan 0036, Armenia*

[146] *York, Physics and Astronomy Dept.; 4700 Keele St.; Toronto M3J 1P3, Canada*

[147] *ETH Zurich, HPK F 23 Schafmattstr. 20 8093 Zürich, Switzerland*

2015-11-25

Contents

List of Figures

List of Tables

Acronyms, Abbreviations and Terms

$\mathcal{O}(n)$	of order n
3D	3 dimensional (also 1D, 2D, etc.)
kt $\cdot$ MW $\cdot$ year	exposure, expressed in kilotonnes $\times$ megawatts $\times$ years, based on 56% beam uptime and efficiency
kt $\cdot$ year	exposure (without beam), expressed in kilotonnes times years
APA	anode plane assembly
BLM	(in Volume 4) beamline measurement (system); (in Volume 3) beam loss monitor
CC	charged current (interaction)
CDR	Conceptual Design Report
CE	Cold Electronics
CF	Conventional Facilities
COB	cluster on-board (motherboards)
CP	product of charge and parity transformations
CPA	cathode plane assembly
CPT	product of charge, parity and time-reversal transformations
CPV	violation of charge and parity symmetry
CRP	Charge-Readout Planes
DAQ	data acquisition

DIS	deep inelastic scattering
DOE	U.S. Department of Energy
DRAM	dynamic random access memory
DUNE	Deep Underground Neutrino Experiment
ECAL	electromagnetic calorimeter
ESH	Environment, Safety and Health
eV	electron volt, unit of energy (also keV, MeV, GeV, etc.)
FD	far detector
FE	front end (electronics)
FGT	Fine-Grained Tracker
FPGA	field programmable gate array
FS	full stream (data volumes)
FSCF	far site conventional facilities
FSI	final-state interactions
GAr	gaseous argon
GEANT4	GEometry ANd Tracking, a platform for the simulation of the passage of particles through matter using Monte Carlo methods
GENIE	Generates Events for Neutrino Interaction Experiments (an object-oriented neutrino Monte Carlo generator)
GUT	grand unified theory
HV	high voltage
L	level, indicates depth in feet underground at the far site, e.g., 4850L
LAr	liquid argon
LArTPC	liquid argon time-projection chamber
LBL	long-baseline (physics)

LBNF	Long-Baseline Neutrino Facility
LEM	Large Electron Multiplier
LNG	liquefied natural gas
MC	Monte Carlo (detector simulation methods)
MH	mass hierarchy
MI	Main Injector (at Fermilab)
MIP	minimum ionizing particle
MTS	Materials Test Stand
MuID	muon identifier (detector)
ND	near neutrino detector
NDS	Near Detector Systems; refers to the collection of detector systems at the near site
near detector	except in Volume 4 Chapter 7, *near detector* refers to the *neutrino* detector system in the NDS
NND	(used only in Volume 4 Chapter 7) near neutrino detector, same as ND
NSCF	near site conventional facilities
PD	photon detection (system)
PMT	photomultiplier tube
POT	protons on target
PPM/PPB/PPT	parts per million/billion/trillion
QA	quality assurance
QE	quasi-elastic (interaction)
RCE	reconfigurable computing element
RIO	reconfigurable input output
RPC	resistive plate chamber

S/N	signal-to-noise (ratio)
SBN	Short-Baseline Neutrino program (at Fermilab)
SiPM	silicon photomultiplier
SM	Standard Model of particle physics
SSP	SiPM signal processor
STT	straw tube tracker
t	metric ton, written *tonne* (also kt)
tonne	metric ton
TPC	time-projection chamber (not used as 'total project cost' in the CDR)
TR	transition radiation
WLS	wavelength shifting
ZS	zero suppression

Chapter 1

Overview

1.1 An International Physics Program

The global neutrino physics community is developing a multi-decade physics program to measure unknown parameters of the Standard Model of particle physics and search for new phenomena. The program will be carried out as an international, leading-edge, dual-site experiment for neutrino science and proton decay studies, which is known as the Deep Underground Neutrino Experiment (DUNE). The detectors for this experiment will be designed, built, commissioned and operated by the international DUNE Collaboration. The facility required to support this experiment, the Long-Baseline Neutrino Facility (LBNF), is hosted by Fermilab and its design and construction is organized as a DOE/Fermilab project incorporating international partners. Together LBNF and DUNE will comprise the world's highest-intensity neutrino beam at Fermilab, in Batavia, IL, a high-precision near detector on the Fermilab site, a massive liquid argon time-projection chamber (LArTPC) far detector installed deep underground at the Sanford Underground Research Facility (SURF) 1300 km away in Lead, SD, and all of the conventional and technical facilities necessary to support the beamline and detector systems.

The strategy for executing the experimental program presented in this Conceptual Design Report (CDR) has been developed to meet the requirements set out in the P5 report [1] and takes into account the recommendations of the European Strategy for Particle Physics [2]. It adopts a model where U.S. and international funding agencies share costs on the DUNE detectors, and CERN and other participants provide in-kind contributions to the supporting infrastructure of LBNF. LBNF and DUNE will be tightly coordinated as DUNE collaborators design the detectors and infrastructure that will carry out the scientific program.

The scope of LBNF is

- an intense neutrino beam aimed at the far site,

- conventional facilities at both the near and far sites, and

- cryogenics infrastructure to support the DUNE detector at the far site.

The DUNE detectors include

- a high-performance neutrino detector and beamline measurement system located a few hundred meters downstream of the neutrino source, and

- a massive liquid argon time-projection chamber (LArTPC) neutrino detector located deep underground at the far site.

With the facilities provided by LBNF and the detectors provided by DUNE, the DUNE Collaboration proposes to mount a focused attack on the puzzle of neutrinos with broad sensitivity to neutrino oscillation parameters in a single experiment. The focus of the scientific program is the determination of the neutrino mass hierarchy and the explicit demonstration of leptonic CP violation, if it exists, by precisely measuring differences between the oscillations of muon-type neutrinos and antineutrinos into electron-type neutrinos and antineutrinos, respectively. Siting the far detector deep underground will provide exciting additional research opportunities in nucleon decay, studies utilizing atmospheric neutrinos, and neutrino astrophysics, including measurements of neutrinos from a core-collapse supernova should such an event occur in our galaxy during the experiment's lifetime.

1.2 The LBNF/DUNE Conceptual Design Report Volumes

1.2.1 A Roadmap of the CDR

The LBNF/DUNE CDR describes the proposed physics program and technical designs at the conceptual design stage. At this stage, the design is still undergoing development and the CDR therefore presents a *reference design* for each element as well as *alternative designs* that are under consideration.

The CDR is composed of four volumes and is supplemented by several annexes that provide details on the physics program and technical designs. The volumes are as follows

- Volume 1: *The LBNF and DUNE Projects*[3] provides an executive summary of and strategy for the experimental program and introduces the CDR.

- Volume 2: *The Physics Program for DUNE at LBNF*[4] outlines the scientific objectives and describes the physics studies that the DUNE Collaboration will undertake to address them.

- Volume 3: *The Long-Baseline Neutrino Facility for DUNE*[5] describes the LBNF Project, which includes design and construction of the beamline at Fermilab, the conventional facilities at both Fermilab and SURF, and the cryostat and cryogenics infrastructure required for the DUNE far detector.

- Volume 4: *The DUNE Detectors at LBNF* describes the DUNE Project, which includes the design, construction and commissioning of the near and far detectors.

More detailed information for each of these volumes is provided in a set of annexes listed on LBNF and DUNE's shared *Proposals and Design Reports* page.

1.2.2 About this Volume

The first part of Volume 4: *The DUNE Detectors at LBNF* of the CDR describes the strategies for implementing the near and far detectors (Chapter 2) and outlines the DUNE management structure (Chapter 3). The next part describes the technical designs: the reference and alternative designs for the far detector and the synergies between them (Chapters 4, 5 and 6), and the near detector systems design (Chapter 7). Following this, Chapter 8 describes the designs for the computing infrastructure and physics software, and Chapter 9 provides an overview of the ongoing and planned prototyping effort. The software and computing efforts, as well as some of the prototyping activities are off-project. Chapter 10 summarizes and concludes the volume.

1.3 Introduction to the DUNE Detectors

1.3.1 Far Detector

The proposed far detector (FD) will be located deep underground at the SURF 4850L with a fiducial mass of 40 kt. It consists of four cryostats instrumented with Liquid Argon Time Projection Chambers (LArTPCs). It is assumed that all four detector modules will be similar but not necessarily identical, allowing for evolution of the LArTPC technology to be implemented.

LArTPC technology provides excellent tracking and calorimetry performance. It is ideal for massive neutrino detectors that require high signal efficiency, effective background discrimination, capability to identify and precisely measure neutrino events over a wide range of energies and high resolution reconstruction of kinematic properties. The full imaging of events in the DUNE detector will allow study of neutrino interactions and other rare events with unprecedented detail. The detector's huge mass will result in data sets large enough to enable precision studies and the search for CP violation.

The mature LArTPC technology, pioneered by ICARUS, is the result of several decades of worldwide R&D. Nonetheless, the size of a single $10-$kt DUNE detector module represents an extrapolation by over one order of magnitude relative to the ICARUS T600, which is the largest detector of this kind operated to date. To address this challenge, DUNE is developing both a reference and an alternative design (see Figure 1.1), and is engaged in a comprehensive prototyping effort. A list of synergies between the reference and alternative designs has been identified and is summarized in Chapter 6. Common solutions for DAQ, electronics, HV feedthroughs, and so on, will be

pursued and implemented, independent of the details of the TPC design choice. The development of the two detector module designs is a considerable advantage, and it is made possible by the convergence of previously separate international neutrino efforts into the DUNE collaboration.
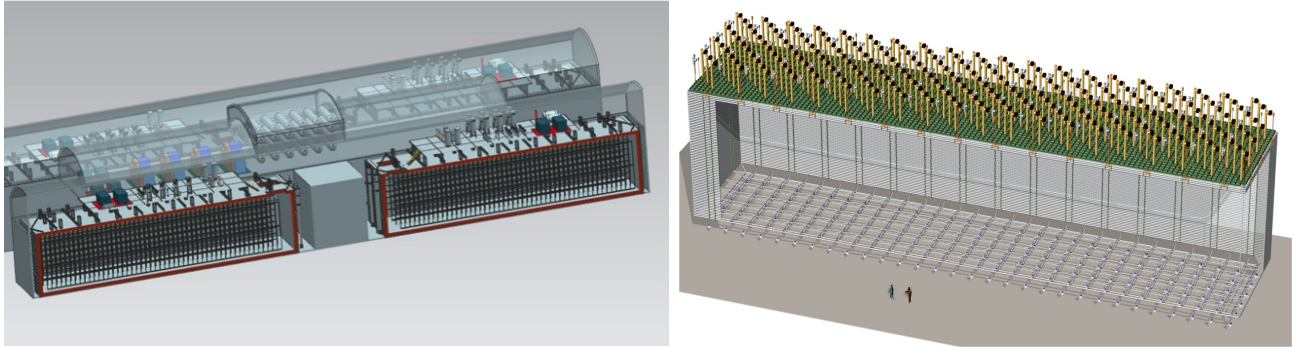
Figure 1.1: 3D models of two 10-kt detectors using the single-phase reference design (left) and the dual-phase alternate design (right) for the DUNE far detector to be located at 4850L.

Interactions in liquid argon (LAr) produce ionization charge and scintillation light. The electrons drift in a constant electric field away from the cathode plane towards the segmented anode plane. The prompt scintillation light is observed by photodetectors that provide the absolute time of the event. The reference design, described in Chapter 4, adopts a single-phase readout, in which the readout anode is composed of wire planes in the LAr volume. The alternate design, discussed in Chapter 5, considers the dual-phase approach, where ionization charge is extracted, amplified and detected in gaseous argon above the liquid surface. The dual-phase design allows a finer readout pitch (3 mm), a lower detection-energy threshold, and better pattern reconstruction of the events. Both the reference and alternate designs include systems to collect the scintillation light.

A comprehensive prototyping strategy for both designs is being actively pursued, as described in Chapter 9. The reference design, closer to the original ICARUS design, is currently being validated in the 35-t prototype LAr detector at Fermilab (see Section 9.2). The novel alternative design approach has been proven on several small-scale prototypes, and a 20-t dual-phase prototype is being constructed at CERN, intended for operation in 2016. Full-scale engineering prototypes will be assembled and commissioned at the CERN neutrino platform; they are expected to provide the ultimate validation of the engineered solutions for both far detector designs around the year 2018.

A test-beam data campaign will be executed at the CERN Neutrino Platform in the following years to collect a large sample of charged particle interactions to study the detector response with high precision.

The deployment of the four 10-kt modules at SURF will take several years and be guided by principles detailed in Chapter 2. According to this strategy, DUNE adopts the lowest-risk design that satisfies the physics and detector requirements and allows installation of the first 10-kt detector module as early as possible. Accordingly, the first 10-kt module will implement the reference design.

A clear and transparent decision process will be adopted for determining the design of the second

and subsequent modules. The decision will be based on physics performance, technical and schedule risks, costs and funding opportunities. Besides taking advantage of technological developments, a flexible approach to the far detector design acknowledges the diversity of DUNE and offers the potential to attract additional interest and resources into the collaboration. A staged approach provides access to an early science program while allowing for new developments to be implemented over the relatively long installation period of the experiment.

1.3.2   Near Detector Systems

DUNE will install a near neutrino detector (NND) $\sim$0.5 km downstream of the target and a Beamline Measurement System (BLM) $\sim$300 m upstream of the NND. These are collectively called the Near Detector Systems (NDS). The NDS will allow DUNE to reduce systematic errors to match the high-statistics phase precision sensitivity for the long-baseline neutrino oscillation studies. The primary role of the neutrino detector is to measure the spectrum and flavor composition of the beam to high precision. This detector will be magnetized so that it can charge-discriminate electrons and muons produced in the neutrino charged current interactions; it will therefore be capable of making separate measurements of the neutrino and antineutrino fluxes.

In addition, exposure to the intense neutrino flux provides the opportunity to collect neutrino interaction data sets of unprecedented size, enabling an extended science program. The near detector therefore provides an opportunity for a wealth of fundamental neutrino interaction measurements which are an important part of the ancillary scientific goals of the DUNE collaboration.

The reference design for the neutrino near detector (NND) design is the NOMAD-inspired fine-grained tracker (FGT) and is described in Chapter 7. The NND subsystems include a central straw-tube tracker and an electromagnetic calorimeter embedded in a 0.4-T dipole field. The magnet yoke steel will be instrumented with muon identifiers.

The Beamline Measurement System (BLM), designed to measure the muon flux from hadron decay, is located in the region of the beam absorber at the downstream end of the decay region. It is intended to monitor the beam profile on a spill-by-spill basis and will operate for the life of the experiment.

Chapter 2

Implementation Strategy

2.1 Overview

Recommendation 12 of the Report of the Particle Physics Prioritization Panel (P5) states that for a Long-Baseline Neutrino Oscillation Experiment to proceed "The minimum requirements to proceed are the identified capability to reach an exposure of 120 kt $\cdot$ MW $\cdot$ year by the 2035 timeframe, the far detector situated underground with cavern space for expansion to at least $40-$kt LAr fiducial volume, and $1.2-$MW beam power upgradable to multi-megawatt power. The experiment should have the demonstrated capability to search for supernova bursts and for proton decay, providing a significant improvement in discovery sensitivity over current searches for the proton lifetime." The strategy presented here meets these criteria. The P5 recommendation is in line with the CERN European Strategy for Particle Physics (ESPP) of 2013, which classified the long-baseline neutrino program as one of the four scientific objectives with required international infrastructure.

2.2 Strategy for Implementing the DUNE Far Detector

The LBNF Project will provide four cryostats at the 4850L of the Sanford Underground Research Facility (SURF) in which the DUNE Collaboration will deploy four $10-$kt (fiducial) mass far detector LArTPCs. DUNE contemplates two options for the read out of the ionization signals: single-phase readout, where the ionization is detected using wire planes in the liquid argon volume; and dual-phase readout, where the ionization signals are amplified and detected in gaseous argon above the liquid surface. An active development program for both technologies is being pursued in the context of the CERN neutrino platform, as well as the the Fermilab SBN program.

The viability of the LArTPC technology has been proven by the ICARUS experiment with single-phase wire plane LArTPC readout, where data was successfully accumulated over a period of three years. An extrapolation of the observed performance and implementation of improvements in the design (e.g., cold electronics) will allow the single-phase approach (see Chapter 4) to meet DUNE

requirements, and is hence adopted as the *reference design*.

The reference design is already relatively advanced for the conceptual design stage. Modifications of the reference design will be approved by the DUNE technical board. A preliminary design review will take place as early as possible, utilizing the experience from the DUNE 35-t prototype; the design review will define the baseline design that will form the basis of the TDR (CD-2). Once defined, changes to the baseline will fall under a formal change-control process. An engineering prototype consisting of six full-sized drift cells will be validated at the CERN neutrino platform. This engineering prototype at CERN is a central part of the risk mitigation strategy for the first $10-$kt FD module. Following experience at the CERN neutrino platform, the DUNE technical coordinator will organize a final design review. The CERN single-phase prototype provides the opportunity for production sites to validate manufacturing procedures ahead of large-scale production for the far detector. Three major operational milestones are defined for this single-phase prototype: 1) engineering validation – successful cool-down; 2) operational validation – successful TPC readout with cosmic-ray muons; and 3) physics validation with test beam data. Reaching milestone 2 will allow the retirement of a number of technical risks for the construction of the first $10-$kt detector module.

In parallel with preparation for construction of the first $10-$kt detector module, the DUNE Collaboration recognizes the potential of the dual-phase technology and strongly endorses the already approved WA105 experiment at the CERN neutrino platform, which includes the operation of the 20-ton prototype and the $6 \times 6 \times 6$ m^3 WA105 demonstrator. Many DUNE collaborators are participants in the WA105 experiment. A concept for the dual-phase implementation of a far detector module is presented in detail as an *alternative design* in Chapter 5. This alternative design, if demonstrated, could form the basis of the second or subsequent $10-$kt far detector modules, to achieve improved detector performances in a cost-effective way.

The DUNE program at the CERN neutrino platform will be coordinated by a single manager. Common technical solutions will be adopted wherever possible. The charged-particle test-beam data will provide essential calibration samples for both technologies and will enable a direct comparison of the relative physics benefits.

For the purposes of cost and schedule, the reference design for the first far detector module is adopted as the reference design for the subsequent three modules. However, the experience with the first $10-$kt module and the development activities at the CERN platform are likely to lead to the evolution of the TPC technology, both in terms of refinements to single-phase design and the validation of the operation of the dual-phase design. The technology choice for the second and subsequent LArTPCs will be based on risk, cost (including the potential benefits of additional non-DOE funding) and physics performance (as established in the CERN charged-particle test beam).

As already stated, this strategy allows flexibility with respect to international contributions and provides the possibility of attracting interest and resources from a broader community with space for flexibility to respond to the funding constraints from different sources.

2.3 Strategy for Implementing the DUNE Near Detector Systems

Within the former LBNE collaboration the neutrino near detector (NND) design was the NOMAD-inspired fine-grained tracker (FGT), which was developed through a strong collaboration of Indian and U.S. institutions. DUNE adopts the FGT concept as the *reference design* for the NND according to the following guidelines:

- The primary design consideration of the DUNE NND is the ability to adequately constrain the systematic errors in the DUNE long-baseline oscillation analysis.

- The secondary design consideration for the DUNE NND is the self-contained non-oscillation neutrino physics program.

- It is recognized that a detailed cost-benefit study of potential NND options has yet to take place and such a study is of high priority to DUNE.

The cost and resource-loaded schedule are based on the design presented in Chapter 7.

The contribution of Indian institutions to the design and construction of the DUNE FGT near detector is a vital part of the strategy for the construction of the experiment. The reference design will provide a rich, self-contained physics program. From the perspective of the high-statistics phase of the long-baseline oscillation program, there may be benefits of augmenting the FGT with a relatively small LArTPC that would allow for a direct comparison with the far detector, or adding a high-pressure gaseous argon TPC. At this stage, the benefits of such options have not been studied, nor are alternative designs for the NND presented in the CDR; they will be the subject of detailed studies in the coming months.

A full end-to-end study of the impact of the reference NND design on the oscillation systematics has yet to be performed. Many of the elements of such a study are in development, for example the Monte Carlo simulation of the FGT and the adoption of the T2K framework for implementing near detector measurements as constraints in the propagation of systematic uncertainties to the far detector. After the CD-1-R review, the DUNE Collaboration will initiate a detailed study of the optimization of the NND. To this end a task force will be set up with the charge to

- Deliver the simulation of the reference design of the NND and possible alternatives;

- Undertake an end-to-end study to provide a quantitative understanding of the power of the NND designs to constrain the systematic uncertainties on the long-baseline oscillation measurements; and

- Quantify the benefits of augmenting the reference design with a LArTPC or high-pressure gaseous argon TPC.

High priority will be placed on this work and the intention is to engage a broad cross section of the collaboration in this process. The task force will be charged to deliver a report by July 2016. Based on this report and input from the DUNE technical board, the DUNE executive board will refine the DUNE strategy for the near detector.

Chapter 3

DUNE Project Management

3.1 Overview

The international DUNE Project is responsible for managing all contributions to the design, construction, installation and commissioning of the DUNE near and far detectors.

As described in CDR Volume 1: *The LBNF and DUNE Projects*, the DUNE Project is integrated within the DUNE Collaboration (*the collaboration*). The collaboration, in consultation with the Fermilab director, is responsible for forming the international project team. The leaders of this team are the Technical Coordinator (TC) and Resource Coordinator (RC), who are jointly appointed by the DUNE Co-Spokespersons and the Fermilab Director. The project receives appropriate oversight from stakeholders including the Fermilab Directorate and DOE. A detailed description of the collaboration structure along with its advisory and coordinating structures is contained within Chapter 4 of CDR Volume 1: *The LBNF and DUNE Projects*.

The DUNE Project is responsible for coordinating the work packages assigned to each of the international partners contributing to the effort. These individual work packages, which are supported through independent funding agencies, have internal management structures that are responsible for satisfying the tracking and reporting requirements of the supporting agencies. However, the entire project scope (including non-DOE partner contributions) will be subject to the DOE critical decision process.

The international DUNE Project Office maintains a schedule for the entire project and tracks individual contributions through detailed sets of milestones embedded within the schedule. It is also responsible for ensuring that the interfaces between the different work package deliverables are well defined and that all of these deliverables meet safety and operational readiness requirements for installation at Fermilab and the Sanford Underground Research Facility. Project Office members including the Project Manager are appointed by the TC. The managers of the collaboration detector and prototyping organizations report to the Project Manager and provide the required interface between the DUNE project and the other members of the collaboration contributing to these efforts. As members of these organizations, they participate in all discussions related to

the design, construction, installation and commissioning of individual detector elements. Managers have the primary responsibility for implementing collaboration plans developed within their organizations.

Following this model, the DUNE-US project will have its own project office and management structure. All normal DOE project management requirements will apply to the DUNE-US project. In its role as host, the DOE will provide financial support for both the international DUNE Project Office and the DUNE-US Project Office. The DUNE TC, who acts as Project Director in the context of the international DUNE project, also serves as the DUNE-US Project Director. However, each project office will have its own project manager. Other equivalent positions within the project offices may be filled by the same individuals in cases where the TC believes this sharing of resources to be most efficient. Some project office staff may also overlap with the LBNF project office as appropriate.

3.2 WBS

The DUNE Project will manage all contributions to the design, construction, installation and commissioning of the DUNE near and far detectors through an international Work Breakdown Structure (WBS). The WBS organizes the Project's tasks and deliverables into convenient components and is used to organize the cost and schedule for the DUNE project. The DUNE Project consists of two major subsystems: the Near Detector (WBS 130.03), shown to WBS level 4 in Figure 3.1, and the Far Detector (WBS 130.05), shown to WBS level 3 in Figure 3.2.

The DUNE Project organization and structure will evolve as the project becomes more fully internationalized.
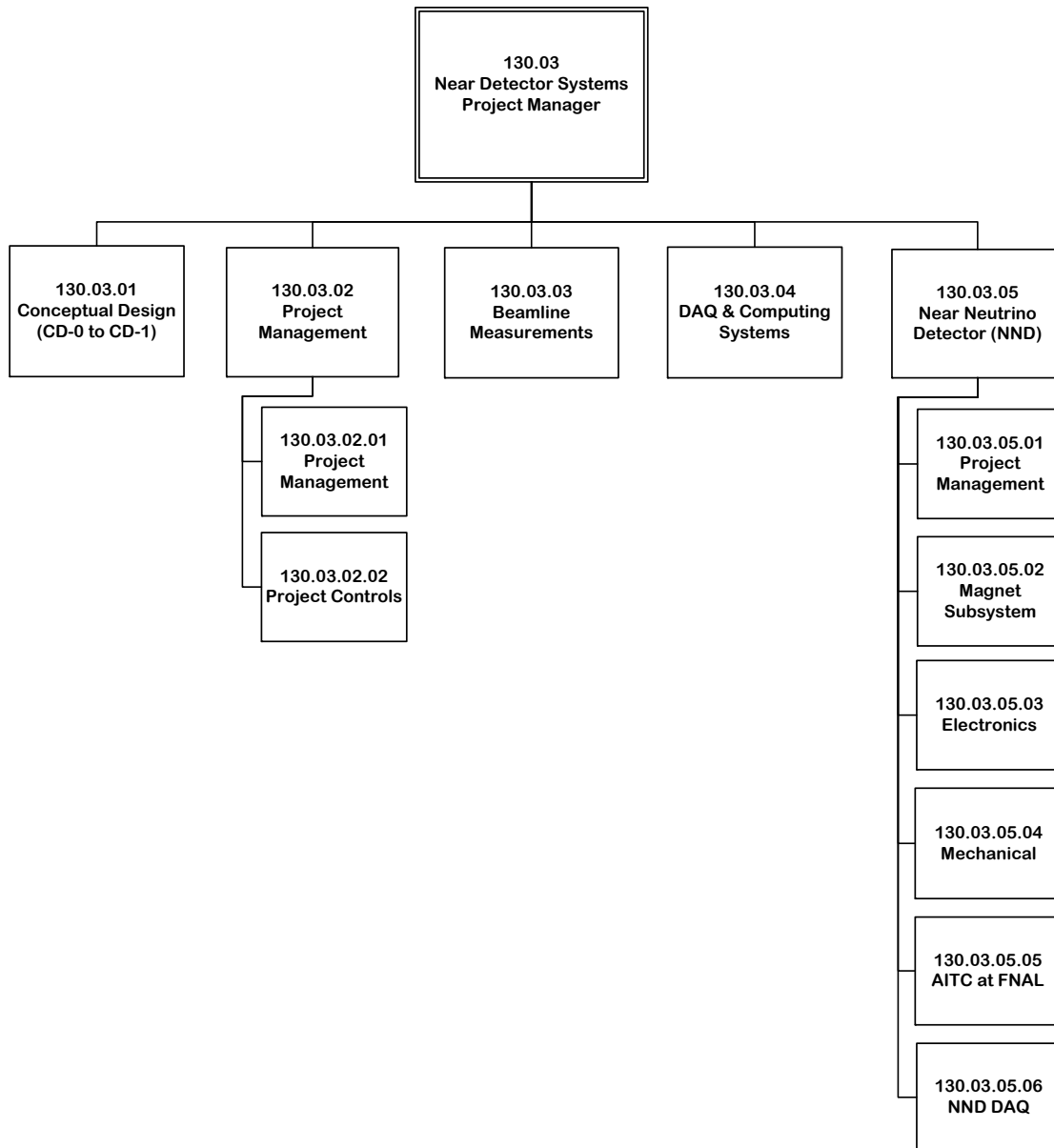
Figure 3.1: Near detector Work Breakdown Structure.
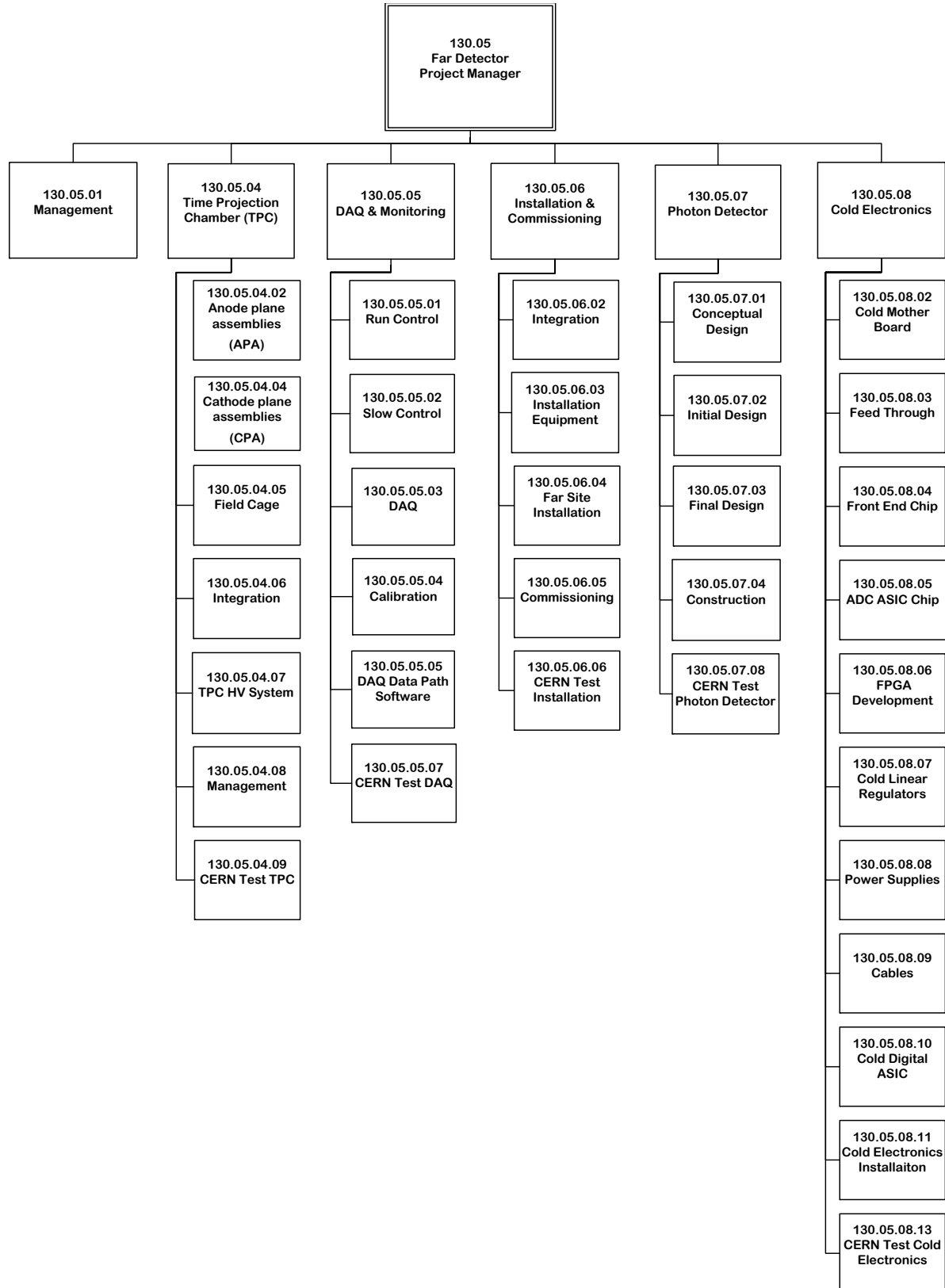
Figure 3.2: Far detector Work Breakdown Structure.

Chapter 4

Far Detector Reference Design: Single-Phase LArTPC

4.1 Overview

This chapter describes the reference design of the DUNE far detector. The reference design consists of four nominal $10-$kt fiducial mass, single-phase LArTPC modules, augmented with photon detection systems. A "single-phase" detector is one in which the charge generation, drift and collection all occur in liquid argon (LAr). The scope of the far detector includes the design, procurement, fabrication, testing, delivery, installation and commissioning of the detector components:

- Time Projection Chamber (TPC)

- Data Acquisition System (DAQ)

- Cold Electronics (CE)

- Photon Detector System (PD)

The LArTPCs will be housed in cryostats provided by LBNF, described in Volume 3: *The Long-Baseline Neutrino Facility for DUNE*. The reference design is based largely on the LBNE far detector design as of January 2015, documented in Annex 4A: *The LBNE Design for a Deep Underground Single-Phase Liquid Argon TPC* [6]. This annex provides the detailed descriptions of the systems and components that the DUNE reference design incorporates; the differences between the DUNE and LBNE designs are clearly indicated in this chapter. Differences include detector size, APA and CPA placement, and small changes to the APA dimensions.

The detector modules will be constructed sequentially with the first module coming online as soon as possible and the rest at a regular pace thereafter. A model of the underground experimental area with the four $10-$kt LArTPCs is shown in Figure 4.1.
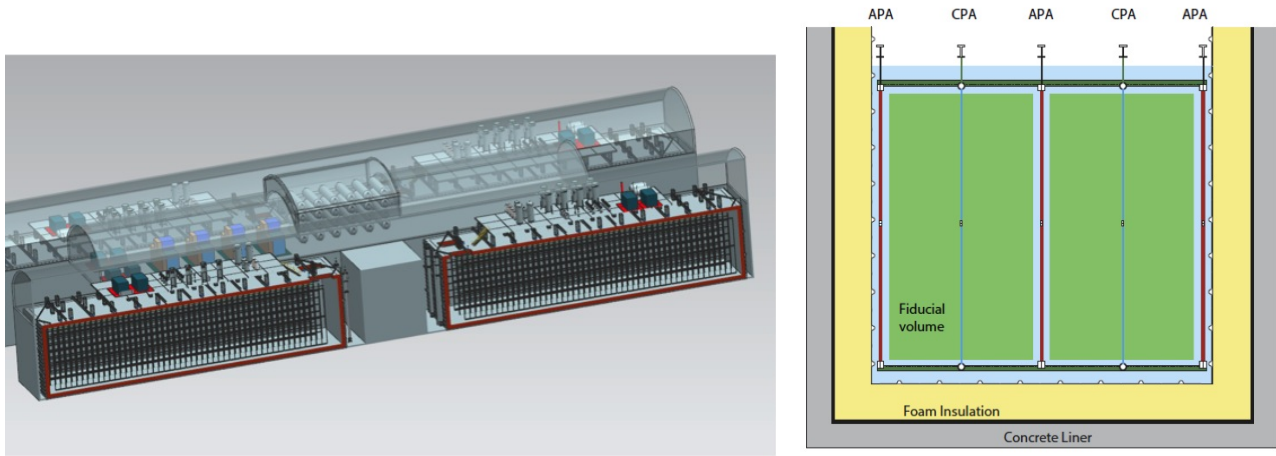
Figure 4.1: Left: 3D model of the reference design for the DUNE far detector to be located at the 4850L. Right: Schematic view of the active detector elements showing the plane ordering of the TPC inside the detector.

Planning for the conventional facilities calls for construction of the second cryostat to be completed prior to filling the first so that it may serve initially as a liquid storage facility. The detector technology is expected to improve in the coming years with MicroBooNE, the SBN program and the CERN neutrino platform. DUNE's staged program allows selection of optimal designs for each module as the technology evolves.

The reference design presented in this chapter and documented in the project cost and schedule is patterned after the successful ICARUS experiment, but adapted to the local site requirements at SURF and the scaled up detector size. The TPC configuration is shown on the right in Figure 4.1. The TPC, described in Section 4.3, is constructed by placing alternating high-voltage cathode planes and anode readout planes in a bath of ultra-pure liquid argon. Particles interacting in the argon generate electron-ion pairs and scintillation light.

The single-phase design offers the advantage that the charge is collected directly without gain, enabling precision charge calibration. However, signal levels are low, requiring the use of cold electronics (Section 4.5). The readout is based on stereo induction and collection planes, requiring a deconvolution of the induced signal. A photon detection system (Section 4.6) provides the t_0 (event time) for physics processes that are uncorrelated with the LBNF neutrino beam.

4.2   Reference Design Expected Performance

The physics requirements are described in Volume 2: *The Physics Program for DUNE at LBNF*, for the long-baseline oscillation, atmospheric, supernova and nucleon decay physics programs. This section outlines the numerical detector performance parameters needed to meet the requirements and the ability of the far detector reference design to achieve these performance parameters.

The expected performance of the far detector reference design is based on the measured performance of the ICARUS[7] and ArgoNeuT[8] detectors, scanned Monte Carlo events[9] and newer studies with automated reconstruction, which are described in Sections 8.4.1, 8.4.2 and in Annex 4C: *Simulation and Reconstruction* [10]. Simulation and reconstruction studies are ongoing. While many components are in place, a full end-to-end simulation, reconstruction and analysis chain does not yet exist. Many of the numerical detector performance requirements are estimates; some of them correspond to achievements by ICARUS and ArgoNeuT, although these detectors differ somewhat from the DUNE far detector. Additional parameters will be calibrated using the data from LArIAT and the two CERN prototypes, the *Full-Scale Detector Engineering Test and Test Beam Calibration of a Single-Phase LArTPC* and the *Long Baseline Neutrino Observatory Demonstration (WA105)*.

Table 4.1 lists the required performance values, achieved values (if any) and the values expected from DUNE. The rest of this section describes each parameter and its connection to the detector design and physics goals.

Table 4.1: Preliminary summary of the most important performance parameters of the DUNE reference design far detector. For each parameter, the table lists the performance requirement, performance achieved by other detectors and projected performance for DUNE. References are given. Notes: [1]For a MIP at the CPA, minimum in all three views, for any track angle; [2]Achieved for the collection view; [3]In order for the fiducial volume to be known to $\pm 1\%$, the resolution performances are reported separately in the x, y, and z directions, where z points along the neutrino beam axis; [4]For a sample of stopping muons; [5]For short electron tracks (stubs) with $E > 5\,\mathrm{MeV}$.

Parameter	Requirement	Achieved Elsewhere	Expected Performance
Signal/Noise Ratio[1]	$9:1$	$10:1$ [11, 12][2]	$9:1$
Electron Lifetime	$3\,\mathrm{ms}$	$> 15\,\mathrm{ms}$ [12]	$> 3\,\mathrm{ms}$
Uncertainty on Charge Loss due to Lifetime	$< 5\%$	$< 1\%$ [12]	$< 1\%$
Dynamic Range of Hit Charge Measurement	$15\,\mathrm{MIP}$		$15\,\mathrm{MIP}$
Vertex Position Resolution[3]	$(2.5, 2.5, 2.5)\,\mathrm{cm}$		$(1.1, 1.4, 1.7)\,\mathrm{cm}$ [13, 14]
$e - \gamma$ separation ϵ_e	> 0.9		0.9
$e - \gamma$ separation γ rejection	> 0.9		0.99
Multiple Scattering Resolution on muon momentum[4]	$\sim 18\%$	$\sim 18\%$ [15, 16]	$\sim 18\%$
Electron Energy Scale Uncertainty	$\sim 5\%$	$\sim 2.2\%$[17]	From LArIAT and CERN Prototype
Electron Energy Resolution	$0.15/\sqrt{E(\mathrm{MeV})}$ $\oplus 1\%$	$0.33/\sqrt{E(\mathrm{MeV})}$ [17] $+1\%$	From LArIAT and CERN Prototype
Energy Resolution for Stopping Hadrons	$< 10\%$		From LArIAT and CERN Prototype
Stub-Finding Efficiency[5]	$> 90\%$		$> 90\%$

The signal-to-noise ratio requirement is motivated by the need to detect small signals in a large detector that has a low signal rate, while limiting the required output data volume. It is set at 9:1

for a minimum-ionizing particle (MIP) in all three views, for any orientation of the track. This ratio is required for all particles in the detector, specifically those ionizing the liquid argon close to the CPA, where the reattachment effects are greatest. Since the strategy is to zero-suppress the data, it is important that the data volume from random excursions of the noise over the zero-suppression threshold compose a vanishingly small fraction of all ADC samples, and that it preserve the detector's ability to detect sub-MIP signals (e.g., signals from nuclear de-excitation photons or isolated hits on the edges of electromagnetic showers). Since the noise in the detector may vary by channel and by time, and in addition to thermal noise from the wires and the electronics, may include coherent noise sources from electromagnetic pickup and acoustical vibrations of the wires, among other sources, sufficient contingency on the signal-to-noise ratio is necessary to ensure that the detector meets the physics requirements. A value of 10:1 was achieved by ICARUS[11, 12] and even higher values were achieved by Long Bo[18]. Similar to the DUNE design, Long Bo used cold electronics, although its wires were much shorter than those planned for DUNE.

The electron lifetime requirement is set at 3 ms to preserve the signal-to-noise ratio across the entire detector volume in the presence of noise sources that are not yet foreseen. A shorter lifetime also places demands on the dynamic range of the ADCs: the gain will need to be large enough to detect weak signals at the CPA, but small enough to record strong signals near the APAs without saturation, if possible. The calorimetric energy resolution of low-energy electrons is highly sensitive to the lifetime for electrons that do not record flashes in the photon-detection system. The energy resolution is approximately 20% for electrons of energy below 50 MeV (see Section 4.2.1) without corresponding photon flashes in a detector with a 2.5-m maximum drift length, assuming only an average correction is applied for the lifetime. This resolution rapidly degrades for shorter lifetimes and longer drift lengths. For a maximum drift length of 3.6 m and an electron lifetime of 1.5 ms, the energy resolution is estimated to degrade to 44%. A lifetime of 3 ms is consistent with that achieved by the 35-t prototype. The ICARUS Collaboration has reported a much longer lifetime, >15 ms[12].

The charge loss due to lifetime effects is expected to be well measured in the DUNE far detector. In addition to the cosmic-ray muons which accumulate at a rate of 0.26 Hz (see Annex 4B: *Expected Data Rates for the DUNE Detectors* [19]), the laser calibration system and purity monitors will provide detailed time-dependent measurements of the electron lifetime. This limit is placed at 1% in order to meet the energy-scale and resolution requirements for electrons, and to a lesser extent, to meet the requirements of dE/dx-based particle identification algorithms.

The dynamic range requirement is placed at 15 MIP in order to detect, without ADC saturation, particle ionization densities from one MIP up to the last hit on a track before a particle stops. The typical application is for protons, where data from ArgoNeuT show roughly a factor of 15 between the lowest-charge hit and the highest. Nonetheless, particles also travel along wires and dense showers may require even more dynamic range before saturation. The desire to measure sub-MIP signals also expands the desired dynamic range. MicroBooNE set a requirement of 50 on the signal dynamic range[20]. The dynamic range requirement is effectively a compound requirement on the noise level, electron lifetime and number of bits in the ADC.

The primary vertex position resolution requirement is intended to keep it from being a significant source of uncertainty on the fiducial volume determination, though this effect is mitigated if the resolution is well known. The current resolution from PANDORA, a pattern recognition program

developed at Cambridge, easily meets this requirement. The axis along which the resolution is the weakest is that of the neutrino beam direction and the asymmetry in the achieved resolution is not a result of detector anisotropy. Tighter demands on the primary vertex position resolution will be made by topological selection of $\pi^0 \to \gamma\gamma$ decays, which require pointing of the photon-induced showers back to the primary vertex.

In order to reduce the neutral-current background to ν_eCC events by a factor of roughly 100, information from the dE/dx of the initial $\sim 2.5\,\mathrm{cm}$ of an electromagnetic shower must be combined with the topological $\pi^0 \to \gamma\gamma$ selection[9]. Current Monte Carlo studies indicate that, for showers with enough hits in the initial part to measure dE/dx, the performance of the ionization method is roughly 90% electron efficiency with a 90% rejection factor for single photons. A topological hand-scan indicates that a ν_eCC signal efficiency of $\sim$80% with a 95% rejection of neutral-current background can be obtained. With optimizations to the dE/dx analysis and automating the pattern-recognition identification of π^0 decays by topology, it is anticipated that the requested level of 99% π^0 rejection can be obtained at 90% signal efficiency.

The momentum of muons in ν_μCC events is an important ingredient in measuring the ν_μ energy spectrum in the far detector, which is one of the inputs to the oscillation parameter fits. Muons that stop in the detector volume will be well measured using their range. For those that are not contained the distribution of deviations of the muon track from a straight line is a function of the muon momentum. The expected performance of $\pm 18\%$ on the muon momentum was achieved by ICARUS for a sample of stopping muons, where the momentum measured by multiple scattering was compared against that obtained from the range. It is anticipated that the resolution will deteriorate for higher-energy muons because they scatter less.

The requirements on the electron energy-scale uncertainty and the resolution are driven by the need to analyze the reconstructed ν_e energy spectrum to extract oscillation parameters in the high-statistics phase of DUNE. A fraction of the energy of an electromagnetic shower escapes in undetected low-energy photons that can be simulated, but this fraction must be calibrated in data in order to give confidence in the uncertainty. An absolute energy scale will need to come from test-beam data — LArIAT and the CERN prototypes, the *Full-Scale Detector Engineering Test and Test Beam Calibration of a Single-Phase LArTPC* and the *Long Baseline Neutrino Observatory Demonstration (WA105)*. Analyzing $\pi^0 \to \gamma\gamma$ decays in ICARUS[17] gives an achieved $\pm 2.2\%$ uncertainty on the electromagnetic energy scale. The same data also constrain the energy resolution. The proposed data sets from the test-beam experiments will measure these, though the results will need to be extrapolated to the DUNE far detector geometry and readout details using a full simulation. Similarly, the detector response to hadrons — protons, charged pions and kaons — will be calibrated to the necessary precision by LArIAT and the CERN prototypes.

Absent from the list is a requirement on the two-hit resolution. In the direction parallel to the drift field, this resolution is expected to be very good, of the order of $2\,\mathrm{mm}$, given existing ArgoNeuT data and simulations. The resolution in the other two dimensions is governed by the wire spacing. Separation of hits is important for pattern recognition, for counting tracks near the primary vertex (which is important for classifying neutrino scatters as quasi-elastic, resonant, or DIS), and for associating dense groups of tracks in showers between views. More study is required to determine the required two-hit resolution.

It is expected that as the software tools improve and as measurements from MicroBooNE and the dedicated test-beam programs become available, the uncertainties on the projected performance will become smaller.

4.2.1   Expected Performance for Low-Energy Events

Low-energy (5–50 MeV) events require special consideration. Electron-type neutrino interactions appearing close together in time constitute the signature for a supernova burst event. A $5-$MeV electron is expected to hit four wires in the DUNE far detector, and given the signal-to-noise requirement above, it is anticipated that this signal will be easy to separate from noise with the required 90% efficiency. (Similarly, the photon-detection system is expected to detect the energy from a proton decay event resulting in a $100-$MeV kaon with high efficiency.)

Work is currently underway using the LArSoft simulation package to characterize low-energy response for realistic DUNE detector configurations. So far, most studies have been done with the MicroBooNE geometry, with the results expected to be generally applicable to the larger DUNE detector. For a preliminary understanding of achievable energy resolution, isotropic and uniform monoenergetic electrons with energies of 5–50 MeV (which should approximate the ν_eCC electron products) were simulated and reconstructed with the LArSoft package. The charge of reconstructed hits on the collection plane was used to reconstruct the energy of the primary electrons. (Compared to induction-plane and track-length-based reconstruction in this preliminary study, collection-plane hit charge gave the best resolution results; however, improved reconstruction based on broader information should be possible.) Figure 4.2 shows the results of a resolution study. A correction to compensate for loss of electrons during drift, $Q_{\mathrm{collection}} = Q_{\mathrm{production}} \times e^{-T_{\mathrm{drift}}/T_{\mathrm{electron}}}$ (where T_{drift} is the drift time of the ionization electrons, and T_{electron} is the electron lifetime), using Monte Carlo truth to evaluate T_{drift}, improved resolution significantly. This study indicated that photon-time information will be valuable for low-energy event reconstruction. Some of the resolution was determined to be due to imperfect hit-finding by the nominal reconstruction software. A tuned hit-finding algorithm did somewhat better (Figure 4.2), and further improvements for reconstruction algorithms optimized for low-energy events are expected.

Also under study is the potential for tagging ν_eCC absorption events ($\nu_e + {}^{40}\mathrm{Ar} \rightarrow e^- + {}^{40}\mathrm{K}^*$) using the cascade of de-excitation γ rays (that Compton-scatter in the detector); this should serve the dual purposes of rejecting background and isolating the CC component of the supernova burst signal. Reconstructing these gammas also improves the neutrino energy measurement.

4.2.2   Reference Design Optimization

Considerations of physics reach as well as cost, schedule and risk enter the optimization of the detector design parameters. Ideally one would like to estimate the asymptotic far-future performance of a full simulation, reconstruction and analysis chain, replicated for each design parameter choice and then choose the values that maximize sensitivity while minimizing the cost and producing timely physics results. While the GEANT4 simulation is fairly mature, it needs to be tuned to
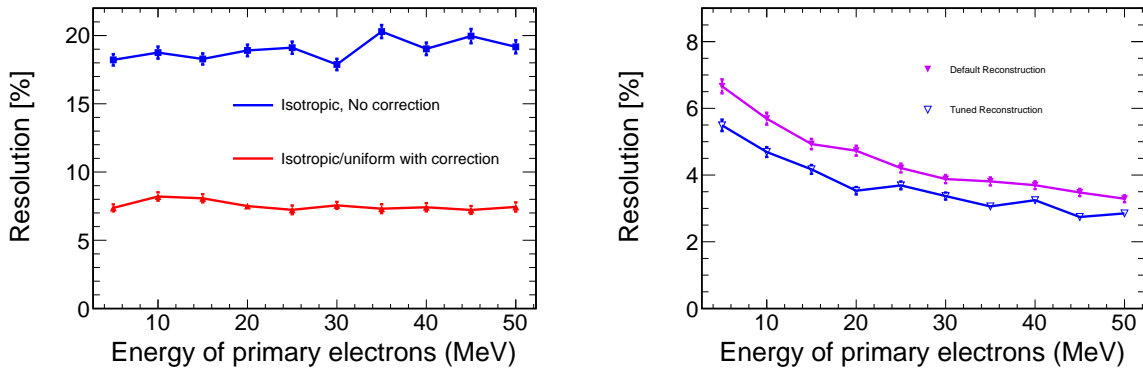
Figure 4.2: Left: Comparison of energy resolution (defined as σ/E, where σ is the spread of the collection-plane-charge-based event energy E for a monoenergetic electron), with and without electron-lifetime correction, as a function of electron energy (assumptions: 3 ms drift time, 1.63 mm/μs drift velocity, and 2.5 m maximum drift length). The blue curve is the energy resolution of isotropic and uniform electrons without electron-lifetime correction. The red curve is the energy resolution with electron-lifetime correction based on MC truth. Right: Comparison of energy resolution before and after tuning the reconstruction algorithm (for fixed position/direction electron events).

data from the 35-t prototype and MicroBooNE so that realistic signal and noise modeling, which are inputs to the optimization procedures, can improve the performance modelling. The reconstruction tools are under development (see Section 8.4) and thus, physics sensitivity is currently optimized using estimates of detector performance that are input to the Fast Monte Carlo. The DUNE collaboration plans to establish a detector performance optimization task force to review various possible detector optimizations in light of the new collaboration and project organizations. This section briefly outlines the considerations and procedures that have been and will be used to optimize these parameters: the wire pitch, wire angle, wire length and maximum drift length. The wire length, angle and pitch are directly related to the APA dimensions, as discussed in Section 4.3 and the APA dimensions are constrained by the needs of manufacturing, storage, transport and assembly.

Wire Pitch

The spacing between neighboring sense wires in the APAs is an optimizable parameter. In principle it is freely adjustable for all three wire planes, though to minimize the anisotropy of the detector response, similar wire pitch should be chosen in all three planes. The choice of a ∼5 mm pitch is documented in[21]. The pitch of the grid plane wires is less important as they are not instrumented, though the grid wires do shadow the optical detectors and therefore should not be made with too fine a pitch.

The signal-to-noise ratio is expected to be proportional to the wire spacing, assuming that the noise on a channel is not impacted by the presence of nearby wires, and that the signal is divided among the available channels. Thermal noise and uncorrelated electronics noise satisfy these conditions. Coherent noise is a special case — filters may be applied either online or offline to reduce its

impact.

The signal-to-noise ratio requirement is set so that zero-suppression can function without elaborate noise filtering. A high signal-to-noise ratio improves pattern-recognition performance, calorimetric PID performance and dE/dx-based $e - \gamma$ separation. It is also important for detecting sub-MIP signals, such as nuclear de-excitation photons, and it is important when adding up the energy of hits on the edges of showers or on the ends of stubs initiated by supernova neutrino interactions.

The signal-to-noise ratio is expected to be higher in the collection plane than in the two induction planes. The need to deconvolve the bipolar signals while filtering noise in the induction planes means that the collection plane will be the most reliable in performing dE/dx measurements, though for tracks that travel in a plane containing a collection wire and the electric field, the induction planes will be critical for recovering PID efficiency. Reducing the spacing between wires will have an adverse impact on the detector performance parameters that depend on the signal to noise, with the effect seen more prominently in the induction-plane data.

The main benefit of a finer wire pitch is the ability to obtain higher resolution measurements of the ionization density left by events in the detector. The spatial resolution in the plane perpendicular to the electric field is also affected by transverse diffusion of the drifting electrons. It can be argued that the wire spacing does not need to be much smaller than the typical width induced by diffusion, though deconvolution and/or fitting techniques that combine signals from nearby wires can recover some of the resolution lost to diffusion. Noise may limit the amount of resolution gained using these techniques.

The separation of electrons from photons using the dE/dx measured in the initial part of an electromagnetic shower is described in Annex 4C: *Simulation and Reconstruction* [10]. The first 2.5 cm of a shower is the most important, since subsequent showering stages have not yet taken place, leaving one MIP for an electron and two for a photon conversion to two electrons, though sometimes the subsequent showering starts earlier. As the first hit cannot be used to measure dE/dx (since it is not known where in the volume of argon viewed by that wire the track started, the second and subsequent hits must be used. But the shower can be aligned unfavorably along the wires of one view or another, resulting in few usable hits. If no hits are useful, then the dE/dx method cannot be used. Reducing the spacing between wires in all three views increases the precision of the measurement of the initial part of the shower for $e - \gamma$ separation purposes. The current study described in [10] only uses the collection plane wires; thus with a more optimal strategy, some of the efficiency that is lost with 5-mm wire spacing compared with 3-mm spacing can be recovered by examining the other two views.

Separation of multiple close tracks is improved with more closely spaced wires. The position resolution of hits is expected to be much better along the drift direction than in either of the axes perpendicular to it as the sampling frequency times drift velocity is much smaller than the wire spacing. As long as the tracks that should be separated from one another travel at an angle with respect to the APA plane, then the fine time resolution will help with the pattern recognition even if the wire pitch is large.

The reconstruction of short tracks, such as low-energy protons ejected by the struck nucleus at the primary vertex of a neutrino scattering event, is improved with higher spatial resolution. A

reduced wire pitch also allows more precise measurements of the distance between the primary vertex and photon conversion points, which is the other component of $\pi^0 \to \gamma\gamma$ separation from electrons. Topological identification of two EM showers and their displacement from the primary vertex is expected to provide a factor of ten to twenty in NC background rejection while retaining at least 90% efficiency for ν_eCC events. A hand-scan study comparing liquid argon TPC detector performance in topological separation of NC events from ν_eCC events in a detector with 5-mm wire pitch and a detector with 10-mm wire pitch[22] showed no degradation in performance with the coarser wire pitch. Automated topological selection has yet to be developed, though it is anticipated that this finding will remain true, given that the radiation length in liquid argon is typically ∼30 times the typical wire spacing.

The gains in physics from a finer wire pitch must be balanced against the increased cost of the electronics and online computing resources needed to read out the additional wires. In addition, the additional cold electronics components would likely create a higher heat load in the liquid and manufacturing the APAs would likely take longer due to the higher density of wires.

The spacing between the planes is customarily chosen to be similar to the spacing between the wires within the planes, though this, too, is an optimizable parameter. Narrowing this spacing improves the sharpness of the signals (in time) in both the induction and collection planes, though electronics shaping and diffusion will limit the ultimate signal sharpness. These functions can be deconvolved, though deconvolution and noise filtering produce artifacts in the signals. Studies varying the spacing between the planes can be performed to estimate the impact on two-hit time resolution.

Using automated tools, future studies will estimate the performance of the dE/dx-based $e - \gamma$ separation as a function of the wire pitch for events that do not contain showers identified topologically as π^0 decay candidates. Evaluation of the wire pitch will need to be done separately for this class of events since dE/dx-based separation and topological separation are correlated.

Wire Angle

Like the wire pitch, the choice of the angles of the induction-plane wires relative to the collection plane wires affects the physics performance of the detector. Because the wires wrap from one side of each APA to the other, a discrete ambiguity is added to the continuous ambiguity of identifying where along the wire the charge was deposited.

Reconstruction of 3D objects based on 2D data (channel number vs. time) requires associating hits in one view with those in at least one other. If two wires cross only in one place, the ambiguity is removed once the hit is associated in the two views. If the wires cross more than once, three views are required in order to break the ambiguity of even isolated hits.

This association can most easily be done using the arrival time of the hits. If the time of a hit is different from that of all other hits in the event, then the association is easy. In more complex cases, where dense showers produce many hits at similar drift distances, misassociation can happen. In this case, the discrete ambiguity makes it possible to displace a reconstructed charge deposition by

multiple meters from its true location. In the case that the U and V angles are the same and the number of times a wire wraps around an APA exceeds one, then even a single, isolated hit can be ambiguous. A small difference in the U and V angles breaks this ambiguity, though misassociation still occurs in events with multiple nearby hits close in time. The use of clustering methods assists in obtaining the correct ambiguity choices for hits in dense environments.

Reducing the wire angle reduces the number of crossings, but does not eliminate the possibility of misassociating hits in events with multiple hits arriving simultaneously on their respective wires. Reducing the angle aligns the shapes of features in the different views making it easier to correlate them. The angle chosen for the DUNE far detector reference design ensures that no induction wire crosses any collection wire more than once.

On the other hand, reducing the wire angle worsens the resolution of 3D reconstruction of hits in the vertical direction. It also worsens the resolution on the measured separation between the primary vertex and photon conversion points, though as pointed out above, the radiation length is much longer than the wire spacing. The number of hits available for dE/dx separation of electrons from photons degrades for vertically-going showers if the wire angle is reduced. A parametric study of a figure-of-merit based on the measurability of the two photon-conversion lengths as a function of the induction-plane wire angles is provided in[23].

The impact on the physics sensitivity of a small number of hits that are misreconstructed by many meters from their true locations is estimated to be larger than that incurred by the degraded resolution of each hit in the vertical dimension[24], though studies have yet to be performed to estimate the impact on event detection efficiency, particle ID performance and energy resolution. Hits with locations that are misreconstructed by large distances are not expected to contribute properly to energy sums and may cause pattern recognition failures, such as missing tracks or splitting of tracks into multiple pieces. Advances in algorithms to break ambiguities in complex environments can allow for steeper wire angles.

The fact that the channel count must be an integer multiple of 128 in an APA also constrains the wire angles as functions of the APA frame dimensions, though a procedure to find the proper arrangement of channels that most closely approximates the optimized wire pitches and angles and meets the channel count constraint may cause small deviations in the parameters.

Wire Length

The length of the collection-plane wires is determined by the APA dimensions (or vice-versa) and the length of the induction-plane wires is determined by their angle and the APA dimensions. The APA dimensions are largely constrained by transport and handling needs as well as stiffness and production cost issues as they get larger. Capacitance and noise increase with wire length; this effect would likely not be masked by electronics noise since the cold electronics is expected to have very low noise. Therefore, in order to meet the signal-to-noise requirement with a finer wire spacing, the wires may need to be made shorter.

On the other hand, longer wires lower the cost of the detector, as fewer electronics channels and

APA frames — and winding time and materials — are needed to instrument a given volume of liquid argon.

It is anticipated that much of the work needed to study the impact of the wire pitch will inform the wire length choice due to its impact on the signal-to-noise ratio.

Maximum Drift Length

The maximum drift length is another optimizable parameter. In this case, the driver for longer lengths is the cost of the detector. A longer drift length assigns more liquid argon to be read out by any given channel, reducing the APA count and the channel count. A longer drift length also increases the fraction of liquid argon that is fiducial. Fiducial cuts will be made around the APA planes to ensure containment and to minimize the impact of dead argon inside the APA planes. Reducing the APA count thus reduces the amount of non-fiducial liquid argon.

A longer drift length, and the correspondingly longer electron drift time, increase the likelihood that the electron will attach to impurities as it drifts towards the anode plane. Once the drift length has been specified, therefore, the requirements on the signal-to-noise ratio, the electron lifetime and the dynamic range are coupled.

Increasing the drift length also degrades position resolution due to diffusion, where the spread of a drifting packet of charge increases in proportion to the square root of the drift time. Charge deposited near the APAs remains well measured, though charge deposited near the CPAs will suffer from both attenuation and diffusion, lowering the signal-to-noise ratio. Small-signal detection efficiencies and PID performance may decrease for events near the CPAs. Sophisticated reconstruction and analysis algorithms can be used to recover resolution that is thus lost, but the resolution may be limited by noise. Simulation studies in advance of CD-2 will address the impact of diffusion and noise on the particle reconstruction performance.

4.3   The Time Projection Chamber (TPC)

4.3.1   Overview

The scope of the Time Projection Chamber (TPC) subsystem includes the design, procurement, fabrication, testing and delivery of anode plane assemblies (APAs), cathode plane assemblies (CPAs), the field cage and the high voltage system.

The TPC is the key active detector element of each DUNE far detector module. It is located inside the cryostat vessel and is completely submerged in liquid argon at 88 K. The TPC is constructed of modular APAs, CPAs and field-cage modules. The APAs and CPAs are assemblies of wire planes and are tiled into alternating APA-CPA rows along the length of the cryostat. The resulting rows are called *anode planes* and *cathode planes*, respectively. (Note the different uses of the word

plane.) Field-cage modules enclose the four open sides between the anode and cathode planes. When proper bias voltages are applied to the APAs and CPAs, a uniform electric field is created in the volume between the anode and cathode planes. A charged particle traversing this volume leaves a trail of ionization in the ultra-pure liquid argon. The electrons drift toward the anode wire planes, inducing electric current signals in the front-end electronic circuits connected to the sensing wires. The current-signal waveforms from all sensing wires are amplified and digitized by the front-end electronics and transmitted through cold (immersed) cables and feedthroughs to the data acquisition (DAQ) system outside of the cryostat. While electrons drift toward the APAs, positive ions drift toward the CPAs at a velocity five orders of magnitude slower than that of the electrons and therefore contribute little to the signal on the wires.
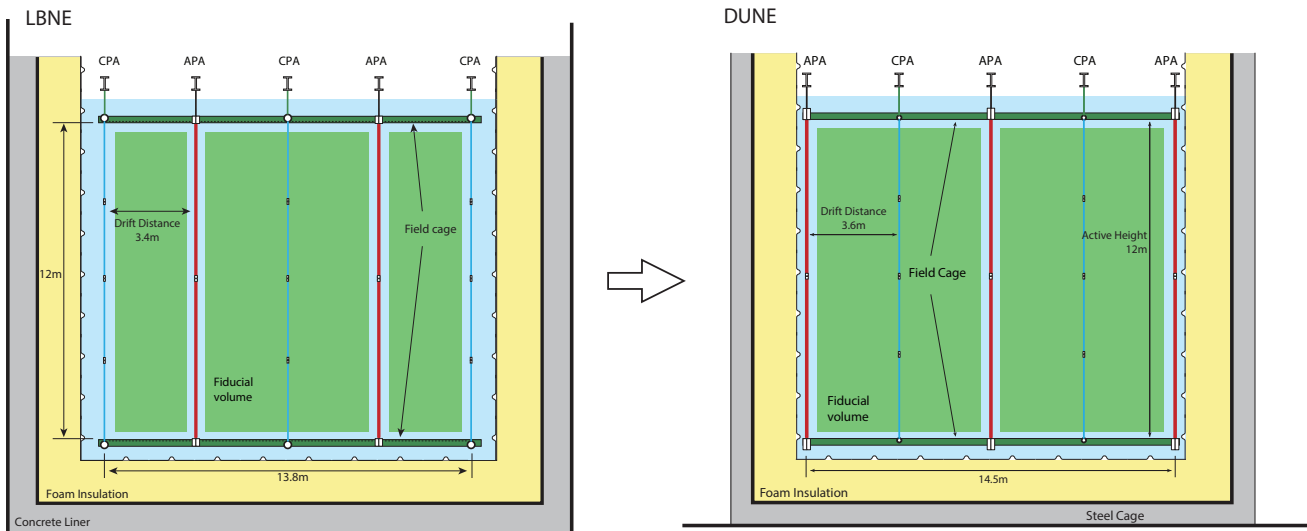
Figure 4.3: Cross sections of the LBNE 5−kt TPC (left) and the DUNE 10−kt TPC (right). The exchange of the APA and CPA positions significantly reduces the energy stored in the TPC by eliminating the two ground-facing cathode planes. This allows an increase in the detector's fiducial volume given the same cryostat volume. The length of the DUNE TPC is 58 m along the direction of the neutrino beam (into the page).

The TPC active volume (Figure 4.3) is 12 m high, 14.5 m wide and 58 m long in the beam direction. Its three rows of APA planes interleaved with two rows of CPA planes are oriented vertically, with the planes parallel to the beamline. The electric field is applied perpendicular to the planes. The maximum electron-drift distance between a cathode and an adjacent anode is 3.6 m. This requires a −180 kV bias voltage on the cathode plane to reach the 500 V/cm nominal drift field. The anode plane assemblies are 2.3 m wide and 6 m high. Two 6 m modules are stacked vertically to instrument the 12 m active depth. In each row, 25 such stacks are placed edge-to-edge along the beam direction, forming the 58 m active length of the detector. Each CPA has the same width, but half the height (∼3 m) as an APA, for ease of assembly and transportation. Four CPAs will be stacked vertically to form the full 12-m active height. Each cryostat houses a total of 150 APAs and 200 CPAs. Each facing pair of cathode and anode rows is surrounded by a field cage assembled from panels of FR-4 glass-reinforced epoxy laminate sheets with parallel copper strips connected to resistive divider networks. The entire TPC is suspended from five mounting rails under the cryostat ceiling (see Figure 4.4).
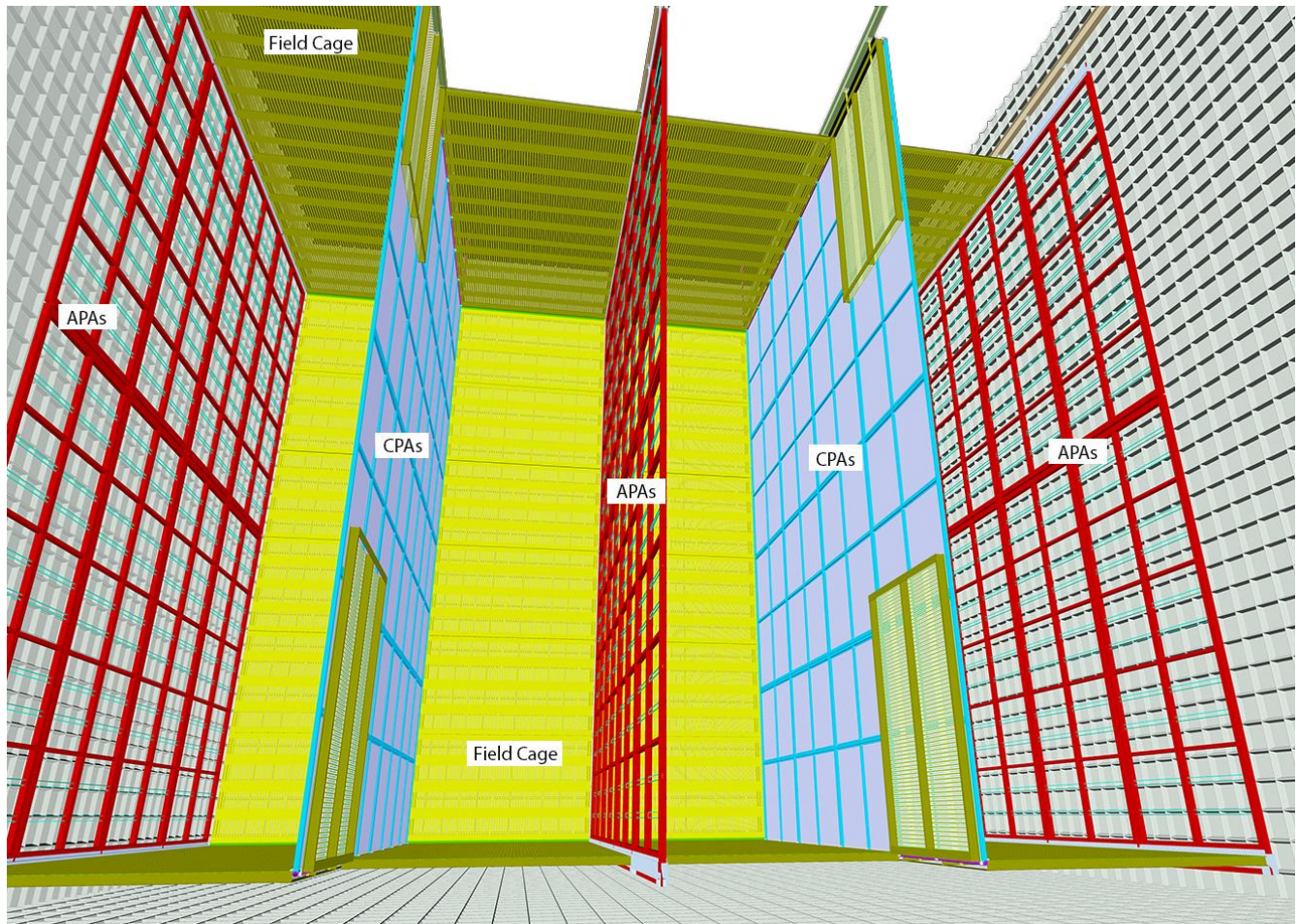
Figure 4.4: A view of the partially installed TPC inside the membrane cryostat. The APAs are shown in red, CPAs are in cyan, field-cage modules in yellow/green. Some of the field-cage modules are in their folded position against the cathode (providing aisle access during installation).

The units of construction of the active detector are the APAs, CPAs and field-cage modules. These are modular elements of a size optimized to simplify their manufacture, satisfy commercial highway and underground transport requirements, and facilitate handling and efficient installation in the cryostat. The units will be fully tested in LN_2 (or LAr) at the assembly site. They will be tested again at the far detector site before installation and will be monitored continuously during and after installation to detect any failures.

4.3.2 Anode Plane Assemblies (APA)

An APA is constructed from a framework of lightweight, rectangular stainless steel tubing, with four layers of wires wrapped on each side of the frame. From the outside in, the first wire layer is a shielding (grid) plane, next are two induction planes and the collection plane. The front-end electronics boards are mounted on one end of the APA frame and protected by a metal enclosure. The APAs are 2.3 m wide, 6.3 m high, and 12 cm thick. The height is chosen for fabrication purposes and compatibility with underground transport limitations. The 2.3-m width is set to fit in a standard High Cube container for storage and transport with sufficient shock absorbers and clearances.

Wire Planes

APAs are strung with wire of 150 μm diameter copper beryllium (CuBe) alloy for high tensile strength, good electrical conductivity, excellent solderability and a thermal-expansion coefficient compatible with that of the stainless steel frame. The wires will be epoxied to fiberglass wire-bonding boards and then soldered to copper traces on the boards for electrical connections.

Four planes of wires cover each side of an APA frame as shown in Figure 4.5.

These four planes of wires are labeled, in order from the outside in: G (for grid), U, V and X. Table 4.2 summarizes the key parameters of each of the wire planes.

Table 4.2: Parameters of the four planes of wires on an APA

Label	Function	Orientation (from vertical)	Pitch (mm)	Number	Bias Voltage (volt)
G	Shield/grid plane	0°	4.79	960	−655
U	1st induction plane	+35.7°	4.67	800	−365
V	2nd induction plane	−35.7°	4.67	800	0
X	Collection plane	0°	4.79	960	+860

The distance between wire planes is 4.76 mm (3/16 inch, a standard printed circuit board thickness). Each wire plane is biased to a particular voltage such that the ionization electrons from charged particle tracks will drift past the first three wire planes and be completely collected by
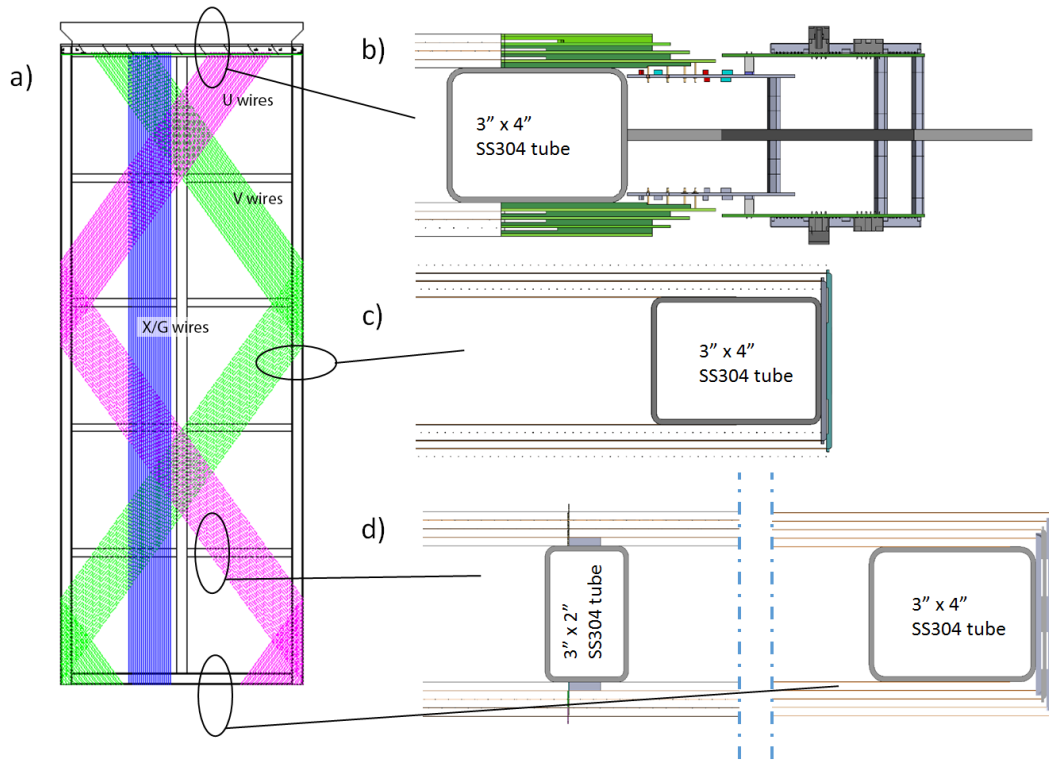
Figure 4.5: Illustration of the APA wire wrapping scheme (left), and three cross sectional views (right). At left, small portions of the wires from the three signal planes are shown in color: magenta (U), green (V), blue (X). The fourth wire plane (G) above these three, parallel with X, is present to improve the pulse shape on the U plane signals. At right, the placement of the wire planes relative to the stainless steel frame is shown for different locations on the APA. See Table 4.2 for wire plane parameters.

the collection wire plane (X). The V wires are DC-coupled to the readout electronics to minimize the maximum voltage on the other wire planes. A grounded mesh plane with good optical transparency, located 4.8 mm behind the collection plane, prevents the electric field around this set of wires from being distorted by the metal frame structure and the wires on the opposite side of the frame. It also shields the sensing wires from potential EM interference from the silicon photomultipliers (SiPMs) on the photon detectors, mounted within the frame. Each wire on the U, V and X planes is connected to a front-end readout channel. The grid plane wires are not read out, but serve the important purpose of shielding the U wires from responding to distant moving charges. The total number of readout channels in an APA is 2560, for a total of 384,000 in each cryostat.

The wires on the two induction planes (U and V) are wrapped in a helical pattern around the long edges of the wire frame (Figure 4.5a). This technique makes it possible to place readout electronics only at one short edge of an APA frame, and allows tiling of the APAs on the other three sides with minimal dead space (∼1.3% of active area). Although wires on the induction planes are sensitive to tracks on both sides of an APA, the vertical collection-plane wires are only sensitive to one side, and therefore able to resolve this ambiguity. The upper APAs in the cryostat will have their readouts at the top edge of the frame (as shown in Figure 4.5), while the lower APAs will mount their electronics at the bottom edge. These readout electronics are located within the LAr volume but outside of the TPC active volume. On the readout end of an APA, 20 sets of front-end readout boards with 128 channels each (40U+40V+48X) are distributed on both sides of the APA, reading out the 2560 sense wires.

With the APA length and width constrained by transportation and handling limitations, the angles on the induction plane wires are chosen so that they wrap less than one full revolution around the APA. This avoids an ambiguity problem where three wires from three readout planes intersect more than once on an APA face (discussed in Section 4.2.2). Precise values of wire angle and wire pitch (see Table 4.2) were chosen to give an integral number of wires across the boards at the electronics end of the APA as well as an integral number of wire slots in the boards along the sides of the APA. A preliminary study[23] has shown that this wire layout meets the physics requirements.

The APAs facing the cryostat walls are sensitive on both sides, similar to those in the middle of the TPC. However, the negative bias voltage on their outer grid planes prevents any electrons drifting from the cryostat walls toward the sensing wires. The electronics for the outer X wire plane can be eliminated to save cost. Alternatively, these double-sided APAs can be utilized by adding another cathode plane with a small negative bias between the cryostat wall and the anode plane to form a very shallow veto region.

APA Frame

At the nominal wire tension of 5 N, the total of 3520 wires exerts a force of ∼7.0 kN/m on the short edges of the APA, and a ∼1.5 kN/m force on the long edges. The wire frame must be able to withstand the wire tension with minimal distortion, while minimizing dead space due to the thickness of the frame. The wire frame is constructed from stainless steel tubes welded in a jig.

Structural analysis has shown that the maximum distortion of the frame due to wire tension is less than 0.5 mm. The total mass of a bare frame is ∼260 kg.

All tube sections are vented to prevent the creation of trapped LAr volumes. The three long tubes have slots cut in them so the photon detectors can be inserted into the APAs after the wires are installed. The two long outer members of the frame are open-ended, so the photon detector cables can be threaded through them to reach the signal feedthroughs on the cryostat roof. These long tubes can potentially be used to carry signal and power cables from the bottom APA cold electronics boards to the signal feedthroughs. This could significantly reduce the cable length compared to, e.g., running the cables from the middle bottom APAs along the floor and then up the wall.

APA Wire Bonding and Support

The wire bonding boards physically anchor the wires at the edges of an APA and provide the interface between the wires and the cold electronics at the readout end of the APA. The four planes of wires are attached to their respective wire bonding boards through a combination of epoxy and solder. During winding of the X layer onto the APA, the wires are placed across the top surface of the X wire board. The wires are then glued down with a strip of epoxy at the leading edge of the board. After the epoxy has cured, the wires are soldered onto the copper pads under each wire, and then the wires are cut beyond the pads. The V, U and G planes are attached on top of the X boards and similarly populated with wires, one layer at a time. An array of pins is pushed through holes in the stack of wire bonding boards, making electrical connections between the wires and the capacitor-resistor (or CR) board, which is located between the wire boards and the front-end electronics boards. The CR boards distribute the bias voltages to each wire through current-limiting 20 MΩ resistors, and bring the charge signal through high voltage AC coupling capacitors to the cold electronics.

These readout boards, as described in Section 4.5, generate an estimated ∼160 W of heat per APA which may produce a small quantity of argon bubbles. Stainless steel covers are placed over the readout boards to contain the bubbles and direct them to the gas volume of the cryostat. This is particularly important for the bottom APAs where the bubbles must be contained and funneled through the vertical hollow frame members to the top of the cryostat to prevent the bubbles entering the TPC active volume.

Comb-like wire support structures (see Figure 2.9 in Annex 4A: *The LBNE Design for a Deep Underground Single-Phase Liquid Argon TPC* [6]) are located on each of the four cross beams (see Figure 4.5) so that the longitudinal wires are supported every 1.2 m and the angled wires about every 1.5 m while introducing only millimeter-scale dead regions. The support structure is composed of strips of thin G10 sheet, with notches machined at correct intervals. These wire supports play a key role in minimizing wire deflection due to gravity and electrostatic force, enabling the use of a moderate wire tension and reducing the risk of wire breakage. They also maintain the correct wire pitch and wire plane separation even if the APA frame has a small amount of twist and warp. If a wire breaks after installation, these intermediate wire support will limit the movement of the broken wire such that it will not travel too far into the drift volume

and make contact with the field cage. To further reduce the risk and impact of a broken wire, a new wire support scheme is being developed that can be applied to the outer wire planes near the bottom of the TPC to prevent a broken wire from contacting the field cage.

Wire-winding Machines

A winding machine will be constructed to lay the 3520 wires onto each APA. It has sufficient versatility that the same mechanism can wind both the angled and the longitudinal layers. Its working concepts are illustrated in Figure 4.6.
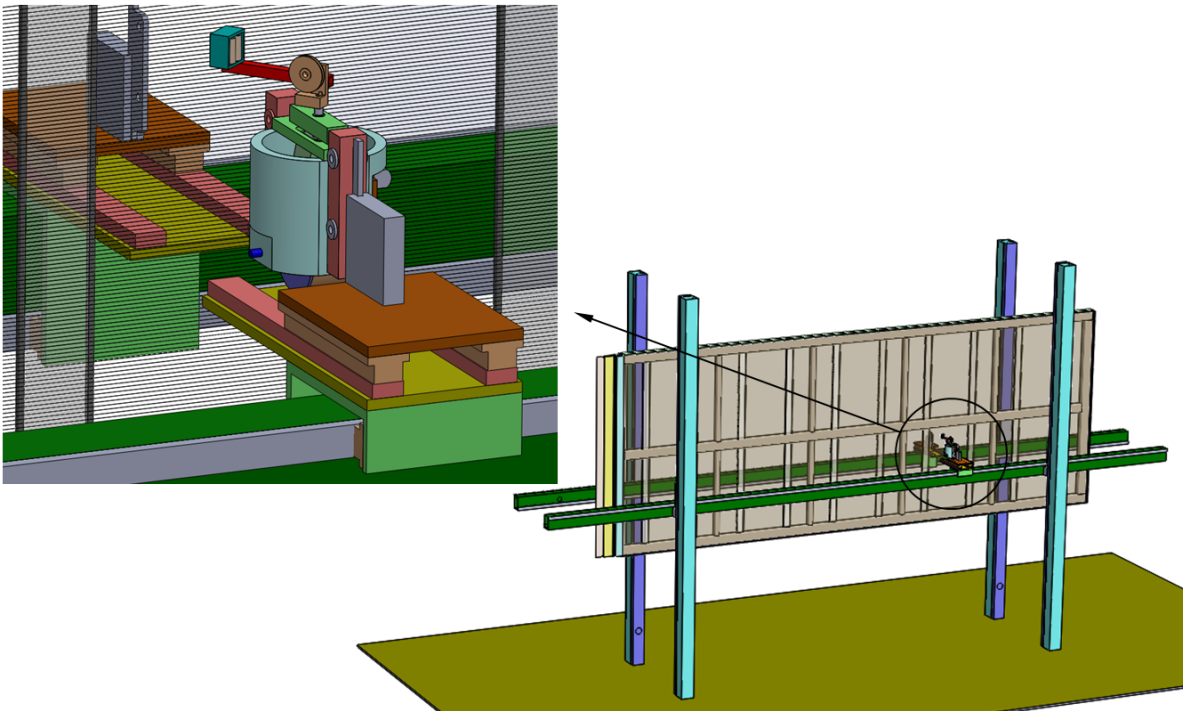
Figure 4.6: Illustration of the wire winding machine concept. The tensioner head is passed from one side of the APA to the other as it is moved around the APA to wind wire onto the APA frame. The horizontal/vertical positioning systems on each side of the APA are made of commercial linear motion components.

The wire tensioner is a self-contained unit that includes the wire spool. It is designed so that correct wire tension is maintained, independent of the wire-feed rate and direction. The APA, oriented horizontally in the device (with one of its long edges down), is held off the ground by a couple of posts. There are X-Y positioners on either side of the APA; the tensioner is moved across the face of the APA by one of these positioners, unspooling tensioned wire as it moves. When the tensioner arrives at the edge of the APA it is passed across to the positioner on the other side of the APA while placing the wire into the appropriate slots of the edge boards. In this way the entire layer of wire can be placed on the frame.

Although a large part of an entire plane of wires can be wound in one continuous process, a more fault-tolerant procedure will be adopted in which the winding machine will be paused periodically

to solder the last wire winding. This intermediate soldering step will prevent the unraveling of a large section due to an accidental broken wire. An automatic soldering robot will solder the wire ends after the wires have been laid down on the APA. A wire-tension measuring device will scan the newly placed wires and record the wire tension of each wire. Any wires with abnormal tension will be replaced manually.

4.3.3 Cathode Plane Assemblies (CPAs)

There are two cathode planes in each detector module. Each cathode plane is tiled from a four-unit-high by 25-unit-wide array of CPAs. Figure 4.7 shows the building blocks of a cathode plane.
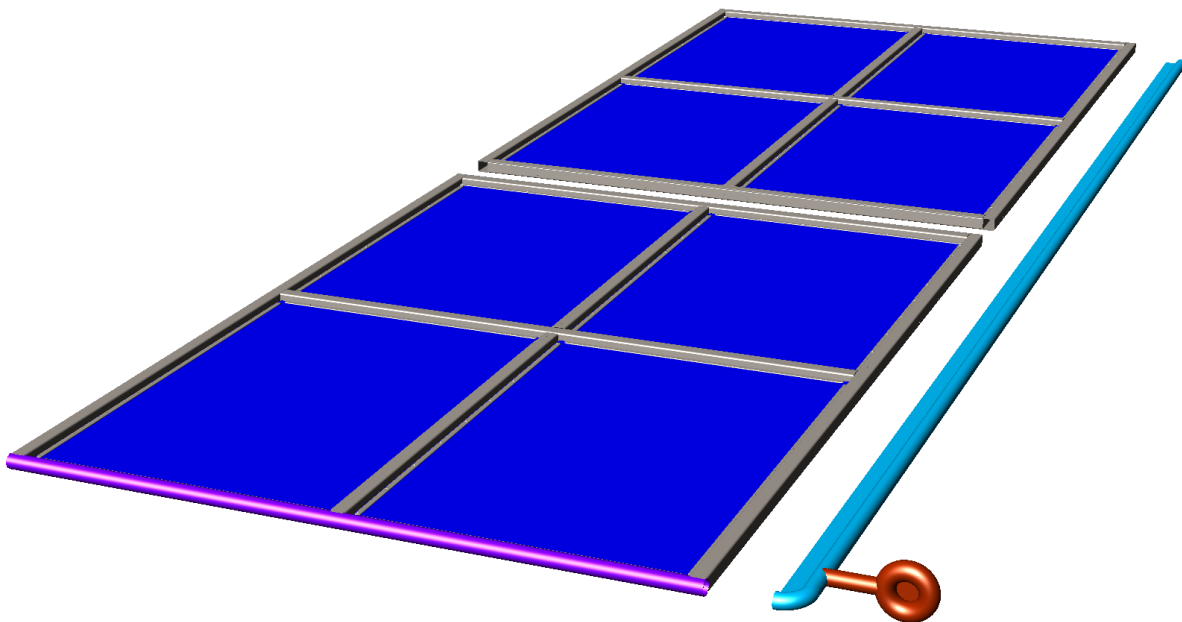
Figure 4.7: Conceptual design of the cathode plane components near a corner. Two flavors of CPAs (outer and inner unit) are used to make up the entire cathode plane; all CPAs are roughly 2.3 m wide by 3 m tall. The cathode plane is terminated at right and left ends by the end pieces (cyan colored). An HV receptacle (orange) connects with the HV feedthrough from the cryostat ceiling.

Each CPA is 2.3 m wide (identical to the APA width) and 3 m tall (half of APA height) for ease of fabrication, assembly and handling. Each CPA is made of a stainless steel framework, with panels of solid stainless steel sheets mounted between the frame openings. Along each vertical column of four CPAs, there are two slightly different versions: the outer CPAs (top and bottom rows), and the inner CPAs (2nd and 3rd rows). The inner CPAs use all rectangular tubes for the frame structure, while the outer CPAs use 5-cm OD round tubes on the outside edge of the CPA facing the floor or ceiling of the cryostat to minimize the surface electric field (shown in magenta in Figure 4.7). Two sets of field-shaping end pieces are installed at the two ends (e.g., right and left) of a CPA wall to properly terminate the cathode wall with rounded edges. All CPAs are suspended from the ceiling using G10 hangers under fiberglass rails to insulate the CPAs from the cryostat.

A recent design decision exchanged the positions of the CPAs and APAs in the detector relative to the earlier LBNE reference design, placing the APAs adjacent to the cryostat wall instead of the CPAs. This change reduces the stored energy on each cathode plane by about 60%. Nevertheless, due to the enormous area of the stainless steel cathode plane, there is still nearly 100 Joules of energy when biased at 180 kV, risking physical damage to the thin membrane structure as well as to the CPA structure in the event of a high-voltage discharge. In addition, in such an event, a huge voltage swing could occur on the cathode plane in tens of nanoseconds, injecting a charge pulse to the sensing wires with a large peak current that could damage the front-end electronics.

To mitigate this risk, analysis of the electrical properties of the cathode has been carried out with the goal of developing a cathode design that will substantially slow down the total energy release in case of a discharge. The best solution appears to be replacing the metallic cathode structure by non-conductive materials with a robust and highly resistive surface coating. Many choices of resistive/anti-static coating and commercially produced anti-static sheet materials are available. Studies are underway to identify a suitable coating and base material for this application. Since the electrical current feeding the field cage resistive dividers is supplied through the cathode, a special current-distribution feature must be designed to minimize voltage drop along this 58-m-long, highly resistive structure.

4.3.4   Field Cage

In the TPC, each pair of facing cathode and anode planes forms an electron-drift region. A field cage must completely surround the four open sides of this region to provide the necessary boundary conditions to ensure a uniform electric field within, unaffected by the presence of the cryostat walls.

Each $10-$kt detector module requires $\sim$2000 m^2 of field cage coverage. In the current reference design, the field cages are constructed using multiple copper-clad FR-4 sheets reinforced with fiber glass I-beams to form modules of 2.3 m $\times$ 3.6 m in size. Parallel copper strips are etched on the FR-4 sheets using standard printed circuit board fabrication techniques. Strips are biased at appropriate voltages provided by a resistive-divider network. These strips create a linear electric-potential gradient in the LAr, ensuring a uniform drift field in the TPC active volume. Simulations have shown that the non-uniformity of the drift field quickly drops to about 1%, roughly a strip pitch away from the field-cage surface.

Since the field cage completely encloses the TPC drift region on four sides, while the solid cathodes block the remaining two, the field cage sheets must be perforated to allow LAr recirculation in the middle third of the TPC volume. The "transparency" of the perforation will be determined by a detailed LAr computerized fluid dynamic (CFD) study.

The resistor-divider network will be soldered directly onto the field-cage panels. Multiple resistors will be connected in parallel between any two taps of the divider, in order to provide fault tolerance. One end of the divider chain is connected directly to the cathode, while the other end is connected to ground at the APA through resistors of the appropriate value. A pair of field-cage modules will be pre-attached to the outer CPA modules through hinges, such that the field-cage modules can be rotated into their final position during installation, or folded back if aisle access is needed

(see Figure 4.4). In addition to the resistor-divider network, surge suppressors such as varistors or gas discharge tubes will be installed between the field-cage strips to avoid the occurrence of an over-voltage condition between field-cage electrodes and the cathode in the event of a high voltage discharge.

The major challenge of this field-cage design is minimizing the electric field near the edges of the thin copper strips. One solution is to cover all copper edges with a thick layer of solder mask (an acrylic-based polymer with a high dielectric strength) as part of the standard PCB fabrication process. This construction is currently being implemented in the 35-t prototype TPC (see Section 7.5 of [6]). Figure 4.8 shows a section of this partially constructed field cage.
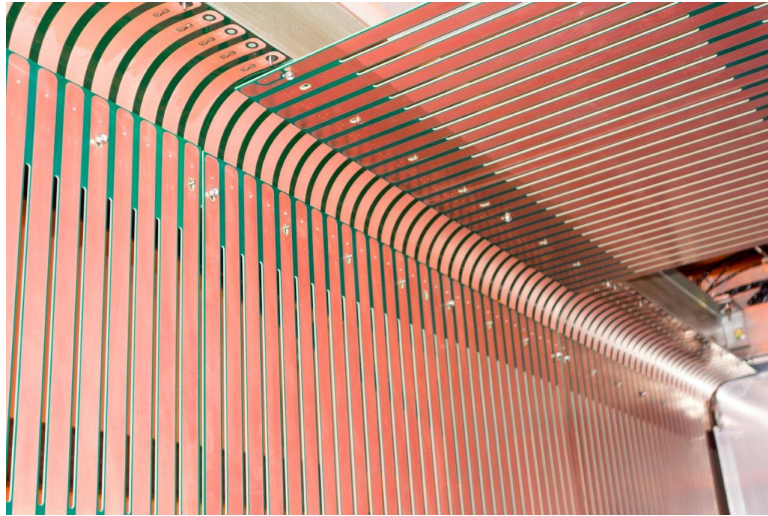
Figure 4.8: A corner of the 35-t TPC field cage during construction

The 35-t prototype test results will be evaluated to determine if this technique is suitable for the much larger far detector modules.

In the meantime, alternative concepts are being actively developed to further minimize the electric field on the field cage. One example is application of a very high-resistance coating on the outside surface of the field cage such that the surface potential distributes uniformly across the gaps between conductors and therefore eliminates the high-field region near the conductor edges. The challenge here is ventilation of this field cage surface without significantly increasing the field at the edge of the perforations. Another concept is to use roll-formed metal profiles as the field-cage electrodes and support them with insulating beams. These profiles have large edge radii; this makes their surface electric field relatively low, which in turn makes it possible to place them even closer to the cryostat walls to improve the efficiency of LAr use. A sample profile is shown in Figure 4.9.

With only a 20-cm distance separating the field cage from a ground plane, the electric field on the field cage is still under 12 kV/cm. The ends of the profiles still have high electric field, however; a possible solution is to cover the ends with UHMW polyethylene caps. This design may also cost significantly less than the reference design with PCBs.
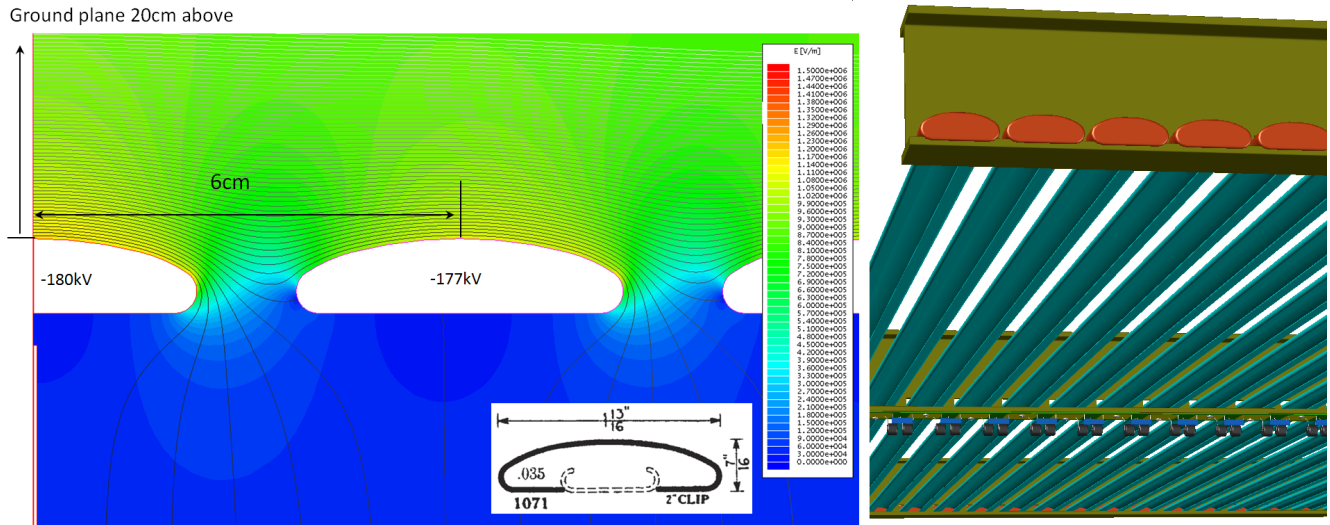
Figure 4.9: Left: electrostatic simulation of a field cage design that uses roll-formed metal profiles as the field-cage electrodes. Right: a conceptual design of a field-cage module using this profile.

4.3.5 High Voltage Components

The two cathode planes are biased at -180 kV to provide the required 500 V/cm drift field. Each cathode plane will be powered by a dedicated HV power supply through an RC filter and feedthrough.

The power supplies for the cathode planes must be able to provide -200 kV at 1 mA current. The output voltage ripple must not introduce more than 10% of the equivalent thermal noise from the front-end electronics. The power supplies must be programmable to trip (shutdown) their output at a certain current limit. During power on and off, including output loss (for any reason), the voltage ramp rate at the feedthrough must be controllable to prevent damage to the in-vessel electronics from excess charge injection. High-voltage feedthroughs must be able to withstand -250 kV at their center conductors in a 1 atm argon gas environment when terminated in liquid argon.

The current candidate for the high-voltage power supplies is the Heinzinger PNChp series, which has the lowest output ripple specification. Additional filtering of the voltage ripples is done through the intrinsic HV cable capacitance and series resistors installed inside the filter box. Established techniques and practices will be implemented to eliminate micro-discharges and minimize unwanted energy transfer in case of an HV breakdown.

To ensure safe and reliable operation, the feedthroughs will be tested at a much higher voltage than expected in routine operation ($\sim$250 kV) in LAr. The feedthroughs will be mounted on the ceiling of the cryostat, their cold ends reaching through the gas ullage space and submerging into the LAr. The center conductor on the cold side of a feedthrough will be insulated and shielded by a grounded shroud at least 50 cm below the surface of the liquid to ensure bubble free operation at the tip. Figure 4.10 shows an example of the feedthrough and filter box made by the UCLA

group for the 35-t prototype TPC, as well as the conceptual design of a feedthrough suitable for the far detector TPCs.

Figure 4.10: Top: The high voltage feedthrough and filter developed by the UCLA group for the 35-t TPC. The total length of the feedthrough is about 2 m, and its main body has an OD of 3.8 cm. It was tested up to 150 kV. Bottom: a conceptual design of a new feedthrough for the far detector.

4.3.6   TPC Prototyping and Tests

Several prototype TPC modules were constructed during the LBNE project design phase. The initial prototypes were fractional-scale or partial models of the APA and CPA. The CPA prototype was used to evaluate field-shaping electrode attachment techniques. A 40% scale APA prototype was constructed earlier on to study the placement of the wire-wrapping boards and wire-support structures. It was also used to develop the prototype winding machines. The prototypes were subjected to numerous thermal cycles down to liquid-nitrogen temperature to test the integrity of the wire-to-board and board-to-frame bonds.

The second set of prototypes are scale models of the APA and CPA. They are being used to validate the designs and to evaluate production procedures. These functional prototypes will be installed in the 35-t prototype cryostat and are expected to be operational in 2015.

A TPC prototype proposed for installation in a CERN test beamline requires six full-size APAs with fully instrumented readout electronics, six full-size CPAs and complete field cage coverage. This prototype will be constructed using identical APAs, CPAs and field-cage panels as designed for the far detector. Additional features will be installed to ensure proper TPC operation given the half-height cryostat configuration. The construction and assembly of all TPC mechanical components will use the same materials and techniques as designed for the far detector, with the exception of the degree of automation for wiring the APAs, which will be reduced.

4.4 Data Acquisition (DAQ) System and Monitoring

The scope of the Data Acquisition (DAQ) system and monitoring includes design, procurement, fabrication, testing, delivery and installation of the following components (see Figure 4.11):

- LArTPC detector readout,

- Photon detector readout,

- Computer farm,

- artDAQ software toolkit,

- Run Control and Slow Control,

- Timing system, and

- Calibration system.

The DAQ system is required to

- collect data with a very high uptime (the goal is >99%);

- collect beam neutrino, atmospheric neutrino and proton decay candidates (generally all interactions with total energy deposition above about 100 MeV) with a high resolution (smart or no zero-suppression) with no dead-time;

- collect interactions with total energy below 100 MeV with some low amount of zero-suppression loss;

- trigger at the time of the beam pulses, irrespective of how little energy is deposited in the detector;

- collect data with the most favorable zero-suppression possible over a period of >10 s (supernova trigger);

- assemble data from sub-detectors into a unified event for offline analysis; and

- provide access to the shift operator and others to control and monitor the data collection and detector status, view online histograms and monitor (and provide for offline use) historical status of measured detector parameters.

This section outlines a conceptual design intended to meet the required performance for the DAQ for the DUNE far detector. To reduce considerably the times when none of the far detector modules are collecting data (particularly important for supernova detection) and to allow the designs of the DAQ in the different $10-$kt modules to be entirely different if desired, the DUNE DAQ employs

a decoupled design. The synchronization, triggering, data collection and run-state in the different
10−kt modules are completely independent in real time and are only coupled by processes running
asynchronously (in the same fashion as a batch queue) in the hour or so after data collection (see
Section 4.11 of [6]). This allows one detector module to be restarted without interrupting data
collection in the others.

The layout of the DAQ is shown schematically in Figure 4.11.
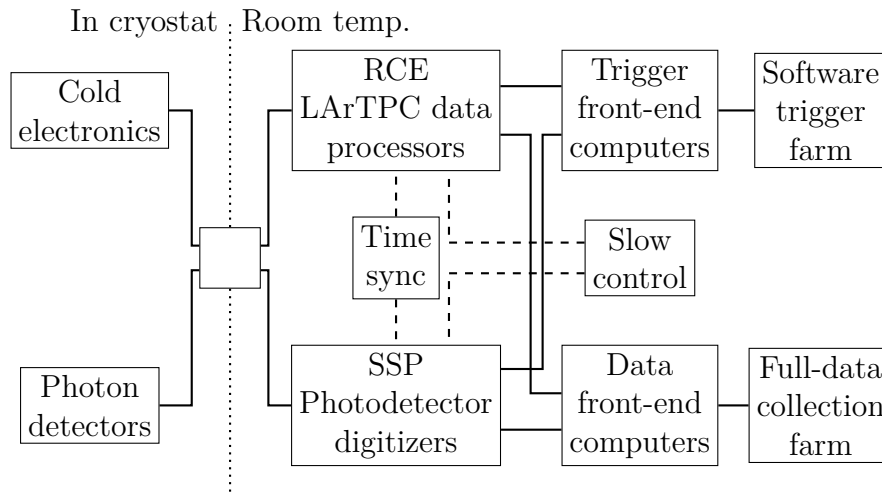
Figure 4.11: Block diagram layout of the main components of the DAQ subsystem.

To collect full detail of the most important events (deadtimeless detection of all those with energy
deposition of 100 MeV and above), while avoiding tricky communication to flag neighboring chan-
nels to those that have large hits, a model is used in which the digitized data are collected twice
from the initial data storage that is associatated with each peice of hardware.

The first collection supplies a centralized software-based trigger farm continuously with zero-
suppressed information (a threshold on each channel detects hits above the noise level; this causes
the ADC samples to be kept in a time window around the hit). The second collection reads the
full data at the times and in the regions selected by the trigger. This is similar to the multi-level
triggering in a collider experiment, but with only one level of triggering. The software trigger farm
also records the continuous stream of zero-suppressed hits in an archival ring buffer on disk to
allow later analysis of supernova candidates.

LArTPC detector readout The LArTPC signals are digitized in the cold in a continuous flash-
ADC stream at 2 MHz, (not zero-suppressed) and serialized on 12,000 high-speed links per 10−kt
module that exit the cryostat. The data are received by LArTPC data processors called RCEs
(Reconfigurable Computing Elements) housed in industry-standard aTCA crates on COB (cluster-
on-board) motherboards that are designed at SLAC for a wide range of applications. The RCEs
are part of a network of field programmable gate arrays (FPGAs) that buffer the full raw data,
zero-suppress it for passing to the trigger and accept requests for data-fetching from the trigger.
The FPGAs in the RCEs are from the Xilinx Zynq family and contain a full Linux processor system
on the chip. They facilitate the high-speed data transfer from firmware into DRAM memory that
is accessible from Linux. A fast data-transfer network using the Ethernet protocol is used on the

COBs and in the aTCA crates to allow for development of more sophisticated zero-suppression algorithms for improved supernova acquisition.

Photon detector readout is performed by the SiPM signal processor (SSP) described in Section 4.6.1. The additional buffering required for the separate trigger and data collection paths is implemented in the SSP front-end computers.

Computer farm Both the LArTPC and photon detector data are received in commodity Linux computers, with no deadtime, from where the data are routed to the trigger and full-data collection farms of computers. Although the front-end computers are logically distinct as shown in Figure 4.11, one physical computer is sufficient for all the processes for each rack of APA readout electronics.

artDAQ software toolkit (from Fermilab) supplies the real-time data collection functionality (buffering, matching event parts, synchronization, inter-process communication, etc.) in a modern design that facilitates the efficient use of multicore commodity computers running on the Linux computer farms. The multicore functionality is crucial in the high data-rate environment on DUNE. The detector-specific code is supplied by DUNE groups (this is centered in the UK), along with detector-specific triggering (also UK). The architecture provided by artDAQ can be tailored for each experiment and is entirely suitable for the "collect-twice" architecture envisioned for DUNE.

Run Control and Slow Control software framework manages the control, status display and status archival of the experiment. It is based on the design of the DAQ of the ICECube experiment[25]. This exploits a combination of readily available, well-supported packages [message passing (zeroMQ), a web-framework (Django), databases (postgres)] to give the shift operator a unified view of the status of the running experiment, and views of the monitoring data including customized views and historical views. The database of slow-control measurements is exported to the host lab to give access for offline programs.

Timing system To acomplish the software-based deadtimeless data acquisition in DUNE, it is necessary to synchronize the clock across all readout boards. This is accomplished in two stages. The main cavern-wide distribution uses the design from the NOνA experiment, which distributes a 64-MHz clock, synchronization pulses and cable-delay correction on RJ45 cables. The overall clock is synchronized using a GPS receiver and transferred from the surface over optical fiber. The synchronization is transferred from the COBs to the electronics in the cryostat over the same cabling as provides the data links.

Calibration system The calibration is done in three stages: (1) Pedestal and charge-injection pulser events are used to calibrate and remove drifting of the individual electronic channel responses. (2) External UV lasers are directed into the cryostat through glass-tube ports, and swivelling mirrors select the trajectories of the beams through the cryostat to provide calibration of the field non-uniformities and attenuation. (3) Cosmic-ray muons are used for the determination of the energy scale and for calibration cross-checks.

The time sequence, trigger deadlines and buffering of the readout are all shown in Figure 4.12. This figure shows time in the horizontal direction on a logarithmic scale to indicate how long after the particles appear in the detector each process can start and must finish. There is one level
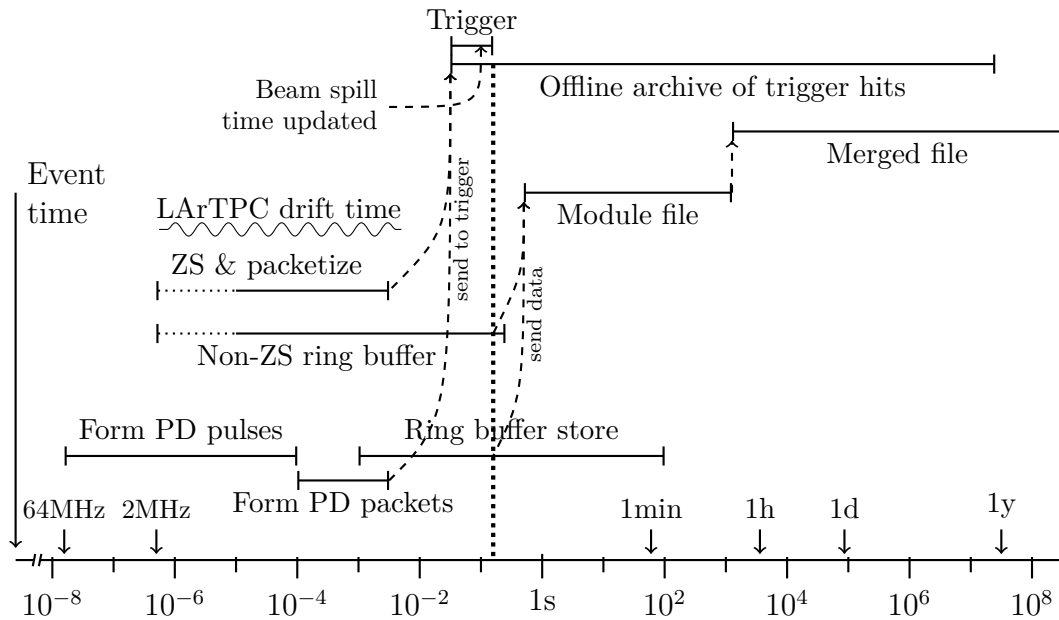
Figure 4.12: Main DAQ steps displayed relative to the event time.

of triggering, with a trigger deadline (latest time a trigger decision can arrive) of 0.16 s after the event has occurred, indicated by the vertical dotted line. This is long enough that in 99% of the cases, a message will arrive from the Fermilab site to update the predicted time of a neutrino spill with the actual time in order that the detector can be triggered independently of any signals in the detector. This operation has been used successfully on MINOS for many years.

As shown in Figure 4.12, prior to the trigger time and independently in each detector module, the detector readout assembles packets of data corresponding to fixed time intervals and sends them to the trigger event builders. Both the LArTPC readout and the SSP readout send zero-suppressed data, suitable for triggering, to a set of event-builder processes that run in parallel, each accepting all the data from the entire $10-$kt module for a specific time interval and performing trigger algorithms on them. All time intervals are processed so that the trigger has no dead time. The data from the LArTPC and SSP are also stored in ring buffers to await collection after an affirmative trigger decision — in the case of the LArTPC, this data is not zero-suppressed. The data are built into events in a "10kt-module file" that is written to disk. About an hour later, an offline process merges the data from the separate $10-$kt module files and archives them at the host lab.

To maximize data collection for a supernova, the continuous zero-suppressed trigger data is kept in a large buffer area on disk. During the extended period of this event, it is desirable to collect data that are cropped more gently than the zero-suppressed data stream. The non-zero-suppressed ring buffers on the current design of RCEs are sufficient for 0.4 s of buffering; during a supernova, the trigger farm can send instructions in the trigger messages to manage storage of data in these buffers. Two possible extensions to this method are (a) extend the memory to buffer longer, either on the RCEs or elsewhere in the aTCA crate, or (b) use the powerful intercommunications between RCEs to ensure that information read from neighboring channels around the time of a potential supernova event candidate is kept.

At the 4850L, the data rate in the trigger is dominated by the unwanted radioactivity from ^{39}Ar and ^{85}Kr. The cosmic rays that occur about once per minute, on the other hand, are the major source of events that should be collected on the data stream; the physics beam events, atmospheric neutrinos and other candidate events are included in this data budget. Table 4.3) gives estimates of the rate of occurence of these events and the expected steady-state data rate (after the derandomization provided by the buffering in the front-end computers).

Table 4.3: Estimated data rates in the DAQ system

Process	Rate (kHz/APA)	Data rate (MBytes/s)
Generic 2.3 ms interval	0.43	6,000
Cosmic-ray muons (4850L)	6×10^{-7}	1×10^{-5}
Radioactivity	~ 64	1.9
Electronics noise (not common mode)	~ 1	0.03

The requirements are met in this conceptual design by the very high throughput provided by modern off-the-shelf components and the parallelism provided by artDAQ, which makes the design extendable to avoid bottlenecks. The triggering allows the zero-suppression to be tuned to optimize for the final level of noise, while retaining the maximum level of information for the important physics events.

This DAQ design is being prototyped for the 35-t tests in 2015 (see Section 9.2.2), with two COBs (containing 16 RCEs) and eight SSPs. The artDAQ software toolkit is being used to implement the readout, event-building and triggering, although the "collect-twice" model will not be implemented for the 35-t test.

4.5   The Cold Electronics (CE)

The TPC read-out electronics are mounted on the APA front-end (Figure 4.13) in LAr.

These electronics are therefore referred to as the "Cold Electronics" (CE) subsystem. The scope of the CE subsystem includes design, procurement, fabrication, testing, delivery and installation of

- front-end electronics cards installed on the APAs,

- signal feedthroughs mounted on the cryostat,

- power supplies and cabling.

The following are the most significant requirements for the CE:

- minimize channel capacitance and noise,
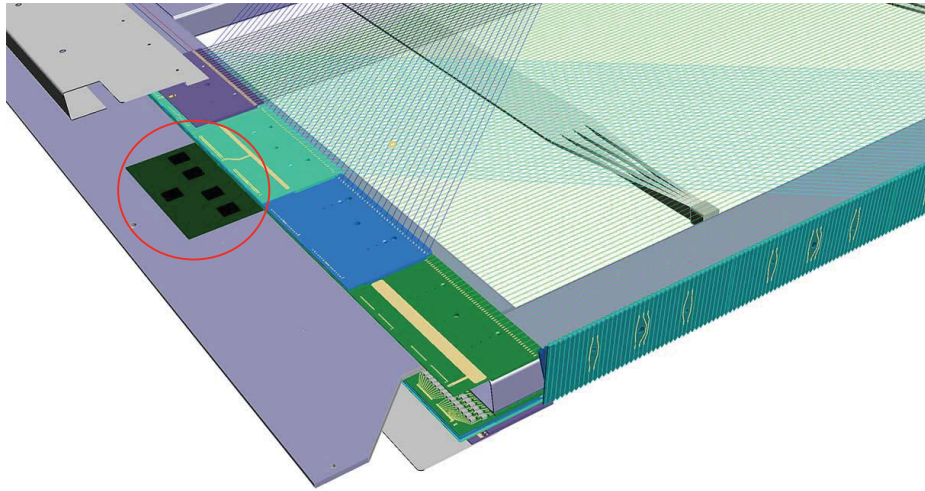
Figure 4.13: The front-end electronics, shown in the red circle, as mounted on an APA. (Note that this figure was not updated to show the current photon detection system scheme.)

- minimize dissipated power per channel in the LAr,

- read out the TPCs and transmit their data to the DAQ,

- record the channel waveforms continuously without dead time,

- provide sufficient precision and range to satisfy the Key Physics Parameters,

- operate for the life of the facility without significant loss of function, and

- use only materials that are compatible with high-purity liquid argon and that have minimal natural radioactivity.

The CE are implemented as ASIC chips using CMOS technology, which performs well at LAr temperatures[26], and provides amplification, shaping, digitization, buffering and multiplexing (MUX) of the signals. The CE architecture is manifested in the Front End Mother Board (FEMB), a 128-channel board which uses eight 16-channel Front End (FE) ASICs and eight 16-channel ADC ASICs (Figure 4.14).

The FE ASIC provides amplification and pulse shaping, while the ADC ASIC comprises a 12-bit digitizer and an 8:1 MUX stage with two pairs of serial readout lines in parallel. A Cold Digital Data (COLDATA) ASIC chip (Figure 4.15) mounted on each FEMB provides an additional MUX of 4:1 and is capable of driving the data at 1 Gb/s through 30 m of copper cable to the feedthrough and on to the DAQ. Tables 4.4 and 4.5 list the CE device counts and key parameters.

An important aspect of CMOS technology is that the lifetime at cryogenic temperatures is well understood and can be well controlled, *provided that close control is maintained over the implementation details*. This precludes the use of commercial devices, which are not intended for use in LAr, and which are produced by proprietary processes over which DUNE has no control. It is worth noting that the FEMB, together with the FE and ADC ASIC chips, has already been proto-
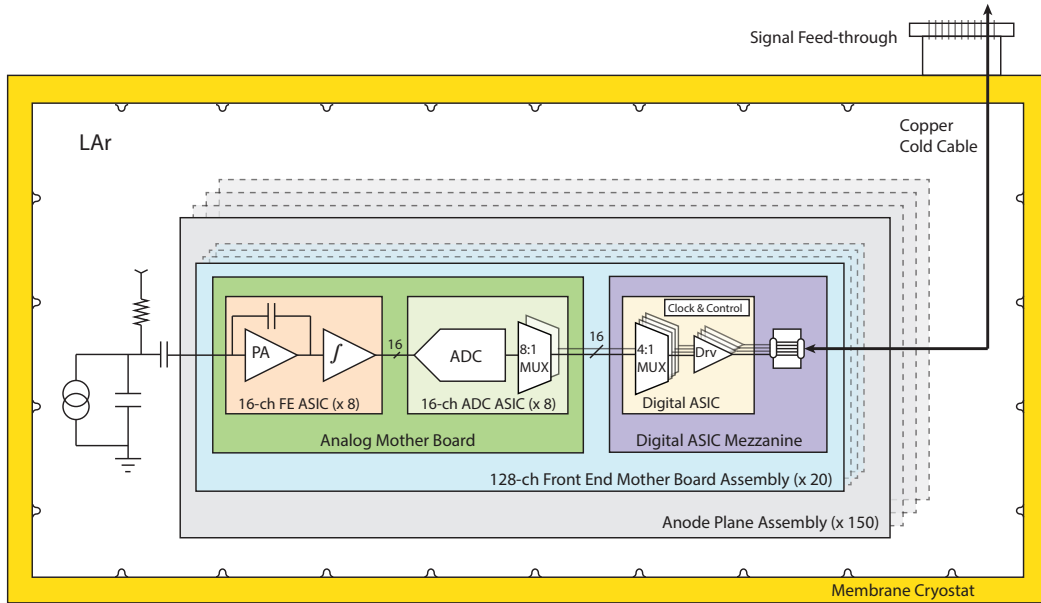
Figure 4.14: The CE architecture. The basic unit is the 128-channel FEMB. FEASIC: Front End ASIC. PA: Pre-amplifier. $\int$: Shaper. MUX: Multiplexer. Drv: Driver.
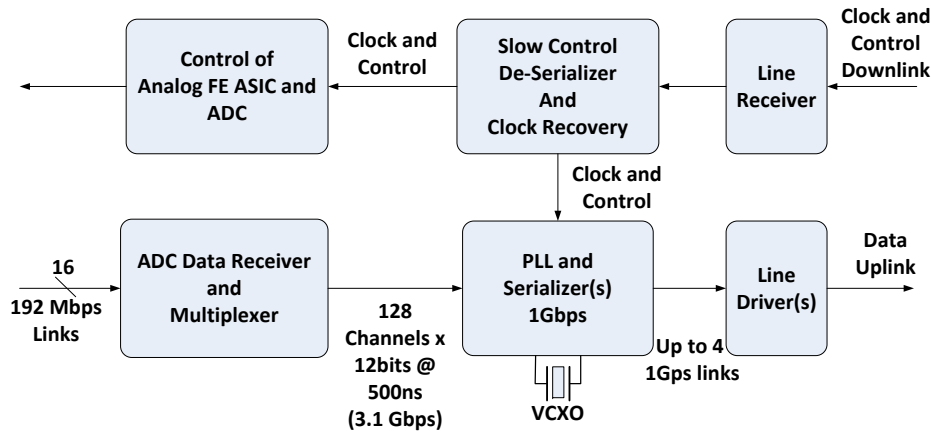
Figure 4.15: Functional block diagram of the COLDATA ASIC. PLL: Phase Locked Loop. VCXO: Voltage-Controlled Crystal Oscillator

Table 4.4: CE device counts

Parameter	per FEMB	per APA	per 10 kt Detector
Channels	128	2560	384,000
FE & ADC ASIC Chips	8	160	24,000
COLDATA ASIC Chips	1	20	3,000
FEMB	1	20	3,000
Signals-Out	4	80	12,000
APA	—	1	150

Table 4.5: CE key parameters

Parameter	Value
Signal-to-Noise (in LAr)	9:1 for 1 μs peaking time
MUX Level	32
Sampling Frequency	2 MHz
ADC Resolution	12 bits
FE Peaking Time	0.5, 1, 2, 3 μs (selectable)
FE Gain	4.7, 7.8, 14, 25 mV/fC (selectable)
Calibration Precision	1%
Power dissipation	11 mW/channel

typed and tested using a commercial FPGA to perform the role of the COLDATA ASIC, which is currently under development. The 1-Gb/s data rate can be achieved with copper links and without zero-suppression or data compression. This greatly reduces the complexity of the COLDATA ASIC, with a corresponding decrease in overall risk, including risk of failure-to-implement (within a fixed schedule and budget). The COLDATA work is especially challenging, with final production not scheduled to begin until late 2019. Alternative approaches are currently under study.

Good reliability of cold electronics has been achieved in several previous experiments. More than 8,000 cold electronics boards are used to read out ~180,000 channels in the ATLAS Liquid Argon Calorimeters with a failure rate of ~0.02% in 11 years of operation so far. The failure rate is less than 0.2% for ~13,000 channels of cold preamplifiers installed in the Liquid Krypton Calorimeter of the NA48 experiment for 17 years of operation. Lifetime studies of CMOS cold electronics for DUNE have been carried out to understand the aging mechanism due to channel hot carrier effects[27]. The design of the analog front end and ADC ASICs in 180-nm CMOS technology follows these design rules to secure lifetimes two orders of magnitude higher than the 30 years of experiment lifetime.

4.6   The Photon Detection System

The scope of the photon detector (PD) system for the DUNE far detector reference design includes design, procurement, fabrication, testing, delivery and installation of the following components:

- light collection system including wavelength shifter and light guides,

- silicon photo-multipliers (SiPMs),

- readout electronics,

- calibration system, and

- related infrastructure (frames, mounting boards, etc.).

LAr is an excellent scintillating medium and the photon detection system will exploit this property in the far detector. With an average energy of 19.5 eV needed to produce a photon (at zero field), a typical particle depositing 1 MeV in LAr will generate 40,000 photons with wavelength of 128 nm. At higher fields this will be reduced, but at 500 V/cm the yield is still ∼20,000 photons per MeV. Roughly 1/4 of the photons are promptly emitted with a lifetime of about 6 ns while the rest have a lifetime of 1100–1600 ns. Prompt and delayed photons are detected in precisely the same way by the photon detection system. LAr is highly transparent to the 128-nm VUV photons with a Rayleigh scattering length of (66 ± 3) cm [28] and absorption length of >200 cm; this attenuation length requires a LN2 content of less than 20 ppm. The relatively large light yield makes the scintillation process an excellent candidate for determination of t_0 for non-beam related events. Detection of the scintillation light may also be helpful in background rejection and triggering on non-beam events.

The photon detection system reference design described in this section meets the required performance for light collection for the DUNE far detector. This includes detection of light from proton decay candidates (as well as beam neutrino events) with high efficiency to enable 3D spatial localization of candidate events. The TPC will provide supernova neutrino detection. The photon system will provide the t_0 timing of events relative to TPC timing with a resolution better than 1 μs (providing position resolution along drift direction of a couple of mm).

Alternative photon detector designs are under investigation to improve both light detection for the low-energy supernova events and their momentum resolution through determination of the event t_0.

Figure 4.16 shows the layout for the photon detector system, which will be described in the following sections.

4.6.1   Reference Design

The PD system is mounted as modules on the APA frames. A PD module is the combination of one light-guide (also called a "bar" due to its shape) and 12 SiPMs, as shown in Figure 4.16 (a). To enable this, the the reference design for mounting the PDs onto the APA frames calls for ten PD modules per APA, approximately 2.2-m long, 83-mm wide and 6-mm thick, equally spaced along the full length of the APA frame, as shown in Figure 4.16 (b).

The 128-nm scintillation photons from LAr interact with the wavelength shifter on the surface of the bar, and the wavelength-shifted light, with a peak intensity around 430 nm, is re-emitted inside the bar and transported through the light-guide to 12 silicon photo-multipliers (SiPMs) mounted at one end of the bar.

The wavelength shifter converts the scintillation photons striking the bar surface and directs them into the bar bulk with an efficiency of ∼50%. A fraction of the wavelength-shifted optical photons are internally reflected to the bar's end where they are detected by SiPMs with quantum efficiency well matched to the wavelength-shifted photons. The light guides are coated with TPB (1,1,4,4-tetraphenyl-1,3-butadiene). A testing program is currently underway to determine the absolute
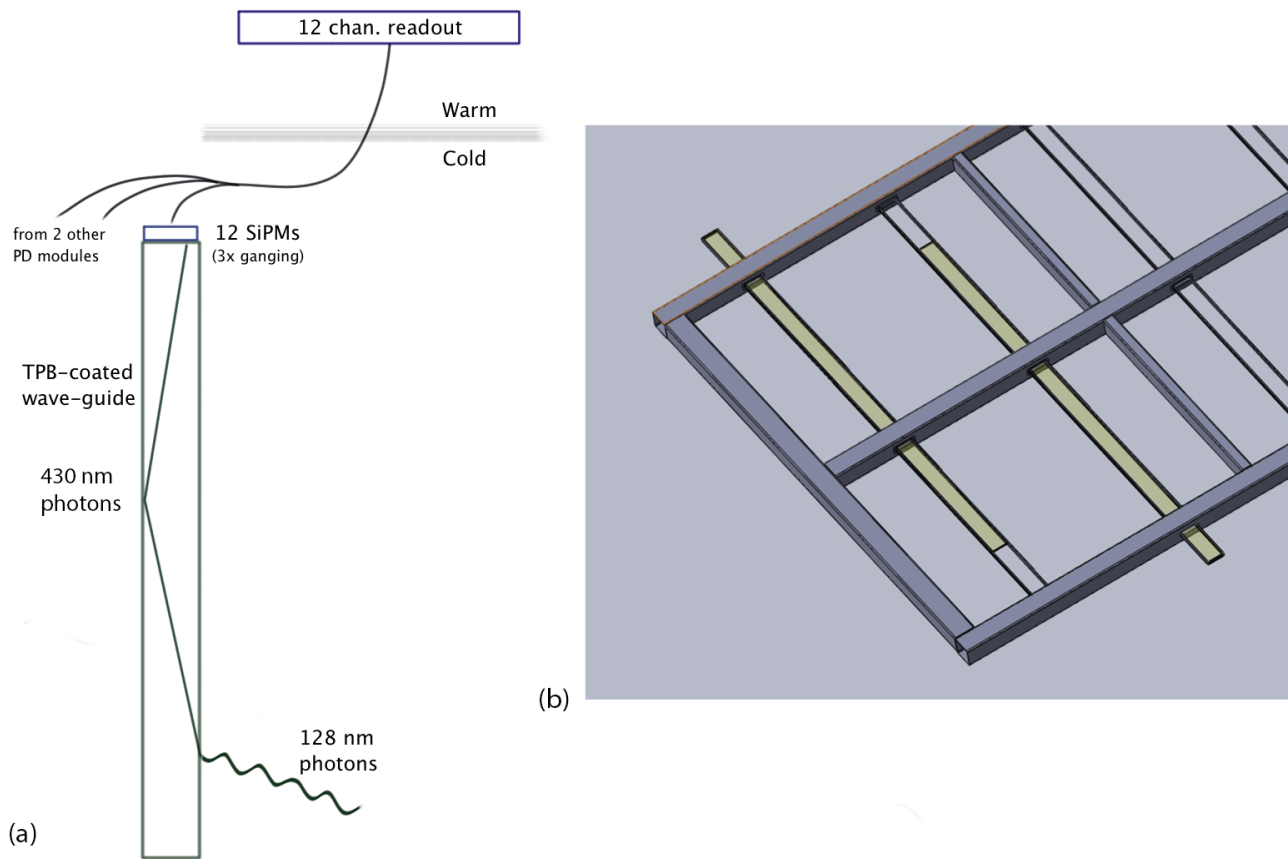
Figure 4.16: Overview of the PD system showing a cartoon schematic (a) of a single PD module in the LAr and the channel ganging scheme used to reduce the number of readout channels. Panel (b) shows how each PD module will be inserted into an APA frame. There will be 10 PDs instered into an APA frame.

performance of the light guides in LAr.

The SiPMs used in the reference design are SensL C-Series 6 mm^2 (MicroFB-60035-SMT) devices. These SiPMs have detection efficiency of 41%; the detection efficiency combines QE and effective area coverage accounting for dead space between pixels. While the C-Series SensL SiPMs are not rated for operation below $-40°$ C their performance has been excellent for this application. At LAr temperature (89 K) the dark rate is of order 10 Hz (0.5 p.e. threshold) while after-pulsing has not been an issue. Extensive testing is underway to ensure that the SiPMs can reliably survive the stresses associated with thermal cycling in LAr and long-term operation at LAr temperature.

The SiPMs are read out using shielded twisted-pair cable, one per SiPM, but the expected final design will have three SiPMs ganged together and each readout cable will contain four individual channel cables to keep the cost and cable packing density down. During the R&D phase of the project each SiPM was read out individually in order to maximize the information gathered.

The front-end electronics reside outside of the cryostat in instrumentation racks. A custom module for receiving SiPM signals has been designed and built. The module also performs signal processing in the front-end as preprocessing for trigger and DAQ. The module is called the SiPM Signal Processor (SSP) and consists of 12 readout channels packaged in a self-contained 1U module. Each channel contains a fully-differential voltage amplifier and a 14-bit, 150-MSPS analog-to-digital converter (ADC) that digitizes the waveforms received from the SiPMs. There is no shaping of the signal, since the SiPM response is slow enough relative to the speed of the digitization to obtain several digitized samples of the leading edge of the pulse for the determination of signal timing. Digitized data is processed by a Xilinx Artix-7 Field-Programmable Gate Array (FPGA). The use of the FPGA processing allows for a significant amount of customization of the SSP operation.

Once the DUNE collaboration arrives at a refined set of physics requirements for the photon detection system a set of criteria for a calibration system will be determined. In the absence of such criteria two calibration systems are being explored, and will be tested in the 35-t phase-II test. The first system, developed by ANL, utilizes five fiber-fed diffusers mounted on the TPC CPA which uniformly illuminate the photon detectors. An alternative design is employed on the IU prototypes and uses LED-driven fibers mounted alongside the waveguides.

4.6.2   Alternative Designs

Three alternative photon detector designs are currently being considered for the PD system. More extensive descriptions of the alternative designs can be found in Section 5.3 of [6].

The first alternative is based on a TPB-coated acrylic panel with an embedded S-shaped wavelength-shifting fiber. The Louisiana State University (LSU) group has developed prototypes based on this design in an attempt to allow an increase in detector size and hence increase geometric acceptance of the PD system and reduce overall system cost.

In this design, a single acrylic panel PD module has the same dimensions as the reference design and consists of a TPB-coated acrylic panel with an embedded multi-lobed "S-shaped" wavelength

shifting (Y11) fiber. The fiber is read out by two SiPMs (one on the top edge, and the other on the bottom edge of the plate), which are coupled to each end of the fiber and serve to transport the light over long distances with minimal attenuation. The double-ended fiber readout has the added benefit of providing some position dependence to the light generation along the panel by comparing relative signal sizes and arrival times in the two SiPMs. The WLS fiber converts the 430-nm light from the TPB to light with a peak intensity of 480–500 nm, which is well-matched to the peak photon-detection efficiency of typical SiPMs.

A prototype of a second alternative, under investigation by the Colorado State University (CSU) group, is intended to address an issue with the reference design, in which the application of TPB to acrylic, or other base materials, has been found to cause a significant decrease in attenuation length (down to about 30 cm) of the light guide. This prototype has a thin TPB-coated acrylic radiator located in front of a close-packed array of blue-green (Y11) WLS fibers. The prototype is two-sided and has two identical fiber arrays and radiators mounted back-to-back with a tyvek reflector between. This design allows for a reduction in the number of SiPMs required per PD module. Three SiPMs per side are needed per PD module (again the same dimensions in length and width as the reference design) for a total of six SiPMs per PD module.

The Indiana University (IU) group has advanced the CSU design and arrived at the third alternative design by replacing the Y11 fiber with a reference-design-dimensioned cast bar doped (by Eljen Technology) with the same wavelength shifter as the Y11 fiber. The TPB-coated acrylic radiator has also been replaced with a thin-fused silica plate coated with TPB. This prototype has demonstrated an attenuation length greater than 2.5 m and early indications point to it meeting the SN neutrino energy requirement. It has the highest light collection efficiency of any prototype tested so far.

4.6.3   Technology Selection

The alternative designs have all demonstrated the ability to detect LAr scintillation light, and development work is continuing. A testing program is underway comparing the various alternatives against the reference design. The Tall Bo large dewar at Fermilab and the cryogenic detector development facility at CSU are being used to compare the performance of full-scale and near-full-scale prototypes in LAr utilizing alpha sources and cosmic muons. Data from the 35-t prototype will also provide input into the technology decision.

4.7   Installation and Commissioning

The scope of the Installation and Commissioning (I&C) task includes the design, procurement, fabrication, labor, testing and delivery of equipment and infrastructure to support installation and commissioning of the detector at the far site. The following are included in the scope:

  • detector installation planning;

- installation equipment design and procurement;

- construction of a full scale mockup, consisting of four APAs, two CPAs and associated field cage, to test installation operations and equipment;

- procurement of support rails for the TPC;

- procurement and installation of relay racks to house the electronics provided by other subsystems for detector operation;

- material receipt, storage and transport to underground at the far site;

- installation of the TPC, photon detection and DAQ systems at the far site (support for detector checkout will be provided by the subsystems); and

- coordination of the commissioning for the detector and personnel to support detector operations.

I&C will have many interfaces with LBNF, and LBNF has certain responsibilities of its own, including the following.

- Excavation and outfitting of the the caverns is the responsibility of the Conventional Facilities (CF) subproject of LBNF.

- Construction and installation of the cryogenics system and cryostats is the responsibility of the cryogenics system subproject of LBNF.

4.7.1   Equipment and Services

The I&C system provides permanently installed equipment that is used by multiple detector systems and/or is integral to the installation process. This includes the relay racks, cable management and support rails for the TPC. I&C is also responsible for several detector-specific aspects of the cavern outfitting, including a clean area enclosure near the cryostat hatch to isolate the open hatch and the TPC components from the cavern environment.

The TPC elements (APAs and CPAs, described in Section 4.3), are supported by a set of five support rails permanently mounted at the top of the cryostat. The rails are supported by rods spaced at 5-m intervals from anchor points at the cryostat roof. The rods are installed with an angle bias that allows the rails to return to a level condition after the cryostat and TPC are cooled.

The TPC and photon detectors require various electrical services for operation, including bias voltages, power and control signal. These services follow a grounding plan (still under development) discussed in Section 4.7.3. The electrical services pass through a total of 78 feedthrough ports located on top of the cryostat, above every other APA junction. A relay rack is located adjacent to each port. The rack space is shared between the TPC, photon detection system readout and

power supplies. For the upper APA of each pair, the cables are pre-installed and routed from the cold side of the feedthrough down and along the support rail to the location where they connect to their corresponding APA. For the lower APAs with the electronics near the floor of the cryostat, the cables are routed from the cold side of the feedthrough down the sides of the cryostat. The lower APA cables are routed in cable trays supported from the cryostat walls.

4.7.2   TPC Installation Process

Once detector components arrive at the far site they are put in a facility used for both storage and testing/checkout, called an integration facility. Material is moved from the integration facility to the cavern (after undergoing checkout) via the Yates shaft. As installation space in the cavern is very limited, the moves will take place at the rate of installation. Most items can be transported inside the Yates shaft cage, however, the APAs are too long to fit in the cage and therefore are slung underneath it in a special container that holds four APAs in an internal rack. This cleaner rack can be extracted from the outer container into the clean area used for installation. The TPC components will have been cleaned and protected to a level suitable for installation into the cryostat as part of the TPC production process, and will have arrived at the far site in clean containers.

The clean area enclosure, in the range of class 100,000 (ISO 8 equivalent), provides an area for personnel to gown with the appropriate clean-room clothing and safety shoes. A large closable door is located at the drift junction where TPC storage containers can be parked to allow unloading of the TPC components directly into the clean area.

The TPC installation process requires the temporary installation of several items in the cryostat before it is filled with argon.

- A lighting system with emergency backup lighting will be installed and then removed in sections as the TPC installation proceeds. (This lighting will be filtered to the appropriate spectrum to protect the photon detection system installed in the APAs.)

- A filtered air ventilation system with air-monitoring sensors and alarms will be installed to ensure adequate air quality for work inside the cryostat. The system will also include a high-sensitivity smoke-detection system that is interlocked to the power for all devices inside the cryostat.

- A raised floor will be installed at the bottom of the cryostat to protect the cryostat membrane and provide a flat surface above the corrugations of the cryostat. A modular design will allow it to be removed in sections as the TPC installation progresses.

A combination of commercial and specially designed tooling will be required for TPC installation. All of the detector components and equipment inside the cryostat will be inserted through hatches located at one end of the cryostat. Temporary fixed scaffolds with integral stair towers will provide personnel access into the cryostat. A rolling scaffold, on the cryostat raised floor, also with an integral stair tower, will provide access to the top of the cryostat where the TPC connections are

made. Special fixtures and commercial gantry hoists are required to move APAs from a horizontal orientation in storage racks to a vertical orientation at the cryostat hatches. Special platforms located at the cryostat hatches will support each lower APA section while its upper APA section is connected. The platform will have multiple levels to allow personnel to access the connection points at the top of an APA and at the junction between an upper and lower APA. The installation equipment and installation procedures will be tested with a full-height mock TPC section at a suitable location at Fermilab.

Installation of the TPC is preceded by installation of the DAQ, including relay racks and TPC cables, in order to allow immediate testing of APAs upon their placement in the cryostat.

The TPC installation starts with installation of the cathode planes, one row at a time, starting with the top row of a plane, and progressing, one CPA at a time, from the far end of the cryostat to the hatch end. As each cryostat-length row is completed, it is lifted, and the next row is attached below it in the same manner; this is repeated until all four rows of the cathode plane are in place. At this point, the end-wall field cage is installed at the non-hatch end of the cathode plane.

APA installation begins next. An APA, electronics side down, is first moved into the cryostat and held temporarily in the area of the hatch. A second APA, its pair, is positioned above the first, electronics side up. The two APAs are joined at the center, lifted and attached to the support rail. The connected pair is moved along the support rail to its designated position and, except for the first pair, connected to the previously installed adjacent stacked pair. At this point the power and signal cables are connected to the APAs for testing. After proper functioning is confirmed, the field cage sections between the APAs and their facing CPAs are installed and the raised floor sections in that area are removed. This APA and field cage installation process is repeated progressing towards the hatch end of the cryostat until the entire anode plane is in place; the field cage is then installed. The process is then repeated for the other anode planes. Once TPC installation is complete, the installation equipment and the scaffolding is removed from the cryostat.

Once the TPC is installed and all temporary equipment is removed from the cryostat, the hatches are closed and all channels of the detector are tested for expected electronics noise. After successful testing, the cryostat hatches are sealed and the purge proceeds, followed by a cool-down of the cryostat and detector. At this point extensive detector testing will be conducted prior to filling with LAr. Filling each 10−kt cryostat requires approximately six months, after which a several-month-long detector commissioning phase begins.

4.7.3   Grounding

The detector will have approximately 300,000 channels of electronics with an intrinsic noise level less than 1,000 electrons. The channels will be connected to signal collection wires that are up to 7 m long, thus grounding, shielding and power distribution are critical to the success of the experiment. The installation and commissioning group will develop a detector grounding plan that coordinates between the CF power distribution, cryostat design and the detector systems. The grounding will be configured such that each detector is on an isolated and separate detector ground that is referenced to building ground through a safety saturable inductor. Dielectric breaks will be

used on all conductive piping/services that penetrate the cryostat. A copper ground plate under the steel top plate of each cryostat will be provided as part of the cryostat and used to serve as a central star ground point.

Chapter 5

Far Detector Alternative Design: Dual-Phase LArTPC

5.1 Overview

This chapter describes an alternative far detector design for DUNE. The first detector module to be installed will use the reference design described in Chapter 4, however this alternative design is under consideration for one or more subsequent modules. This design implements a dual-phase liquid argon time projection chamber (LArTPC) augmented with a light-readout system. "Dual-phase" refers to the extraction of ionization electrons at the interface between liquid and gas argon and their amplification and collection in the gas phase.

This dual-phase design is the result of 13 years of R&D consisting of two consecutive design study programs funded since 2008 by the European Union: LAGUNA and LAGUNA-LBNO. The LAGUNA-LBNO design study was concluded in August 2014. In collaboration with industrial partners, LAGUNA-LBNO designed an innovative, optimized and cost-effective configuration for a long-baseline experiment.

The studies focused on the underground implementation of a very large LAr detector (GLACIER) and produced many technical advances with respect to the tank, field cage and cathode, charge multiplication, collection and readout, as well as advances in the areas of assembly sequencing and logistics for the detector and full costing. The full design and the related technical developments are described in Annex 4E: *LAGUNA/LBNO Part 2* [29], which was submitted to the EU at the conclusion of the design study. This chapter describes the detector configuration and components, and describes how the design meets the DUNE far detector physics requirements.

The scope of a dual-phase far detector module for DUNE includes the design, procurement, fabrication, testing, delivery, installation and commissioning of the detector components:

- Charge-Readout Planes (CRP), including extraction grid, Large Electron Multiplier (LEM) and anode and readout planes;

- Cathode, field cage and high voltage system;

- Electronics and data acquisition;

- Chimneys, isolated volumes used for electronics feedthroughs;

- Slow Controls; and

- Light-readout system.

The detector components and the liquid argon (LAr) will be housed in cryostats provided by LBNF, described in Volume 3: *The Long-Baseline Neutrino Facility for DUNE* [5]. Similar to the reference design, this alternative design satisfies the performance requirements on the DUNE far detector, described in Chapter 4 for the reference design. Parameters specific to the dual-phase design are listed in Table 5.1.

Table 5.1: Performance parameters specific to the dual-phase far detector design

Parameter	Requirement	Achieved Elsewhere	Expected Performance
Gas phase gain	20	200	20-100
Electron Lifetime	3 ms	> 3 ms 35-t prototype	> 5 ms
Minimal S/N after 12 m drift	9:1	$> 100{:}1$	12:1-60:1

5.2   Highlights of the Design

This innovative dual-phase design is similar in many ways to the single-phase design, but implements some unique features and offers several advantages over it, in particular

- higher gain, leading to a larger signal-to-noise ratio (S/N);

- larger fiducial volume, enabling very long drift paths;

- lower detection threshold;

- finer readout pitch (3 mm), implemented in two identical collection views, x and y;

- fewer readout channels (153,600 vs 384,000 for a reference design $10-$kt module); and

- the absence of dead material in the LAr volume.

Following the GLACIER concept[30] (see Figure 5.1), the DUNE dual-phase LArTPC detector design has a fully homogeneous liquid argon volume, in which electrons drift upwards vertically towards an extraction grid just below the liquid-vapor interface. From there they are extracted from the liquid into the gas phase, amplified, and collected on a finely segmented anode[31, 32, 33].
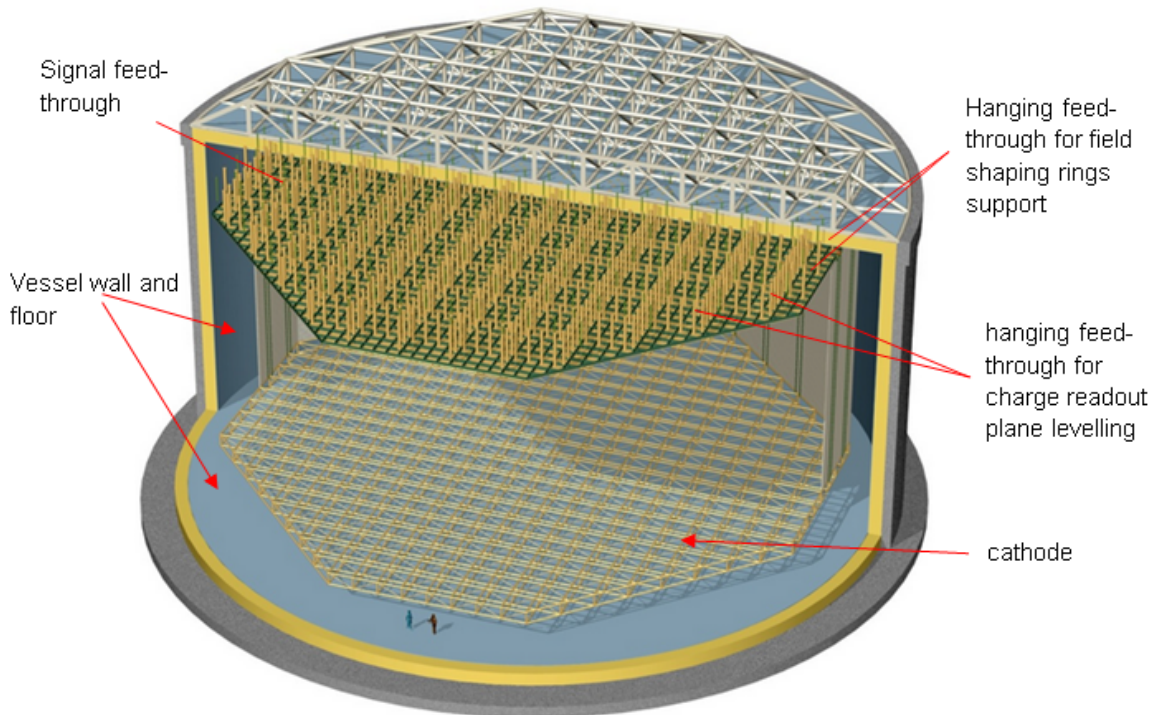
Figure 5.1: The 50−kt LBNO detector, GLACIER

The electron amplification in the gas phase enables a robust and tunable signal-to-noise ratio. The detector configuration is similar to a single-phase LArTPC. The features of the dual-phase design, e.g., high gain, allow achieving very long drift paths and large detector dimensions while minimizing the number of readout channels.

5.2.1 Charge Collection, Amplification and Readout

An extraction efficiency of 100% of the electrons from the liquid to the gas phase is achieved with an electric field of the order of 2 kV/cm across the liquid-gas interface, applied between an extraction grid submersed in the liquid and charge amplification devices situated in the ultra-pure argon gas.

These amplification devices, called Large Electron Multipliers (LEMs), are horizontally oriented 1-mm-thick printed circuit boards with electrodes on the top and bottom surfaces. They are drilled through with many holes that collectively form a micro-pattern structure; when a 3-kV potential difference is applied across the electrodes the ionization electrons are amplified by avalanches (Townsend multiplication) occurring in the pure argon gas in this micro-pattern structure[34] due to the high electric field (30 kV/cm).

The use of avalanches to amplify the charges in the gas phase increases the S/N ratio by at least one order of magnitude with a typical gain of 20–100, significantly improving the event reconstruction quality. It also lowers the threshold for small energy depositions and provides a better resolution

per volumetric pixel (voxel) compared to a single-phase LArTPC.

The charge is collected in a finely segmented 2D (x and y) readout anode plane at the top of the gas volume and fed to the front-end electronics.

The collection, amplification and readout components are combined in an array of independent (layered) modules called Charge Readout Planes (CRPs). A CRP is composed of several 0.5×0.5-m^2 units, each of which is composed of a LEM/anode sandwich. These units are embedded in a mechanically reinforced frame of FR-4 and stainless steel. The CRP structure also integrates the submersed extraction grid, which is an array of x and y oriented stainless steel wires, 0.1 mm in diameter, with 3.125-mm pitch. Thicknesses and possible biasing voltages for the different layers are indicated in Figure 5.2.
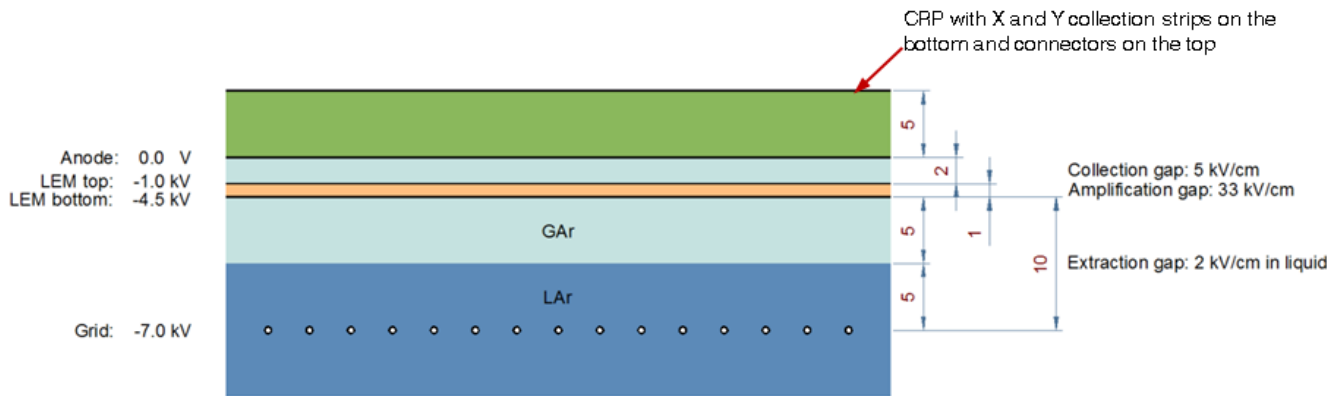
Figure 5.2: Thicknesses and HV values for electron extraction from liquid to gaseous Ar, their multiplication by LEMs and their collection on the x and y readout anode plane. The HV values are indicated for a drift field of 0.5 kV/cm in LAr.

Each CRP is independently suspended with stainless-steel ropes linked to the tank top deck. This suspension system allows adjustment of the CRP distance and parallelism with respect to the LAr surface, and keeps the extraction grid immersed.

Figure 5.3 shows the top of two side-by-side units and Figure 5.4 shows the x and y readout views.

A CRP provides an adjustable charge gain (with a minimal required gain of 20) and two independent, orthogonal readout views, each with a pitch of 3.125 mm. The LEM/anode sandwiches in the same CRP unit are interconnected with short flat cables so that each readout channel corresponds to a total strip length of 3 m.

Combined with the time information coming from the LAr scintillation readout by the PMT arrays (t_0), a CRP provides 3D track imaging with dE/dx information. The CRPs and their components are described in Section 5.4.

The typical amplification achieved by this design, between 20–100, improves the S/N ratio and thus compensates for the charge losses that occur along the very long drift paths due to the presence of electronegative impurities. Therefore, despite the longer drift length, this design requires no
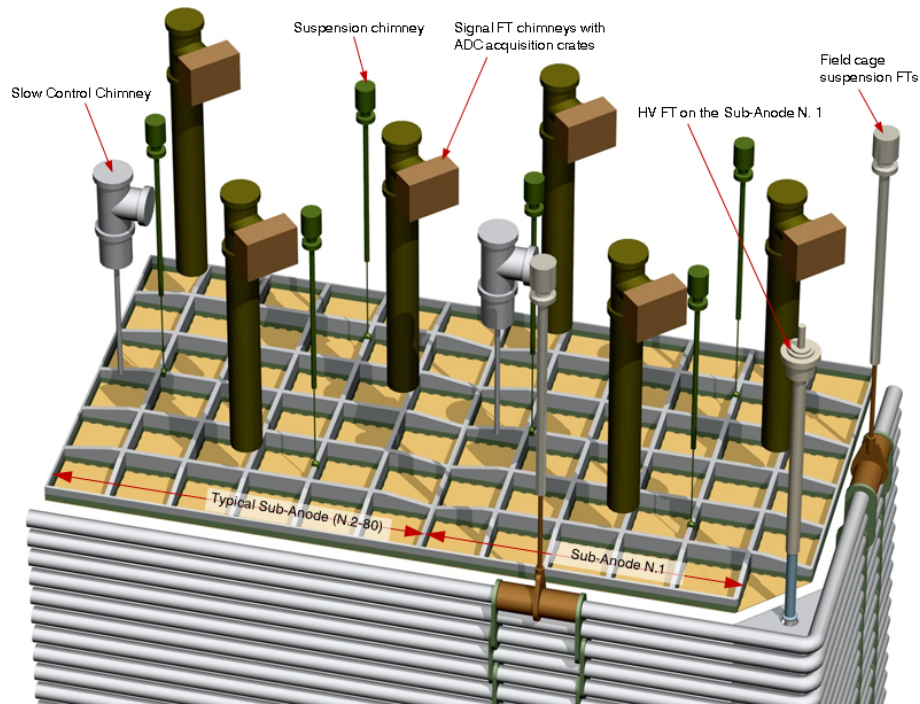
Figure 5.3: Two DUNE CRP 3 m×3 m units side by side. On the left one of the 79 equal CRP units, on the right the 1st CRP unit with a chamfered LEM/Anode Sandwich for the insertion of the high voltage feedthrough.
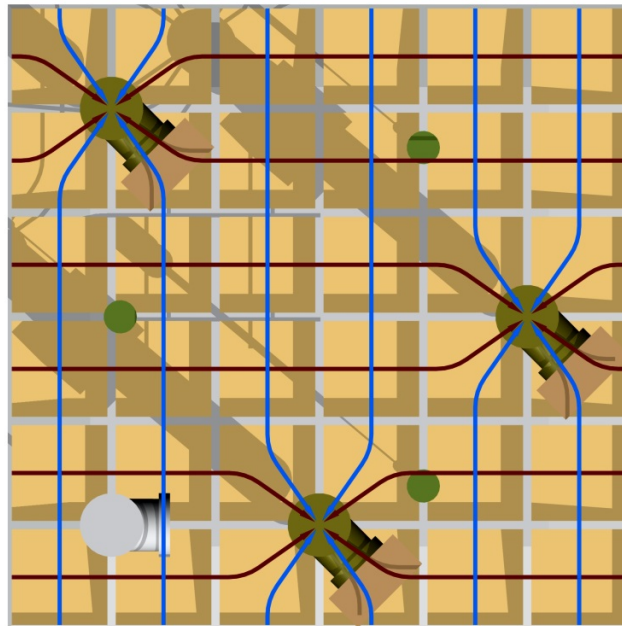
Figure 5.4: Signal collection in the x and y views of the 3×3 m^2 DUNE CRP unit by the 3 SFT chimneys.

higher purity of the LAr than does the reference design, around 0.1 ppb (or 100 ppt) of oxygen equivalent, and yields a 3-ms electron lifetime. The required level of purity can be reached by starting from commercially available ppm-level bulk argon and filling a non-evacuated vessel[35].

The S/N ratio can exceed 100 for a minimum ionizing particle (MIP) after a drift path of 12 m (given an electron lifetime of 3 ms, a drift field of 0.5 kV/cm and a LEM gain of 180). With the same drift field, the same electron-lifetime conditions and a LEM gain of 25, the S/N is larger than 50:1 for tracks up to 6 m from the anode; it reaches 14:1 for MIP tracks that are 12 m from the anode.

5.2.2 Electronics and "Chimneys"

The electrical signals from the collected charges are passed to the outside of the tank via a set of dedicated signal feedthrough "chimneys" (insulated volumes filled with nitrogen that pass through the top layer of insulation). The cryogenic front-end (FE) electronics cards, housed at the bottom of the chimneys, are based on analog preamplifiers implemented in CMOS ASIC circuits for high integration and large-scale affordable production. Within the chimneys, the cards are actively cooled to a temperature of about 110 K and isolated with respect to the LAr vessel by a cold feedthrough. This feedthrough is connected to the CRP via short flat cables of (0.5 m length) in order to minimize the input capacitance to the preamplifiers. Each chimney collects 640 readout channels.

The chimney design allows access to and replacement of the FE from the outside without contaminating the LAr volume. The digital electronics and DAQ system are completely outside the cryostat and are housed in microTCA racks mounted on each signal feedthrough chimney.

Other feedthroughs are planned for the cathode HV connection, the CRPs' suspension and level adjustment, the high voltage and signal readout of the PMTs, and the monitoring instrumentation (level meters, temperature probes, strain gauges, etc.).

5.2.3 Cathode, Field Cage and HV System

The drift field (E $\simeq$ 0.5 kV/cm) inside the fully active LAr volume is produced by applying high voltage to the cathode plane at the bottom of the cryostat and is kept uniform by the field cage, a stack of 60 equally spaced field-shaping electrodes, polarized at linearly decreasing voltage from the cathode voltage to almost ground potential, reached at the level of the charged readout plane. The electrodes are rectangles made of stainless-steel tubes (diameter 140 mm, vertical pitch 200 mm) with rounded corners, running horizontally (and stacked vertically) around the active volume (see Figure 5.5).

The field cage is held in place by mechanical structures hung from the top deck of the vessel that also provide insulation. The cathode structure, constructed of a reinforced frame to guarantee its planarity, is suspended from the field cage and hangs near the bottom of the cryostat. It is a
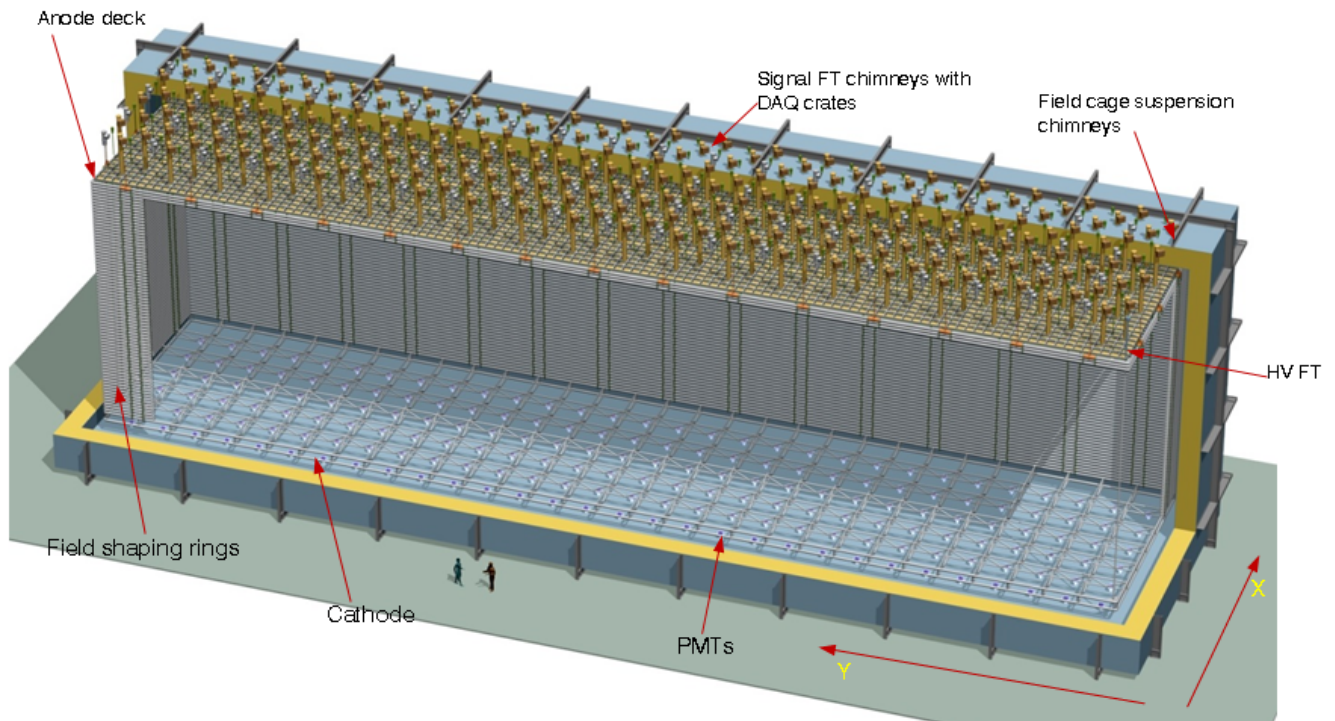
Figure 5.5: The DUNE dual-phase detector (partially open) with cathode, PMTs, field cage and anode plane with chimneys.

segmented structure of tubes of different sizes arranged in a grid to minimize weight, limit sagging and avoid high electric field regions in its proximity. The segmented structure allows scintillation light to pass through and be detected by uniform arrays of photomultipliers (PMTs) mounted 1 m below it at the bottom of the tank.

5.3   Detector Configuration

The detector for the 12.1−kt active mass module is built as a single active volume 60 m long, 12 m wide and 12 m high, with the anode at the top, the cathode near the bottom and an array of 180 photon detectors (PMTs, 1 per 4 m^2) located at the bottom of the vessel underneath the cathode. The active volume (see Figure 5.6) is surrounded by the field cage. These components are described in Section 5.2.3.

The proposed design optimally exploits the cryostat volume of 14(w)×14.1(h)×62(l) m^3 with an anode active area of 12×60 m^2 and a drift length of 12 m, corresponding to an active mass of 12.096 kt of LAr (10.643 kt fiducial).

The design is based on the 20−kt LAGUNA-LBNO design study with a CRP unit size adapted to the dimensions on the active area. The cryostat height could be increased to achieve 15-m drift, resulting in an active mass of 15.12 kt (13.444 kt fiducial). This 15.1−kt configuration, apart

from the longer drift distance and field cage, would have the same characteristics of the 12.1−kt configuration, given that the covered active area is exactly the same. With these transverse dimensions, every additional meter of drift length provides a 1−kt increase in the active mass at a moderate additional cost.
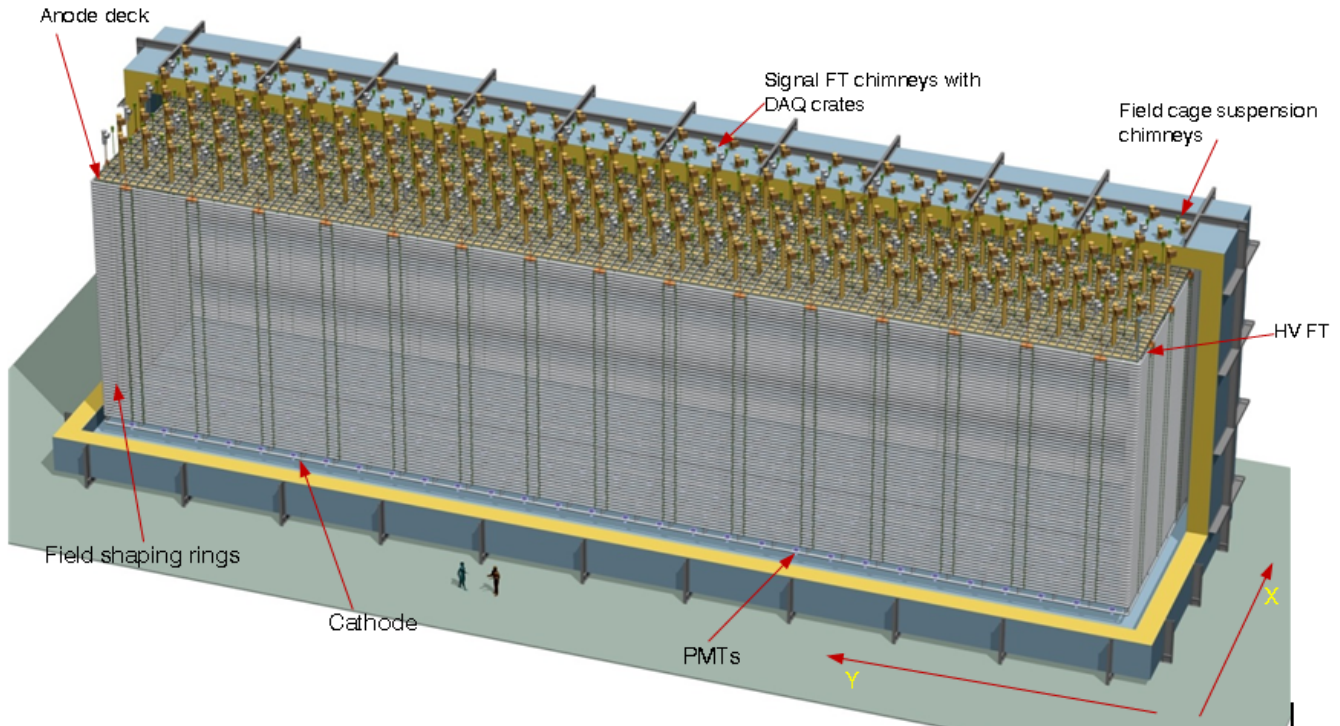
Figure 5.6: The DUNE dual-phase detector with cathode, PMTs, field cage and anode plane with chimneys.

The ionization electrons in the liquid phase drift in a uniform electric field towards the anode plane at the top of the active volume. This is made by by an array of 80 independent CRP modules, 3×3 m^2 each. The extraction of the electrons from the liquid to vapor phase is performed thanks to the submersed horizontal extraction grid, integrated in each CRP structure. A CRP unit includes 36 (0.5 m$\times$0.5 m) LEM/anode sandwiches, providing tunable amplification and charge collection on two independent views organized in strips of 3-m length and 3.125-mm pitch. There are 1920 readout channels for each CRP. Signals in each CRP unit are collected via three signal feedthrough chimneys hosting the the front-end cards with the cryogenic ASIC amplifiers (640 channels/chimney) which are accessible and replaceable without contaminating the pure liquid argon volume. Each chimney is coupled to a microTCA crate ensuring the signals' digitization and data acquisition. These crates are connected via optical fiber links to the DAQ back-end. The total number of readout channel per 10−kt module is 153,600.

Each CRP unit is independently suspended by three stainless steel ropes. The vertical level of each CRP unit can then be automatically adjusted with respect to the LAr level via three suspension feedthroughs, electrically operated from outside. A Slow Control feedthrough, one per CRP unit, is used for the signals readout for level meters and the temperature probes and to apply the HV bias on the two sides of the LEMs and on the extraction grid. The number of components and

parameters for the 12−kt (15−kt) dual-phase LArTPC are summarized in Tables 5.2 and 5.3.

Table 5.2: Sizes and Dimensions for the 12−kt (15−kt) dual-phase LArTPC

Item	Value(s)	
Active volume width and length	W = 12 m	L = 60 m
Active volume height	H = 12 m (H = 15 m)	
Active volume/LAr mass	8,640 (10,800) m^3	12,096 (15,120) metric ton
Field ring vertical spacing	200 mm	
Field ring tube diameter	140 mm	
Anode plane size	W = 12 m	L = 60 m
CRP unit size	W = 3 m	L = 3 m
HV for vertical drift	600–900 kV	
Resistor value	100 MΩ	

Table 5.3: Quantities of Items for the 12−kt (15−kt) dual-phase LArTPC

Item	Number
Field rings	60 (75)
CRP units	4 × 20 = 80
LEM/Anode sadwiches per CRP unit	36
LEM/Anode sandwiches (total)	2,880
SFT chimneys / CRP unit	3
SFT chimneys (total)	240
Readout channels / SFT chimney	640
Readout channels (total)	153,600
Suspension FT / CRP unit	3
Suspension FTs (total)	240
Slow Control FT / sub-anode	1
Slow Control FTs (total)	80
HV feedthrough	1
Voltage degrader resistive chains	4
Resistors (total)	240 (300)
PMTs (total)	180 (1/4 m^2)

A number of factors make the dual-phase TPC concept as described in this chapter well suited to large detector sizes like the DUNE far detector.

In this design, the charge attenuation on the long drift paths is compensated by the charge amplification in the CRPs. This configuration also simplifies construction by optimally exploiting the long vertical dimensions of the cryostat, providing a large homogeneous fiducial volume free of embedded passive materials (effectively increasing the detector size), reducing the number of readout channels, and ultimately lowering costs. The CRPs collect the charge in a projective way, with practically no dead region and read the signals out in two collection views, eliminating the need

for induction views, which simplifies the reconstruction of complicated topologies. The tunable high S/N provides operative margins with respect to the noise and electron lifetime conditions and lowers the threshold on the minimal detectable energy depositions .

The dual-phase readout scheme has been successfully demonstrated on several prototypes through R&D over a span of more than 10 years. The design of very large (20–50 kt) underground detectors based on this concept has been developed in great detail in the context of the LAGUNA and LAGUNA-LBNO design studies. The CERN WA105 demonstrator, described in Section 9.4, is intended to prototype a full-scale implementation of this technique, as well as demonstrate other technologies developed for the construction of large underground TPC detectors.

A complete configuration, based on the double-phase design, been optimized for the $10-$kt detector module of the DUNE far detector.

5.4   The Charge Readout System

In the dual-phase LArTPC concept, the ionization electrons are multiplied in avalanches occurring inside detectors, the Large Electron Multipliers (LEMs), located in the argon gas phase above the liquid argon level. The drift field of the TPC brings the electrons up to the liquid argon surface where they can be extracted into the gas using a 2-kV/cm electric field defined across the liquid-gas interface. This extraction field is applied between a submersed extraction grid (stainless steel wires tensioned in both x and y directions) and the bottom side of the LEMs. The LEMs are printed circuit boards oriented horizontally, with conductive layers (electrodes) on the top and bottom surfaces, and many holes drilled through. The holes form a micro-pattern structure within which the amplification occurs. By applying voltages across the two electrodes of the LEM, a 30-kV/cm electric field region is defined in the holes[34]. Electrons transiting these high electric field regions in the holes trigger Townsend multiplication in the pure argon gas.

The amplified charge is then collected and recorded on a 2D anode consisting of two sets of 3.125-mm-pitch gold-plated copper strips that provide the x and y coordinates (and thus two views) of the event.

Typical electric fields between each stage of the readout are illustrated in Figure 5.7. Table 5.4 shows the inter-stage distance and the tolerances required to obtain uniformity of gain to within $\sim$5%.

Table 5.4: Interstage distances and electric field settings of the dual-phase readout components.

Component	Distance [mm]	Tolerance [mm]	Electric field [kV/cm]
Anode-LEM top electrode	2	0.1	5
LEM top-bottom electrode	1	0.01	30-35
LEM bottom electrode-grid	10	1	2 (in LAr) and 3 (in GAr)
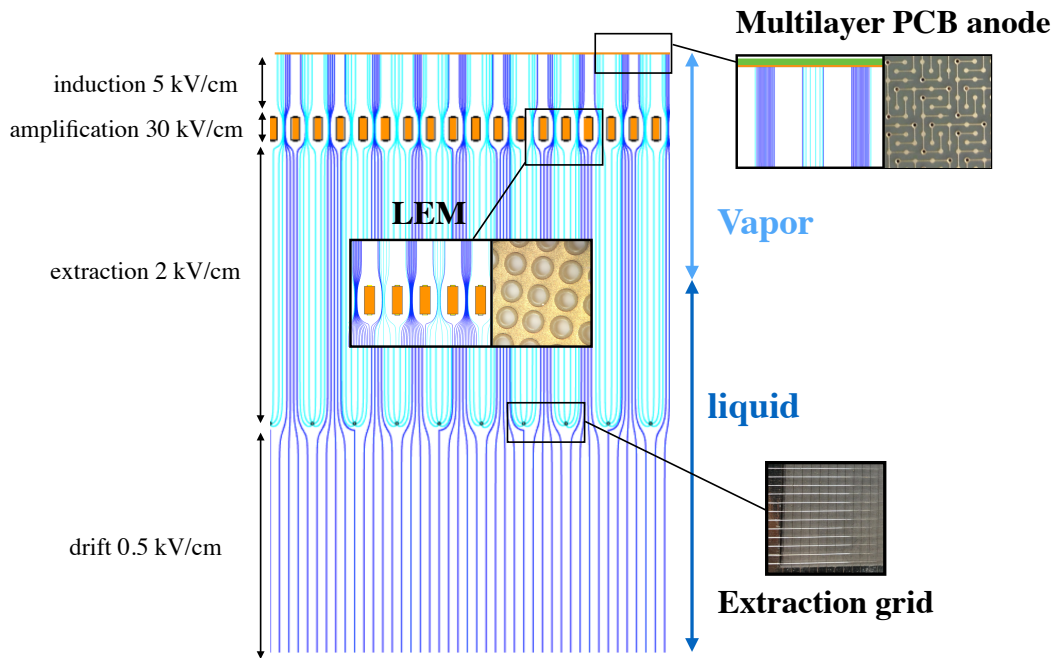
Figure 5.7: Illustration of the electric fields in the amplification region of a dual-phase LArTPC. The simulated field lines in dark blue indicate the paths followed by the drifting charges (without diffusion).

The extraction grid, LEM and anode are assembled into three-layered "sandwiches" with precisely defined inter-stage distances and inter-alignment, which are then connected together horizontally into modular units of area 9 m^2. These units are called Charge Readout Planes (CRPs).

5.4.1   The Charge Readout Plane (CRP)

Each CRP is an independent detector element that performs charge extraction, multiplication and collection, and has its own high voltage system and independent signal feedthroughs. The entire area of the LEM and anode in a CRP is active.

The LEM and corresponding anode are pre-mounted in units of 50×50 cm^2, called LEM/Anode Sandwich (LAS) modules, before being assembled with an extraction grid into a CRP. Each anode in a LAS is segmented in 50-cm long x and y strips . Adjacent LAS anodes are bridged together to form readout strips of the required length by connecting short flat cables to KEL connectors soldered onto the top sides of the anodes. The signals from the last anode in each strip chain are brought to feedthroughs mounted on the other side of the front-end electronics embedded inside dedicated signal-feedthrough chimneys using 50-cm-long flat cables.

The LBNO 20-kt detector design (described in [29]) featured modularized CRPs of dimensions of 4×4 m^2, with 2-m long anode strips. For the DUNE cryostat geometry, a size of 3×3 m^2 with a strip length of 3 m is found to be optimal. The description in this section is based on the LBNO 4×4 m^2 CRP.

Each CRP is independently hung from the vessel deck through its three suspension feedthroughs. It has its own high voltage system and independent signal and slow-control feedthroughs. Figure 5.8 illustrates the 4×4 m^2 CRP; its characteristics are summarized in Table 5.5.
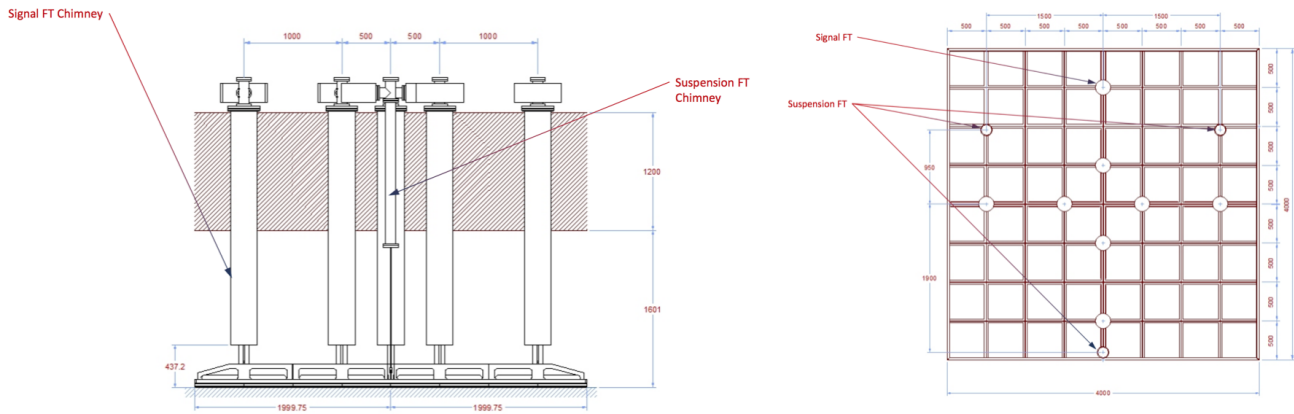
Figure 5.8: Side and top views of the 4×4 m^2 CRP designed for LBNO (units in mm).

Table 5.5: Numbers of components of the 4×4 m^2 CRP designed for LBNO

Component	Number
50×50 cm^2 anode panels	64
50×50 cm^2 LEM panels	64
Signal feedthroughs	8
Suspension feedthroughs	3
Readout strip length (m)	2
Number of channels	5120

The entire area of the LEM and anode is active, as noted earlier, and each adjacent 50×50 cm^2 LAS module has a gap of only 0.5 mm. Therefore, the 4×4 m^2 area of the CRP is fully active; the 0.5-mm edge gaps occurring every 50 cm do not interfere with the charge collection in the anode, given its readout pitch of 3.125 mm.

The extraction grid consists of 100 μm diameter stainless steel wires tensioned in both x and y directions over the entire 4-m length/width of the CRP with 3.125 mm pitch. They are soldered into groups of 32 on independent wire-tensioning pads oriented perpendicularly to the side of the CRP frame. Each wire-tensioning pad consists of a printed circuit board (PCB) for HV-connection that is fixed very precisely to a mechanical wire holder. The PCB has 32 soldering pads with 200-μm grooves for precise positioning of the wires. During the wire-soldering process each wire is tensioned by 150-g lead weights and positioned in a groove. (With this method better than 50 μm precision on the wire pitch, measured under the microscope, was achieved for the LBNO-WA105 prototypes.) The PCB is then mounted on the wire holder and the tension of the group of 32 wires can be precisely adjusted by pushing the holder against the CRP's FR4 frame with two screws.

The wires, ∼3 m long in both x and y directions, have their sags minimized to ∼0.1 mm thanks to x and y oriented supporting comb-teeth blades (see Figure 5.9) inserted between anode planes

of 1 m×1 m size. The array of blades penetrates the liquid surface and has the additional benefit of maintaining the liquid level still.
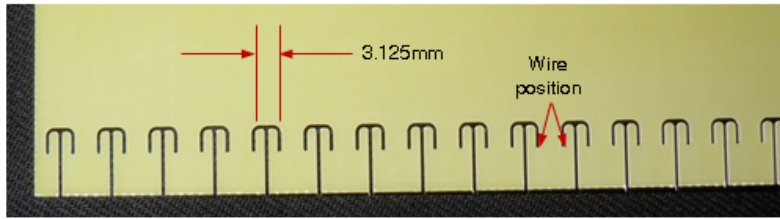
Figure 5.9: Comb for hanging extraction grid wires

The 4×4 m^2 CRP has 5120 readout channels in total. The signals from the CRP are read out through eight signal feedthroughs (SFTs) chimneys at the bottom of which the front-end electronics cards are mounted. Amplified signals are transmitted to the DAQ system located on top, outside of the vessel. Each chimney groups 640 channels.

The 3×3 m^2 DUNE CRP, is a down-sized version of the LBNO CRP; it has three signal feedthrough chimneys and 1920 readout channels.

Three suspension feedthroughs are arranged as an equilateral triangle whose barycenter coincides with that of the CRP; they suspend the CRP at the required position and precisely adjust the CRP level with respect to the liquid argon surface. Figure 5.10 shows a 3D view of the CRP, where the signal chimneys (discussed in Section 5.6) and the stiffening frame are visible.
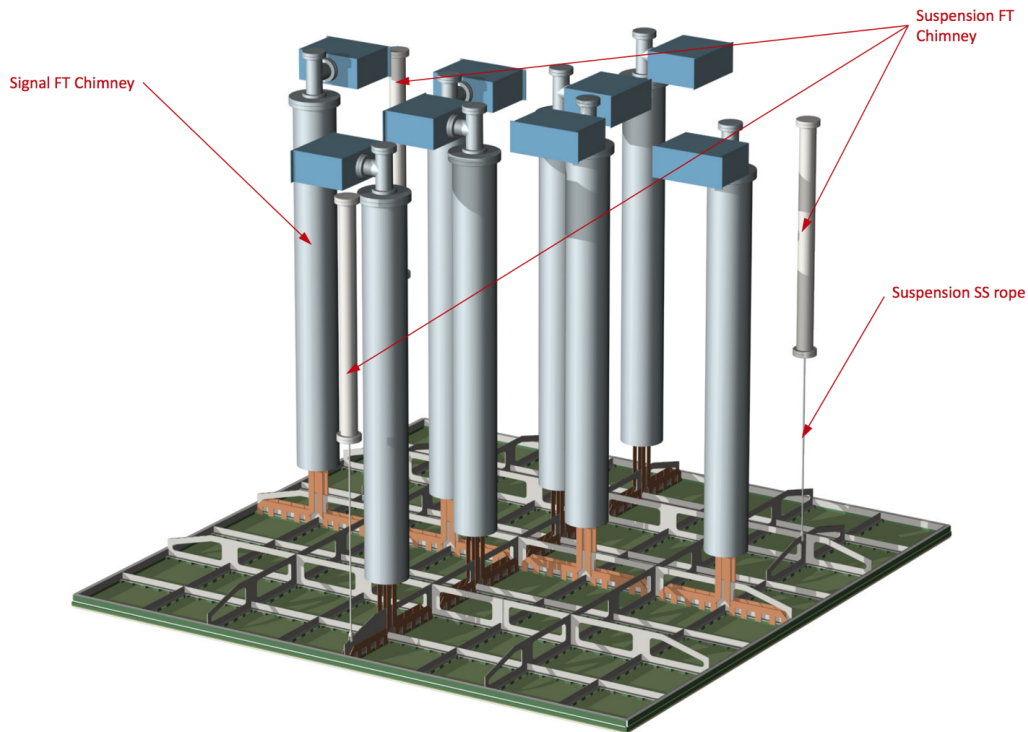
Figure 5.10: 3D view of the 4×4 m^2 LBNO CRP.

5.4.2   The LEM/Anode Sandwich (LAS)

LAS modules, the CRP building blocks composed of 50×50-cm^2 LEM-anode sandwiches, have been extensively studied as part of the ongoing CERN WA105 prototyping efforts (see 9.4). The LEMs and the anodes are produced by a PCB manufacturing company called ELTOS (`www.eltos.it`). Their designs are the outcome of intensive R&D effort over the last few years, aimed at maximizing the S/N ratio for the large-area readouts envisioned for use in giant dual-phase LArTPCs. Figure 5.11 shows the LEMs and anodes. This section summarizes key features of the LAS.
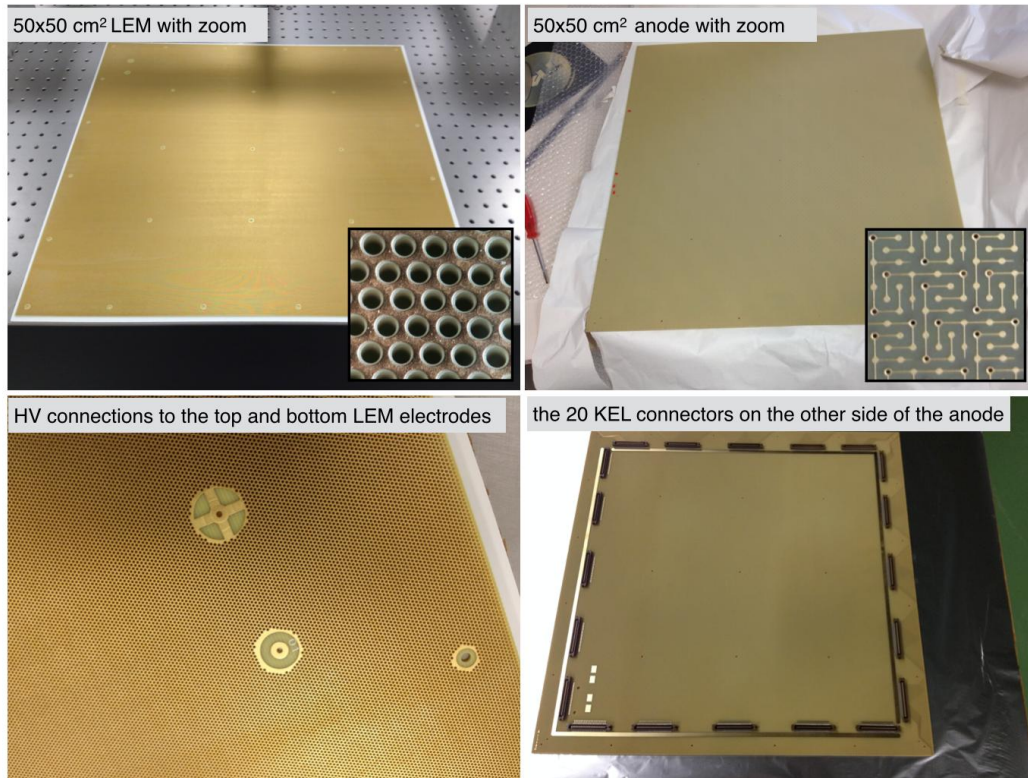
Figure 5.11: Top: pictures of the LEM and anode along with microscope views. Bottom: close up of the LEM HV connectors and back view of the anode with the KEL signal connectors to bridge to the adjacent LAS or to connect flat cables going to the signal feedthrough

The 50×50 cm^2 anode: Each 50×50 cm^2 anode is manufactured from a single multilayer printed circuit board (PCB). The readout strips for both x and y views consist of a pattern of gold-plated copper tracks with a 3.125-mm readout pitch. The two views have superimposed track patterns that are electrically insulated from one another. Electrical insulation in the points where the x and y tracks would superimpose is achieved by having tracks crossing over and under each other using a system of vias between the top and bottom layers of the PCB.

The design of the track patterns forming the strips is such that both x and y views collect the same amount of charge, independent of the angle of charged-particle tracks with respect to the readout strip orientation. The tracks pattern should then ensure a uniform and isotropic coverage

of the strip surface while minimizing the strip capacitance. These criteria have driven a thorough design optimization. Various PCB layouts were tested in order the achieve the best performance, as described in [36]. The final layout and schematic of the anode are shown in Figure 5.12.
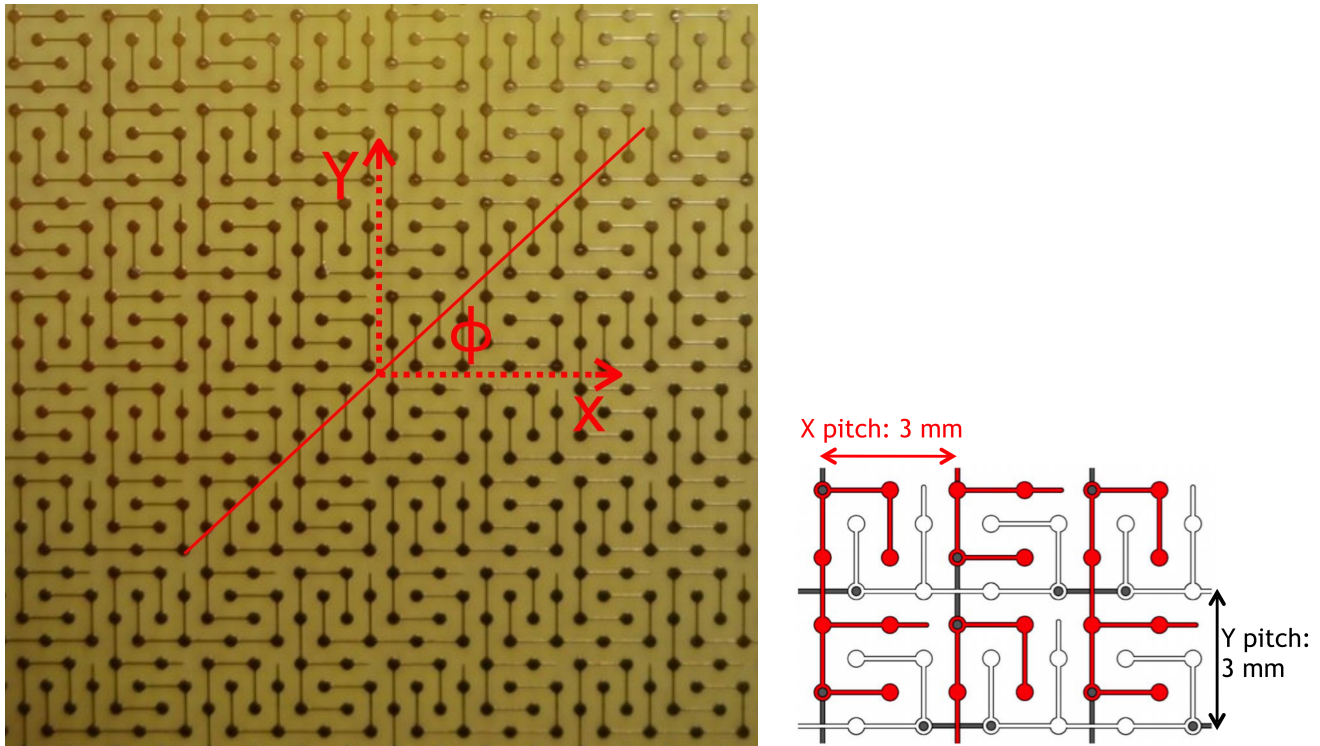
Figure 5.12: The 2D anode (left) and its schematic showing the interconnections ensuring continuity within each view while preserving insulation with respect to the perpendicular view (right). One view is filled in red and the other in white.

As result of this optimization, the electrical capacitance of the readout strips has been limited to only 150 pF/m, which translates into an electronic noise of about ∼1000 electrons for a 2-m readout length. Figure 5.13 (right) shows that the charge-sharing asymmetry between the two views is kept within 1%. The two views can thus be treated in a completely equivalent way from the point of view of the reconstruction. The response in terms of the charge collection per unit pathlength $\Delta Q/\Delta s$ is independent of the charged-particle tracks' azimuthal angle ϕ (see Figure 5.13 left and middle).

The 50×50 cm^2 LEM: Each LEM is built from a 1-mm-thick copper-clad epoxy PCB with 500 μm diameter holes drilled through, surrounded by a 40-μm dielectric rim. The holes are arranged in a honeycomb pattern with a pitch of 800 μm, resulting in about 200 holes per cm^2 and $\mathcal{O}(500,000)$ holes over the entire 50×50 cm^2 area. The holes provide confinement for the UV photons produced during the avalanche process and thus act as a mechanical quencher to prevent photon feedback. This property makes the LEM suitable for operation in ultra-pure argon vapor without the addition of a quenching gas.

The amplification of the drifting charges in pure argon vapor at 87 K with LEMs has been extensively demonstrated on a chamber with 10×10 cm^2 area readout (see e.g., [37, 38]) as well as on
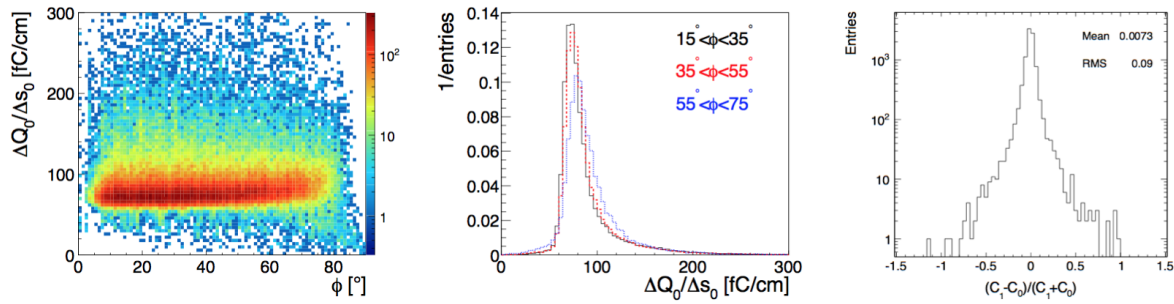
Figure 5.13: Charge deposition per unit of pathlength measured on LEM view 0 ($\Delta Q_0/\Delta s_0$) as a function of the track angle ϕ (left) and projection of the $\Delta Q_0/\Delta s_0$ distribution in three ϕ intervals (middle). The right plot shows the distribution of the difference between the total charge collected on both views normalized to their sum

a larger device consisting of a 40×80 cm^2 readout[31]. Both setups were successfully and stably operated at constant gains of at least 15, corresponding to S/N $\approx$ 60 for MIPs. Recent studies[39] systematically characterize the impact of the rim size, insulator thickness, hole diameter and hole layout on 10×10 cm^2 area LEMs. The response in terms of maximal reachable gain and influence on the collected charge uniformity, as well as the long-term stability of the gain, has been thoroughly compared for these different layouts. Some results are shown in Figure 5.14. Gains of almost 200 were reached and the LEMs could be operated at stable gains of at least $\sim$15 after a charging up period of about a day.
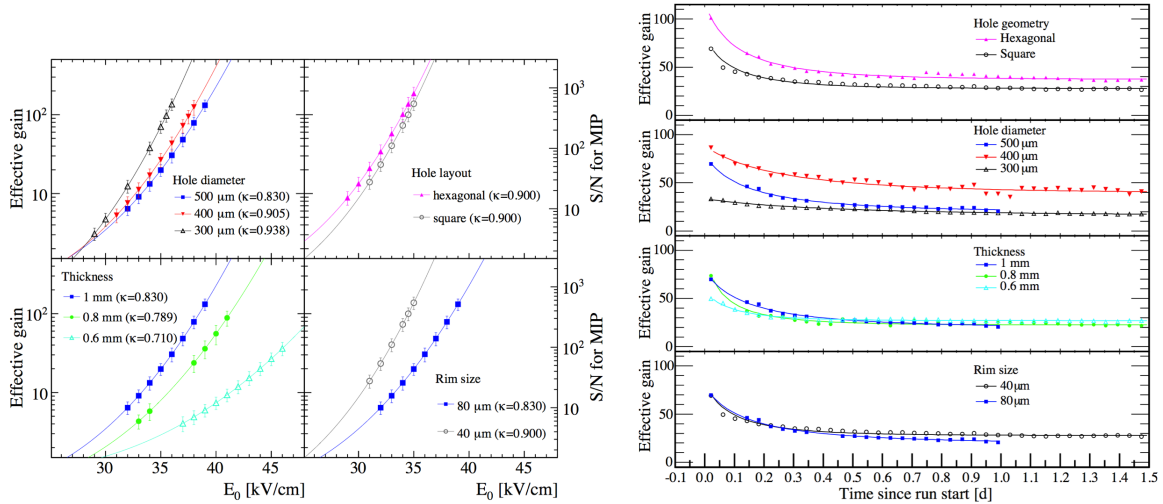
Figure 5.14: Performance of the LEMs with different geometry parameters. Left: effective gain vs. LEM electric field; right: the stabilizations of the effective gain over time.

LAS Assembly: Figure 5.15 shows the LEM/anode sandwich (LAS). A LAS is fixed together with 29 M2 PEEK screws, each containing a precisely machined 2-mm-thick pillar to guarantee a constant inter-stage distance between LEM and anode on the entire 50×50 cm^2 area. The dead zones caused by the supporting pillars and the two HV pins on the LEMs are minimized and make up less than 0.5% of the total area. The inter-stage distance between the LEM and anode in the

LAS has been measured at many points. The results are shown in Figure 5.15 and are described in [40]. They indicate that the planarity is within the required tolerance of 2 mm $\pm$ 100 μm .
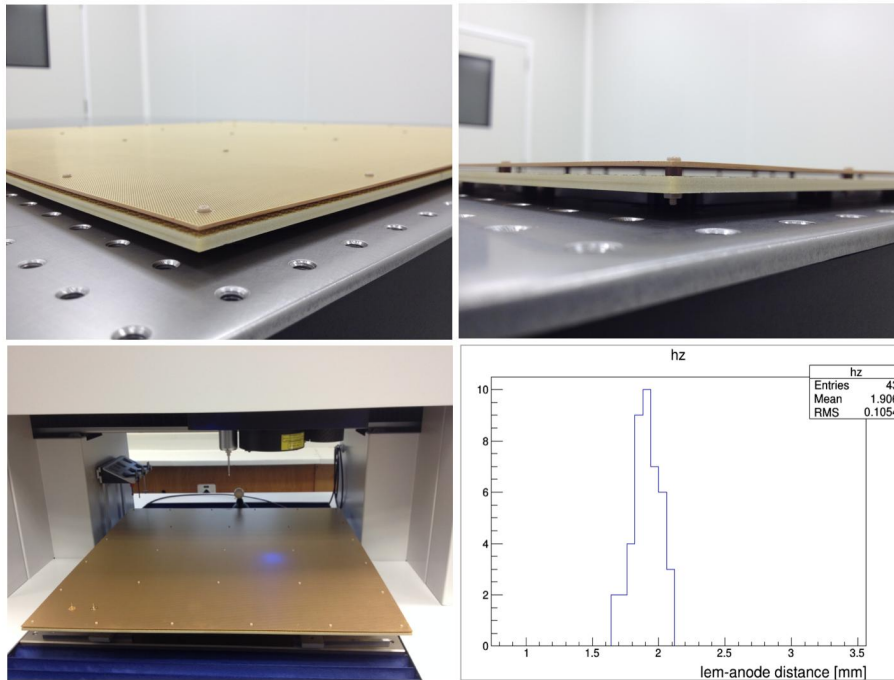
Figure 5.15: Close up pictures of the LEM/anode sandwich. The two bottom figures show a the measurement at the CERN metrology lab and a histogram illustrating the measured gap between the LEM and anode in various points. As can be seen the distribution is centered on the nominal distance of 2 mm and has an RMS of about 100μm.

The entire mounting sequence of the sandwich as well as that of the different elements of the CRP are being addressed in the WA105 prototype detectors. An example of a sandwich assembly on a 3×1 m^2 CRP is shown in Figure 5.16.

5.5 The Field Cage, High Voltage System and Cathode

This section describes the design of the high voltage system, field cage and cathode for the TPC. It is inspired by the LBNO 20-kt and 50-kt detector designs, described in [29], which can be simplified and down-sized for the DUNE detector (12 kt or 15 kt), due to the shorter drift path and the rectangular aspect ratio of the detector. The much shorter transverse dimension of DUNE's with respect to the LBNO design (12 m vs 40 m span) permits a lighter cathode structure (less sag requires less compensation) and a simpler hanging system for the drift cage and the cathode.

In the LBNO design the field cage is composed of equally spaced octagonal rings stacked around the active volume that create a uniform drift field; they have an intensity that is adjustable in the range 500 to 1000 V/cm. This leads to a cathode voltage of up to 2 MV when operating at the maximal field intensity of 1 kV/cm over a drift distance of 20 m.

Figure 5.16: Pictures of the assembly of a $3 \times 1\text{m}^2$ CRP

Two different approaches have been developed for the drift-field high voltage generation system. The first one uses an external HV power supply and uses HV feedthroughs to penetrate into the detector volume. The WA105 demonstrator will use this approach for its drift of 6 m and a cathode voltage up to 600 kV. The second approach places a HV generator, the Greinacher HV multiplier, directly inside the LAr volume. It is an innovative technique, with some advantages relative to the first approach. This technique particularly suits giant-scale detectors that require a very high voltage of ∼1–2 MV.

The DUNE detector (12-m drift) requires a voltage of 600 kV in order to operate at a field intensity of 0.5 kV/cm. This voltage is a factor of 3.3 higher than that of the reference design (Chapter 4) and it will be tested during the WA105 detector operation at 1 kV/cm over a 6-m drift.

The field cage designed for the LBNO 20-kt detector (20-m drift path) is composed of 99 octagonal field-shaping coils manufactured from 316L stainless-steel tubing and long radius elbows to EN 10217-7 shop. The straight pipes and the elbows are assembled to form the coils by using a combination of welded and clamped joints.

The coils are supported by 32 off-hanging columns of G-10CR glass fibre/epoxy-laminated sheet insulating material, built in the form of chains, and suspended from the tank deck structure.

Each coil is designed as a series of fully welded infill tubes intended to fit between pairs of hanging support columns to form one section of the field cage. Short sections of the field-shaping coils are integrated as pins into links to assemble each chain. Longer sections and corner sections of the field-shaping coil are then fixed between the hanging columns to complete each coil (Figure 5.17). The combined assembly of 99 sets of field shaping coils within the 32 off-hanging columns provides

a complete field cage.
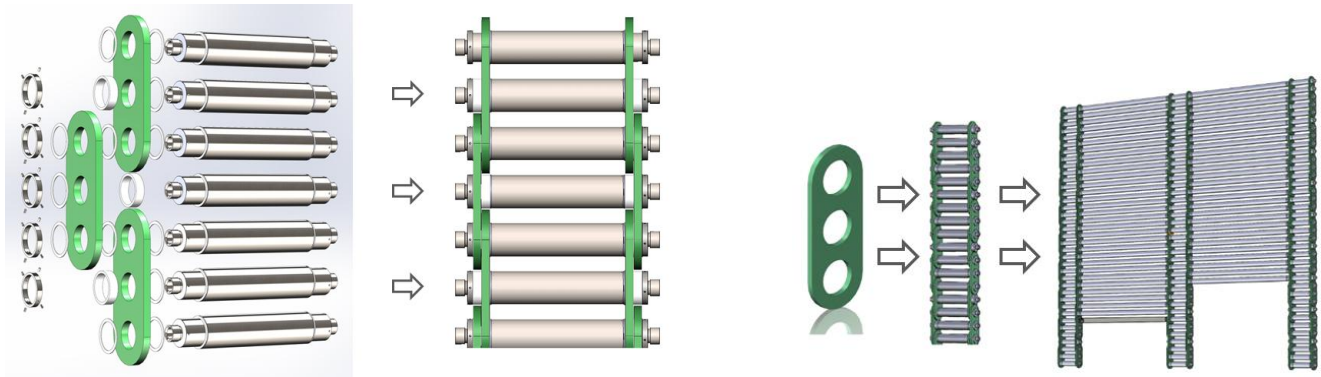
Figure 5.17: Left: assembly of the elements of a hanging chain. Right: construction of a field cage section from the hanging chains and the field shaping coil elements.

The infill tube specifications assume an outer tube diameter of 139.7 mm, which is common to the cathode structure. This allows a thinner wall, 1.6 mm, to be used in non-structural parts of the coils. Although a non-standard size, the total length of this tube can be manufactured as a special mill run. This will make it possible to save 21 tons of material relative to the standard tubes (wall thickness of 2.0 mm). The wall thickness of the link pins is 2.6 mm; this will provide sufficient stiffness to resist the bending torques across the link pins. All specialist preparation and welding of the link pins will be carried out in shop facilities under controlled fabrication. This includes the rough machining of the end fittings, preparation of the tube ends and the jig-welding of the complete assemblies. Further machining, after welding, will be carried out to ensure correct alignment and tolerance levels in conjunction with the hanging columns. Vent holes will be incorporated into the tubes as required to facilitate construction and to allow purging with GAr/LAr on commissioning.

Manufacturing, transportation and underground construction considerations were a fundamental part of the field-shaping coil design process, in collaboration with the LAGUNA-LBNO industrial partners. The requirement of construction in a clean-room environment within the completed membrane tank presented considerable challenges in terms of logistics and the development of the overall concept for fabrication. It was concluded that a modular construction approach would be required in order to (1) maximize off-site shop fabrication and minimize on-site assembly, and (2) ensure the cleanliness of construction and minimize the installation time. Each field-shaping coil is broken down into sets of three main construction modules (for more details see [29]).

Although separate components, the field shaping coils and the cathode structure share identical features and dimensions. Thus, the maintenance of common interfaces is an important advantage of the overall field cage design.

The DUNE 12-kt detector field cage would require 60 stacked rectangular rings used to cover the 12 vertical meters of drift volume.

The LBNO cathode design for the 50-kt detector follows an extensive review of options and analysis. The design incorporates features to minimize the static deflection of the cathode and to maximize the electrostatic performance. (To avoid regions with high electric fields, the electric field is limited

to 50 kV/cm.) Similar to the field-shaping coil, and for the same reasons, the cathode is designed as a modular structure ensuring a minimal on-site assembly time. The cathode is designed as a fully welded tubular rectangular 3D-grid structure in 2 m×2 m modules, 1 m deep in the vertical direction supported only from the periphery (Figure 5.18).
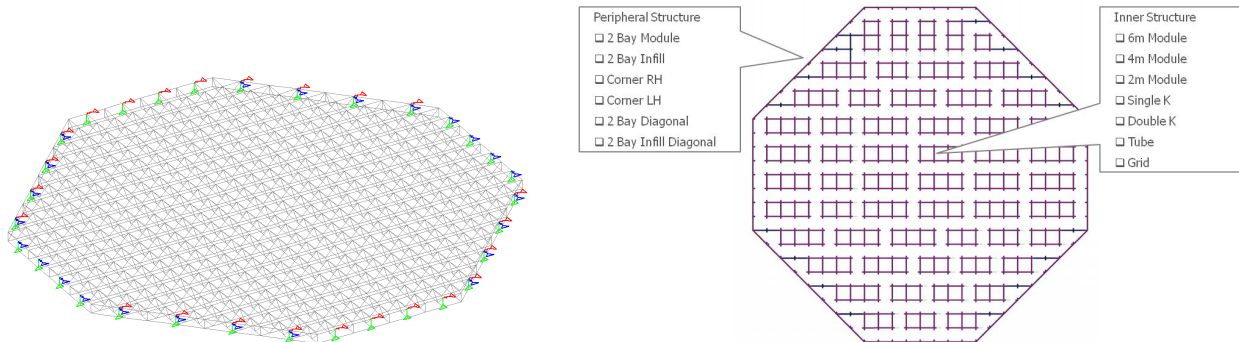
Figure 5.18: Left: cathode plane design for the LBNO detector. Right: breakdown of the cathode structure in construction modules.

The top and bottom grid structures for the cathode are manufactured from 139.7-mm OD tubes with wall thickness 2.6 mm to EN 10217-7 in 316 stainless steel. The bracing structure is manufactured from 60.3-mm OD tubes with wall thickness 2.6 mm, also to EN 10217-7 in 316 stainless steel. A grid structure comprising 10-mm OD tubes with wall thickness 1 mm, arranged in a single plane at 100-mm centers, is fitted to the top of the cathode. The maximum module size for this structure is 6 m, comprising three full 2 m×2 m×1 m deep modules of the cathode structure. The preparation and welding of the modules will be carried out in controlled facilities at the fabrication shop. Vent holes are incorporated into the grid structures to facilitate construction and to allow purging with GAr/LAr on commissioning. High levels of quality control will be possible with the modular construction design, and following inspection, each module will be cleaned to ISO 8 cleanliness standard and double-wrapped prior to dispatch and transportation to the site for installation and final assembly.

The cathode outer top tubular structure is identical to the bottom-most field-shaping coil; they use tubes of the same outer diameter (139.7 mm). The spans are the same (48 m for the 50-kt LBNO detector) and the vertical distance separating these components is the same as for the remaining field-shaping coils (200-mm centers). The cathode will be attached at the bottom of each hanging column by a split link in G-10CR. The cathode attachment points will also incorporate locally thickened sections of tube (as in the hanging chains) included as part of the peripheral structure nodes.

The complete assembly procedure, logistics and tooling for the field cage and cathode is described in [29]. It is expected that the general design, adapted to the rectangular geometry, and the basic elements for the cathode construction would be similar for the 12-kt DUNE detector, but down-sized to the less challenging requirements.

5.6 The Electronics, Chimneys and DAQ

5.6.1 Overview

The LBNO 20–50-kt detector designs, developed in the LAGUNA-LBNO design study have channel counts in the range of 500,000 to 1,000,000. This large number has spawned extensive R&D over the last few years into large-scale charge-readout solutions optimized for double-phase detectors. The solutions that have been developed provide high integration levels, and significant cost reduction and performance improvement. They can be fully adopted for the DUNE far detector double-phase alternate design, which foresees 153600 channels for each 10-kt far detector module.

The R&D activities (ongoing since 2006) have focused effort on two main areas:

- development of cold front-end ASIC electronics, and

- development of low-cost, largely scalable data acquisition systems (DAQ) based on modern telecommunications technologies.

One of the goals of the WA105 $6\times6\times6$ m^3 demonstrator, a LArTPC with 7680 charge-readout channels described in Section 9.4, is to test the large-scale readout system developed in the LAGUNA-LBNO design study. Annex 4I: *WA105 TDR* [35] and [41] provide detailed descriptions of the charge-readout electronics, including the cold front-end ASICs and the DAQ.

The LAGUNA-LBNO design was driven both by cost and by the particular use of the electronics for the dual-phase readout, which implies larger signals from the detector relative to single-phase, effectively releasing requirements on noise. Section 5.4 describes the charge readout system. Recall that the Large Electron Multipliers (LEMs) amplify the ionization charges by at least a factor 20, and that by adjusting its voltage, the LEM gain is tunable from there up to 200. When the charges reach the segmented anode, they are equally shared among two perpendicular collection views. The front-end amplifier connected to the anode, given the capacitance of the anode strips, would have a S/N ratio of 14 at unitary LEM gain. Considering a minimal LEM gain of 20, the amplifier provides an overall S/N ratio of 140. The S/N ratio is boosted by the LEM gain, thus implying less stringent requirements on the preamplifier noise.

The electronics consists of front-end amplifiers that are implemented as cryogenic CMOS ASICs connected to the anode with 50-cm cables; they are completely accessible from the outside while remaining very low-noise. The amplifiers must be housed in separate volumes that are completely distinct from the tank volume in order to replace them as needed without contaminating the pure argon inside the cryostat. These volumes are called chimneys.

Flat, 2-m-long cables inside each chimney connect front-end cards to digitization electronics, housed in microTCA (μTCA) crates [42] at the chimney exits, outside the cryostat. This design provides a way to maintain the front-end at cryogenic temperatures but keep it accessible, and maintain the digital electronics externally, at room temperature. This provides risk mitigation and significant flexibility.

The digitization units in the μTCA crates are synchronized with the White Rabbit (WR) time-distribution standard[43], which was originally designed to achieve sub-ns accuracy. This built-in accuracy, while not a critical aspect of the system design, is much better than what is needed to align the 400-ns samples of the charge readout. WR was adopted for its practical integration aspects and for cost reduction; its very high timing accuracy is a bonus. WR is also used in this design as a dedicated network network for the trigger distribution.

The light-readout digitization electronics (see Section 5.8) is also implemented in μTCA and provides triggers from the photomultipliers (PMTs) that are distributed to the DAQ via the WR network.

Commercial high-bandwidth and high-computing-power back-end cards are used for event-building and are coupled to a farm for online processing, which is implemented for event filtering, data reconstruction, calibrations and data-quality assessment.

5.6.2   Front-end Cryogenic Amplifiers and Chimneys

In the framework of the R&D related to LAGUNA-LBNO since 2006, several generations of prototypes of cryogenic ASIC 0.35 microns CMOS multi-channel preamplifier chips have been developed. The capability to operate at cryogenic temperatures means that cables can be shorter (in WA105 these cables are just 50 cm long), which reduces the associated capacitance for the connection to the detector. It also makes it possible to reach an optimal amplifier S/N ratio at a temperature around 110 K, which can be easily achieved in the GAr at the top of the cryostat.

Another significant feature of the design is the ad-hoc designed chimneys, which enable the front-end electronics to remain a very short distance from the detectors in the CRP and accessible for repairs without opening the cryostat. Chimneys are separate, insulated, cylindrical volumes that penetrate the cryostat top, their lower half immersed in GAr, their upper half outside the tank at room temperature. The front-end electronics cards are installed inside the chimneys near the bottom. The chimneys are filled with inert gas and have a cooling system to keep the electronics at the optimal temperature. A cold feedthrough at the bottom of each chimney isolates the cards from the inner volume of the vessel and allows connection from the anode to the electronics; a warm feedthrough (FT) at the top allows connection to the digitization electronics on the outside.

The first ASIC versions were designed principally for the readout of charge from collection and induction wire planes, and could also handle bipolar signals. Since 2012 some versions of the dual-phase have been developed specifically to match the dynamic range of signals coming from the two collection views of the anode PCB after LEM amplification. As described in Section 5.4, each collection view is instrumented with strips of 3.125-mm pitch and 3-m length (150 pF/m capacitance). For this pitch, simulations of electromagnetic showers predict that a single channel will collect a maximum 40 MIP. The design of the dual-phase cryogenic ASIC is based on a LEM minimal gain of 20, which corresponds to 1200 fC for this maximal signal.

Two versions of the dual-phase ASIC chips have been produced for WA105, both with 16 readout channels. The first version has a constant gain in the region 0–40 MIP. The second is characterized

by a double-slope gain. This second solution optimizes the resolution while preserving a large dynamic range. It is characterized by a high-gain region extending up to signals of 10 MIP, after which the gain is reduced by a factor of three in order to enable a better overall match for a dynamic range of 40 MIP. It provides the best resolution in the MIP region (dE/dx measurements) without limiting the dynamic range for showers, which can still reach up to 40 MIP (see Figure 5.19). This double-slope regime has been optimized on the basis of simulations of hadronic and electromagnetic showers. Both ASIC versions, compatible with the LEM signal dynamics, are implemented in the CMOS 0.35 μm technology; they have 16 channels, 18-mW/channel thermal dissipation or less, about 1300 electrons ENC at 250-pF input detector capacitance, and operate with this best S/N ratio at about 110 K.
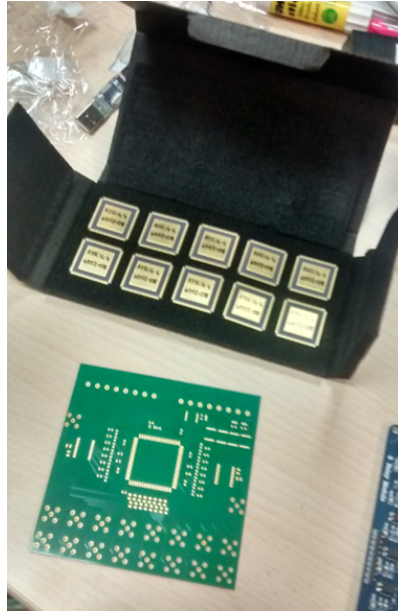
Figure 5.19: Front-end 16 channels cryogenic ASIC amplifier with the double-slope gain implementation

The implementation of the double-slope gain regime is obtained by replacing the feedback integration capacitor of the OPAMP with a MOS capacitance, which changes its value above a certain threshold voltage. This effect is also present during the discharge phase and it can be corrected with the inclusion in the feedback loop of an additional branch with a diode and a resistor designed to keep the RC value roughly constant during discharge. This branch can be selected/deselected with an internal switch for all the channels in the ASIC (see Figure 5.20).

In the design under implementation in WA105 and proposed for DUNE, there are 640 channels per chimney. The 40 ASIC amplifiers needed for the readout of each group of 640 channels will be arranged on 10 pairs of front-end cards plugged into the FT at the bottom of each chimney. Each front-end card holds two ASIC chips and a few discrete components. Particular care has been taken in testing several options (gas discharge tubes, metal oxyde varistors, double diodes) for the surge-arrestor components, which have to protect the ASICs from occasional sparks occurring in the CRP. This study was aimed at maximizing the protection efficiency, testing the components' durability for a very high number of sparks and minimizing the input capacitance seen by the pre-amplifiers. Double-diodes have been selected as the best solution given their performance and capacitance. The total dissipation of the front-end electronics will be about 11.5 W per chimney. This heat source is minor with respect to the heat conduction from the flat cables going to the digitization
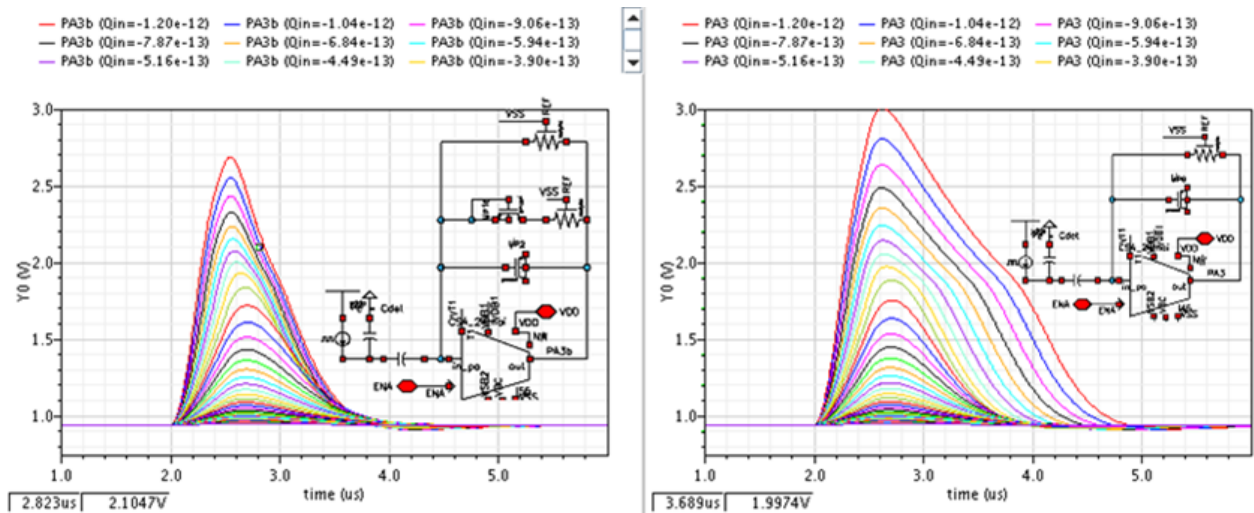
Figure 5.20: Response of the double-slope ASIC amplifier to progressively larger pulses with and without the diode/resistor feedback branch

electronics and from the walls of the chimney. The front-end cards are kept at low temperature by a cooling system installed at the bottom of chimney that compensates for this overall heat flow. The front-end electronics is coupled to the DAQ system, described in Section 5.6.3, that is based on 12-bit ADCs, matching the needed dynamic range quite well. Figure 5.21 shows the 3D model of the signal FT chimneys hosting the cryogenic ASIC amplifiers.

A signal FT chimney prototype for 320 channels built for the $3\times1\times1$ m^3 WA105 prototype is shown in Figure 5.22.

Pairs of cryogenic electronics front-end cards are mounted at the end of sliding G10 blades which can be extracted from the top of the chimney. The blades, which also carry the flat cables for the connections, slide on guides mounted inside the chimney. By moving the blades, the front-end cards can be plugged/unplugged to/from connectors on the top side of the cold FT at the bottom of the chimney. This FT completely isolates the chimney from the LAr vessel. Connectors are mounted on the bottom of the FT for the 50 cm flat cables coming from the CRPs.

5.6.3　Digital Electronics and DAQ Architecture

The DAQ system proposed for the dual-phase DUNE detector design is based on two industrial standards:

- MicroTCA (μTCA) standard for the distributed data network[42]

- White Rabbit (WR) standard for the distributed clock network[43]
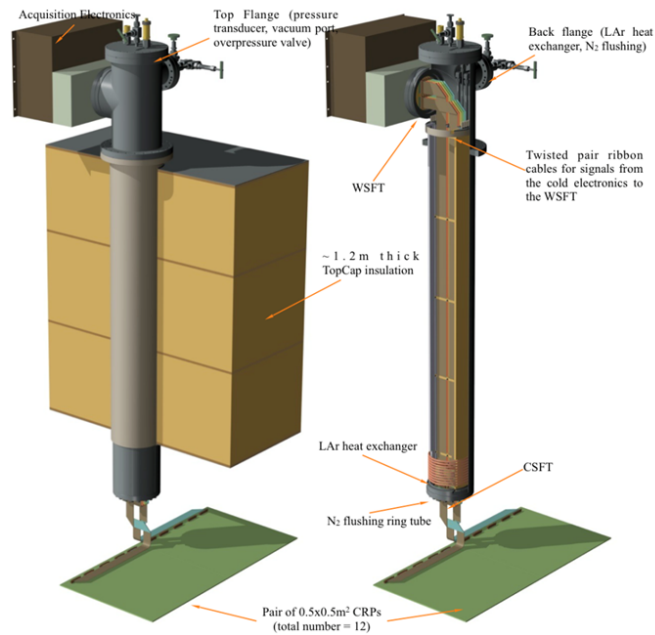
Figure 5.21: 3D model of the signal feedthrough chimneys
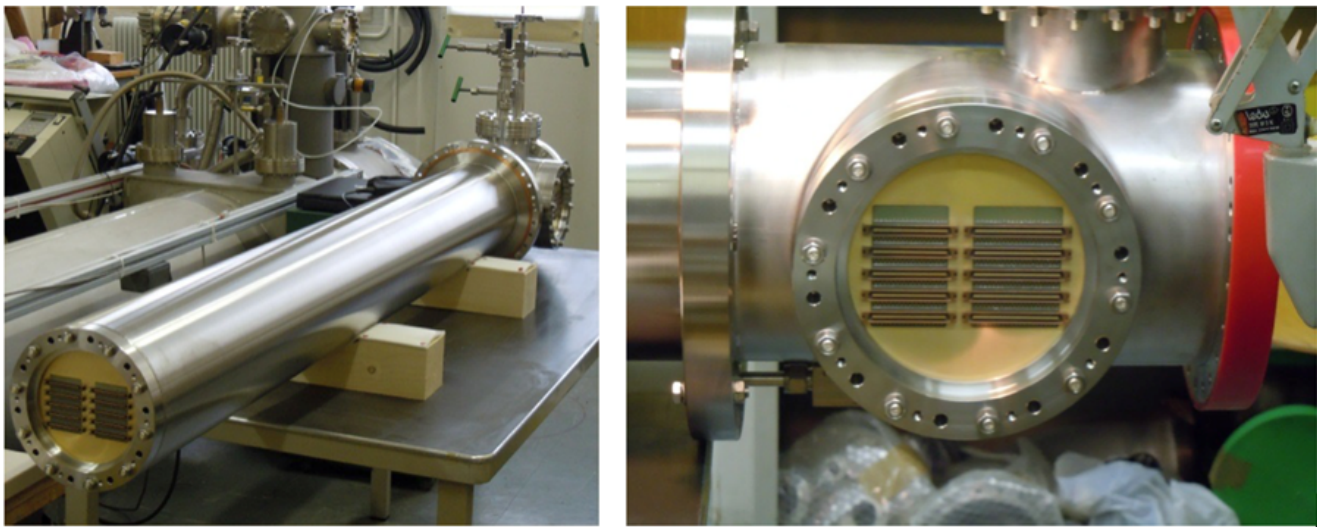
Figure 5.22: Prototype of the signal feedthrough chimney built for the WA015 3×3×1 m^3 prototype

The analog electrical signals from the front-end electronics ASICs transit through the signal chimneys up to the digitization boards in the μTCA crates (DAQ L1). The backplane of each μTCA crate (a *shelf*) is connected through a 10GbE up-link to the next level (DAQ L2). The L2 directly connects the μTCA crates to FPGA-based high-performance back-end processing boards. The design calls for a lossless transmission scheme all the way down to the back-end processing board, which applies all filtering algorithms and does the event building. The Huffman lossless algorithm is easy to implement and typically provides a factor of 10 compression on LAr events.

Recorded data are sent to a local storage level where Object Storage Servers (OSS) and Meta-Data Servers (MDS) are connected with the event-building workstations via a 10/40-GbE network (Ethernet or InfiniBand). In parallel, signals from a high-stability common clock and time synchronization signals are distributed (using the WR standard) to the L1 digitization cards, through a dedicated, deterministic network. The WR network is also used to transmit the trigger time-stamp signals, which can be generated either by the PMTs' readout electronics or by additional sources, e.g., for WA105 operation in the charged particle beam, the beam trigger counters. The clock is derived from a Master Clock generator connected to the WR Grand-Master switch. WA105 will implement this DAQ scheme, and additional details may be found in [35].

5.6.4   MicroTCA Standard and Applications

The MicroTCA (μTCA) standard offers a very compact and easily scalable architecture to handle a large number of channels at low cost. The μTCA or related standards — such as ATCA or xTCA — are now well known in the HEP community and have been integrated into various designs at CERN (e.g., LHC upgrades), DESY, etc. μTCA fulfills requirements of the telecommunication industry and offers the ability to interconnect distributed applications while providing a standard, compact and robust form factor with simplified power supply management, cooling, and distribution of internal clocks. The backplane of a μTCA crate (the μTCA shelf) accommodates high-speed serial links; they are arranged in a variety of topologies to support a variety of protocols, including Ethernet 1GbE or 10GbE, PCI Express, SRIO, etc. Use of Ethernet-based solutions is proposed for both data and clock distribution, through the μTCA backplanes. This choice obviously optimizes the connections between the various components of the system. Constraints imposed on the data transfer bandwidth point towards use of the 10GbE protocol. For the clock distribution, dedicated lanes on the backplane must be defined by the user. The μTCA standard also offers so-called *clock* lanes, which distribute the timing signals to all boards hosted in the crate and which may be used for any type of signal.

The signal digitization boards plugged into a μTCA shelf are called Advanced Mezzanine Cards (AMCs)[44]. Each AMC is connected to one or two μTCA Carrier Hub (MCH) boards through the backplane serial links. The MCH provides a central switch function allowing the AMCs to communicate with each other or with external systems through an up-link access. The MCH manages both the 10GbE uplink and the WR bi-directional clock distribution. Figure 5.23 provides a sketch of the backplane layout and its implementation in a particular shelf type selected in the design of the system.

The production version DAQ designed for the WA105 DAQ is based on the μTCA.1 standard,
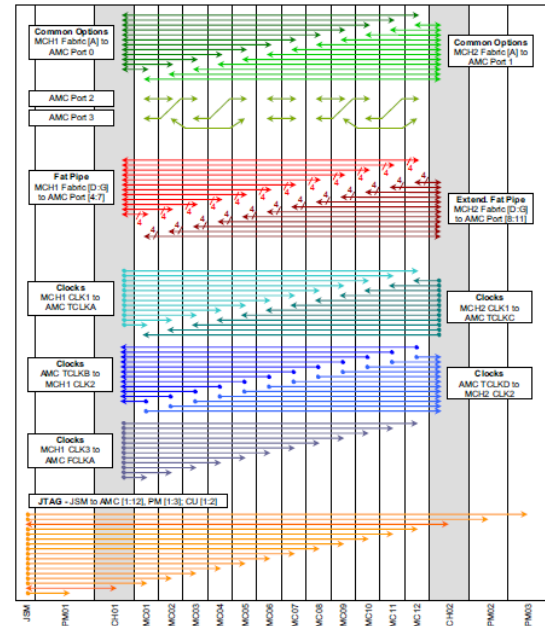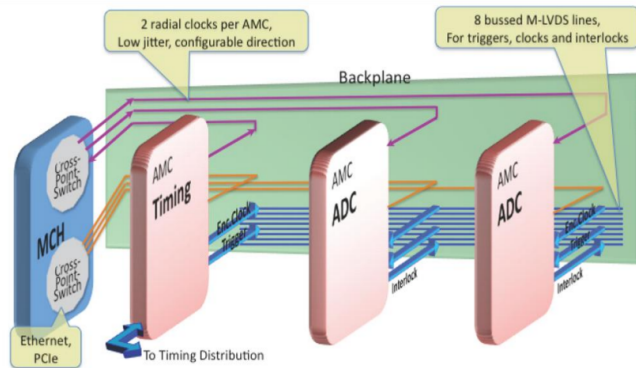
Figure 5.23: Left: global microTCA crate organization. AMCs (providing basic ADC functions) are connected to the crate controller or MCH which up-links the external systems. A dedicated AMC for the clock receives dedicated signals (master clock, trigger signals) from the timing distribution system and transcript them onto the backplane. Right: backplane layout of the Schroff 11850-015 reference.

with connections to the user input signals from the front side only. These connections are made with VHDCI cables in order to minimize the number of cables. One μTCA shelf is connected to each signal chimney, reading out 640 channels corresponding to 10 AMCs.

Many types of μTCA shef are available on the market, e.g. 11850-015 8U from Schroff for μTCA.1 standard, NATIVE-R9 from NAT for μTCA.4 standard. The cost of these items is quickly decreasing due to the fast pace of developments by the internet providers. These items all have redundant power supplies, redundant MCHs and offer different segmentations to connect the AMCs.

The advantage of this architecture is that it limits the DAQ electronics developments to the AMC only since that is the component that provides the functionalities for the digitization, data formatting and compression, event time-stamping and data transfer through the backplane. For WA105, the AMC is a double-size module (also compatible with μTCA.4 standard) with a single input connector and a 10GbE link to the backplane. The input stage performs the 64-channel digitization through eight 8-channel, 14-bit ADC chips read out at a 2.5-MHz frequency. The ADC readout sequence is controlled by two FPGAs that make the data available on a double port memory. Readout of the data is performed continuously and they are stored in a local buffer. The recorded samples, each corresponding to a drift window, are selected in coincidence with the received trigger. When a trigger occurs, the samples written in the memory can be treated with compression algorithms (such as Huffman or RLE) or zero-suppression (if required) and transmitted over the network until the end of the drift window, which closes the event. These operations are managed by a third FPGA, which sends the data on the shelf backplane in order that they can be transmitted to L2. This readout scheme and hardware implementation have been validated for WA105 on a Stratix 4 prototype board, shown in Figure 5.24.
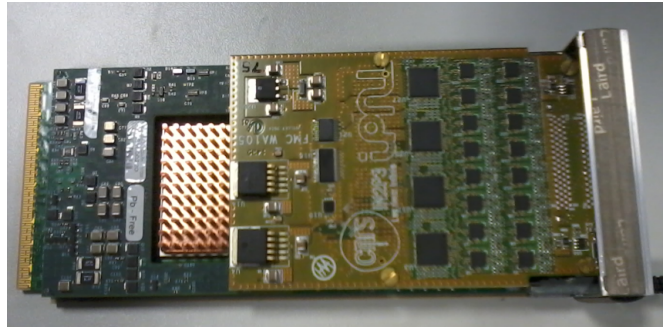
Figure 5.24: Prototype of AMC, using μTCA.1 standard, and hosting 64 ADC channels on a mezzanine board. This prototype is used as a validation of the full and final ADC chain in WA105.

5.6.5   Back-end and Event Builder

A network hierarchical structure is implemented for the back-end and event builder in which all crates are interconnected to a dedicated back-end FPGA processing board (such as S5-PCIe-HQ, Figure 5.25).

Figure 5.25: FPGA processing board based on Stratix V from Altera. The board features a dual QSFP+ cages for 40GigE or 10GigE links, 16 GBytes DDR3 SDRAM, 72 MBytes QDRII/II+, two SATA connectors and is programmable via OpenCL.

This kind of board is used for massive data processing in many fields (medical imaging, stock market, etc.) that require parallel processing with reduced power consumption (it dissipates only 10% of the power dissipated by an equivalent CPU for a comparable number of operations). This particular board has two QSFP+ cages to bring the data directly to the FPGA for the lowest possible latency. Up to 8×10GbE links without data loss are available per board. The board performs further data processing, filtering and transmission to the highest level for storage. This type of board is widely used and the present generation, based on the Altera Stratix V, will evolve to the Aria X and the Stratix X. Stratix X will be probably available at the time of construction of the DUNE DAQ system. Programming of the back-end processing board is achievable through the OpenCL software suite where a kernel code, on top of a host code, allows programming the FPGA directly in a high-level language without a classical VHDL synthesis chain. OpenCL applications are transparent to the hardware used for procesing (FPGAs, CPUs, GPUs). This highly flexible feature is fully adapted to the requirements of large DAQ systems, where conditions of filtering, event building, etc., may evolve with time.

5.6.6   Timing Distribution System and White Rabbit (WR) Standard

The clock distribution will use a parallel, independent network to distribute the signal from a GPS-disciplined Master Clock down to each μTCA shelf, through specific switches. Technically, the WR standard is based on a combination of Synchronous Ethernet (Sync-E) and Precision Time Protocol (PTP, IEEE1588), where the Ethernet clock is generated by a GPS-disciplined clock. At the level of each shelf, this high-accuracy clock is made available to each AMC through dedicated lines off the backplane. As discussed before, the μTCA standard accommodates special lanes for clock transmission. The trigger signals (time stamps) are encoded and sent through this dedicated WR network which has enough bandwidth for this transmission without interfering with the PTP synchronization signals. The requirements on the synchronization for the charge readout are quite loose since the typical readout frequency is of the order of a few MHz. The requirements for the PMT readout on the contrary are more stringent. The goal is to provide a nanosecond synchronization at the level of all L1 elements. This goal is typically achievable with the WR standard[43].

The WR provides an extension to the Ethernet network with Gb/s data transfer speed and allows for accurate synchronization among the different network nodes. It provides a common clock for the physical layer in the entire network, allowing sub-nanosecond synchronization accuracy and 20-ps jitter time. The WR network is designed to host up to thousands of nodes and to support distance ranges around 10 km using fiber cables. It ensures that all the Ethernet frames sent are delivered after no more than a fixed delay (controlled latency). The order of the frames should be preserved. A typical application scheme is displayed in Figure 5.26.
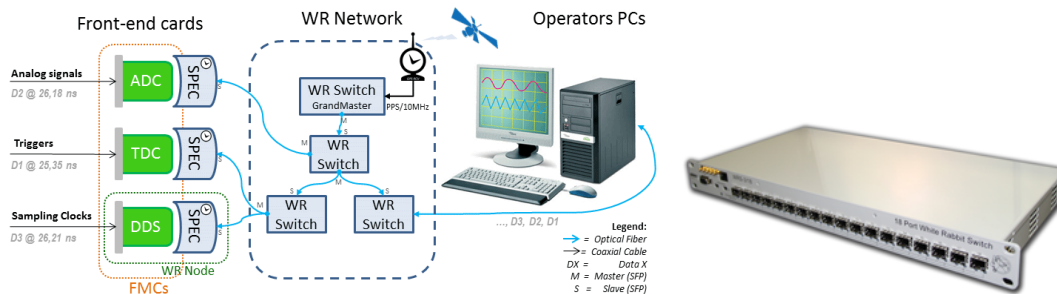
Figure 5.26: Left: general organization of a typical WR network. Right: standalone WR switch.

The WR application in the μTCA standard is currently engineered to easily interconnect μTCA cards. The WR switch can therefore be connected directly to its different nodes in the same rack to facilitate maintenance and limit the space occupied. The implementation scheme is based on the integration of a WR mezzanine board on the MCH of each shelf. In the future a full integration of the WR within the μTCA DAQ system would be very powerful. The current WR implementation scheme is based on the integration of a WR mezzanine board on the MCH of each shelf. The development of this WR MCH is in progress for the WA105 demonstrator (on a MHC produced by the company NAT); the companies producing the MCH and the WR slave to be integrated show clear interest in this development.

5.7   The Slow-Control System

The slow-control system for the far detector is designed to monitor the detector operation conditions, in particular, the following physical quantities inside the tank:

- temperatures (with platinum resistors),

- pressures (with commercial piezoelectric sensors),

- LAr levels (with custom-made capacitive sensors and electronics), and

- deformations of materials (with resistive strain gauges).

In addition, the slow-control system provides the hardware infrastructure needed to monitor traces of O_2, N_2 and H_2O impurities in the tank, to monitor and control the high- and low-voltage power supplies, heaters, lighting system and cryogenic video system. It will also interface to the cryogenic system and to the motorized system that adjusts the position of each Charge Readout Plane (CRP).

The design of the slow-control system is part of a continued, progressive prototyping effort aimed at developing a control system dedicated to multi-kiloton LAr dual-phase detectors. It has been designed in the framework of the LAGUNA-LBNO design study and the WA105 experiment. WA105 represents a first, fully engineered, implementation of this design, which can be extrapolated to larger detector scales. The design also benefited from the successful example and the expertise developed in the context of the ArDM experiment[45] which is currently operating a LArTPC for dark matter searches in an underground laboratory (LSC, Spain).

The slow-control system introduces the use of National Instruments Compact RIO (Reconfigurable Input Output) modules for acquisition of all the physical quantities of interest. Figure 5.27 shows a rack prepared for the WA105 $3 \times 1 \times 1$ m^3 prototype that is ready to be tested at CERN.

The entire slow-control system of the WA105 demonstrator will be managed through a single LabView interface[41] which will provide access to all the sensors, control the actuators and provide the platform for the video monitoring system both inside and outside the tank. Supervisory software will be implemented in the CERN UNICOS (UNified Industrial Control System) framework [46] to provide the operator interface for the monitoring of all the physical quantities and the handling of alarms.

As discussed in Section 4.1, the charge-readout system is implemented via CRP modules of 3×3 m^2. Each CRP is an independent detector, hence its instrumentation can also be treated as independent. A complete list of the sensors planned for use in both the 3×3 m^2 DUNE CRP module and and the $3 \times 1 \times 1$ m^3 WA105 prototype is provided in Figure 5.28.

The number of sensors for the far detector CRP is extrapolated from the number for the prototype and is not yet final but it should be considered as an upper limit. The sensor instrumentation of the $3 \times 1 \times 1$ m^3 WA105 prototype has also led to the design of a custom Slow-Control Feedthrough (SCFT), based on the use of weldable connectors for high vacuum (see Figure 5.29). A specific
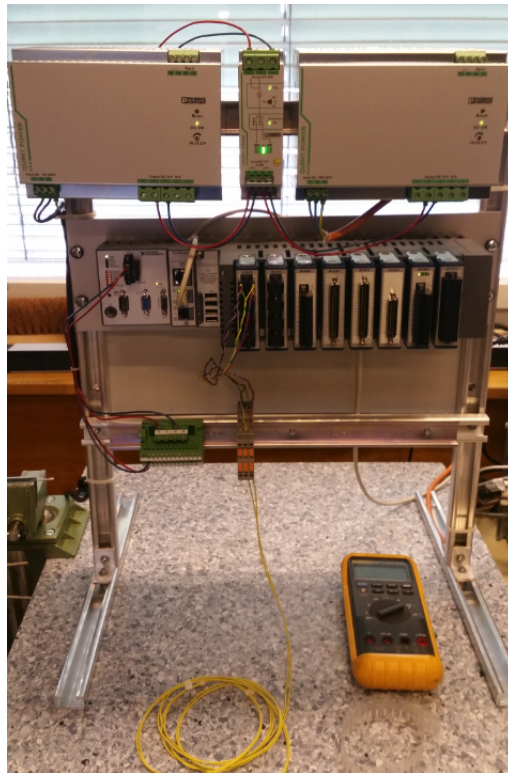
Figure 5.27: The rack is a prototype of the entire Control System; it embeds modules for resistive temperature sensors, pressure sensors, strain gauges, liquid argon level meters, control for heaters. On the upper part a redundant 24 V power supply provides fault tolerant power to the National Instrument controller and modules. Calibration of modules and sensors is ongoing.

process	measurement	sensor	range	resolution	connector to flange	# of sensors	remote IO	# of NI modules	# of sensors	remote IO	# of NI modules
						LAr-Proto			Far Detector 4×4 m² module		
PCS											
	temperature LM	Pt 10k	85-300K	0.1 K	D-SUB	80	yes	28 (NI9219)	4	yes	1 (NI9219)
	temperature CRP	Pt 1k	85-300K	0.1 K	D-SUB	24	yes	6 (NI9219)	4	yes	1 (NI9219)
	temperature SFT	thcouple Ktype	85-300K	0.1 K	MSK-3-C16	18	yes	2 (NI9213)	24	yes	3 (NI9213)
	pressure	Keller PAA-21Y	0-2 bar	10^{-5} mbar	dedicated	8	yes	1 (NI9208)	12	yes	4 (NI9208)
	level	coax cap. filling	2 m	1 mm	SMA	2	yes	-	-	-	-
	level CRP	plate	2.5 cm	100 μm	SMA	8	no	2 (NI9203)	4	no	1 (NI9203)
	level field-cage	plate	2.5 cm	100 μm	SMA	3	no	-	-	no	-
	strain gauge	HBM full bridge	2.5 cm	gauge fact. 2	D-SUB	24	yes	6 (NI9237)	8	yes	2 (NI9237)
	trace ana N_2	Gowmac	0-100 ppm	10 ppb	-	1	yes	-	1	yes	-
	trace ana H_2O	Gowmac	0-50 ppm	10 ppb	gas/liquid handling	1	yes	1 (NI9203)	1	yes	1 (NI9203)
	trace ana O_2	AMI	50 ppb-20%	100 ppb	gas/liquid handling	1	yes	-	1	yes	-
	heaters	HS25	25 W	N/A	Caburn	20	yes	PSU + relay	20	yes	PSU + relay
	total PCS					**190**			**79**		
DCS											
	HV LEM	N/A	8 kV	N/A	SHV	24	no	CAEN PSU	128	no	CAEN PSU
	HV PMT	N/A	8 kV	N/A	SHV	5	no	CAEN PSU	16	no	CAEN PSU
	LV LEDs	N/A	24 V	N/A	D-SUB	6	no	24 DC	60	no	24 V DC
	total DCS					**35**			**204**		
DSS											
	temperature GTT	Pt 10 k	85-300 K	0.1 K	D-SUB	45	no	12 (NI9219)		no	
	cryo camera	webcam	N/A	N/A	USB	4	yes	1 (cRIO-9082)	4	no	1 (cRIO-9082)
	IR camera	webcam	N/A	N/A	USB/TCP IP	2	no	1 (cRIO-9082)	2	no	1 (cRIO-9082)

Figure 5.28: List of the slow control sensors for the 3×1×1 m³ WA105 prototype and far detectors CRP

SCFT for the DUNE 3×3 m^2 CRP would be based on this design.
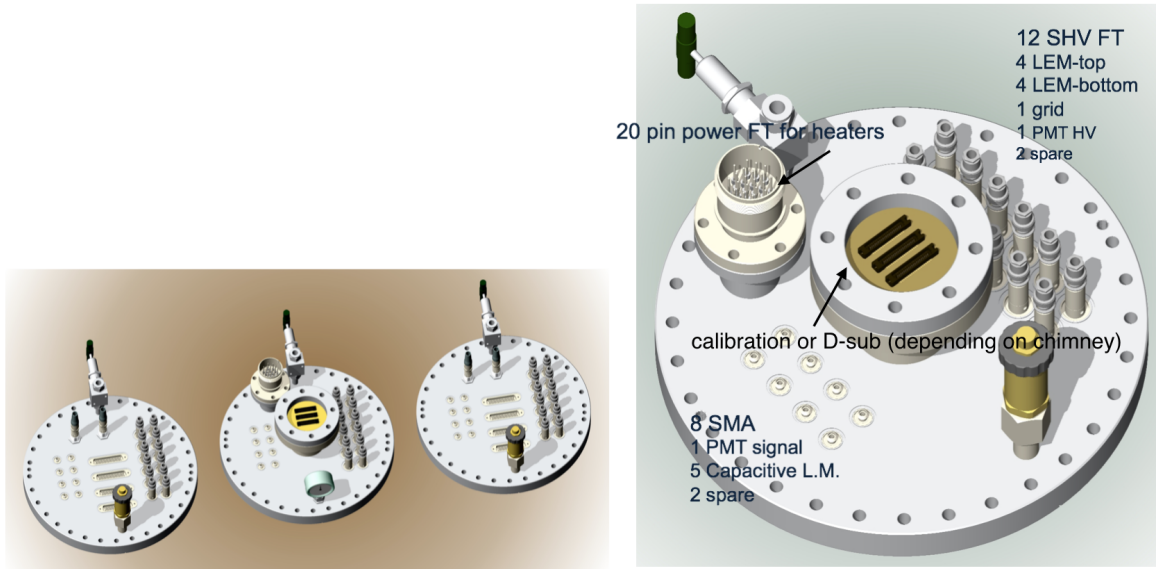
Figure 5.29: The 3 SCFTs providing weldable connectors for all the instrumentation inside the $3 \times 1 \times 1$ m^3 WA105 tank. The number of sensors per module in the DUNE far detector will be drastically reduced with respect to this WA105 prototype.

5.8   The Light-Readout System

The light-readout system developed in the LAGUNA-LBNO design study detects the scintillation light using 8-inch cryogenic PMTs (Hamamatsu R5912-02mod) with TPB coating. The PMTs are placed about 1 m below the cathode. The application of the TPB coating can be done at the level of the glass itself or on a transparent plate mounted over the photocathode surface. The WA105 demonstrator will use 36 PMTs R5912-02mod (1/m^2 of cathode surface). The mechanics for the PMTs' attachment has been carefully studied; it must counteract the PMT buoyancy while avoiding stress to the PMT glass (due to differentials in the thermal contraction between the support and the PMT itself).

The dual-phase LAr detectors designed for LBNO are equipped with a large number of PMTs. Depending on the size of the DUNE detector module and on the density of PMT on the detection surface, this number may be as high as 1000. The large number of photosensors called for a large integration scale solution for the front-end electronics.

Solutions of this kind have been studied, in the framework of the R&D program PMm2 [47, 48], for the instrumentation of giant water Cherenkov detectors. The signal digitization is performed by grouping the PMTs in arrays of 16. Each PMT array is read out by an ASIC chip in AMS SiGe $0.35 \, \mu$m technology. The ASIC, which is called PARISROC (PMT ARrray Integrated in Si-Ge Read Out Chip)[49], provides a complete readout system for triggerless data acquisition. The solution developed by this program represents an important handle for cost reduction.

The front-end electronics for the light readout of the WA105 demonstrator will be based on the solution developed by the PMm2 R&D. The PARISROC ASIC is currently adapted to the time structure of the scintillation light produced in the interactions of secondary particles in neutrino interactions in LAr. The detection of the direct scintillation light (S1) that provides the absolute event time is the main task of the electronics. The electronics will also process the signals from the scintillation light (S2) produced by the electrons as they are extracted and amplified in the gaseous phase.

The PARISROC chip reads the signals of 16 PMTs independently of one another. Each analog channel consists of a low-noise preamplifier with variable and adjustable gain (8 bits) to compensate for the relative PMT gain differences when powered by a single high voltage. The preamplifier is followed by a slow channel for the charge measurement in parallel with a fast channel for the trigger output. The slow channel includes a variable (50–200 ns) slow shaper followed by an analog memory with depth of 2 to provide a linear charge measurement up to 50 pC; this charge is then converted by a 10-bit Wilkinson ADC. The fast channel is composed of a fast shaper (15 ns) followed by a low offset discriminator to auto-trigger down to 10 fC. This auto-trigger feature makes the PMT array completely independent of the other PMT arrays. The threshold is loaded by an internal 10-bit DAC common to the 16 channels.

The variable gain of each preamplifier provides the flexibility to adapt the system to the characteristics of each PMT after it has been correctly calibrated. In the timestamping process, there are two TDC ramps working in phased opposition in order to reduce the dead time (i.e., when the ramp goes to zero) by selecting the other ramp that will be in its active state.

When an event occurs, the value of the correct ramp is digitized and inserted into the data stream that includes: a 24 bit counter that goes much more slowly than the ramps in order to have a coarse time measurement, a flag that indicates which ramp has been digitized, an ID of the channel triggered, and the timestamp and charge information.

The light readout is fully integrated in the WA105 DAQ scheme. A microTCA crate housing the light-readout digitization cards is naturally integrated into this architecture by taking into account the common time distribution and data transmission systems. During the data-taking outside the beam spills, a trigger that can be generated by the light-readout microTCA crate plus its timestamp can be transmitted over the White Rabbit network similarly to the beam triggers.

On the light-readout front-end board there is also an ADC (AD9249 from Analog Devices) that digitizes the PMT charge information on every channel independently. The charge measurement can be correlated with the timing information coming from the PARISROC for better precision on both quantities. A prototype of the light-readout AMC is also being developed by using the Bittware development card S4AM (the same used for the LAr TPC ionization readout developments) and a mezzanine card including the ADC and the trigger circuit (see Figure 5.30).

The PARISROC chip provides the timestamp at nanosecond precision and generates the trigger. In parallel, an ADC AD9249 continuously digitizes all channels independently at 65 MSPS with 14 bits. The FPGA Stratix IV from the Bittware S4AM card controls and programs the ADC and PARISROC. It also receives the data coming from both PARISROC and ADC and controls which information is passed through the network to store for analysis. The charge digitization
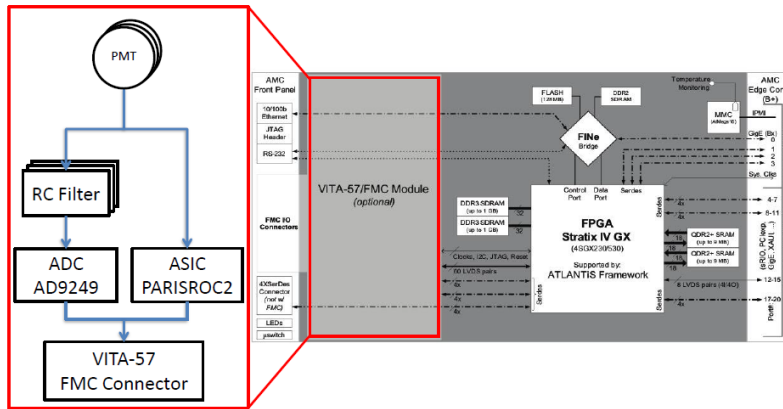
Figure 5.30: Block diagram of the light readout AMC demonstrator

of the light signals is performed at 14 bits in samples of 15 ns. Considering a 5-μs light-signal duration, the digitization will produce more than 300 samples. With this amount of data it is possible to measure not only the total charge generated but also the shape of the signal and the long-component decay of the light.

With this light readout architecture and the White Rabbit time-distribution system, it is possible to achieve 1-ns accuracy at the level of trigger generation for the $t0$ and timestamping of the events. This trigger is sent to the general DAQ and the event builder. Since the charge-readout system of the TPC runs at 2.5 MHz, the minimal time unit in the reconstruction of the drift is 400 ns.

5.9 Installation and Commissioning

5.9.1 Preparatory Work

Before the installation of the detector can begin, a number of preparations must be conducted and boundary conditions must be met in order to enable a safe and efficient process that minimizes the manpower required for the underground detector construction. A careful study of the installation sequence and tools and an optimization of the size and characteristics of the detector elements has been performed in order to facilitate the installation procedures. Some of the most important preparation and installation steps are listed in this section. More detailed explanation and figures are available in [29].

5.9.2 Detector Installation Sequence

This installation procedure has been extensively studied in the framework of the LAGUNA-LBNO design study. A construction sequence for the dual-phase DUNE LArTPC detector module installation was defined based on the use of a slightly modified scaffolding arrangement with respect

to the LBNO design, discussed in [29] (Design: courtesy Technodyne Ltd., Eastleigh, UK). The proposed construction sequence assumes completion of the membrane and insulation system installation together with completion of all tank internal pipework and cable trays. At this stage, sections of the scaffolding will be removed and replaced by the Alimak-Hek or similar climbing access platforms to provide increased functionality to the installation. On completion of the scaffolding revisions and the climbing access platform installation, the entire tank and scaffolding systems will be cleaned in preparation for the detector module installation. The proposed far detector module construction sequence consists of:

1. Complete installation of insulation and membrane, install cable trays from top to bottom for photomultipliers (PMTs) electrical cables.

2. Adjust scaffolding platforms, add Alimak-Hek platform and floor protection.

3. Air purge top level installation.

4. Install hanging columns for detector.

5. Install lowest field shaping coil to stabilize columns, and then install first top 15 levels of field shaping coils.

6. Thoroughly clean top level assembly.

7. Install Charge Readout (CRP) from top scaffolding platform (detailed sequences described in [29].

8. Thoroughly clean top level assembly.

9. Screen off top level to protect Anode (protective screen 1).

10. Air purge top level (allow bleed air into middle and lower levels).

11. Continue installing field shaping coils.

12. Complete installation of field shaping coils.

13. Thoroughly clean field shaping coils, remove protective screen (screen 1) to top level and progressively remove all scaffolding and Alimak-Hek platforms.

14. Screen off field shaping coils (including CRO): protective screen 2.

15. Air purge top and middle levels.

16. Construct Cathode from Modules. Cathode to be raised 300 mm off tank bottom during construction.

17. Thoroughly clean cathode and space used for fabrication.

18. Remove protective screen 2.

19. Fit cathode to field cage using suitable jacks.

20. Screen off entire detector: protective screen 3.

21. Remove floor protection.

22. Add cable trays, junction boxes and cables for PMTs.

23. Install PMTs to tank Bottom (pre-assembled L-flanges). Check out and test PMTs.

24. Clean air purge bottom level.

25. Install temporary enclosure around TCO inside and outside with air lock within the enclosure.

26. Remove protective screen (screen 3) using air lock system to prevent contamination of detector.

27. Close temporary construction openings.

28. Thoroughly clean TCO areas.

29. Remove temporary enclosures.

30. Remove all tools, equipment, etc., through tank roof.

31. Exit via room manways.

32. Close all tank roof openings.

5.9.3   Detector construction program and installation schedule

Both the $3\times3\times1\,\text{m}^3$ prototype detector and the $6\times6\times6\,\text{m}^3$ WA105 demonstrator are planned to be built in advance of the larger 4×10-kt modules of the experiment at SURF. It is expected that valuable information will be gathered from the construction of both the prototype and demonstrator detectors that will ultimately benefit both the planning and construction forecasting for the larger far detector.

For comparison the 20-kt LAr detector for Pyhasalmi was designed for a drift surface (roughly the CRP and cathode area) of $824\,\text{m}^2$ in an octagonal shape with a drift length of $20\,\text{m}$. The dual-phase DUNE LArTPC experiment at SURF has an equivalent area of $12\times60 = 720\,\text{m}^2$ (for one module of $12\,\text{kt}$) with a drift length of 12–$15\,\text{m}$ (fiducial mass $1\,\text{kt}$ / $1\,\text{m}$ drift, total 12–$15\,\text{kt}$). The construction program calculated by Rockplan Ltd, Alan Auld Ltd and Rhyal Eng. Ltd can be seen as a conservative approach for the SURF site, as most of the time corresponds more closely

to the instrumented surface required rather than to the drift length, but neither specific SURF site-related effects nor effects of US legal procedure are taken into account in this construction program.

The DUNE detector module installation program has been divided into three distinct (and separate) stages:

1. Design,

2. Manufacture/Fabrication, and

3. Assembly.

The detector design must be done together with the tank deck design, as the complete detector is suspended from the deck. Fabrication and manufacturing can be started while the tank construction is still on-going. The total time for manufacture/fabrication and construction is calculated to be around six years for a DUNE far detector module, of which

- 14 months is for for manufacture/fabrication off-site,

- 20 months is for for construction/installation + testing, and

- 32 months is for total works (with partial overlap).

Chapter 6

Synergies Between Far Detector Designs

6.1 Overview

As discussed in Section 2.2, two technologies for LArTPCs are being pursued. There are a number of synergies between these development efforts.

Both the reference and alternative designs for the DUNE far detector are liquid argon TPCs. The designs assume nearly identical cryostats (with some differences in the cryostat roof) installed in identical chambers and supported by identical cryogenic systems. The designs differ mostly in their approaches to collection and readout of the ionization signals. In the reference design, the ionization charge is measured by successive wire planes, two induction and one collection, all immersed in the LAr. In the alternative design, the charge is extracted from the liquid to the vapor and then amplified and finally collected on a 2D anode, providing two independent views.

Several of the far detector subsystems offer great potential for synergy between the reference and alternative designs, including the

- Interface to the cryogenics system,

- High voltage,

- Photon detection,

- Calibration,

- Underground installation strategies,

- Local computing infrastructure and DAQ, and

- Detector modeling and simulation.

6.2 Interface to the Cryogenics System

In both designs, ionization electrons have drift lengths on the order of several meters. In order to reach the required millisecond scale for electron lifetime, the electronegative impurities in the LAr must be maintained below the ppb level. The contamination will come primarily from impurities adsorbed onto the tank and detector element surfaces. Given that the detector modules will be housed in cryostats of the same design, using the same industrial LNG cryostat technology and the same cryogenics systems, the process of understanding these sources and minimizing them is to a great extent the same for either TPC design. This leads to expected synergies in the areas of

- Electronegative contamination mitigation,

- Modeling contamination sources,

- Contamination migration modeling,

- Material properties,

- Filtration ,

- Design of the cryogenics system,

- Purity monitoring,

- Roof interfaces (hatch, feedthrough, mounts),

- Grounding and shielding, and

- Installation spaces and cryogenics system needs.

For detecting interactions of beam neutrinos, the requirement for electron lifetime of $> 3\,\text{ms}$ derives from the minimum signal to noise ratio $(\text{S/N} > 9)$ required for MIP signals on induction plane wires from interactions near the cathode to be above the zero suppression thresholds. Initial studies of energy resolution for supernova physics also requires an electron lifetime above $3\,\text{ms}$. The $3\,\text{ms}$ lifetime detector requirement is the same for both the single-phase reference design and the dual-phase alternate design. As the argon purity goal is similar, work on contamination mitigation can be done jointly.

There is much experience in the community to justify confidence that high levels of argon purity can be achieved. Careful design of gas ullage and the recirculation system is vital to avoid trapped pockets of gas and to minimize the mixing of the gas and the liquid at the interface. ICARUS achieved a lifetime above $15\,\text{ms}$ after modification of the cryosystem to extend the lifecycle of the recirculation pump.[12] The materials test stand (MTS) at Fermilab has demonstrated that contaminants in the liquid argon originate from materials in the gas space in the ullage, where the warmer temperatures allow for outgassing of exposed surfaces and that materials immersed in the liquid argon are not a source of contamination.[50] The MTS has measured the contamination rate

for many materials and is available for continued testing of additional materials. The Liquid Argon Purity Demonstrator (LAPD) acheived lifetimes above 14 ms without evacuating the cryostat and with a functioning TPC inside the cryostat.[18]

The phase-1 run of the 35-t achieved a peak 3 ms electron lifetime; however, the purity was still improving when the run ended. The engineers and scientists from LBNF and both DUNE detector options will work together to optimize the cryogenic design for high purity. Two examples are understanding the sources of contamination in the ullage and how this contamination migrates to the liquid and developing a fill procedure that preserves the purity of the incoming liquid. There are several membrane cryostats that will be designed and built over the next 10 years by a common engineering team: the $1 \times 1 \times 3\,m^3$ dual-phase prototype, Short Baseline Neutrino Detector (SBND), WA105, the Single-Phase CERN Prototype (SPCP) engineering prototype as well as the DUNE far detector. Each of these will learn from its predessors and inform its successors. Based on existing measurements and extrapolations to the $10-$kt design a 3 ms lifetime should be readily achievable.

6.3   High Voltage

Both LArTPC designs require a large HV to produce an electric field of the order of $500\,V/cm$ in the drift volume. They both thus require a HV generator, HV feedthoughs and a field cage to correctly shape the electric field. While these elements differ in the two designs, they present a common set of problems to solve, including

- Design rules for HV,

- HV generation,

- HV Feedthroughs,

- Field cage structure, and

- Arc mitigation (Stored energy and discharge).

6.4   Photon Detection

The approaches to photon detection in the two designs is different. The reference design uses TPB-coated light guides instrumented with SiPMs, whereas the alternate design uses large PMTs (also coated with TPB). Nevertheless, several aspects of and techniques used in the development of these systems have strong synergies, including

- Requirements refinement and validation,

- Development and evaluation of photosensors,

- Impact of background light,

- Surface reflectivity, and

- Photon detector calibration.

6.5   Detector Calibration

The challenging requirement on systematic uncertainties calls for a robust program of calibration, which may include the use of calibration sources deployed in the detector, complementary external measurements and data-driven calibration procedures. It is expected that this effort will have significant synergies between the two designs, including

- Active volume,

- Energy scale,

- Energy resolution,

- PID likelihoods, and

- Absolute light yield.

6.6   Underground Installation Strategies

A fundamental aspect of the detector cost optimization is related to the development of a strategy for underground logistics, safety and detector installation. Dimensioning of the components to be transported and assembled underground is a common issue, affording concomitant synergies. Strategies for and requirements on implementing the clean rooms, additional tooling and needs for temporary installations, such as scaffolding, also present opportunities for potential synergies.

6.7   Local Computing Infrastructure and DAQ

Once the electrical signals from the detector have been processed (e.g., by front-end preamplifiers), the treatment of the digitized raw data and their compression can be strongly unified and will therefore provide synergies. The online computing farm will have a very similar layout for both reference and alternative designs. The software triggering and filtering algorithms will be based

on similar local computing architectures, offering strong synergies. Finally, the local data storage and transmission to offsite tier centers will be common.

6.8 Detector Modeling and Simulation

Accurate and detailed detector modeling is required. Simulations are needed for both ionization electrons and scintillation photons. The common detection medium of LAr provides a basis for synergies in this area that include

- Charge generation and transport,

- Charge diffusion and attenuation studies,

- Noise and its impact on the detector performance, and

- Optical model and light propagation.

6.9 Summary

A large set of possible synergies exists between the reference and alternative TPC designs. These synergies will be exploited and developed within the DUNE collaboration and the LBNF team as the program of prototypes, demonstrators and other development activities continues and as the detector modules and the accompanying facilities are constructed. The CERN neutrino platform, in particular, will provide an excellent opportunity for joint detector development.

Chapter 7

Near Detector Reference Design

7.1   Overview

This chapter describes the reference design of the DUNE Near Detector Systems (NDS). The scope includes the design, procurement, fabrication, testing, delivery and installation of the NDS components:

- Fine-Grained Tracker (FGT) near neutrino detector (NND),

- Beamline Measurement System (BLM), and

- NDS Data Acquisition system (DAQ).

Detailed descriptions of the NDS subsystems are provided in Annex 4G: *DUNE Near Detector Reference Design* [51].

The concept and design of the reference DUNE-ND evolved from experience with MINOS, the first generation long-baseline neutrino experiment at Fermilab; NOvA, the second generation experiment; the high resolution NOMAD detector at CERN; and the T2K detector at JPARC. MINOS and NOvA employ functionally identical detectors that fulfill the missions of these experiments, given the statistics and resolution of the respective far detectors. DUNE, the third generation experiment at Fermilab, has more ambitious goals: discovery of CP-violation, discovery of mass hierarchy, and a search for physics beyond PMNS with unparalleled precision. DUNE will have a more intense neutrino source and a higher-resolution massive far detector. To meet the ultimate systematic precision needed to fulfill these goals, the ND must thoroughly characterize the beam composed of muon neutrinos/antineutrinos and electron neutrinos/antineutrinos. It must precisely measure the cross sections and particle yields of various neutrino processes. The particle yields include multiplicity and momentum distributions of pions, kaons and protons produced in the hadronic jet.

The need to precisely quantify the neutrino source and cross sections, including the hadronic composition, motivates a high-resolution ND. The NOMAD experience suggests that a high-resolution detector, capable of measuring $e^\pm$, $\mu^\pm$, π^{-+0}, proton and K^0, would partially meet the challenges of DUNE — the detector must be augmented to measure, and thereby precisely model, the neutrino-nuclear effects. The reference DUNE-ND is a next-generation near detector concept compared to the T2K experiment, and will enrich the physics potential of the DUNE/LBNF program. Complementary LAr detector(s) upstream of the high-resolution ND will enhance the capability of the ND complex.

The reference DUNE-ND, a Fine-Grained Tracker (FGT), consists of a straw-tube tracking detector (STT) and electromagnetic calorimeter (ECAL) inside of a 0.4-T dipole magnet. In addition, Muon Identifiers (MuIDs) are located in the magnet steel, as well as upstream and downstream of the STT. The FGT is designed to make precision measurements of the neutrino flux, cross section, signal and background rate at the percent level.

The Beamline Measurement System (BLM) will be located in the region of the Absorber Complex at the downstream end of the decay region to measure the muon flux from hadron decay. The absorber itself is part of the LBNF Beamline. The BLM will determine the neutrino flux and spectra and monitor the beam profile on a spill-by-spill basis, and will operate for the life of the experiment.

The Near Detector System Data Acquisition system (NDS-DAQ) collects raw data from each NDS DAQ, issues triggers, adds precision timing data from a global positioning system (GPS) and builds events. The NDS-DAQ is made up of three parts: NDS Master DAQ (NDS-MDAQ), Beamline Measurements DAQ (BLM-DAQ) and Near Neutrino Detector DAQ (NND-DAQ).

7.2 The Fine-Grained Tracker

The scope of the DUNE Fine-Grained Tracker (FGT) near neutrino detector includes the design, procurement, fabrication, testing, delivery and installation of all FGT subsystems:

- Central straw-tube tracker (STT),

- Electromagnetic calorimeter (ECAL),

- Dipole magnet (0.4-T) surrounding the STT and ECAL,

- Muon identifiers (MuID): in the magnet steel and upstream/downstream of the STT, and

- Instrumentation for monitoring and control.

A schematic drawing of the FGT design is shown in Figure 7.1.
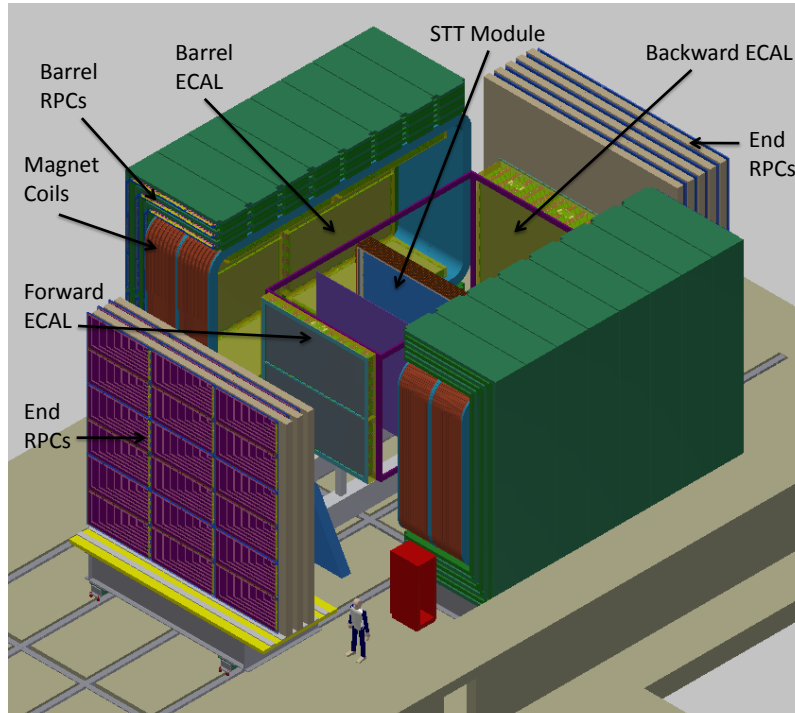
Figure 7.1: A schematic drawing of the fine-grained tracker design.

The DUNE ND is designed to meet the required performance and fulfill the physics program described in Chapter 6 of CDR Volume 2: *The Physics Program for DUNE at LBNF* [4], and in the DAE/DST Detailed Project Report[52]. The most significant requirements[53, 54] for the FGT include:

- Muon energy scale uncertainty better than 0.2% and hadronic energy scale uncertainty better than 0.5% for the low-ν flux measurements;

- Magnetized detector capable of separating μ^+ from μ^- as well as h^+ from h^-, where h is a charged hadron;

- Capability to to separate e^+ from e^- for absolute and relative flux measurements;

- Excellent momentum ($<5\%$) and angular ($< 2\,\mathrm{mrad}$) resolutions for $\mu^\pm$, $e^\pm$, $\pi^\pm$ and proton, and π^0/γ via decay/conversion and K_S^0/Λ produced in ν-induced interactions;

- 4π ECAL coverage to ensure accurate determination of the momentum vector of the hadronic shower;

- 4π MuID coverage to identify muons with a wide range of energies and angles;

- Electron/positron identification through the use of transition radiation (TR) in the entire

tracking detector for low-energy and/or large angle tracks (e.g. γ conversions);

- $\pi/K/p$ identification by dE/dx in the entire tracking detector;

- Identification of π^0 and γ that can mimic ν_e signals at the far detector;

- Use of a variety of nuclear targets, $(C_3H_6)_n$, Ar, Ca, C, Fe, etc., to quantify the impact of nuclear effects in $\nu(\bar{\nu})$-nucleus cross sections; and

- Provision of more than ten times the unoscillated statistics on Ar targets expected in a 40-kt far detector.

The requirements listed above imply the use of a low density, $\rho \sim 0.1\,\mathrm{g/cm^3}$, high-resolution magnetic spectrometer. A summary of the performance requirements is given in Table 7.1 Regardless of the process under study, the goal is to have the systematic error less than the corresponding statistical error.

Table 7.1: A summary of the performance for the FGT configuration

Performance Metric	FGT
Dipole magnetic field	0.4 T
Average target/tracker density	$\rho \sim 0.1$ g/cm^3
Target/tracker Volume	3.5m x 3.5m x 6.4m
Target/tracker Mass	8 t
Vertex Resolution	0.1 mm
Angular Resolution	2 mrad
E_e Resolution	5%
E_μ Resolution	5%
$\nu_\mu/\bar{\nu}_\mu$ ID	Yes
$\nu_e/\bar{\nu}_e$ ID	Yes
NCπ^0/CCe Rejection	0.1%
NCγ/CCe Rejection	0.2%
CCμ/CCe Rejection	0.01%

7.2.1 Straw-Tube Tracking Detector

Straw Tubes

The Straw-Tube Tracking Detector (STT) at the center of the FGT is composed of straw tubes with an outer diameter of 1 cm, as well as radiators and targets that reside next to the straw tubes as shown in Figure 7.2.

The straw walls are made by winding together a film of carbon loaded Kapton XC (inner) and
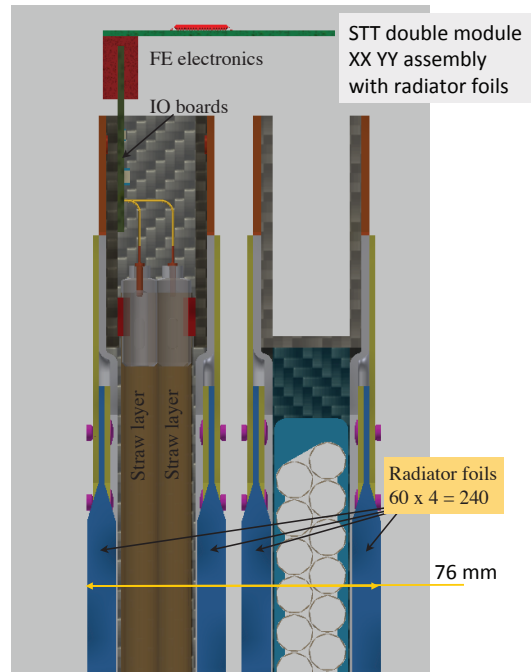
Figure 7.2: A schematic drawing of the Straw-Tube Tracking Detector (STT) design.

a film of aluminum coated Kapton HN (outer), for a total thickness of about $70\,\mu$m. The anode wire is gold-plated tungsten with 20 μm diameter. Two consecutive layers of straws are staggered by a half-diameter, glued, and inserted into a carbon-fiber composite mechanical frame to form a single module. One vertical (YY) and one horizontal (XX) module are then assembled together to form a double-module (XXYY) equipped with frontend electronic readout boards. Figure 7.2 shows a schematic drawing of the STT module with four straw-tube planes and radiators. Each XXYY module equipped with radiators is equivalent to $1.45 \times 10^{-2}X_0$ ($0.2 \times 10^{-2}X_0$ without radiators), with a radiation length $X_0 \sim 5.5$ m. The momentum measurement requires that tracks are detected in at least six straw layers. The staggered double layer design, high number of straw planes and double-end readout will contribute to resolving short track disambiguation.

The straw tubes will be filled with a gas mixture of either 70% Ar plus 30% CO_2 (for modules with nuclear targets) or 70% Xe plus 30% CO_2 (for modules with radiators). The dimensions of each double module in the reference design will be approximately 350 cm×350 cm×8.0 cm, including a nuclear target or four radiator planes and four straw planes. For ease of construction and transportation, each double module is made up of two modules, with two straw layers and dimensions of apppproximately 350 cm×175 cm×4.0 cm. Each module will have a carbon composite frame around the perimeter for support and will have an attached target or radiator.

The modularity of the STT provides for successive measurements using thin nuclear targets (thickness $< 0.1X_0$), while the excellent angular and spatial resolution allows a clean separation of events originating in different target materials.

The STT will have a total of 107,520 straws — corresponding to 336 straws per plane, 1344 straws per module — and 80 modules. Both ends of the straw tubes will be read out, leading to a total number of 215,040 electronics channels. The total mass of the STT, including targets and

radiators, is approximately 8 t. Table 7.2 summarizes the main STT parameters.

Table 7.2: Straw Tube Tracker specifications

Item	Specification
Straw Tube Geometry	1 cm Diameter × 3.5 m Long
Number of Straw Tubes	107,520
Number of Straw Tubes per Plane	336
Number of Straw Tube Planes per Module	4
Number of Straw Tube Sub-Modules per Module	4
Number of Straw Tube Modules	80
Number of Straw Tube Sub-Modules	320
Length of Straw Tube Wire	376.3 km
Number of Electronics Channels	215,040
Number of Modules with Radiators	75
Radiator Thickness per Module	3.6 cm
Radiator Mass per Module	69.1 kg
Number of Modules with Nuclear Targets	10
C Mass per Target Plane	192 kg
Number of Modules with C Target Planes	2
Ca Mass per Target Plane	132 kg
Number of Modules with Ca Target Planes	1
Ar Target Geometry	5.08 cm Diameter × 3.5 m long
Number of Ar Targets per Plane	68
Ar Mass per Target Plane	112 kg
Number of Modules with Ar Target Planes	1
Fe Mass per Target Plane	96.5 kg
Number of Modules with Fe Target Planes	1

In addition to tracking charged particles and measuring Transition Radiation (TR), the STT provides dE/dx measurement to identify particles. Figure 7.3 provides a sample of pions, kaons and protons identified via dE/dx in the STT.

Radiator Targets

Radiators will be placed in the downstream STT modules and will serve as targets for both neutrino interactions and Transition Radiation (TR) production. Each STT module contains four radiators, where each radiator consists of 60 layers of 25-μm polypropylene $(C_3H_6)_n$ foils, which are embossed to keep 125-μm air gaps between consecutive foils. The mass of each radiator is ~17 kg and the thickness is ~9 mm. The use of thin plastic foils regularly spaced allows the emission of transition radiation for electron/positron identification, which is detected by the Xe gas in the straws. The plastic radiators account for about 83% of the mass of each STT module and also provide the main (anti)neutrino target. Overall, a radiator mass of about 5 tons is required to achieve the
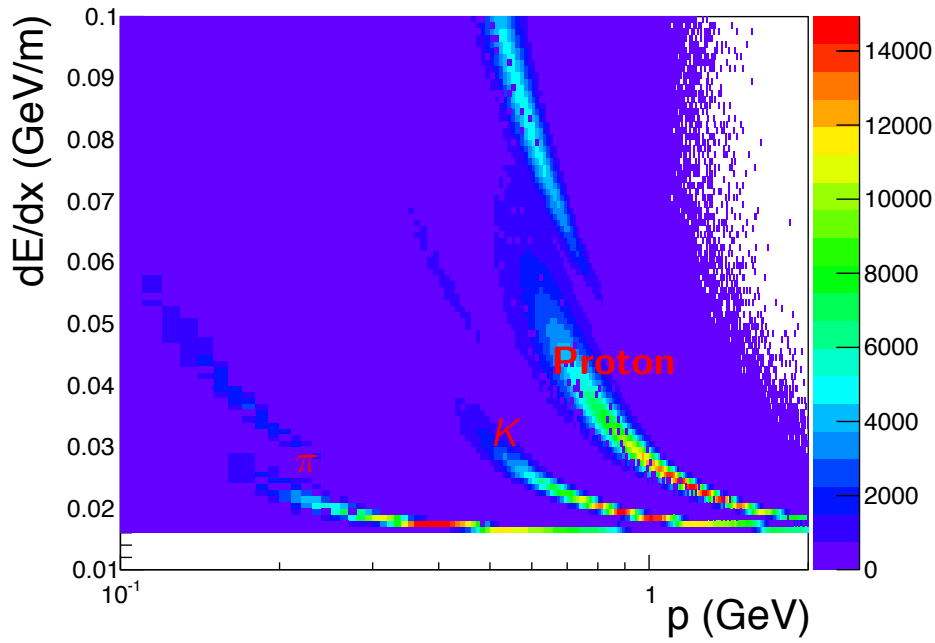
Figure 7.3: Simulated distributions of dE/dx for different particles in FGT.

physics sensitivity discussed in Chapter 6 of CDR Volume 2: *The Physics Program for DUNE at LBNF* [4] and the DAE/DST Detailed Project Report[52].

Nuclear Targets

A set of different nuclear targets will be installed in front of the most upstream STT modules, which will not be equipped with radiators. The most important nuclear target is the argon target that matches the DUNE far detector. This target will consist of planes of cylindrical tubes filled with argon gas pressurized to 140 atm ($\rho = 0.233$), with sufficient Ar mass to provide $\sim$10 times the unoscillated statistics expected in a 40−kt far detector. The proof-of-concept design consisted of 0.5-inch diameter, 3.5-m-long stainless steel tubes, with wall thickness 0.065-inch. In order to minimize the mass of the tube walls, the use of a single plane of C-composite tubes with 2-inch diameter and a wall thickness of 0.04-inch is under investigation.

Relevant to argon, a crucial target is calcium which has the same atomic weight ($A = 40$) as argon but is isoscalar. Since most nuclear effects depend on the atomic weight A, inclusive properties of (anti)neutrino interactions are expected to be the same for these two targets. This fact will allow the use of both targets to model signal and backgrounds in the DUNE far detector (argon target), as well as to compare DUNE results for nuclear effects on argon with the extensive data on calcium from charged lepton scattering.

An equally important nuclear target is carbon (graphite), which is essential in order to get (anti)neutrino interactions on free proton, through a statistical subtraction procedure from the main polypropylene target $(C_3H_6)_n$. The availability of such a free-proton target will allow accurate flux determinations and cross section measurements, and, for the first time, a direct model-

independent measurement of nuclear effects — including both the primary and final-state interactions — on the argon target relevant for the far detector oscillation analysis. The required carbon target mass is about 0.5 t (in addition to the carbon in the STT frames). The corresponding expected number of events on H target are $5.0(1.5) \times 10^6 \pm 13(6.6) \times 10^3 \ \nu(\bar{\nu})$ CC, where the uncertainty is dominated by the subtraction procedure.

A stainless steel target in the form of a single thin slab will provide service measurements of (anti)neutrino cross sections for the INO experiment in India.

Finally, cylindrical tubes similar to those used for the pressurized Ar gas can be filled with standard and heavy water (H_2O and D_2O). The statistical subtraction of H_2O from D_2O will result in a quasi-free neutron.

Table 7.2 gives a reference configuration of the radiators and nuclear targets, listed according to their location from downstream to upstream. The final configuartion of the nuclear targets will require detailed Geant4 simulations of FGT and corresonding physics sensitivity studies.

7.2.2 Electromagnetic Calorimeter

An electromagnetic calorimeter (ECAL) will surround the tracking volume on all sides and consist of three separate pieces: Forward ECAL, Barrel ECAL and Backward ECAL. The expected energy resolution is $\sim 6\%/\sqrt{E}$ for the forward ECAL. The ECAL must provide high segmentation in both the transverse and longitudinal directions to reconstruct photons from π^0 decay and electron/positrons from their Bremsstrahlung emissions. The ECAL conceptual design consists of layers of either 1.75-mm-thick (for the forward ECAL) or 3.5-mm-thick (for the barrel and backward ECAL) lead sheets and 2.5-cm-wide by 10-mm-thick plastic scintillator bars, as shown in Figure 7.4.
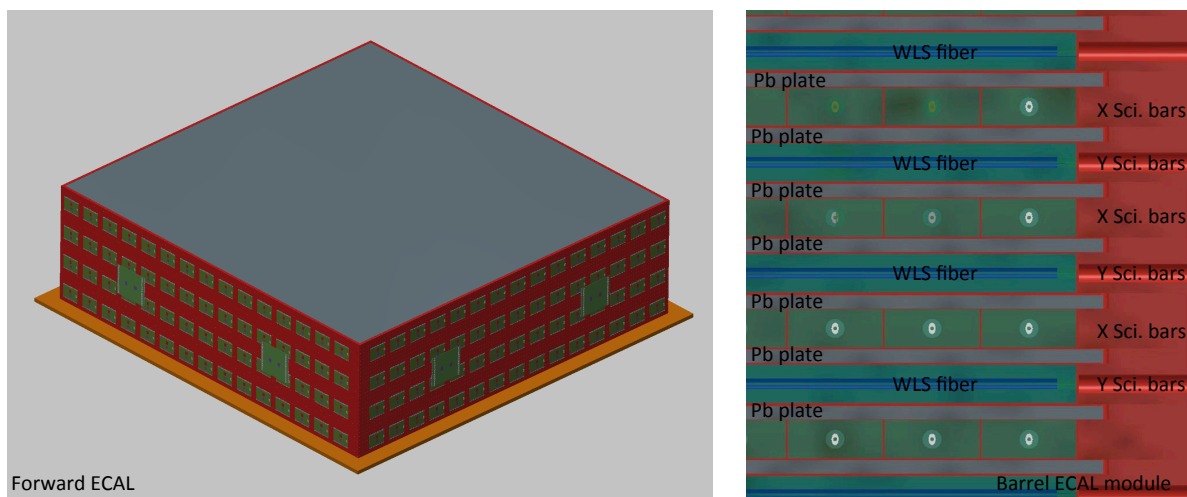
Figure 7.4: Schematic drawing of the forward ECAL equipped with the front-end and back-end readout boards (left), and a cross section of one barrel ECAL module (right), showing the details of the assembly of alternating planes of plastic scintillator and Pb sheets.

The scintillator layers for the Forward and Backward ECAL alternate as XYXYXY..., while the scintillator layers for the Barrel ECAL are all horizontal along the axis of the magnet. The Forward ECAL will consist of 60 layers of scintillator bars, where each bar has dimensions 3.2 m×2.5 cm×1 cm. The Backward ECAL will consist of 16 layers of scintillator bars, where each bar has the same dimensions, 3.2 m×2.5 cm×1 cm. The Barrel ECAL will also consist of 16 layers of scintillator bars, where each bar has the same dimensions, 3.2 m×2.5 cm×1 cm. The parameters of the ECAL design will be further optimized with the help of a full Geant simulation of FGT.

The lead sheets and scintillator bars will be assembled and glued together into complete modules of dimension 3.2 m×3.2 cm×81 cm for the Forward ECAL and 3.2 m×3.2 cm×27.5 cm for the Backward ECAL. For the Barrel ECAL, the module dimensions will also be 3.2 m×3.2 cm×27.5 cm. Two Barrel modules are placed end-to-end along the sides of the inner surface of the magnet (eight Barrel modules total) to provide full coverage of the barrel region. The total numbers of scintillator bars in the Forward (7680), Backward (2048) and Barrel ECAL (16384) is 26112 bars.

The scintillator bars will be extruded with holes in the middle of each bar. The holes will then be fitted with 1-mm-diameter Kuraray wavelength-shifting (WLS) fibers. The fibers will be read out by SiPM (silicon photomultiplier) photosensors at each end. Detailed R&D studies will be performed to optimize the diameter of the scintillator hole, the fiber diameter and the proper coupling between the scintillator and the fiber for optimum light transmission.

The total mass of scintillator is 20.9 t, the total mass of Pb is 70.8 t, and the total number of readout channels is 52,224. Table 7.3 summarizes the specifications of the ECAL.

7.2.3 Dipole Magnet

The STT and ECAL modules reside inside a 0.4-T dipole magnet for the measurement of particle momentum and charge. The magnet will have inner dimensions (inside the coils) 4.5 m wide × 4.5 m high × 8.0 m long. The magnet has four vertical copper coils, stacked horizontally, producing a horizontal magnetic field. The return yoke will be divided into two halves along the longitudinal center line to allow the magnet to be opened to service the detector inside, as shown in Figure 7.1. Each half yoke will be built from eight "C" (C-shaped) sections, and the thickness of the magnet steel will be 60 cm, consisting of 6×10-cm-thick plates. The magnet power requirement with copper coils is ∼2.4 MW, corresponding to 6 kA at 400 V. The water flow required for cooling is 20 liter/s. Figure 7.5 shows the B field results obtained from detailed simulations performed at the Bhabha Atomic Research Center (BARC) in India.

The magnet specifications are summarized in Table 7.4.

The momentum resolution is dominated by multiple scattering in the STT. The momentum resolution is therefore given by $\delta p/p = 0.053/\sqrt{(LX_0)}B$. For B = 0.4T, L = 3m, and X_0 = 4m; the expected momentum resolution is ∼3.8%.

Table 7.3: ECAL specifications

Item	Specification
Scintillator Bar Geometry	3.2m × 2.5cm × 1cm
Number of Forward ECAL Scintillator Bars	7680
Forward ECAL Pb thickness	1.75mm
Number of Forward ECAL Layers	60
Number of Forward ECAL Radiation Lengths	20
Dimensions of Forward ECAL Module	3.2m × 3.2m × 81cm
Number of Barrel ECAL Scintillator Bars	16,384
Barrel ECAL Pb thickness	3.5mm
Number of Barrel ECAL Layers	16
Number of Barrel ECAL Radiation Lengths	10
Number of Barrel ECAL Modules	8
Dimensions of Barrel ECAL Modules	3.2m × 3.2m × 27.5cm
Number of Backward ECAL Scintillator Bars	2048
Backward ECAL Pb thickness	3.5mm
Number of Backward ECAL Layers	16
Number of Backward ECAL Radiation Lengths	10
Dimensions of Backward ECAL Module	3.2m × 3.2m × 27.5cm
Total Length of 1-mm Diameter WLS Fiber	83.6km
Total Number of Scintillator Bars	26,112
Total Number of Electronics Channels	52,224
Total Mass of Scintillator	20,890 kg
Total Mass of Pb	70,800kg
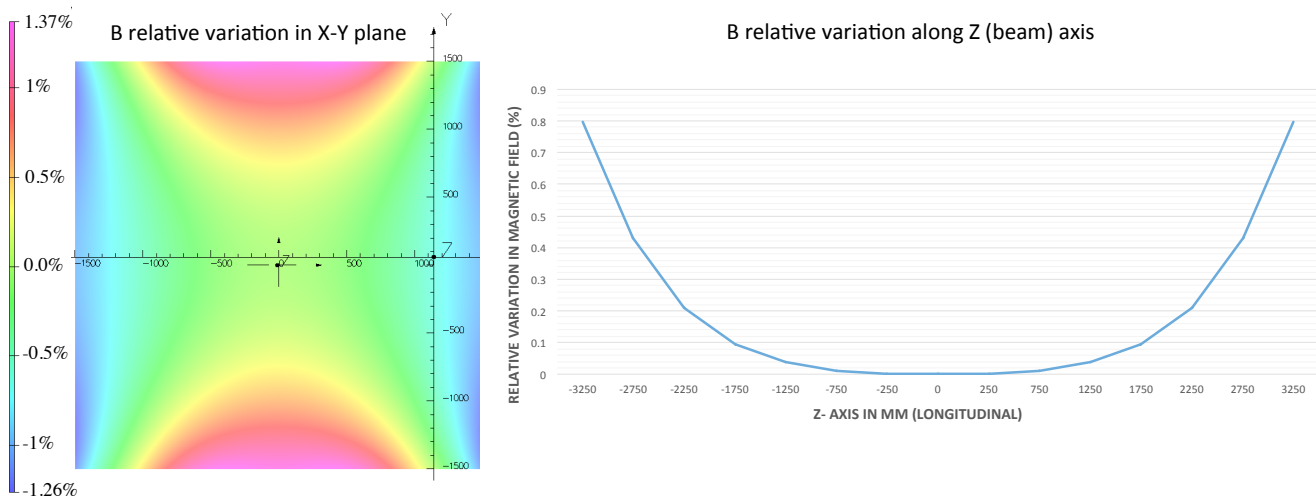
Figure 7.5: Results from the detailed simulations of the magnetic field in the dipole magnet performed at the Bhabha Atomic Research Center (BARC) in India. The plots show the deviations (in percentage) from the nominal field in the (X,Y) plane (left plot) and along the beam axis (right plot).

Table 7.4: Dipole Magnet specifications

Item	Specification
Inner Dimensions	4.5 m×4.5 m×8.0 m
Magnetic Field	0.4 T
Number of "C" Sections	16
Thickness of Steel in the "C" Sections	60 cm
Mass per "C" Section	60 t
Number of Coils	4
Mass per Coil	40 t
Magnet Current	6 kA
Magnet Voltage	400 V
Magnet Power Requirements	2.4 MW
Water Flow for Cooling	20 l/s

7.2.4   Muon Identifier

The sides and ends of the dipole magnet will be instrumented with a muon-identifier detector (MuID) that will distinguish muons from hadrons by the ability of muons to penetrate the iron without showering or interacting. The task of the MuID is to reconstruct the muon track segments and match them with the corresponding charged track reconstructed in the STT. The MuID will consist of 432 resistive plate chamber (RPC) modules interspersed between two 10-cm-thick steel plates of the dipole magnet and between 20-cm-thick steel plates at the upstream and downstream ends of the magnet as is detailed in Table 7.5.

Table 7.5: MuID specifications

Item	Specification
Number of Barrel RPC Trays of Dimension 2.2 m × 4 m	8
Number of Barrel RPC Trays of Dimension 2.5 m × 4 m	16
Number of Barrel RPC Trays of Dimension 2.8 m × 4 m	16
Number of Barrel RPC Trays of Dimension 3.1 m × 4 m	8
Number of END RPC Trays of Dimension 2 m × 6 m	24
Total Number of RPC Trays	72
Total Number of RPC Modules	432
Mass of Downstream Steel Planes	283,500 kg
Mass of Upstream Steel Planes	170,100 kg
RPC Thickness	1.5 cm
Number of 7.65mm Pitch X Strips per Module	256
Number of 7.5mm Pitch Y Strips per Module	128
Total Number of RPC Strips and Electronics	165,888

The choice of RPC is motivated by the combineation of low cost, ability to reach sub-mm space resolution, and existing expertise. The MuID is only meant to provide identification of the muon;

the muon momentum will be measured by the STT inside the magnetic field.

The nominal dimensions of all RPC modules will be 1 m × 2 m with active areas of 96 cm × 196 cm. Each module has 256 X strips at 7.65-mm pitch and 128 Y strips at 7.5-mm pitch. This fine-grained pitch allows to reach spatial resolution of ∼0.7 mm and to disentangle multiple hits resulting from events originated in the magnet iron. The modules will be grouped into trays, each containing six modules, and the trays will be sufficiently wide to allow overlapping modules. The downstream MuID will contain five steel planes of overall dimensions $6 \times 6 \times 0.2\,m^3$ (283.5 t) and five RPC planes, while the upstream MuID will contain three steel planes (170.1 t) of dimensions $6 \times 6 \times 0.2\,m^3$ and three RPC planes. The barrel MuID will contain 24 planes (three layers × eight sides) of RPCs. The RPCs will have a total thickness of 15 mm and a gap width of 2 mm. One possible gas mixture could be Ar (75%), tetraflouroethane (20%), isobutane (4%) and sulphurhexaflouride (1%). A full scale prototype of the RPC modules was built at the Variable Energy Cyclotron Centre (VECC) in India. Figure 7.6 shows a picture taken during the assembly of the prototype and the corresponding efficiency measurement with a cosmic ray telescope.
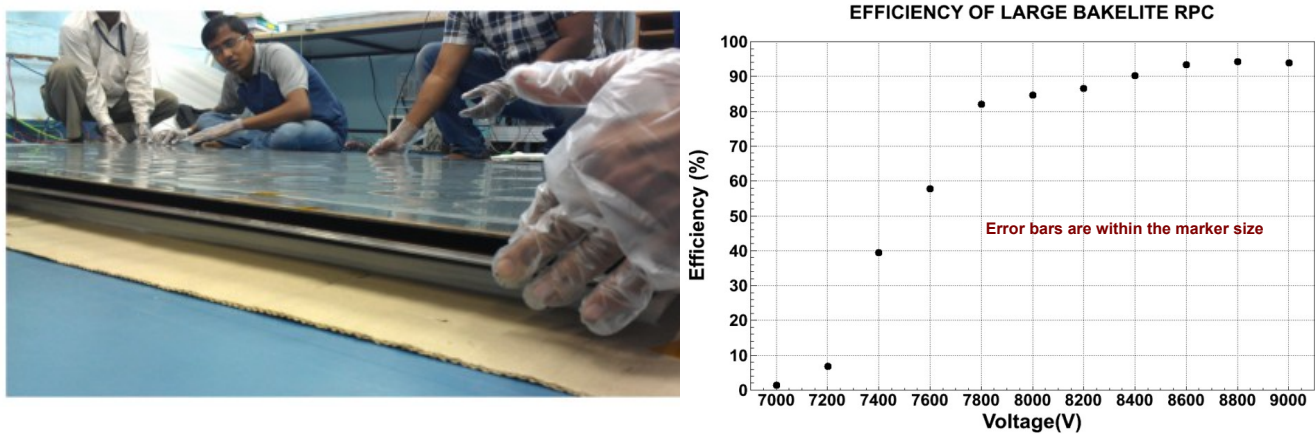
Figure 7.6: Fabrication of a large (2.4 m×1.2 m) RPC prototype at the Variable Energy Cyclotron Centre (VECC) in India (left) and corresponding efficiency tests (right).

7.2.5   Instrumentation

The instrumentation includes both fast readout electronics for the subdetectors and slow control of the subdetectors, involving monitoring the humidity, temperature, gas pressure, etc. There is considerable synergy in the information gathered in the STT, ECAL and MuID. Both the STT and ECAL are required to measure the total charge and the time associated with a given hit. The MuID RPCs are required to provide the position and time associated with a traversing track. Similarly, the slow control of the subdetectors share many features.

The electronics for the three subsystems, STT, MuID, and ECAL, are all "fast" systems, i.e., all of the signals are in the few-to-10 nanosecond range. The requirements for each system are very similar: a fast output and both an ADC and a TDC on each channel. Additionally, for the STT straw tubes it is desirable to wave-form digitize the analog signal in order to enhance the ability

to separate the ionization signal from the transition radiation signal. The total channel count in FGT is 433,152 channels, as shown in Table 7.6.

Table 7.6: The number of electronics channels for each of the three detector systems

Detector	# of Channels
STT	215,040
ECAL	52,224
MuID	165,888

Recently, an interesting new ASIC development for an upgrade to the ATLAS muon system at the LHC has come out of BNL), the VMM2 chip. It handles 64 channels and produces both fast ADC and TDC outputs. It has been fabricated and tested and should be ready by 2017, long before it will be needed for DUNE.

To maintain a low level of humidity and to maintain a desired temperature, both STT and ECAL subdetectors will have dry nitrogen circulating within their outer layers. Magnet coils are cooled by water, while the magnet yokes are instrumented with RPCs that must remain dry. Continuous control of humidity in all these detectors is needed. Temperature must also be continuously monitored in all of the subdetectors in order for the electronics to not overheat. Also, all power sources instrumenting the FGT and its readout need to be monitored for appropriate voltage and current.

Gas leaks need to be monitored in the STT and MuID. The STT will employ Xe gas, which helps with the measurement of transition radiation. Xe gas is expensive and, hence, will be recirculated; leak-monitoring is particularly important here. The requirement on leaks is less stringent for the RPCs, which have less expensive gas.

The water flow (pressure gradient) will be continuously monitored in order to ensure that the magnet does not overheat.

7.3   Matching the ND Requirements for DUNE/LBNF

The scope of the this section addresses how the the reference NND described in Section 7.2 meets the requirements of the oscillation studies described in Section 3.8.2 of [4] and the short-baseline precision measurements described in Sections 6.1.2 and 6.1.3 of the same document. First, we present the oscillation related systematics; the systematics affecting the precision measurements and new-physics search program follows.

7.3.1   Oscillation Analyses

The Table 3.8 in Section 3.6.2 of [4] presents a conservative projection of systematic errors affecting ν_e appearance. The FGT measurement alleviates the systematic errors as enumerated below:

- **Beam ν_e:** The FGT will offer an event-by-event measurement of the beam ν_e via the identification of the emergent e^- in STT while rejecting the $\pi^0 \to \gamma \to e$ background via the determination of the missing-P_T vector to a high degree. In a 5-year neutrino-run (focus-positive) the FGT will accumulate $500,000$ ν_e with $\simeq 55\%$ efficiency and $\geq 95\%$ purity. The resulting ν_e/ν_μ ratio will be determined to $\leq 1\%$ precision. Furthermore, by constraining the sources of ν_e (μ^+, K^+ and K_L^0), the FGT will predict the the ratio of ν_e and ν_μ spectra at the far detector (FD) with respect to the near detector (ND) as a function of the neutrino energy, FD/ND (E_ν).

- **Beam $\bar{\nu}_e$:** Although the FD does not distinguish ν_e from $\bar{\nu}_e$, the FGT will accurately measure the beam $\bar{\nu}_e$ by identifying the emergent e^+ in the STT with efficiency and purity similar to those for ν_e. (We point out that the dominant kaonic source of $\bar{\nu}_e$ is K_L^0; the neutrino spectra from K_L^0 are different from those of K^+ at the FD.) In a 5-year neutrino-run, the FGT will accumulate $40,000$ $\bar{\nu}_e$ and 5×10^6 $\bar{\nu}_\mu$ samples, providing a precise FD/ND prediction for the antineutrino to $\simeq 1\%$. These constraints will be even more valuable during the antineutrino run (focus-negative) where the wrong-sign backgrounds are larger.

- **Cross Sections:** First, the FGT will measure the absolute flux, via ν-e scattering, to $\simeq 2.5\%$ precision. Second, using radiator targets, the FGT will measure exclusive channels, such as quasi-elastic, resonance, coherent-mesons and the inclusive DIS channel with unparalleled precision. Since Argon is the far detector nuclear target, a set of various nuclear targets will allow translation of the cross-section measurements to ν-Ar scattering.

- **Nuclear Effects:** The FGT will employ a suite of nuclear targets including Ar-gas in pressurized tubes, a thin solid calcium target (which has the same A=40 at Ar), a C-target, etc. Specifically, the number of ν-Ar interaction will be 10 times larger than that expected in a $40-$kt FD, without oscillations. Additionally, comparisons of calculations of elastic and inelastic interactions in Ar versus Ca, including FSI effects, indicate negligible differences between the two targets. Thus, the combination of the Ar and Ca targets will provide a strong constraint on the nuclear effects from both initial and final state interactions. Finally, FGT's ability to isolate ν ($\bar{\nu}$) off free-hydrogen, via subtraction of hydrocarbon and carbon targets, will provide a *model-independent* measurement of nuclear effects.

- **Hadronization:** A notable strength of FGT is to identify the yield of π^0 *separately* in neutral-current (NC) and charged-current (CC) interactions. (The estimated π^0 detection efficiency is $\simeq 50\%$.) In addition, FGT will determine the yields of π^- and π^+, the dominant backgrounds to the ν_μ and $\bar{\nu}_\mu$ disappearance. Finally, the measurement of the composition, energy, and angle of the hadronic jet will provide a tight constraint on the overall hadronization models.

- **Energy Scale:** The average density of about $0.1\,\mathrm{g/cm^3}$ (close to that of liquid hydrogen) makes the STT mostly transparent to secondary particles — the entire STT length is equivalent to $\sim 1.4 X_0$ including the various nuclear targets. As a result we will be able to measure accurately the 4-momenta of secondary particles as well as the missing-P_T vector in the CC processes. This redundant missing-P_T vector measurement provides a most important constraint on the neutrino and antineutrino energy scales. The capabilities of this kinematic analysis have been demonstrated by the NOMAD experiment (with similar density and B field). In addition, measurements of exclusive topologies like quasi-elastic, resonance and

coherent meson production offer additional constraints on the nuclear effects affecting the neutrino energy scale (see Section 6.1.2 of [4]). The requirements on the muon energy scale ($< 0.2\%$) and total hadron energy scale ($< 0.5\%$) uncertainties have been already achieved by the NOMAD experiment. The muon energy scale is calibrated with the mass constraint from the K^0 reconstructed in STT and was statistics limited in NOMAD. The total hadron energy scale is calibrated using the y_{Bj} distribution in different energy bins. Compared to NOMAD, FGT will have $\times 100$ higher statistics and $\times 10$ higher granularity.

In summary the FGT will accurately quantify all four neutrino species and predict the ratio FD/ND for them. It will measure the 4-momenta of the outgoing hadrons composing the hadronic jets in a variety of nuclear targets, in essence proving a data-driven *event generator* which can be applied to the FD.

Since the FGT is based upon a different technology than the FD, it cannot account for effects of LAr reconstruction inefficiencies in the FD. The corresponding cancellation could be achieved only with an identical ND, which to some extent is an ill-defined concept due to a number of factors including size, beam profile and composition, rates, etc. However, given the detailed program to calibrate LAr detectors in test beams and multiple neutrino experiments employing LAr detectors, by the time DUNE becomes operational the reconstruction of particles in LAr will likely be well understood. Finally, Section 7.4 outlines the enhancement of the ND complex via the placement of complementary LAr detector(s) upstream of the FGT.

7.3.2 Short Baseline Precision Measurements and Searches

Sections 6.1.2 and 6.1.3 of [4] summarize a rich physics program at the near site providing a generational advance in precision measurements and sensitive searches. This short-baseline physics program and the long-baseline oscillation analyses share similar detector requirements and offer a deep synergy and mutual feedback. The reference FGT meets the requirements of the short-baseline studies as briefly outlined below:

- **Resolution:** The FGT is designed to have an order of magnitude higher granularity than NOMAD, the most precise, high statistics neutrino experiment. The corresponding improvements include better tracking, electron/positron ID through TR, dE/dx measurement providing hadron-ID, 4π calorimetry, 4π muon coverage and a larger transverse area for event containment.

- **Statistics:** The $1.2-\text{MW}$ neutrino source at LBNF will offer a factor of 100 enhancement in statistics compared to NOMAD. The program of measuring ν and $\bar{\nu}$ interactions in a set of nuclear targets, including Ar and H, will enhance the physics potential of precision measurements and searches.

Sensitivity studies to the salient precision measurements and searches can be found in [55, 52].

7.3.3   Future Tasks to Quantify the Systematic Errors

To quantify the systematic errors in oscillation studies and precision measurement program, three
tasks are still outstanding:

- **Geant4 Simulation:** A Geant4 simulation of the FGT is needed to confirm and correct the
  projected systematic errors and the salient sensitivity studies.

- **Event Reconstruction:** A program to reconstruct tracks in STT and to match the informa-
  tion from different subdetectors is needed to identify secondary particles.

- **Translating ND-Measurements to FD:** A concerted effort needs to be mounted to transfer
  the precision measurements in ND to the far detector.

The DUNE collaboration plans to pursue these issues with high priority in the coming years before
CD-2.

7.4   Addition of a Liquid Argon Detector to the NND

The reference FGT ND design concept is not identical to the far detector and it is not possible to
cancel the event reconstruction errors exactly in a near-to-far ratio as was done in MINOS. The
extent to which this lack of cancellation will limit the ultimate precision of the experiment has
yet to be fully explored. However, at the international Near Neutrino Detector workshop held at
Fermilab (July 2014) it was accepted that the FGT offers a sound basis for moving forward and
that a LArTPC or a high-pressure gaseous-argon TPC placed upstream of the FGT would enhance
the near detector capability.

The principal impediment to an identical ND – a LArTPC ND – is the event-pileup problem
due to the high intensity of LBNF. Nevertheless, during the operation of LBNF/DUNE there will
be periods when the accelerator is running at low intensity, for example during the initial ramp-
up and during the periodic shut-downs and accelerator upgrades. A ~100-t LArTPC stationed
upstream of the FGT (the reference ND) would be able to accumulate tens of thousands of neutrino
interactions during the low-intensity runs over the lifetime of the experiment. The FGT will act
as a spectrometer for the emerging muons. In conjunction with the measurements using nuclear
targets in the FGT, including Ar gas, such a LAr-ND would provide a means to accurately validate
in situ the FGT predictions for a LAr detector before the extrapolation to the FD, thus providing
a valuable redundancy check.

Furthermore, for special neutrino interaction topologies, such as neutrino-electron scattering, where
there is a single electron or muon in the final state, the combined LAr-ND and FGT configuration
could provide unique precision measurements.

Conceptual designs for a standalone LArTPC near detector and a gaseous argon TPC near detector
are under consideration and could serve as starting points for the design of this addition to the

FGT. Significant simulation and engineering studies are required to understand whether a liquid or gas argon TPC is optimal for minimizing systematic errors in the long-baseline measurements and to integrate the additional detector system with the FGT design to make a coherent near detector system.

7.5   Beamline Measurements

This section outlines the DUNE strategy for measurements of secondary beam particles downstream of the beam absorber. These measurements are designed to provide constraints on the neutrino flux at the near and far detectors, and monitor the pulse-to-pulse variation for beam diagnostic purposes. The measurements and apparatus described here fall into the category of equipment designed specifically for DUNE to detect muons exiting the decay tunnel.

7.5.1   Design Considerations

The requirements for the beamline measurements, as discussed in the NDC requirements documentation[56], are related to how well the neutrino flux must be known. While external hadron-production measurements can place constraints on the pion and kaon production in the target, they do not provide any constraint on the simulation of other key features, such as the horn focusing, secondary interactions, and the pion scattering and absorption in the air-filled decay volume.

In addition to the external measurements, covered in Section 7.6, that check the simulation of the thick target, horn material, decay tunnel and absorber, it is desirable to constrain the flux by making independent measurements at the 4–5% level of the muons that penetrate the absorber. It would not be practical to do this for all penetrating muons, but sufficient measurements at a few positions can be done in a cost-effective way.

The primary physics goal of DUNE is to measure the transmutation of ν_μ to ν_e over the 1300 km between Fermilab and SURF. It is essential for DUNE to cross-check the estimate of beam ν_e using several methods. There are two dominant sources of beam ν_e: muon decays and kaon decays. The muon systems are designed to directly measure the muons that penetrate absorber with an energy threshold as low as possible, i.e., directly measure those muons whose decays are a major source of beam ν_e. A measurement of the spectrum of those muons will translate directly into constraints on the spectrum of beam ν_e. That constraint has the advantage of being independent of poorly understood neutrino-nucleus cross sections.

Because muons and neutrinos come from the same parent pion and kaon decays, a measurement of the absolute muon flux, in conjunction with the energy spectrum seen in the muon monitors, can constrain the absolute neutrino flux. The goal for the DUNE muon monitors is to determine the absolute muon flux to an accuracy of 5% above a muon energy of 6 GeV (which corresponds to a neutrino energy of 1.6 GeV) in the central part of the absorber.

It is essential to monitor the stability of the beam direction over time. For example, above 6 GeV, the ratio of the Far Detector flux over the Near Detector flux changes by 2%. To keep the change in the neutrino beam less than 1% in all energy bins, the beam direction must be known to a precision of approximately 0.2 mrad. Because the muon monitors will be located approximately 275 m from the beam target, this requires a measurement of the muons to an accuracy of approximately 5 cm.

7.5.2   Muon-Measurement Facilities

The muon measurements are carried out in the region immediately downstream of the hadron absorber at the end of the decay tunnel, below the Absorber Service Building (LBNF 30). A view of the absorber area and the muon alcove is shown in Figure 7.7.
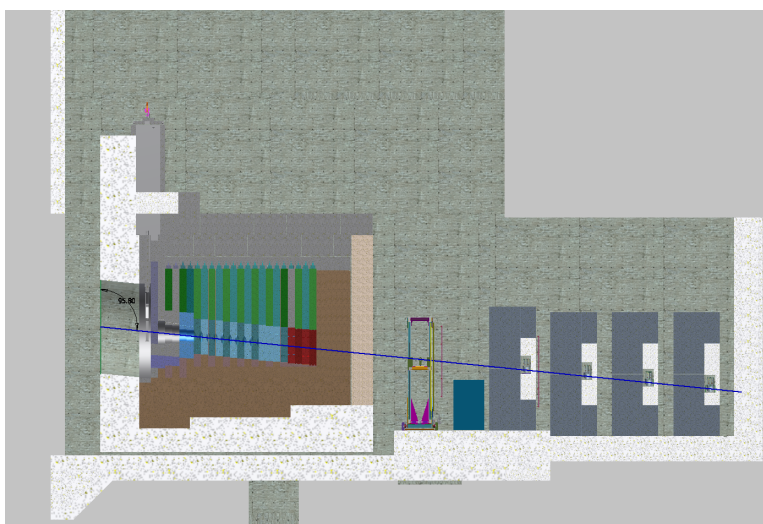
Figure 7.7: Absorber conceptual design. The figure shows the elevation view of the absorber at the end of the decay tunnel. The beam axis is shown by the blue line. The absorber is constructed of several different materials as shown: aluminum core in blue and grey, concrete (grey and tan), and steel (in brown and green).

The axis of the decay pipe cuts across the muon alcove at an angle and the size of the alcove is largely determined by the requirement that it contain the shadow of the four-meter-diameter decay pipe, projected through the alcove.

Figure 7.7 shows the downstream side of the absorber and a conceptual layout of the muon systems described in various sections of this chapter. The absorber itself is encased in concrete. The first set of muon-measurement devices, from left to right, is a variable-pressure gas Cherenkov counters, which mounted on a movable stand in order to scan across the rear surface of the absorber. Following that is an array of diamond ionization detectors and finally a set of stopped-muon counters which are interspersed between walls of steel "blue blocks". The blue blocks are there to provide several depths at which to monitor the stopped muons as they range out in the material. A second array of ionization devices will also be placed farther downstream within the blue blocks.

Figure 7.8 shows the energy lost by a horizontal muon as it traverses the absorber, as a function

of the distance from the beam axis along a 45° line perpendicular to the beam axis.
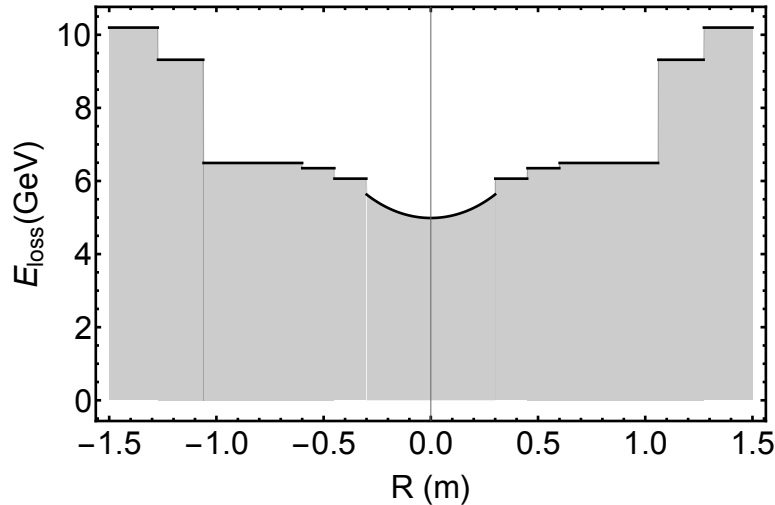
Figure 7.8: The energy loss a muon, parallel to the beam axis, experiences as it traverses the material in the absorber. The muon's energy loss is plotted versus the distance from the beam axis, along a 45° line perpendicular to the beam axis. Muons suffer between 4.7 and 9.3 GeV of energy loss depending upon where they cross the absorber.

In the central region, roughly to a distance of 105 cm, the muons lose between 5.0 to 6.4 GeV, so that the lowest-energy muons leaving the absorber at that point correspond to neutrino energies of ∼1.5 to 2.0 GeV. At a radius of roughly 105 cm, the full thickness of steel causes the muons 10 GeV or more, corresponding to neutrino energies of ∼ 2.6 GeV. From the perspective of the muon systems it will be desirable to lower these thresholds if possible.

7.5.3   Installation and Operation

The muon system detectors, already fully calibrated in the NuMI beam, will be installed as soon as the absorber hall (LBNF-30) is ready. Because the system will be located in a radiation-controlled environment that will not be accessible during beam operation, it is essential that the electronics and gas handling system be both robust and remotely operable. The prototype system in use at the NuMI area can be relocated for that purpose, or if desired a new system may be constructed. Periodic access will be required to the utilities area to replace gas bottles.

The blue blocks associated with the muon systems will be installed first. The positioned stand for the Cherenkov detector system will be installed next. and then the various detectors will be installed. The stopped-muon counters will be placed into the spaces between the blue-block walls on support frames. There will be access to the areas between the shield blocks from the side, and the stopped-muon counters will be designed so that they can be wheeled in from the side. If needed, they could then be moved around to measure the stopped-muon rates across the muon beam.

The muon systems will be operated continuously in order to insure a stable, high-quality neutrino beam. The muon-monitor-system data will be displayed in the control room on a spill-by-spill

basis to monitor the beam stability. Because the system will be located in a radiation-controlled environment that will not be accessible during the beam operation, it is essential that the electronics be designed for remote operation.

7.6 Hadron Production Measurements

7.6.1 Introduction

The technical components that would be needed to implement the strategies described in this section are outside the scope of the DUNE NDS conceptual design. The following information is included in this document because it complements the conceptual design and expands the NDS capabilities to more closely meet the mission need without increasing the project cost.

7.6.2 External Hadron-Production Measurements

Uncertainties on hadron production will translate into uncertainties in the neutrino fluxes in the DUNE far detector, since the neutrinos are produced by hadrons decaying in the decay pipe. Precise calculations of neutrino fluxes in high-energy accelerator beams are limited at present by our knowledge of hadron production cross-sections in hadron-nucleus collisions. The modeling of strong-interaction cascades and hadronic yields from "thick" targets (up to a couple of interaction lengths) relies on detailed knowledge of underlying physics and cross sections, which must be provided as a starting point to simulations. The resulting prediction of the flux of neutrinos, produced from decays of pions, kaons, and muons emerging from a hadronic shower and beam line re-interactions, is an essential part of simulations of most neutrino experiments.

Two-detector neutrino oscillation experiments predict the neutrino flux at the far detector by using neutrino fluxes "calibrated" (or appropriately scaled) by event energy spectra measured in the near detector. However, these experiments rely on beam simulations since the decay pipe (where most beam neutrinos are created) provides different angular acceptance for the two detectors. In addition, experiments using near and far detectors based on different detection technologies further complicate the extrapolation. This chapter outlines the DUNE strategy for augmenting the capabilities of the BLM with external measurements of secondary-beam particles.

7.6.3 Background

A complete knowledge of the momenta and decay points of the kaons, pions and muons would be sufficient to predict the un-oscillated flux of neutrinos at the near and far detector locations. This would require knowledge of

- the phase-space distribution of the initial proton beam;

- details of all materials present in the target, horn and decay pipe areas;

- the electromagnetic focusing characteristics of the magnetic horn;

- the detailed development of the hadron cascade, spawned by the initial proton, that passes through the target/horn/decay pipe; and

- the meson-to-neutrino decay rates.

With careful engineering design and control of the materials in the target area, these items can be simulated accurately, except for hadronic cascades in the target, horn and decay pipe. The simulation of the hadronic cascade requires accurate knowledge of the hadron scattering cross sections, for which there are no first-principle calculations. These cross sections must therefore rely on models, which in turn require hadron-production measurements that span particle type, particle energy and the various materials found in the target, horn and decay pipe.

At present, a sufficient body of hadron-production measurements does not exist to achieve DUNE's desired accuracy of 4–5%, as determined by the irreducible error on the statistical uncertainty for the appearance-measurement background, although this is expected to improve over time. A program of hadroproduction measurements has been approved as US-NA61 to run at CERN.

7.7 The Data Acquisition System (DAQ) and Computing

The scope of the Near Detector System DAQ (NDS-DAQ) and computing includes the design, procurement, fabrication, testing, delivery and installation of all the NDS-DAQ subsystems:

- NDS Master DAQ (NND-MDAQ),

- Near Neutrino Detector DAQ (NND-DAQ),

- Beamline Measurements DAQ (BLM-DAQ), and

- NDS Computing.

7.7.1 NDS DAQ

The Near Detector System (NDS) Data Acquisition system (NDS-DAQ) collects raw data from each NDS individual DAQ, issues triggers, adds precision timing data from a global positioning system (GPS), and builds events. The NDS-DAQ is made up of three parts, as shown in the block diagram of Figure 7.9, a master DAQ and one each for the near neutrino detector (NND, which is the FGT) and the BLM systems. The names for these are, respectively, NDS-MDAQ, NND-DAQ and BLM-DAQ.
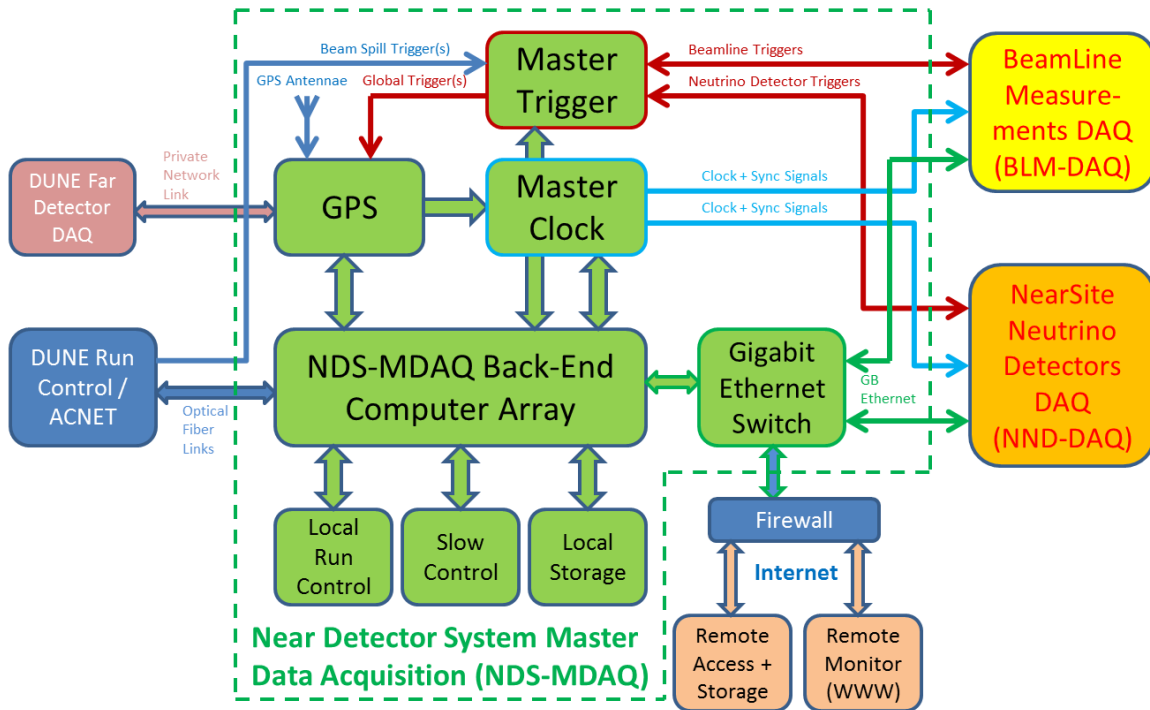
Figure 7.9: Near Detector System DAQ block diagram: The NDS-DAQ consists of the NDS Master DAQ (green blocks), the Beamline Measurement DAQ (yellow summary block) and the Near Neutrino Detectors DAQ (orange summary block). The NDS-DAQ connects to other portions of DUNE and LBNF, shown here in other colors (blue, light red, tan).

NDS Master DAQ

The NDS Master DAQ (NDS-MDAQ) is designed to provide a high-level user interface for local run control and data taking, as well as for secure remote control and monitoring. It will serve as the primary interface to the NND-DAQ and BLM-DAQ and will include

- the slow-control system,

- online data and DAQ performance monitoring,

- raw data collection,

- building of events, and

- data storage.

The NDS-MDAQ includes hardware two-way triggering for both the NND-DAQ and BLM-DAQ, and GPS hardware for precision time-stamping and global clock synchronization. The design is currently based on a channel count estimate of approximately 433,000 from the near neutrino detector, plus $< 1,000$ from the beamline detectors. Custom electronic components for the NDS-DAQ are based on existing custom designs from other experiments, e.g., T2K and ATLAS, and

implement commercial components for the trigger modules, clock and timing synchronization, GPS and environmental monitoring.

Near Neutrino Detector DAQ (NND-DAQ)

The Near Neutrino Detector Data Acquisition system (NND-DAQ) collects raw data from the DAQ in each NND subdetector and connects to the NDS Master DAQ via Gigabit Ethernet. A block diagram of the NND-DAQ is shown in Figure 7.10.
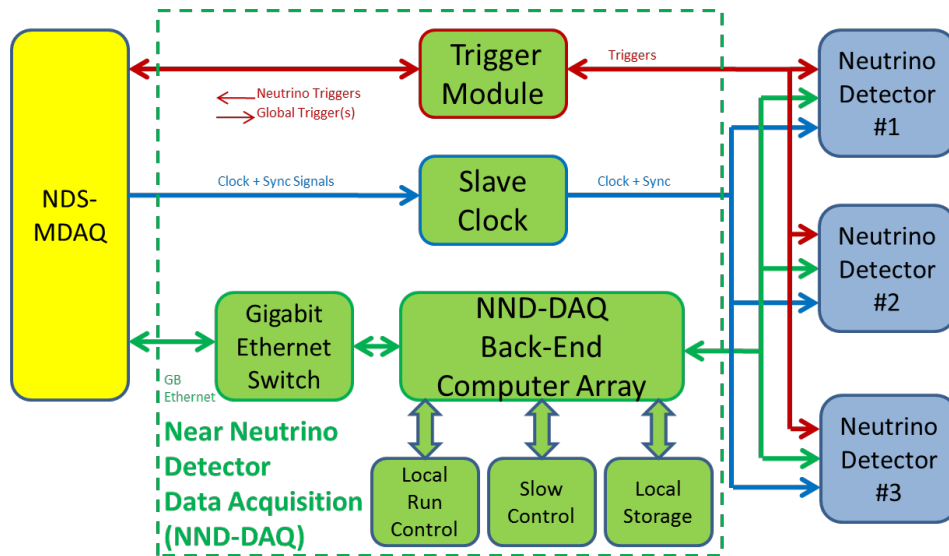
Figure 7.10: A block diagram of the Near Neutrino Detector DAQ (NND-DAQ).

The NND-DAQ will mainly consist of a scalable back-end computer array, interconnected to the individual subdetector DAQs via Gigabit Ethernet and specialized electronics modules for trigger processing and clock synchronization. It interfaces to the NDS-MDAQ for run control and data collection. The NND-DAQ will also have its own local run-control setup, consisting of a number of desktop workstations to allow independent local runs that include NND subdetectors only; this is useful during detector commissioning, calibration runs, stand-alone cosmic runs, or other runs where the beam is stopped or not needed.

The quantity of computers required for the NND-DAQ back-end system is highly dependent on the number of channels and expected data rates of the individual neutrino detectors. One back-end computer should be able to handle approximately 3,000 channels for sustainable and continuous runs. Assuming a total of 433,000 channels for all NND subdetectors combined, about 150 back-end computers would be needed.

Trigger signals from each subdetector will be collected and pre-processed by a trigger electronics module, similar in design to the NDS trigger or master-clock modules of the NDS-MDAQ design. Depending on the run mode, this module could feed local trigger decisions to the detector DAQs for data collection, or it could forward NDS triggers from the NDS-MDAQ or higher levels to the NND subdetector DAQs. A slave-clock electronics module, similar to the master-clock module in

the NDS-MDAQ, distributes clock- and time-synchronization signals from the NDS-MDAQ to all NND subdetectors.

Beamline Measurements DAQ (BLM-DAQ)

The BLM-DAQ will mainly consist of a scalable back-end computer array, inter-connected to the individual beamline measurement detector DAQs via Gigabit Ethernet and specialized electronics modules for trigger processing and clock synchronization. It interfaces to the NDS-MDAQ for run control and data collection. It will also have its own local run-control setup, consisting of a number of desktop workstations to allow independent local runs that include beamline measurement detectors only; this is useful during detector commissioning, calibration runs, stand-alone cosmic runs or other runs where the beam is stopped or not needed.

7.7.2 NDS Computing

The computing system encompasses two major activities: online computing with required slow-control systems, and offline computing for data analysis and event simulation. The computing components are based on currently available commercial computing and gigabit networking technology, which is likely to improve over the next years without driving costs up for the final design.

Chapter 8

Software and Computing

8.1 Overview

The three primary components of the DUNE Software and Computing effort include the computing hardware, software infrastructure and reconstruction. This chapter summarizes the much more detailed information presented in Annex 4B: *Expected Data Rates for the DUNE Detectors* [19], which describes the data sources and rates for the far and near detector designs, and provides a reference to the parameters and assumptions used in estimating these characteristics, and Annex 4C: *Simulation and Reconstruction* [10].

Simulated data samples provide the basis for detailed studies of detector performance, inform detector design choices, and enable the development of automated event reconstruction. Detailed Monte Carlo predictions of expected data distributions enable extraction of physics results from the DUNE experiment. Several important sources of systematic uncertainty come from detector modeling, and varying the assumptions incorporated in the simulations provides the mechanism by which these systematic uncertainties can be estimated. Simulations are also needed to extrapolate from auxiliary data samples (such as test-beam or in situ measurements, using events not passing signal-event selection requirements) to the signal selection samples.

The Software and Computing effort is not part of the DUNE project; it is supported by non-project funds. It is coordinated by the DUNE collaboration and across the LBNF/DUNE project.

8.2 Computing Infrastructure

There are many factors that influence the data to be collected and processed in DUNE, e.g., rates, volume, etc. Reference [19] contains information on both the reference and alternative designs for the far detector.

8.2.1 Raw Data Rates

Types of data (using a supernova burst example)

DUNE is a multipurpose apparatus and will pursue a variety of physics goals. This will result in data streams of differing characteristics that will need to be processed and collected both in real time and offline, as well as different strategies and algorithms for handling these streams.

As one example, consider the difference between neutrino oscillation physics with beam neutrinos and the search for supernova neutrino bursts. Signals produced by beam events will be characterized by total energy in the GeV range, and therefore various aspects of handling the signal and the data (e.g., thresholds for zero suppression, etc.) can be optimized for minimum-ionizing particles. Since the energy scale of signals produced by supernova neutrino burst interactions is in the range of tens of MeV, it is expected that lower thresholds will be needed while processing these data in real time. This will result in considerable additional contribution from radiological backgrounds, which leads to an expected data rate that is quite significant.

Another differentiating feature of supernova neutrino bursts is that *multiple neutrinos are expected to arrive and interact in the detector volume within seconds of each other*, as opposed to a single vertex produced by a beam neutrino (or any other localized interaction and/or decay). This presents an opportunity to apply the DAQ architecture presented in Section 4.4 to make these data "self-triggering," i.e., to use the buffer memory in the LArTPC detector readout to detect a corresponding signature in the data stream and trigger recording of the potential supernova neutrino burst event.

The characteristic time scale for such a supernova neutrino burst data capture will be ~10 s. Given the large amount of data arriving within this time period (see [19]) and practical limits on the bandwidth of the connection between the RCE data processors and front-end computers in the DAQ, the buffer in the data processor will not have sufficient capacity (due to design and cost considerations). It can effectively buffer about 0.4 s of streaming data which is likely enough for the trigger decision but not for the complete supernova event capture. Local storage attached to the data processors will be necessary to record the data at full-stream (no zero-suppression). Preliminary estimates indicate that a storage device such as a SSD (one or two per board) will have speed sufficient for this purpose. With the trigger properly tuned, the number of times data are written to the SSD can be kept sufficiently low so as to ensure their longevity. Once captured in this manner, the data can then be transmitted to the rest of the farm within the available bandwidth.

The core elements of the DAQ system now exist as prototypes. The system as a whole, with the capabilities described in this section, is in the conceptual design stage.

Assumptions

According to the present baseline design, the Far Detector will consist of four identical modules of 10 kt each. (For the purposes of this document, the effect of possible variations in the design of these modules on the estimation of data characteristics will not be addressed.) A few basic assumptions have been made.

- Estimates correspond to the "full detector," i.e., they are effectively normalized to 40 kt.

- The accelerator spill cycle is 1.2 s with beam expected for 0.667 of each calendar year.

- Zero-suppression (ZS) thresholds will be set at levels that preserve signals from minimum-ionizing particles while effectively removing data due to electronics noise.

- The DAQ will be able to trigger based on spill times and will be able to reject isolated ^{39}Ar decays on at least a per-APA basis. (For DAQ details see Section 4.4.)

Far Detector LArTPC Parameters

The basic parameters presented below are also listed in [19].

- TPC channel count: 1,536,000 (i.e., four times the 384,000 channel count for each 10 kt module)

- Maximum drift Time: 2.25 ms

- Number of drift time windows in one DAQ readout cycle: 2.4

- ADC clock frequency: ∼2.0 MHz

- ADC resolution (bits): 12

In addition to these parameters, there are other factors affecting data rates and volumes, such as implementation of ZS in the DAQ RCE processors, contribution from radiological and cosmological backgrounds, and DAQ trigger configuration (e.g., the case of low-energy events).

Non-ZS maximum event size (corresponding to a snapshot of the complete TPC) can be calculated as a product of

- channel count,

- number of ADC samples per total drift (collection) time,

- drift time windows in one DAQ cycle, and

- ADC resolution.

This results in a total of 24.9 GB of TPC data in one readout (drift time).

Zero suppression greatly reduces the event size. An overly conservative estimate (leaning to the higher end of the range of values) based on a LArSoft Monte Carlo simulation of GeV-scale events suggests a zero-suppressed and uncompressed event size of $\sim$2.5 MB. After compression this event size is expected to reduce to $\sim$0.1 MB. This particular simulation employed a less-than-optimal schema for packing data and it is expected that these sizes can be further reduced.

Some of the driving ZS and full-stream (FS) annual data volumes are summarized in Table 8.1. Regarding the numbers in the row characterizing ^{39}Ar, once DAQ-level rejection of isolated ^{39}Ar decay events is invoked, a residual amount of data is accepted when the decay is accidentally coincident with beam-ν activity. These numbers are therefore given for information only and do not represent the DUNE estimates of actual data to be committed to mass storage. The data required to record this background is reduced to 3% of the "with-beam-ν" estimate of table 8.1 and is thus negligible, being an order of magnitude smaller than the data associated with the beam neutrino interactions themselves.

Table 8.1: Annual data volume estimations for zero-suppressed (ZS) data from various sources. An additional full-stream (FS) data estimation is given for supernova burst (SNB).

Source	Event Rate	Event Size	Data Rate	Annual Data Volume
^{39}Ar (ZS)	11.2 MHz	150 B	1.7 GB s^{-1}	53 PB
all in-spill				159 TB
with-beam-ν				79 GB
cosmic-μ (ZS)	0.259 Hz	2.5 MB	647.4 kB s^{-1}	20 TB
beam-ν (ZS)	8770 year^{-1}	2.5 MB	0.69 kB s^{-1}	22 GB
beam-ν (FS)	8770 year^{-1}	24.9 GB	7 MB s^{-1}	218 TB
SNB cand. (ZS)	12 year^{-1}	16.7 GB	6366 B s^{-1}	201 GB
SNB cand. (FS)	12 year^{-1}	46.1 TB	17.5 MB s^{-1}	553 TB

Far Detector Photon Detector (PD) Parameters

There are variations in the basic parameters of the Photon Detector currently in the R&D stage. The numbers presented below should be considered as ballpark values to be made more precise at a later time.

- Readout channel count: 24,000 (i.e., four times the 6000 channel count for each 10-kt module)

- Trigger rate is uncertain at this point due to ongoing investigation; one approach assumes one trigger per spill cycle

- ADC resolution (bits): 12

- ADC digitization frequency: 150 MHz

It is assumed that a few dozen samples will be recorded in each channel, and that zero suppression of channels with signals below a chosen threshold will be enforced, reducing the data volume by an order of magnitude. This results in 360 kilobyte per spill cycle, and as regards requirements on data handling, should be considered negligible compared to other data sources.

Near Detector Data Rates and Parameters

The near detector is subject to an intense R&D effort and its parameters are currently being optimized. The most relevant parameters of the Fine-Grained Tracker (FGT) are listed below.

- Straw Tube Tracker (STT) readout channel count: 215,040

- STT Drift Time: 120 ns

- STT ADC clock frequency and resolution (bits): 3 ns intervals, 10 bit

- ECAL channel count: 52,224

- Muon Detector Resistive Plane Chambers (RPC) channel count: 165,888

- Average expected event rate per spill: ~1.5

Since there are large uncertainties in estimates of the detector occupancy levels per event, broad assumptions must be made in order to estimate the data rate. The current estimate (as quoted in the Near Detector section of [19]) is ~1.0 MB s^{-1}, which translates into ~30 TB year^{-1}.

8.2.2 Processed Data

For the purposes of this document, *processed data* is defined as most of the data that is not considered "raw," i.e., it is data *derived* from raw (including possibly multiple stages of calibration and reconstruction) as well as data produced as a result of Monte Carlo studies.

There are uncertainties in anticipated quantities of all of these types of data. Table 8.1 contains a range of numbers reflecting limiting cases such as ZS vs FS. Depending on the optimum readout strategy, an annual raw data volume of 1 TB to 1 PB may be collected. Assuming that the data undergoes a few processing stages, DUNE can expect to handle as much as ~2 PB of data annually for reconstruction and a lesser volume for final analysis purposes.

For Monte Carlo, at the time of writing, the typical annual volume of data produced has been of the order of a few tens of terabytes. Initial expectations are that the MC sample size for beam events will need to be 10–100 times that of the data. With collaboration growth and more detailed

studies (e.g., of systematics) undertaken, this estimate is likely to increase.

8.2.3 Computing Model

Distributed Computing

Given that the collaboration is large and widely dispersed geographically, a fully distributed approach to computing is planned, based on the experience of the LHC experiments. This includes not only "traditional" grid technologies as deployed during the first decade of this century, but also more recent technologies such as cloud computing and the Big Data methodology. This combination will allow the collaboration to better leverage resources and expertise from many of its member institutions and improve the overall long-term scalability of its computing platform.

DUNE will operate a distributed network of federated resources, for both CPU power and storage capability. This will allow for streamlined incorporation of computing facilities as they become available at member institutions and for staged construction and commissioning of the detector subsystems. A modern Workload Management System will be deployed on top of grid and cloud resources to provide computing power to DUNE researchers.

Raw Data Transmission and Storage Strategy

Fermilab will be the principal data storage center for the DUNE experiment. It will serve as a hub where the data from both the facility (e.g., the beam, target and cryogenics) and the far and near detector systems are collected, catalogued and committed to mass storage. This will obviously require transmission of data over considerable distances (certainly for the far detector). The far detector DAQ systems will be located underground in the vicinity of the far detector modules at SURF, adding the step of transmitting the data from 4850L to the surface.

Raw data to be collected from the DUNE detectors are considered "precious" due to the high cost of operating both the facility (LBNF) and the DUNE detectors. This leads to three basic design elements in the data transmission and storage chain:

- Buffering:

  - Buffers will be provided for the DAQ systems to mitigate possible downtime of the network connection between 4850L and the surface.

  - Buffers will be provided at the surface facility to mitigate downtime of the network connection between the far site and Fermilab.

- Robust transmission: data transfer needs to be instrumented with redundant checks (such as checksum calculation), monitoring, error correction and retry logic.

- Redundant replicas: it is a common practice in industry and research (e.g., the LHC experiments) to have a total of three geographically distributed copies of "precious" data. Distribution of the replicas may include countries other than the United States, where the data will be collected. This provides protection against catastrophic events (such as natural disasters) at any given participating data center, and facilitates rebuilding ("healing") lost data should such an event happen.

Data Management

Data will be placed into mass storage at Fermilab. As described above, additional copies (replicas) will be distributed to other properly equipped computing centers. For example, consideration is given to both Brookhaven National Laboratory and NERSC as candidates for the placement of extra replicas. A given replica does not need to reside in its entirety at a single data center; the replicas can be "striped" across multiple data centers if that becomes optimal at the time the Computing Model is implemented.

Recent progress in network and storage technologies have made possible *federation of storage* across multiple member-institution data centers. In this approach, data can be effectively shared and utilized via the network ("data in the grid").

For data distribution, DUNE will use a combination of managed data movement between sites (such as "dataset subscription," primarily for managed production), and a network of XRootD servers (XRootD is an example of an advanced federated system) for caching processed data and for analysis. A file catalog and a metadata system will be required for efficient data management at scale. Efforts will be made to leverage experience of member institutions in this area, and to reuse existing systems or design ideas whenever possible.

8.2.4 Computing Implications of the Dual-Phase Far Detector Design

Parameters of the alternative Far Detector design (based on the dual-phase technology) are listed in Chapter 2 of [19]. The readout channel count is 614,400 (i.e., four times the 153,600 channel count for each $10-$kt detector module) and the drift time is 7.5 ms. The Photon Detector readout channel count is 720 (i.e., four times the 180 channel count for each 10-kt module).

According to some estimates listed in [19], the "Full Stream" readout will produce 16.09 GB of data for each candidate event. This is about 65% of the data volume in one readout cycle of the reference design. Although signal processing strategies may be implemented differently in the dual-phase design, it can be argued that the total data rate will be of the same order of magnitude or less than that of the reference design.

8.3   Near Detector Physics Software

This section summarizes the current status of the near detector simulation and reconstruction, described in detail in [10].

Two approaches are being pursued for the simulation of the DUNE near detector. The first is a fast Monte Carlo based on parameterized detector responses. The GENIE[57] generator is used to model the interactions of neutrinos with nuclei in the detector, and a parameterization of the achieved NOMAD reconstruction performance is used to model the detector response. The second approach, under development, is a full GEANT4-based simulation.

The fast Monte Carlo tool is based on work done for the far detector (see Appendix A.3 of [55]) and is capable of rapidly evaluating the sensitivity of the detector design to a broad variety of analyses targeting specific final states. The full GEANT4-based simulation and subsequent reconstruction chains will be used to inform the parameterized responses of the fast Monte Carlo, as well as being indispensable tools for simulating and extracting results from the near detector. Figure 8.1 shows the trajectory of a negatively charged muon with an initial momentum of 1 GeV propagating in the straw tube tracker, as simulated using GEANT4.
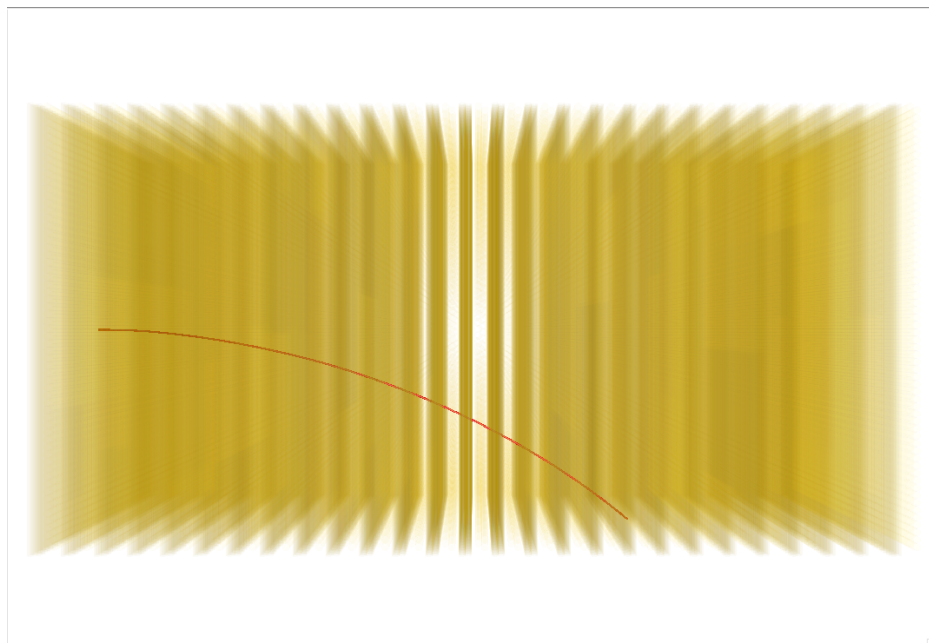

Figure 8.1: The trajectory of a 1 GeV μ^- produced by the GEANT4 simulation of the near detector's straw-tube tracker.

8.4   Far Detector Physics Software

This section summarizes the single-phase and dual-phase far detector simulations and reconstruction, described in detail in [10].

8.4.1   Far Detector Simulation

Detailed GEANT4-based [58, 59] Monte Carlo simulations have been developed for the single-phase and dual-phase far detector designs, incorporating both the TPC modules and the photon detection systems. These simulations provide a basis for detailed studies of detector design and performance, and also enable the development of automated event-reconstruction algorithms.

The single-phase detector simulation is implemented in LArSoft[60], which provides a common simulation framework for LArTPC experiments. LArSoft is based on the *art* framework[61], and is supported by the Fermilab Scientific Computing Division. The comparison of data from ArgoNeuT[8, 62] with LArSoft simulations gives confidence in the reliability of the detector simulation. Future data from LArIAT[63, 64], MicroBooNE[65, 66, 67], and the 35-ton prototype (Section 9.2) will allow further tuning of the LArSoft simulation as experience is gained. The dual-phase detector simulation and hit-level reconstruction are based on the Qscan[68] package, which has been developed over the past decade, and is currently being used for technical design and physics studies for the *Long Baseline Neutrino Observatory Demonstration (WA105)* program.

Events are generated using either the GENIE[57] simulation of neutrino-nucleus interactions, the CRY[69, 70, 71] cosmic-ray generator, a radiological decay simulator written specifically for LArSoft using the decay spectra in [72], a particle gun or one of several text-file-based particle input sources. GEANT4 simulates the trajectories of particles and their energy deposition. Custom algorithms have been developed to propagate the drifting charge and scintillation photons through the detector and to simulate the response characteristics of the TPC wires, readout electronics and photon detectors. Figure 8.2 shows some examples of simulated accelerator neutrino interactions in the MicroBooNE detector.

8.4.2   Far Detector Reconstruction

The reconstruction of particle interactions in LArTPC detectors is an active area of research that has advanced significantly in recent years. In particular, the analysis of the data from the ICARUS[7, 73, 17, 74] and ArgoNEUT experiments[63, 75, 76] required the development of a variety of new reconstruction techniques, forming the basis for precision neutrino physics measurements. Accurate reconstruction is needed not only of neutrino scattering events from the beam, but also atmospheric neutrino events, supernova burst neutrino interactions and nucleon decay events, each with its own requirements. With the advance of both single-phase and dual-phase technologies and expansion of the experimental program to include MicroBooNE[65, 77], the 35-ton prototype and the CERN test experiments, the reconstruction tools have grown in both volume and sophistication, supported by powerful software frameworks such as LArSoft and Qscan.

Fully automated chains of event-reconstruction algorithms are being developed for for both the single-phase and dual-phase detector designs. The first stage of reconstruction involves the processing of the ADC wire signals and the identification of pulses, or "hits" in the 2D space of wire number and charge arrival time. These hits provide the input for a series of pattern-recognition algorithms, which form 2D and 3D clusters, representing individual particle tracks and showers.
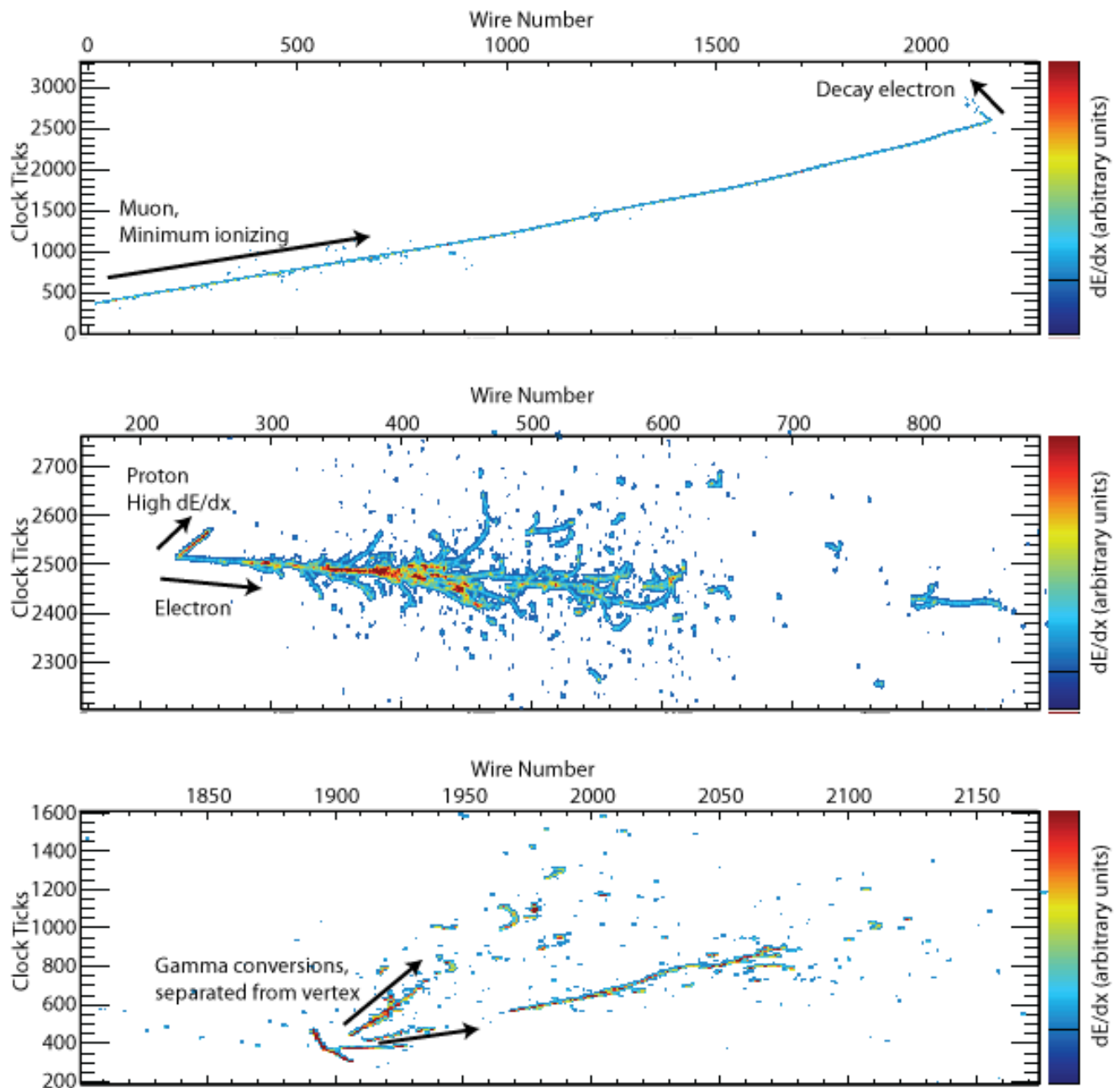
Figure 8.2: Examples of accelerator neutrino interactions, simulated by LArSoft in the MicroBooNE detector. The panels show 2D projections of different event types. The top panel shows a ν_μ charged-current interaction with a stopped muon followed by a decay Michel electron; the middle panel shows a ν_e charged-current quasi-elastic interaction with a single electron and proton in the final state; the bottom panel shows a neutral-current interaction with a π^0 in the final state that decayed into two photons with separate conversion vertices.

A set of high-level algorithms is used to reconstruct the 3D vertex and trajectory of each particle, identify the type of particle and determine the four-momentum. While each stage of the reconstruction chain has been implemented, the algorithms – in particular those addressing the higher-level aspects of reconstruction such as particle identification – are rather preliminary and are in active development.

TPC Signal Processing, Hit Finding, and Disambiguation

The signal-processing steps in the single-phase and dual-phase detector designs are similar but are accomplished with separate software. Both proceed first by decompressing the raw data and filtering the noise using a frequency-based filter. The single-phase signal-processing algorithm also deconvolves the detector and electronics responses at this step. Both the single-phase and dual-phase hit-finding algorithms then subtract the baselines and fit pulse shapes to the filtered raw data. The hit-finding algorithms are able to fit multiple overlapping hits. The main parameters of the hits are the arrival time, the integrated charge, and the width. A raw ADC sum is also retained in the description of a hit, which often carries a better measurement of the total charge. The current algorithms are found to perform well in ArgoNeuT analyses[8] for the single-phase software and during several phases of R&D and prototyping on small-scale dual-phase LAr-LEM-TPC setups[37, 32]. Figure 8.3 shows example event displays of the reconstructed hits in both real and simulated data.

The wrapping of induction-plane wires in the single-phase APA design introduces an additional discrete ambiguity in the data by connecting multiple wire segments to each DAQ channel. A "disambiguation" algorithm is used to break the ambiguity and determine which wire segment generated the charge on each hit. The algorithm forms associations between the collection and induction views, identifying "triplets" of hits that have intersecting wire segments and consistent arrival times. In most events, the majority of hits are associated with a single wire segment, and can be trivially disambiguated. The remaining hits are then disambiguated by clustering them with trivially disambiguated hits.

Photon Detector Signal Reconstruction

Photon detector signals are processed in similar ways to those on the TPC wires. Noise is filtered out, and hits are identified as pulses above the pedestal. Hits are grouped together into clusters in time, called "flashes," for subsequent association with clusters in the TPC. Each flash has a time, a total integrated charge, and a position estimate. The time of an interaction is important in order to help reject cosmic-ray events and also to determine the absolute position of an event along the drift direction. This position is important in order to correct for finite electron lifetime effects for proper charge measurement, which is important for particle identification and extraction of physics results. Signal events which can be out of time from the beam include atmospheric neutrinos, supernova burst neutrinos, and proton decay interactions.

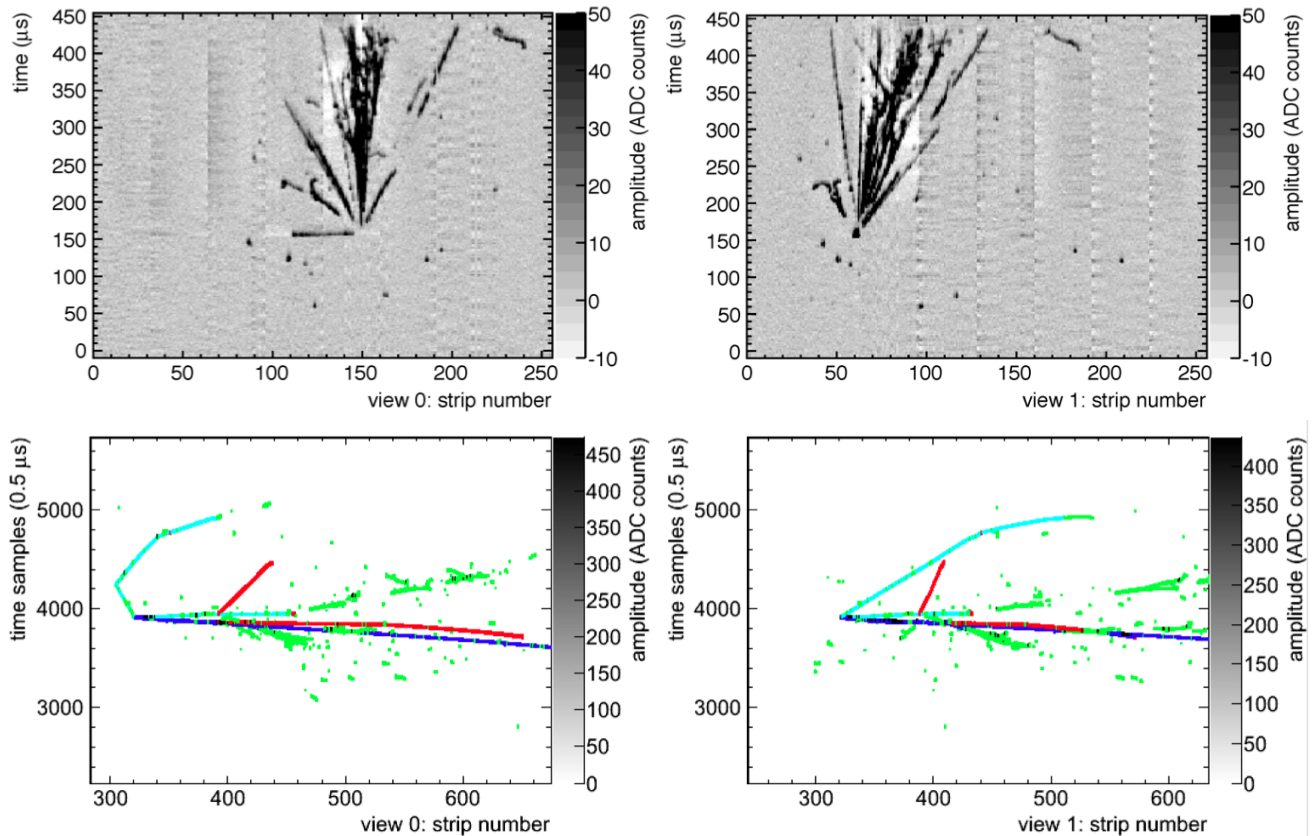Figure 8.3:   Dual-phase LArTPC-reconstructed events for data and MC. Top: Cosmic ray event displays for a hadronic shower candidate. Bottom: Reconstructed hits for a MC simulation of a 5-GeV ν_μ interaction. The secondary particles produced in the two interactions are distinguished by different colors, based on the MC truth information (blue=muon, green=electron, red=proton, cyan=pion). From Ref.[32].

TPC Pattern Recognition

The reconstruction of particles in 3D can be accomplished either by forming 2D clusters and associating them between views, or by first associating 2D hits between views and then clustering the resulting 3D hits. The clustering of hits in LArTPC detectors is a challenging task due to the variety and complexity of event topologies. However, several automated 2D and 3D pattern-recognition algorithms have been implemented using a range of techniques.

One promising suite of reconstruction tools is the PANDORA software development kit[13, 14], which provides fully automated pattern recognition for both single-phase and dual-phase technologies. PANDORA implements a modular approach to pattern recognition, in which events are reconstructed using a large chain of algorithms. Several 2D pattern-recognition algorithms are first applied that cluster together nearby hits based on event topology. The resulting 2D clusters are then associated between views and built into 3D tracks and showers, modifying the 2D clustering as needed to improve the 3D consistency of the event. Vertex-finding algorithms are also applied, and neutrino events are reconstructed by associating the 3D particles to the primary interaction vertex.

Figure 8.4 shows the current efficiency for reconstructing the leading final-state lepton as a function of its momentum for 5-GeV ν_e and ν_μ charged-current interactions simulated in the MicroBooNE detector; the DUNE single-phase detector is expected to perform similarly, although the multiple TPC geometry with wrapped wires requires additional software effort. Figure 8.5 shows the spatial resolution for reconstructing the primary interaction vertex in these 5-GeV event samples, projected onto the x, y and z axes. An estimate of the overall vertex resolution is obtained by taking the 68% quantile of 3D vertex residuals, which yields 2.2 cm (2.5 cm) for ν_μCC (ν_eCC) events.
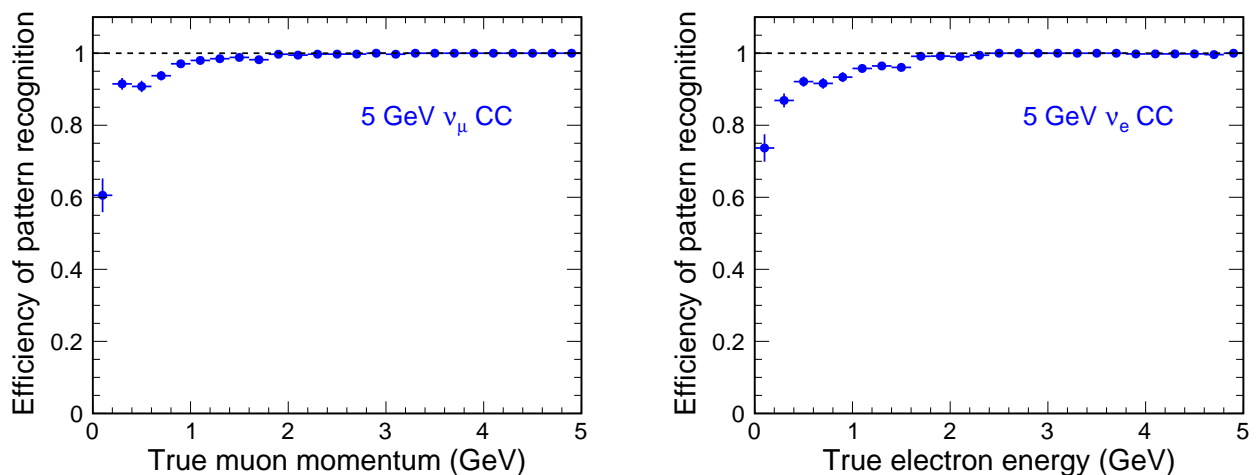

Figure 8.4: Reconstruction efficiency of Pandora pattern recognition algorithms for the leading final-state lepton in 5-GeV ν_μ CC (left) and ν_e CC (right) neutrino interactions, plotted as a function of the lepton momentum. The reconstruction performance is evaluated using the MicroBooNE detector geometry.
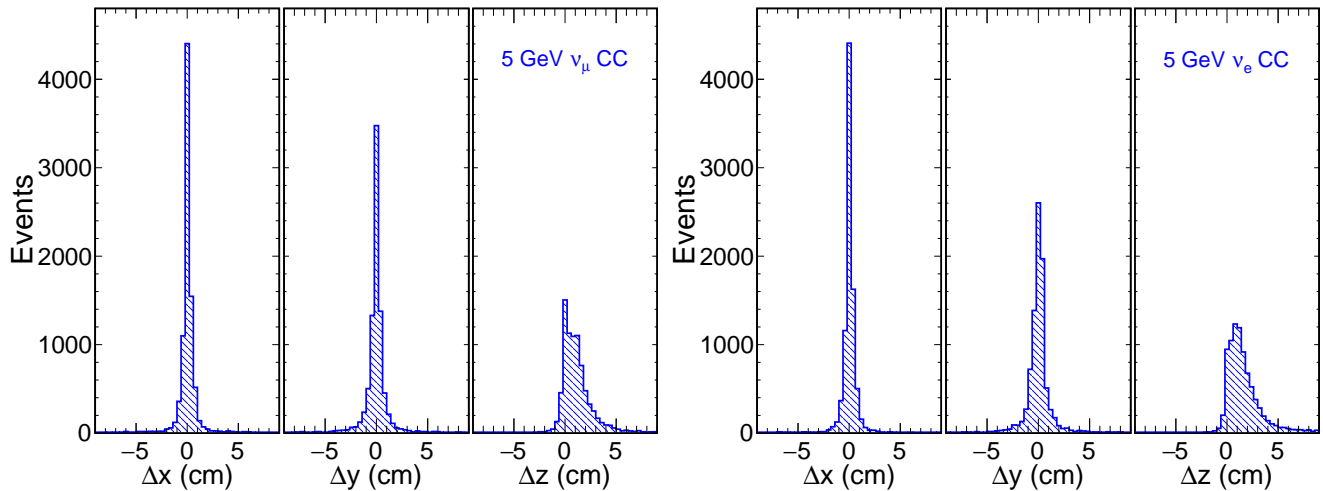
Figure 8.5: Distribution of 2D residuals between reconstructed and simulated interaction vertex for 5-GeV ν_μ CC (left) and ν_e CC (right) interactions in the MicroBooNE detector. The x axis is oriented along the drift field, the y axis runs parallel to the collection plane wires, and the z axis points along the beam direction.

Track Fitting and Shower Measurement

After the pattern recognition stage, a series of high-level reconstruction algorithms is applied to the 2D and 3D clusters; these algorithms fit the trajectories of particle tracks and measure the spatial and calorimetric properties of electromagnetic and hadronic showers. Several high-level techniques have been demonstrated for use in LArTPC detectors using both real and simulated data.

The Kalman filter technique[78] is well-established in high-energy physics, and has been applied to 3D track reconstruction in liquid argon by ICARUS[16]. The technique incorporates the effects of multiple Coulomb scattering, enabling a scattering-based measurement of the track momentum, which is shown by ICARUS to have a resolution as good as $\Delta p/p \approx 10\%$ for the most favorable track lengths. The data from ICARUS have also been used to develop a precise track-reconstruction algorithm, which builds a 3D trajectory for each track by simultaneously optimizing its 2D projections to match the observed data[74]. Another promising track reconstruction technique, based on the local principal curve algorithm, has been implemented for the dual-phase detector, and is shown to provide a precise reconstruction of two-body final states [79, 30].

A full 3D reconstruction of electromagnetic showers is currently in development. In the present scheme, the first stage is an examination of clusters in terms of their 2D parameters, and a selection of shower-like clusters for further analysis. The 3D start position, principal axis, and shower-shape variables are then reconstructed by matching up 2D hits between views. These 3D parameters, combined with calorimetric information, enable a measurement of the total shower energy as well discrimination between electrons and converted photons, based on the ionization energy in the initial part of the shower. The kinematic reconstruction of final-state neutral pions from their $\pi^0 \to \gamma\gamma$ decays can be performed by combining together associated pairs of photons.

Calorimetry and Particle Identification

The reconstructed energy of hits follows from the measured charge after corrections are made for sources of charge loss. The energy of physics objects can then be reconstructed by summing the energy of the associated hits and, when this is combined with a reconstructed trajectory, a measurement of the ionization density dE/dx can be made, which is an important input to particle identification. In order to reconstruct this information, the measured charge on each hit is first obtained from fits to the pulse shapes. The charge loss due to the finite electron lifetime is corrected based on the time of the event, and the path length corresponding to each hit is calculated based on the event trajectory. The effects of recombination, known as "charge quenching," are corrected using a modified Box model[80] or Birks' Law[81]. The identity of a particle track that ranges out in the active detector volume may be ascertained by analyzing the ionization density dE/dx as a function of the range from the end of the track, and comparing with the predictions for different particle species.

In a LArTPC, electromagnetic showers may be classified as having been initiated by an electron or a photon using the dE/dx of the initial $\sim$2.5 cm of the shower. Electron-initiated showers are expected to have dE/dx of one MIP in the initial part, while photon-initiated showers are expected to have twice that. Current algorithms achieve a performance of 80% electron efficiency with 90% photon rejection, and a higher efficiency for fully-reconstructed showers.

Neutrino Event Reconstruction and Classification

Once the visible particles in an event have been reconstructed individually, the combined information is used to reconstruct and classify the overall event. The identification of neutrino event types is based on a multivariate analysis[79, 35, 30, 82], which constructs a number of characteristic topological and calorimetric variables, based on the reconstructed final-state particles. In the present scheme, a Boosted Decision Tree algorithm is used to calculate signal and background likelihoods for particular event hypotheses. The current performance has been evaluated using fully reconstructed ν_e and ν_μ charged-current interactions with two-body final states, simulated in the dual-phase far detector[30]. The correct hypothesis is chosen for 92% (79%) of ν_μ (ν_e) quasi-elastic interactions with a lepton and proton in the final state, and 79% (71%) of ν_μ (ν_e) resonance interactions with a lepton and charged pion in the final state. For selected events, the neutrino energy is estimated kinematically for quasi-elastic interactions using a two-body approximation; otherwise a calorimetric energy measurement is applied. The calorimetric reconstruction takes into account the quenching factors of the different particles, assuming that all hits not associated with the primary lepton are due to hadronic activity. Figure 8.6 shows the resulting energy reconstruction for ν_e CCQE and CC1π^+ events.
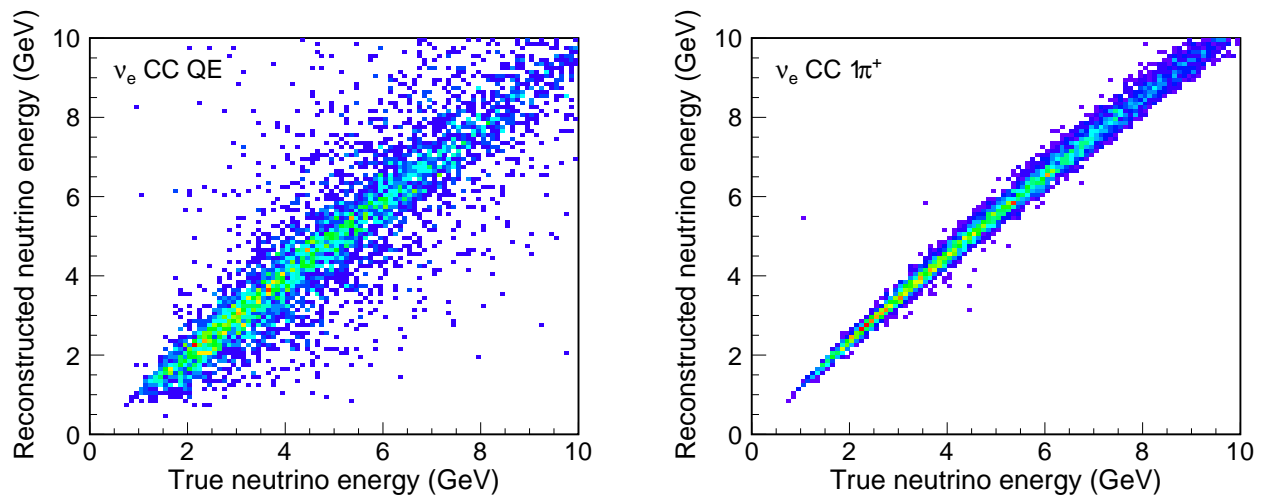
Figure 8.6: Performance of neutrino energy measurement, evaluated using the dual-phase far detector simulation. Distributions of reconstructed versus true neutrino are shown for ν_e CCQE events (left), assuming two-body kinematics, and ν_e CC1π^+ events (right), using a calorimetric energy estimation.

Chapter 9

Prototyping Strategy

9.1 Overview

This chapter describes the prototyping strategy for the DUNE far and near detectors and the efforts that are underway or being planned. These include:

- the 35-ton prototype at Fermilab,

- the single-phase DUNE prototype at CERN,

- the dual-phase LArTPC prototype at CERN known as WA105, and

- prototypes for the Near Neutrino Detector (NND) and Beamline Measurement (BLM) systems

- the LArTPC-based short-baseline neutrino physics program (SBN) at Fermilab.

The single-phase LArTPC prototyping efforts, i.e., the 35-t at Fermilab and the DUNE prototypes at CERN, have evolved from the plans made initially for LBNE, as summarized in Chapter 7 of Annex 4A: *The LBNE Design for a Deep Underground Single-Phase Liquid Argon TPC* [6] and fully described in the *Integrated Plan for LArTPC Neutrino Detectors in the U.S*, a report which was submitted to the DOE in 2009. The 2009 report outlined an R&D program with the goal of demonstrating a scalable LArTPC far detector design for a long-baseline neutrino oscillation experiment. The following list of the detector development components is taken from the Executive Summary of the 2009 report (and edited to remove out-of-date information).

- Materials Test Stand (MTS) program to address questions pertaining to maintenance of argon purity;

- electronics test stands at Fermilab and BNL;

- the Liquid Argon Purity Demonstrator (LAPD) at Fermilab;

- the ArgoNeuT prototype LArTPC;

- the MicroBooNE experiment, a physics experiment that will advance our understanding of LArTPC technology;

- a software development effort that is well integrated across present and planned LArTPC detectors;

- a membrane-cryostat mechanical prototype to evaluate this technology;

- an installation and integration prototype for LBNE, to understand issues pertaining to detector assembly, particularly in an underground environment;

- ∼5%-scale electronics systems test to understand system-wide issues as well as individual component reliability; and

- a calibration test stand that would consist of a small TPC to be exposed to a test beam for calibration studies, relevant for evaluation of physics sensitivities.

This detector development plan has largely been enacted. The MTS is a standard tool used to assess any materials planned for use in LArTPCs. LAPD operated successfully, showing the viability of a "piston purge" in place of evacuation to attain the desired argon purity. The membrane cryostat mechanical prototype became the DUNE 35-t prototype and repeated the demonstration of the piston purge in its Phase-1 operation. ArgoNeuT collected quality data in the NuMI beam and helped spur the integrated reconstruction software development effort now known as LArSoft. The proposed calibration test stand has become the LArIAT facility at Fermilab. The development of cold electronics for LArTPCs continues, with a goal of incorporating most of the signal processing and formatting into analog and digital ASICs. The installation and integration prototype for LBNE has evolved into the 35-t Phase-2 and single-phase CERN prototypes for DUNE, described in this Chapter.

At the time the LBNE document was written, the 35-t membrane cryostat had not yet been fabricated; Section 9.2 provides a summary of the recent and near-future 35-t operations. The 1-kt prototype described in the LBNE document is no longer planned and has been replaced by the DUNE single-phase LArTPC prototype at CERN, which is summarized in Section 9.3 and fully described in Annex 4J: *CERN Single-phase Prototype Detector Proposal* [83]. The prototyping plans made for LBNE were in turn a part of a larger LArTPC detector development program at Fermilab, which is also linked to the short-baseline program at Fermilab; these connections are described in Section 9.6.

The dual-phase WA105 prototype detector has evolved from the European-based design studies performed for LAGUNA-LBNO; the development of these is summarized in Section 4.1. The WA105 detector provides a large-scale implementation of a dual-phase LArTPC as summarized in Section 9.4 and fully described in Annex 4I: *WA105 TDR* [35]. A 20-t engineering prototype of WA105, also described in Section 4.1, is planned for the immediate future.

Both the single-phase and dual-phase prototypes at CERN will be operated in a test beam and calibrated with charged particles (pions, protons, muons, electrons). The data from the CERN prototypes will be combined with data from other operating LArTPCs, such as those in the Fermilab short-baseline and test beam programs and used to refine the simulations of the DUNE far detectors.

The near detector prototyping plans described in Section 9.5 are under development and will utilize particle test beams at CERN and Fermilab. Prototypes of certain short-baseline systems have already been operated in the NuMI beam at Fermilab.

The prototyping efforts enable the Collaboration to acquire the knowledge and skills necessary for successful construction and implementation of the DUNE detectors. They provide guidance in areas such as procurement, construction and installation techniques, in addition to refinement of technical designs and validation of cost and schedule estimates. Operation of the prototypes will provide opportunities to test data-taking and data-handling assumptions and to enhance the development of data analysis tools. Finally, the Fermilab short-baseline program offers experience with large neutrino event samples in LArTPC detectors as well as an opportunity to make detailed measurements of neutrino-argon interactions that are important for DUNE physics.

9.2   The 35-t Prototype

The 35-t (metric ton) LAr prototype was designed to demonstrate that a non-evacuable membrane cryostat could satisfy the DUNE far detector requirement that oxygen contamination of the LAr be less than 100 parts per trillion (ppt) and stably maintain that level. In addition, construction and operation of the 35-t cryostat has also served to identify requirements for procurement of materials and services, to inform procedures for construction and to inform best practices for safe operation. Construction and operation of the 35-t membrane cryostat alone (without detector elements), now called "Phase-1," was successfully completed in 2014.

The second phase of 35-t prototype operations (Phase-2) includes installation and operation of a small-scale, single-phase LArTPC and photon detector in this cryostat, focusing on the performance of active detector elements within the LAr volume. Phase-2 is currently under construction and plans to take data in winter 2015-2016.

9.2.1   35-t Phase-1

The 35-t membrane cryostat was built by the Japanese company IHI, contracted by the LBNE project. Table 9.1 lists the construction materials and dimensions; more information can be found in [84].

The prototype was built in Fermilab's PC-4 facility near the Liquid Argon Purity Demonstrator (LAPD) [85] allowing re-use of a large portion of the LAPD cryogenics-process equipment. The

Table 9.1: 35-t prototype materials and dimensions

Parameter	Value
Cryostat Volume	29.16 m3
Liquid argon total mass	38.6 metric tons
Inner dimensions	4.0 m (L) x 2.7 m (W) x 2.7 m (H)
Outer dimensions	5.4 m (L) x 4.1 m (W) x 4.1 m (H)
Membrane	2.0 mm thick corrugated 304 SS
Insulation	0.4 m polyurethane foam
Secondary barrier system	0.1 mm thick fiberglass
Vapor barrier Normal	1.2 mm thick carbon steel
Steel reinforced concrete	0.3 m thick layer

proximity and size (30 t) of the LAPD vessel offers the possibility using LAPD as a partial storage vessel for LAr if it ever becomes necessary to empty the 35-t cryostat.

The 35-t system employs a submersible pump to move LAr from the cryostat through the filters. Figure 9.1 shows a cutaway view of the cryostat and a photograph of the interior of the completed cryostat.
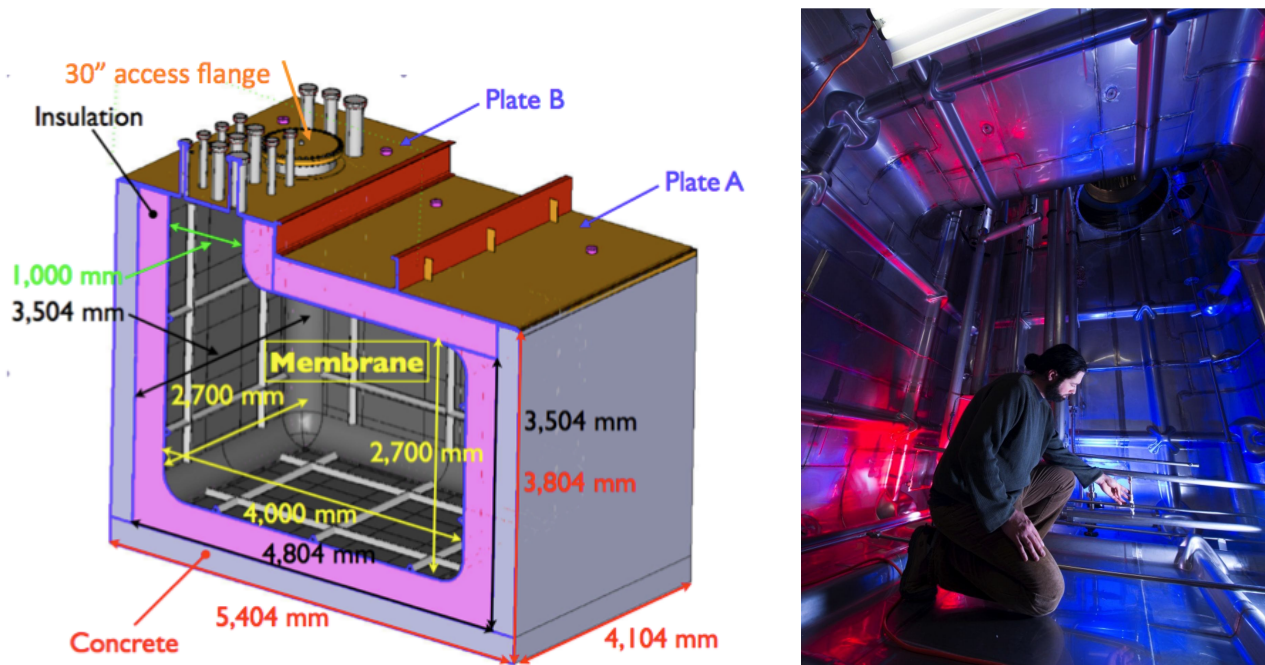
Figure 9.1: (left) Cutaway view of the 35-t prototype cryostat. (right) Interior photograph of the completed cryostat.

The techniques of membrane cryostat construction were demonstrated to be suitable for high-purity LArTPC operations. In particular, welding of corrugated panels, removal of leak-checking dye penetrant and ammonia-activated leak-detecting paints and post-construction-cleaning methods were tested and found to be suitable.

As was demonstrated by LAPD, initial removal of impurities within the cryostat can be achieved by purging with gaseous argon. Accordingly, this was adopted for the 35-t. Figure 9.2 graphically shows the first step of the purification process, removal of the ambient air. The initial state, $t = 0$, reflects the initial values for oxygen, water and nitrogen in the "dry air" state.
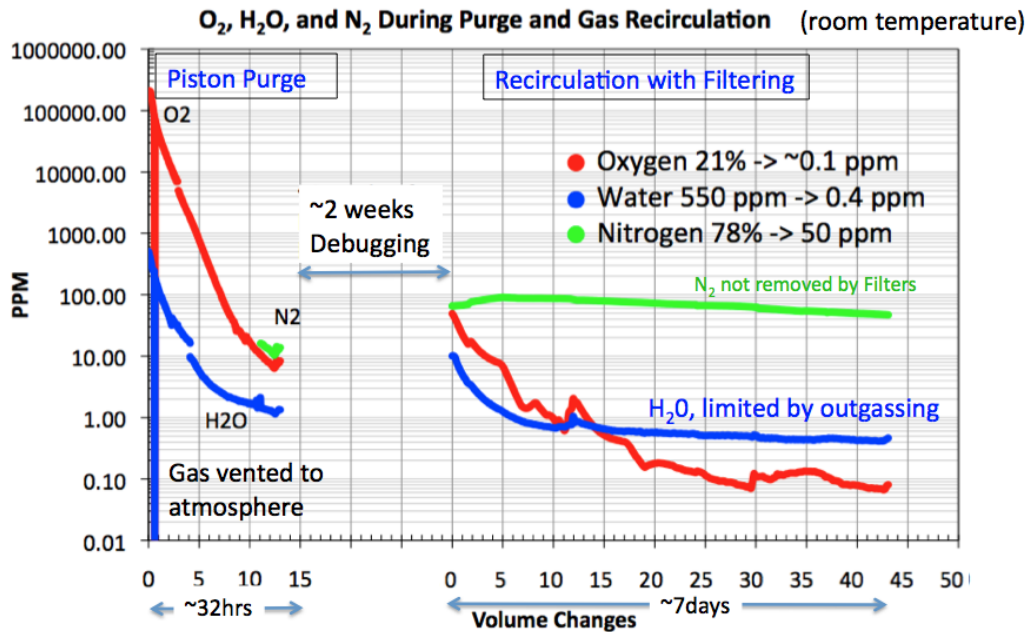

Figure 9.2: Progress of the gas argon purge as it removes impurities from the 35-t. The shown quantities are measured by various gas analyzers. The first stage of the purification is a process called the "Piston Purge". The second stage is "Recirculation with Filtering." The gap between the two steps was due to troubleshooting a leak.

Once the room-temperature, gas purge ceased to improve purity, the cooldown and LAr-fill stage began. A gas/liquid spray method was used to cool the cryostat. This generated a turbulent mixing of cold gas in the cryostat and cooled the entire surface. The cooldown rate was maintained within the limits specified by the cryostat manufacturer. Upon completion of the cooldown, LAr was transferred into the cryostat and purification via recirculation loop started.

During recirculation and purification, dedicated purity monitors were used to measure electron lifetime, which can be translated into equivalent oxygen contamination levels. Figure 9.3 shows the electron lifetime from the start of the LAr pump operation until the end of the Phase-1 run. In general, the electron lifetime improved as a function of pump on-time; despite several events that spoiled the lifetime, electron lifetimes of >2 ms were routinely achieved.

The 35-t Phase-1 run successfully demonstrated that there is nothing inherent to membrane cryostat technology that would preclude achieving the stated goals of the DUNE far detector. In addition, experience gained in operating the 35-t system will inform future design decisions, e.g., developing plans for replacing pumps in a way that prevents loss of purity. Future system designs could avoid the coupling of acoustical vibrations into the cryostat by locating the pumps externally; this would have the added benefit of facilitating maintenance and repair.
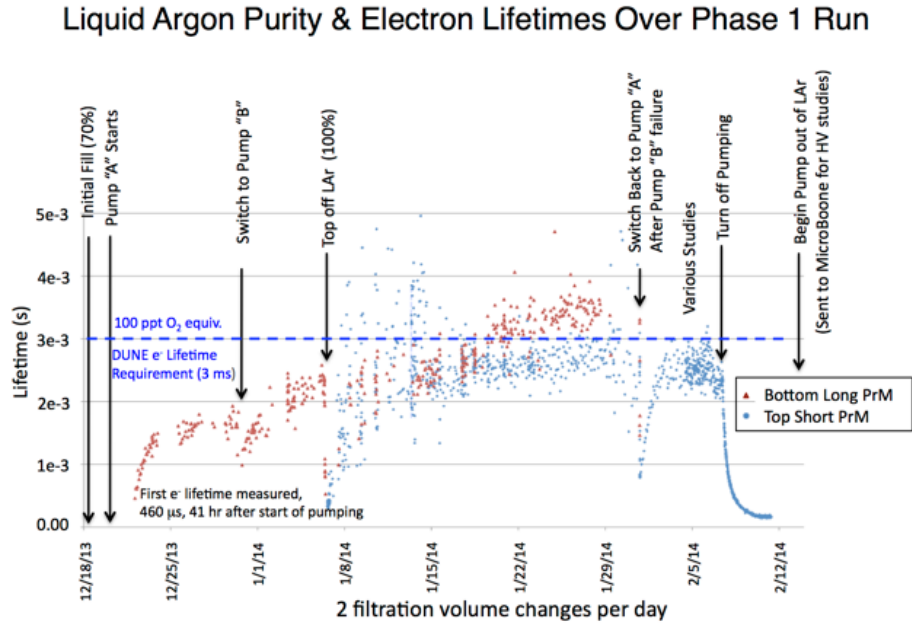
Figure 9.3: LAr electron lifetmes as measured by Cryostat Purity Monitors. Significant events are annotated on the plot. Major divisions on horizontal axis are one week periods. Equivalent purity levels are shown as dashed horizontal lines.

9.2.2 35-t Phase-2

Phase-2 of the 35-t prototype includes a fully operational TPC and photon detector in the cryostat. Commissioning of the TPC is expected in August 2015 after TPC installation, purge, cooldown and LAr fill. Phase-2 operation is planned for several months of cosmic ray running. External plastic scintillator paddles placed around the cryostat will provide both the trigger and rough position measurements of the incoming cosmic rays. Figure 9.4 shows the trial assembly of the TPC outside of the cryostat along with a model of the TPC inside the cryostat.

The Phase-2 prototype incorporates many novel DUNE single-phase far detector design elements as described in previous sections of this document and allows these to be tested in an operational TPC. Some of the more important aspects are collected in Table 9.2.

As can be seen from Table 9.2, successful tests of many of the new design features will require simulation, reconstruction and analysis of 35-t data. This will be performed using the LArSoft package, which is also used to simulate and reconstruct data from ArgoNeuT, MicroBoone and LArIAT. Reuse of software developed for those experiments will greatly facilitate 35-t developments; however, the novel hardware features of the 35-t prototype necessitate new software developments, including:

- code to divide the wrapped wires into as many as five individual linear segments. A hit on a single electronic channel can, in principle, be related to a signal on any of these segments.

- "disambiguation" code to identify which of the possible wire segments was actually respon-
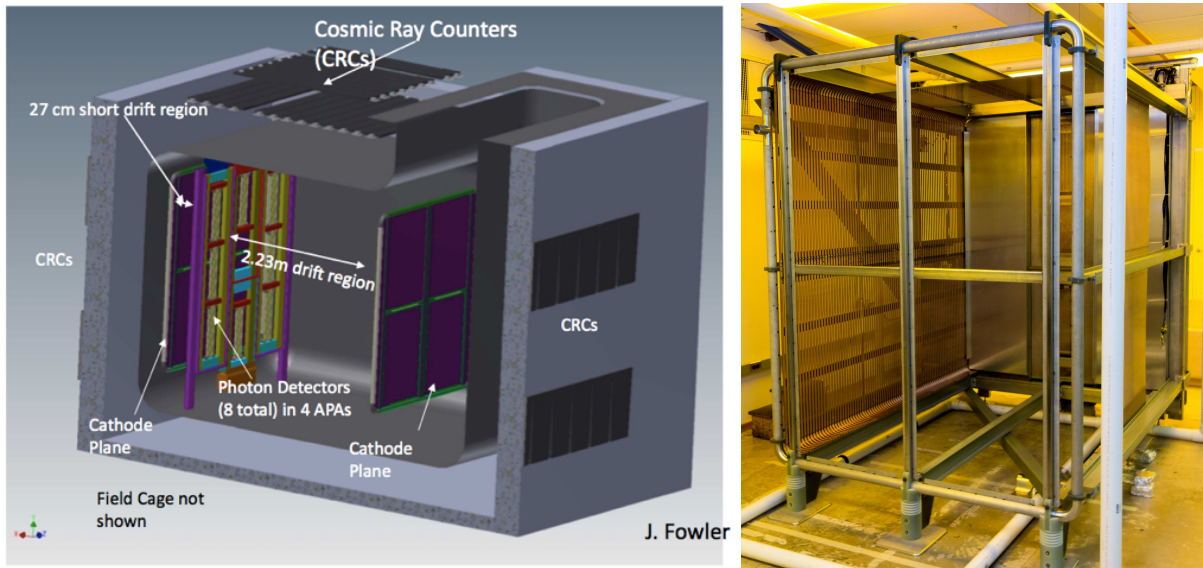
Figure 9.4: (left) Rendering of the 35-t cryostat with TPC and photon detectors installed. Note the position of the APA, which is asymmetrically located between the CPAs (purple) and splits the volume into one large and one very small separate drift regions. The length of the longer one of these is close to what is proposed for the far detector. The other has a shorter drift length due to lack of space. (right) A trial assembly of the TPC.

Table 9.2: 35-t Design Elements

Design Aspect	Section	How Tested
Modular APAs with wrapped wires	4.3.2	Build small-scale APA Modules with FD design
Vertical Gaps between APAs	4.3	Assemble APAs side-by-side. Study reco'd tracks that cross the gaps.
Horizontal Gaps between APAs	4.3	Build two shorter APAs and stack vertically Study reco'd tracks that cross the gaps
Field cage constructed of FR4 Printed Circuit Board	4.3	Operate at HV and measure field uniformity
APAs immersed in active volume	4.3	Study reconstructed tracks that cross APAs
Cold Digital Electronics	4.5	Measure noise performance etc. *in situ*
Waveguide-style Photon Detector	4.6	Install in APAs. Measure lightyield
Triggerless-capable DAQ	4.4	Take data using multiple DAQ modes

sible for the observed hit.

- code for determining the start time of the event (t_0). Since the 35-t prototype DAQ can run "triggerless," methods are needed for finding the t_0 in data. Information from the external scintillator paddles as well as the internal photon detectors can be used.

- Code for "stitching" together track segments observed in different tracking volumes. Since hits can come from either side of the four APAs, there are effectively eight separate tracking volumes, which are treated as separate TPCs.

With these simulation and reconstruction tools in hand, "physics" analysis of the data can be undertaken in the areas of validation of new detector design elements and analysis of basic LArTPC performance. Among the highest-priority analysis tasks are:

- basic detector performance: signal/noise, purity measured with tracks, track direction resolution, photon detector light yield,

- measurement of distortions due to space charge and field non-uniformity, and

- identification of different types of particles: muons, protons, neutrons, pions.

The results obtained by operating and analyzing data from the 35-t Phase-2 prototype are expected to be very valuable in refining the CERN single-phase prototype design, in preparation for the first $10-$kt DUNE far detector module.

9.3   The CERN Single-Phase Prototype

A CERN single-phase prototype detector and accompanying beam-test program is in preparation. As an *engineering* prototype, it is intended to validate the construction of the components planned for the first DUNE $10-$kt detector module at scale and thereby mitigate risks associated with extrapolating small-scale versions of the single-phase LArTPC technology to a full 10-kt detector module. It is intended to benchmark the operation of full-scale detector elements and perform measurements in a well characterized charged-particle beam — an essential step.

The prototype will incorporate components with the same dimensions and features as those for the first 10-kt DUNE far detector module.

9.3.1   Program of Tests and Measurements

Besides validating the performance of the detector components, planning and constructing the CERN prototype will establish and commission production sites and test the installation procedure. Further, before the beam test, many basic detector-performance parameters can be established with

cosmic-ray muons. These data will aid in identification of potentially problematic components, leading to future improvements and optimizations of the detector design. Once it is exposed to a test beam of charged particles of different types and energies it will collect data that can be combined with results from LArIAT and the short-baseline program at Fermilab. Together these measurements will be used to validate MC simulations, and they will serve as data input to DUNE sensitivity studies and allow validation and tuning of tools for event reconstruction and particle identification. The following detector performance measurements are anticipated:

- characterize performance of a full-scale TPC module,

- study performance of the photon detection system,

- test and evaluate the performance of detector calibration tools (e.g., the laser system),

- verify functionality of cold TPC electronics under LAr cryogenic conditions,

- perform full-scale structural test under LAr cryogenic conditions,

- verify argon contamination levels and associated mitigation procedures,

- develop and test installation procedures for full-scale detector components, and

- identify flaws and inefficiencies in the manufacturing process.

The physics sensitivity of the DUNE experiment has so far been estimated based on detector performance characteristics published in the literature, simulation-based estimates and a variety of assumptions about the anticipated performance of the future detector and event reconstruction and particle-identification algorithms. This engineering prototype and the test beam measurements aim to replace these assumptions with measurements to use for full-scale DUNE detector components and the algorithms and thereby enhance the accuracy and reliability of the DUNE physics-sensitivity projections. The collection of beam measurements will serve both as a calibration data set for tuning the MC simulations and as a reference data set for the future DUNE detector. In order to make precise measurements, the DUNE detector will need to accurately identify and measure the energy of the particles produced in the neutrino interaction with argon, which will range from hundreds of MeV to several GeV.

More specifically, the goals of the prototype detector beam-test measurements include the use of a charged-particle beam to

- measure the detector calorimetric response for

  - hadronic showers and

  - electromagnetic showers;

- study e/γ-separation capabilities;

- measure event reconstruction efficiencies as function of energy and particle type;

- measure performance of particle identification algorithms as function of energy for realistic detector conditions;

- assess single-particle track calibration and reconstruction;

- validate accuracy of MC simulations for relevant particle energy and orientation;

- study other topics with the collected data sets:

  - pion interaction kinematics and cross sections,

  - kaon interaction cross section to characterize proton decay backgrounds, and

  - muon capture for charge identification.

A detailed enumeration of the desired minimum integrated particle counts as a function of charged-particle species and momentum is nearing completion. This has led to development of a run plan based on realistic beam composition, particle energies and efficiency information.

An invited technical proposal for the CERN single-phase detector and beam-test program was submitted to the CERN SPSC in September 2015. This proposal is Annex 4J: *CERN Single-phase Prototype Detector Proposal* [83]. The plan includes a first beam run in 2018 before the long shutdown of the LHC. Experience gained from construction, installation and commissioning of this prototype, as well as performance tests with cosmic-ray data are expected to lead to an optimization of corresponding phases of the DUNE single-phase far detector module(s).

9.3.2   Detector Configuration and Components

As mentioned above, the prototype detector components have the same dimensions and features as those of the far detector reference design described in Chapter 4. This includes the TPC and photon detector components, as well as their positioning and spacing within the cryostat.

TPC Configuration

The size of the prototype is in large part determined by the requirement to fully contain hadronic showers of up to several GeV in energy. The particle containment of hadronic showers initiated by charged pions or protons is a critical feature for calorimetric measurements. Simulation studies indicate that showers initiated by $10-$GeV primary pions and protons are contained within a volume measuring 6 m in the longitudinal and 5×5 m^2 in the transverse directions. With the basic APA unit measuring 6×2.3 m^2, the arrangement identified as satisfying the requirement consists of two times three APAs side-by-side, a central cathode and two drift volumes each with

3.6 m drift length. Figure 9.5 shows a view of the CERN single-phase TPC along with the field cage and a view of the TPC within the cryostat.
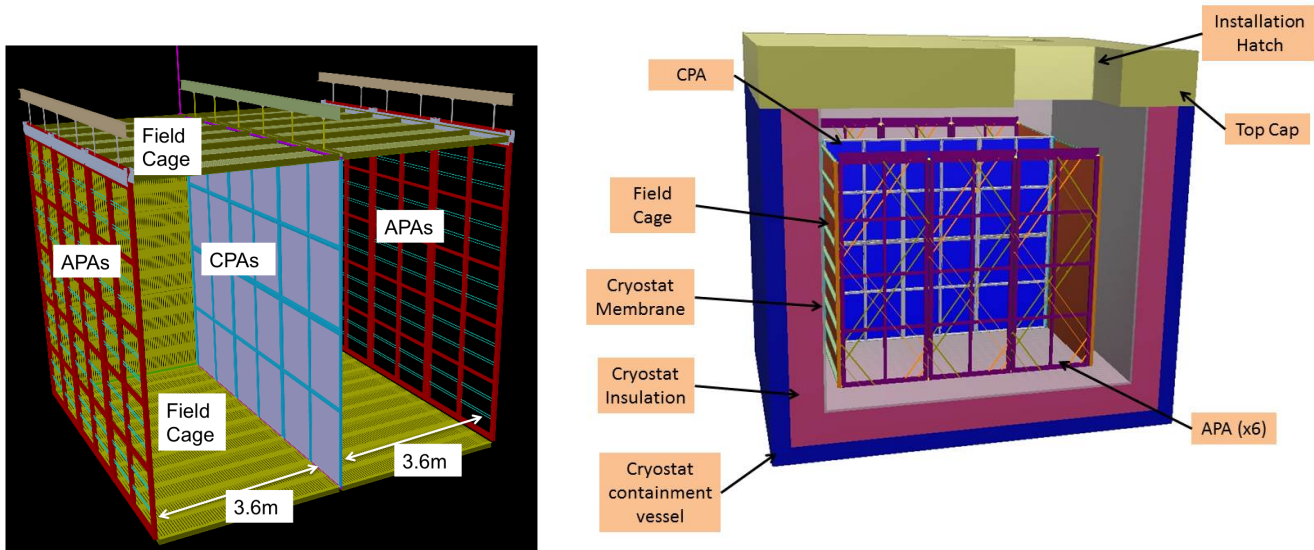

Figure 9.5: View of the CERN single-phase detector TPC (left) and inserted in the cryostat (right).

The TPC readout, photon-detection system, DAQ, slow control and monitoring, as well as the key issues of the installation procedure are described in corresponding sections of Chapter 4.

Cryostat

The CERN prototype uses a membrane tank technology with internal dimensions of 7.8 m (transverse) × 8.9 m (parallel) × 8.1 m (height). It contains 725 tons of LAr, equivalent to about 520 m^3 (where the remaining volume contains the gas ullage). The active (fiducial) detector mass of LAr amounts to 400 tons (300 tons). The external cryostat dimensions are 10.6 m (transverse) × 11.7 m (parallel) × 10.9 m (height).

The cryostat design is scaled up from the 35-t prototype cryostat[84], described in Section 9.2. Unlike the 35-t cryostat, it uses a steel outer supporting structure with an inside metal liner. It is similar to the WA105 dual-phase prototype detector cryostat and to that for the Fermilab Short-Baseline Near Detector (SBND)[86]. The support structure rests on I-beams to allow for air circulation underneath the cryostat; this maintains the temperature within the allowable limits. A stainless-steel membrane contains the LAr within the cryostat. The pressure loading of the cryogenic liquid is transmitted through rigid foam insulation to the surrounding outer support structure. The membrane is corrugated to provide strain relief resulting from temperature-related expansion and contraction. The cryostat top cap consists of the same layers as the cryostat walls. From the inside out, the layers include the stainless-steel primary membrane, intermediate insulation layers and vapor barrier; they all continue across the top of the detector providing a leak-tight seal. The cryostat roof is a removable steel truss structure to which stiffened steel

plates are welded from the underside. They form a flat vapor-barrier surface onto which the roof insulation attaches directly.

The truss structure rests on the top of the supporting structure where a positive structural connection between the two is made in order to resist the upward force caused by the slightly pressurized argon in the ullage space. The hydrostatic load of the LAr in the cryostat is carried by the floor and the sidewalls. In order to meet the maximum deflection of 3 mm between APA and CPA and to decouple the detector form possible sources of vibrations, the TPCs are connected to an external bridge over the top of the plate supported on the floor of the building. Everything else within the cryostat (electronics, sensors, cryogenic and gas plumbing connections) is supported by the steel plates under the truss structure.

All piping and electrical penetrations into the interior of the cryostat are made through the top plate. Penetrations are clustered in one region. The top cap has two large openings for TPC installation, and a manhole to allow entry into the tank after the hatches have been closed.

Cryogenics System

The main goals of the cryogenics system are to purge the cryostat prior to the start of the operations (with argon gas in open and closed loops), cool the cryostat and fill it with LAr. The LAr is continuously purified and the boil-off argon gas is captured, recondensed and purified. The design calls for a 10-ms electron lifetime (30 ppt O_2 equivalent), a quantity that is measured by the detector.

The LAr-receiving facility includes a storage dewar and ambient vaporizer to deliver LAr and gaseous Ar to the cryostat. The LAr goes through the LAr handling and purification system, whereas the gaseous Ar goes through its own purification system before entering the cryostat. Studies are ongoing to standardize the filtration scheme and select the optimal filter medium for both the prototype and future detectors.

During operation, an external LAr pump circulates the bulk of the cryogen through the LAr purification system. The nominal LAr purification flow rate completes one full volume exchange in 5.5 days. The boil-off gas is recondensed and sent to the LAr purification system before re-entering the vessel.

The proposed LAr cryogenics system is based on that of the 35-t prototype, MicroBooNE and SBND, and the current plans for the DUNE single-phase far detector module.

9.4   The WA105 Dual-Phase Demonstrator

In recent years, two consecutive FP7 Design Studies (LAGUNA/LAGUNA-LBNO) have led to the development of a conceptual design (fully engineered and costed) for a 20-kt/50-kt GLACIER-type underground neutrino detector. In these studies, an underground implementation has been

assumed *ab initio* and such constraints have been important and taken into account in design choices. The LAGUNA-LBNO design study, completed in August 2014, has produced many technical developments focused on the construction of large and affordable liquid argon underground detectors addressing the complete investigation of three-flavor neutrino oscillations and the determination of their still unknown parameters. These detectors will be very powerful for non-beam studies as well, such as proton decay, atmospheric neutrinos and supernova neutrinos.

The WA105 experiment, approved in 2013, is designed to provide a full-scale demonstration of these technological developments. It will be exposed to a beam of charged hadrons/electrons/muons of 0.5–20 GeV/c to characterize the detector response to hadronic and electromagnetic showers. A detailed description of the experiment is available in the Technical Design Report of 2014, Annex 4I: *WA105 TDR* [35], and an up-to-date picture of technical developments can be found in the Status Report[41] submitted to the SPSC CERN committee in March 2015. These developments form the basis of the alternative far detector design, described in Chapter 5.

The WA105 demonstrator is a dual-phase LArTPC with an active volume of $6 \times 6 \times 6$ m^3.

These dimensions are motivated by the 4×4 m^2 Charge Readout Plane (CRP) units that are the basic readout components of the large-scale LAGUNA/LBNO 20–50-kt detectors. The $6 \times 6 \times 6$ m^3 active volume is consistent with a fiducial volume that accommodates the CRP size and provides full containment of hadronic showers. Surface operation prohibits drift lengths above 6 m. The footprint of the active volume corresponds to 1:20 of the surface of the LBNO $20-$kt detector. The active volume contains about 300 tonnes of LAr. The important parameters of the detector are presented in Table 9.3 and Figures 9.6, 9.7 and 9.8 provide a 3D drawing and two cut views.

Table 9.3: Parameters for the WA105 demonstrator

Parameter	Units	Value
Liquid argon density	t/m^3	1.38
Liquid argon volume height	m	7.6
Active liquid argon height	m	5.99
Hydrostatic pressure at the bottom	bar	1.03
Inner vessel size (WxLxH)	m^3	$8.3 \times 8.3 \times 8.1$
Inner vessel base surface	m^2	67.6
Total liquid argon volume	m^3	509.6
Total liquid argon mass	t	705
Active LAr area	m^2	36
Charge readout module (0.5 x 0.5 m^2)		36
N of signal feedthrough		12
N of readout channels		7680
N of PMT		36

The dual-phase LArTPC design drifts ionization electrons vertically through the LAr in a uniform electric field up to the liquid-vapor interface, where they are extracted from the liquid into the gas phase.
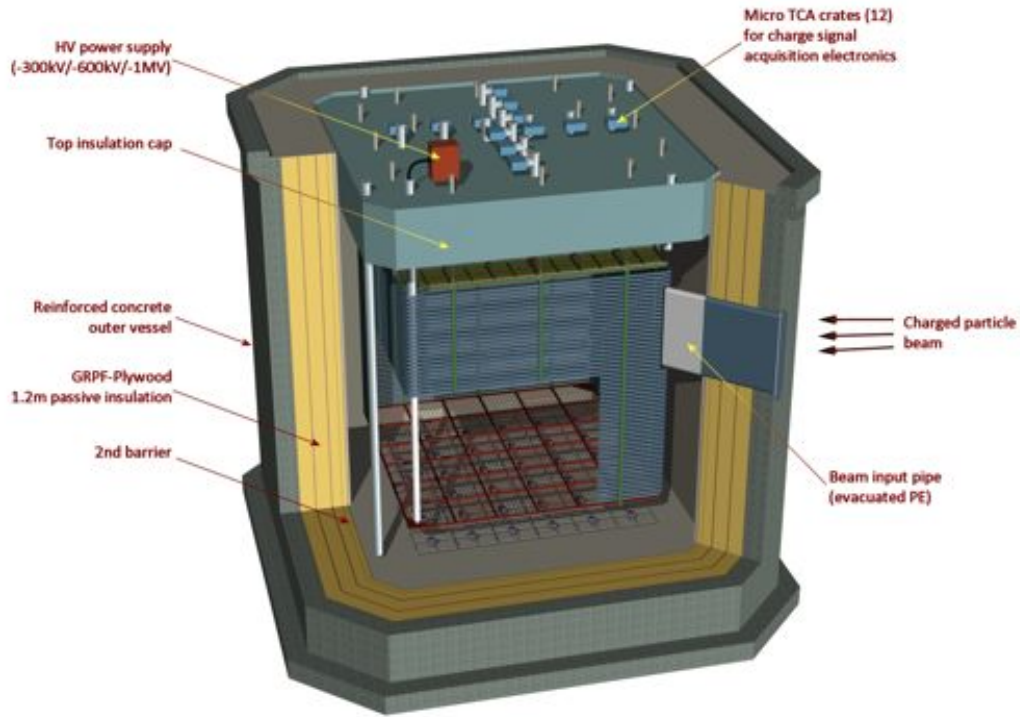
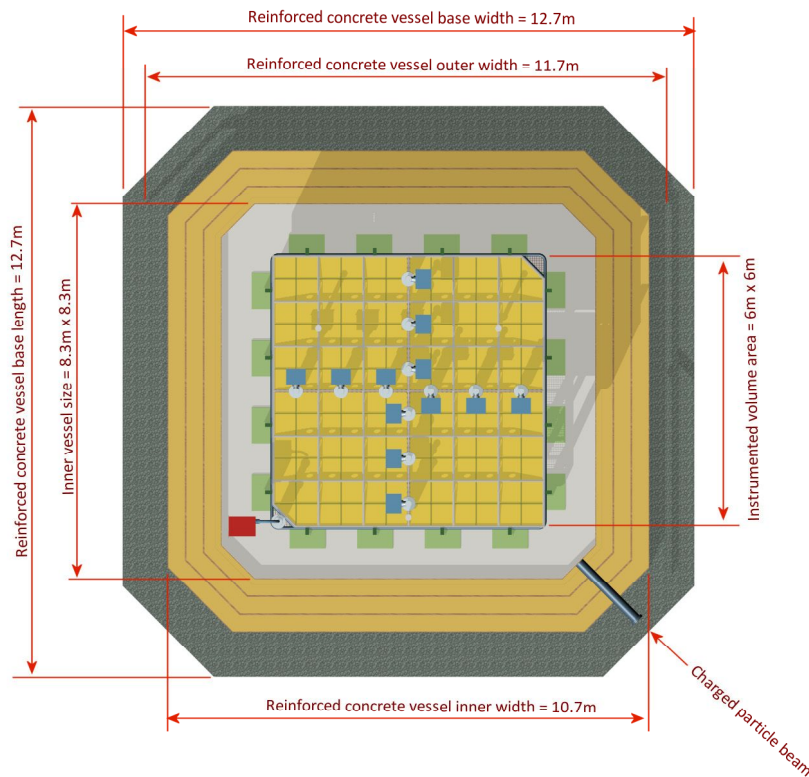Figure 9.6: Illustration of the $6 \times 6 \times 6$ m^3 demonstrator with the detector inside the cryostat

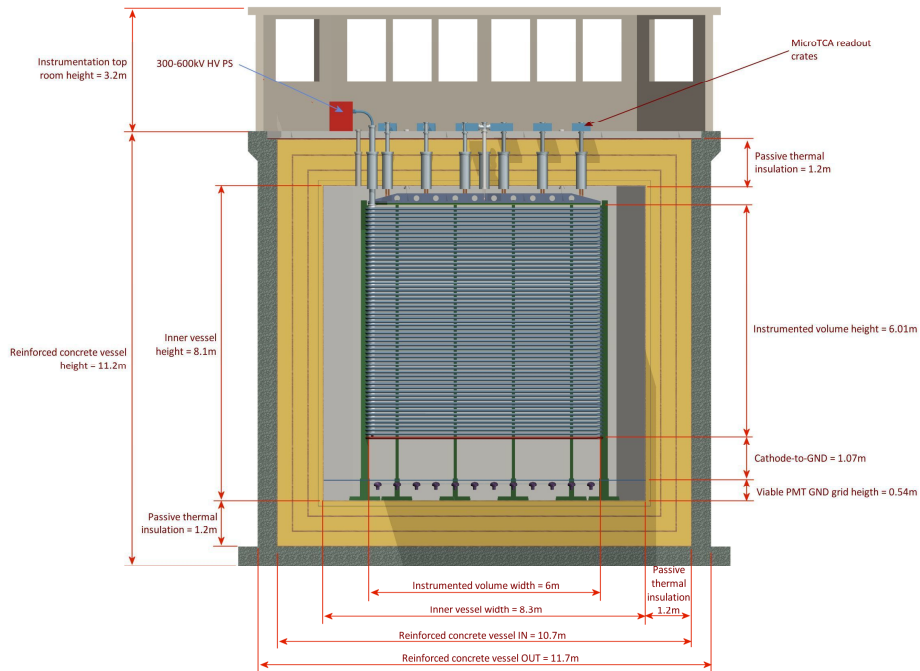Figure 9.7: Plan view section of the $6 \times 6 \times 6$ m^3 demonstrator

Figure 9.8: Vertical cross section of the $6 \times 6 \times 6$ m^3 demonstrator

In the gas, the Charge Readout Plane (CRP) described in Section 5.4, extracts, multiplies and collects the charge.

The drift path in the WA105 demonstrator reaches 6 m. The detector will operate with drift fields of 0.5 kV/cm and 1 kV/cm, corresponding to cathode voltages of −300–600 kV. 600 kV is the voltage also needed for the operation of the DUNE dual-phase detector module with 12 m drift at 0.5 kV/cm. The CRP has an active surface of 36 m^2, with its anode subdivided into strips of 3.125-mm pitch and 3-m length, for a total of 7680 readout channels.

The WA105 demonstrator will establish the techniques developed for the 20/50-kt LBNO detectors, in particular:

- tank construction technique based on the LNG industry with non-evacuated vessel,

- purification system,

- long drift,

- HV system 300–600 kV, large hanging field cage,

- large area double-phase charge readout,

- accessible cryogenic front-end electronics and cheap DAQ electronics, and

- long-term stability of UV light readout.

Furthermore, the $6 \times 6 \times 6$ m^3 demonstrator exposed to the test beam promises a rich physics program to:

- assess detector performance in reconstructing hadronic showers; the most demanding task in neutrino interactions;

- measure hadronic and electromagnetic calorimetry and PID performance;

- full-scale software development, simulation and reconstruction;

- collect high-statistic hadronic interaction samples with unprecedented granularity and resolution for the study of hadronic interactions and nuclear effects;

- assess physics capabilities of the dual-phase versus single-phase performance, in particular: high S/N, 3-mm pitch, absence of materials in long drift space, two collection views, no ambiguities; and

- study systematics related to the reconstruction of the hadronic system (resolution and energy scale), electron-identification efficiencies and π^0 rejection and particle dE/dx identification for proton decay.

The $6 \times 6 \times 6$ m^3 WA105 detector is expected to start taking data in 2018 in the EHN1 Hall extension currently under construction at CERN. The detector components are in an advanced state of design/prototyping, or preproduction. Completion of the WA105 detector design and the preparation of its construction have been progressing very quickly. Many technical design details are benefitting from the implementation of a 20-t ($3 \times 3 \times 1$ m^3) prototype (see Figure 9.9), which corresponds to the readout cell size for the DUNE dual-phase detector module.

Development of this 20-t prototype has verified the complete system integration: production of fully engineered prototype versions of many detector parts, including installation details and ancillary services; establishment of the Quality Assessment (QA) procedures for the construction, installation and commissioning chains; establishment of the procurement processes for the major detector components; and validation of the cost and schedule estimates for WA105. The $3 \times 3 \times 1$ m^3 20-t prototype represents a technical test bed and integration exercise to accelerate the design, procurement, QA and commissioning activities needed for the WA105 demonstrator. In particular, a complete procedure for construction of GTT-licensed corrugated membrane cryostats been established at CERN and a full chain for the procurement, processing, assembly and commissioning of the LEM detectors and anodes has been implemented.

9.5   Near Detector Prototypes

Near detector prototypes are planned for both the neutrino detector and beamline measurements systems.
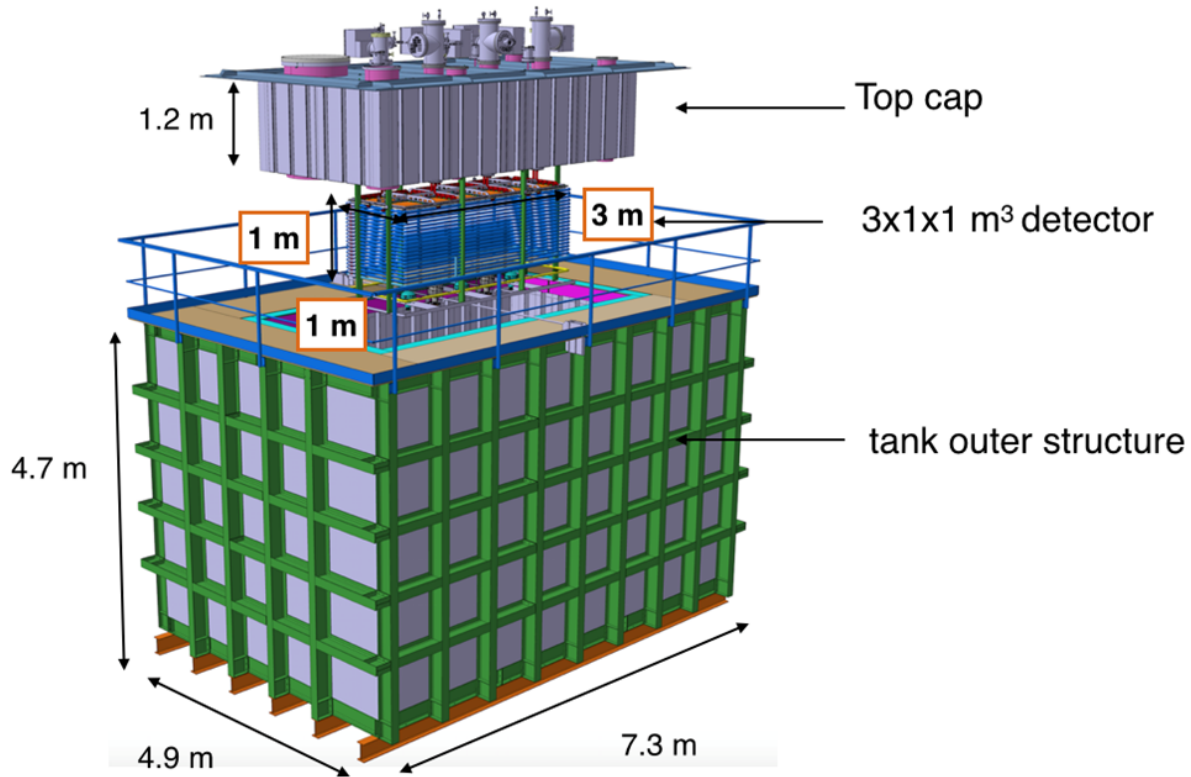
Figure 9.9: Exploded view of the 3×3×1 m³ prototype

9.5.1 Near Neutrino Detector Prototypes

The prototyping plan for the Fine-Grained Tracker (FGT) near neutrino detector, as described in Section 7.2, involves the following major steps:

- Straw-Tube Tracking detector (STT) prototyping,

- ECAL prototyping,

- MuID – RPC development, and

- Dipole magnet studies.

A schematic of the FGT is given in Figure 7.1. The prototyping activity for the reference design will be developed jointly by the participating collaborators in India, with some contributions from institutions in the U.S. or other countries. The prototyping work is spread over a duration of three years. The plan is detailed below.

Straw-Tube Tracking Detector

The proposed Straw-Tube Tracking (STT) detector design provides the central active tracking of the FGT and use straws of 1-cm diameter fabricated from an inner carbon-loaded Kapton (XC) wall and a second aluminum-coated outer Kapton (HN) wall. The details of the STT design are available in Section 7.2.1. The prototype design has two layers of 60 straws each. The straws will have the same dimensions as listed in Section 7.2.1, but half the nominal length, i.e., 1.8 m. The major milestones in the STT prototyping are highlighted below.

The three-year STT R&D and prototyping phase will start with the 3D design of a prototype module. This will include optimization of parameters for the prototype assembly and validation of the mechanical structure using Finite Element Method (FEM) techniques. This process will be a self-feeding system with input from GEANT detector simulations. Figure 9.10 shows the STT simulation. The STT prototype will be fabricated and will undergo extensive tests both in the laboratory and in particle beams at CERN.
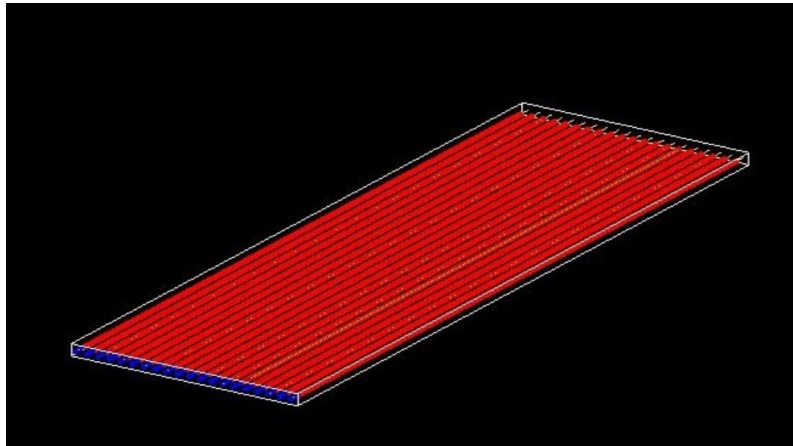

Figure 9.10: GEANT4 simulation of 1 cm straws for the STT prototype

As described in Section 7.2.1, a key feature of the STT is the capability to integrate a series of nuclear targets for (anti)neutrino interactions. The main target is provided by the radiators that are made of thin polypropylene foils (Figure 7.2). The design of the radiator targets has been optimized with simulations of the Transition Radiation (TR) with emphasis on integration into the mechanical structure of the STT modules. The production and design of the plastic foils was discussed with vendors and a half-scale (1.8 m×1.8 m) prototype of the radiator targets will be produced to demonstrate assembly, mechanical properties and overall performance. A preliminary design has been developed for the pressurized Ar gas target (Figure 9.11), based on the use of 0.5-in diameter stainless steel tubes. Prototypes of the pressurized Ar gas tubes will be built to optimize the design of the tubes, including the tube diameter and the possibility of using carbon-composite tubes. Construction of small-scale prototypes of the Ca and C targets is also planned.

The straw tube sense wires were initially proposed as 30-μm diameter gold-plated tungsten, similar to the COMPASS design. In order to minimize the material budget of the mechanical frames used for the STT modules, it is important to reduce the wire tension. To this end, the prototyping includes a detailed study of the possibility of using 20-μm wires instead of the default 30-μm. The
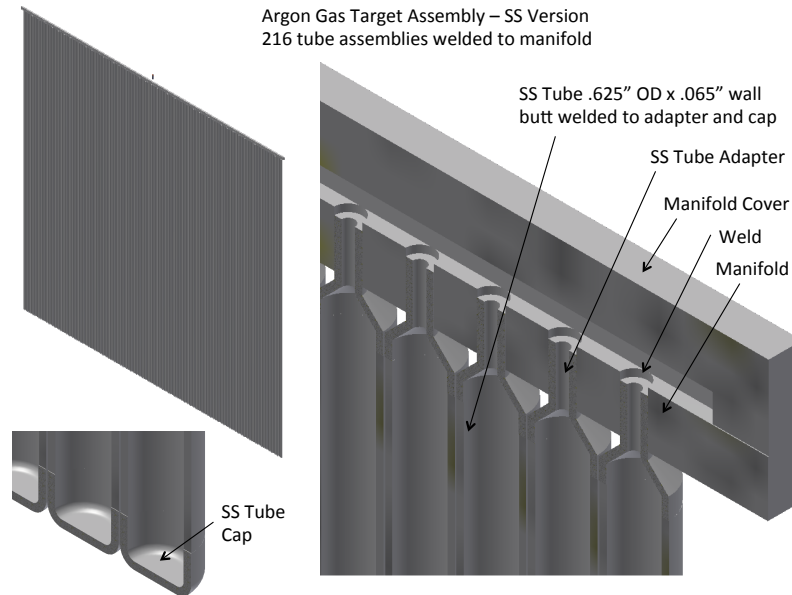
Figure 9.11: Design of the radiator target plane with pressurized Ar gas for STT

tensile strength of these wires inside the straw tubes could affect the signal generation over a long period due to sagging; a detailed study is in progress. Figure 9.12 shows the tension measurement results for 20–30 μm wires using the induced-resonance method. The proposed tension limit on the sense wires is 70 g.

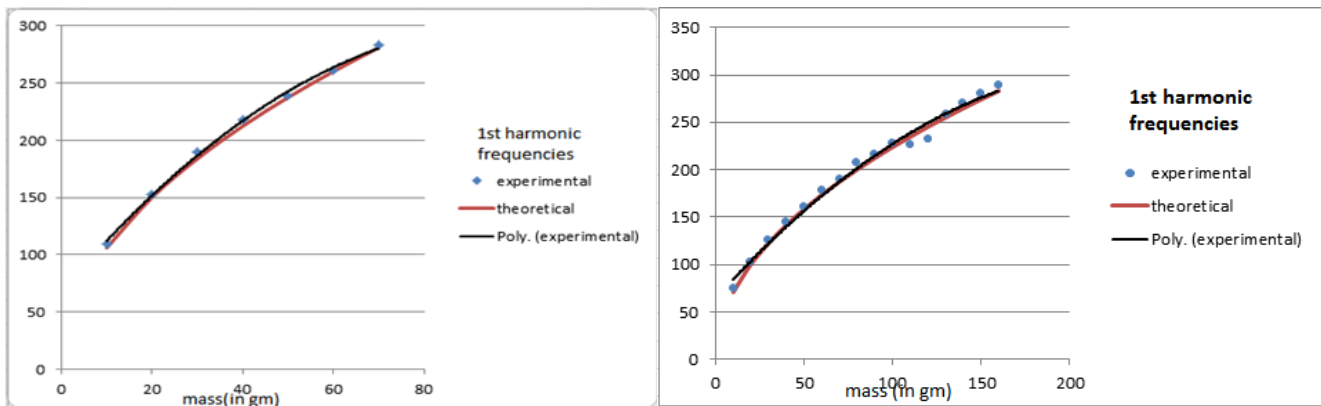Figure 9.12: STT wire-tension measurement studies for 20 μm and 30 μm.

A test chamber with 48 straws of the same dimensions as those for the FGT but with 1-m length has been built and is available for operational studies aimed at understanding the gas flow rates and finalizing the preamplifier selection parameters. Figure 9.13 shows a signal pulse with Ar+CO$_2$ (80:20) gas taken with cosmic rays. The voltage versus amplitude for one of the straws is also shown in Figure 9.13 to establish the QA/QC procedure for the fabricated straws.

We are performing tests of prototype electronics for the signal readout. A four-channel preamplifier has been tested with the test chamber using a radioactive source and the signal has been recorded as shown in Figure 9.14.
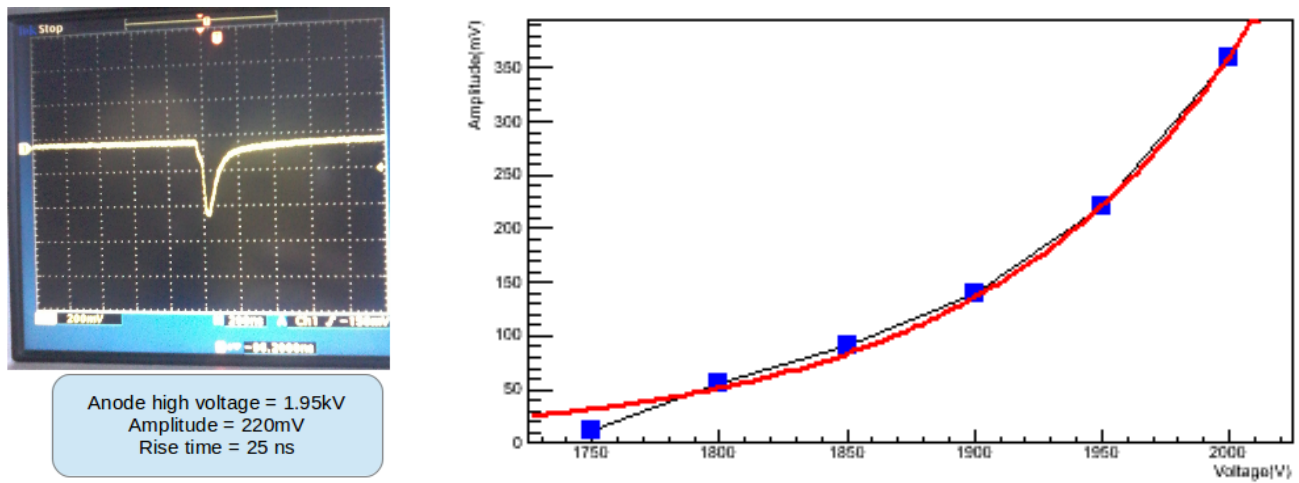
Figure 9.13: Example pulse from the test straw chamber (left) and measurement of voltage vs. amplitude for one of the straws in the test chamber (right).
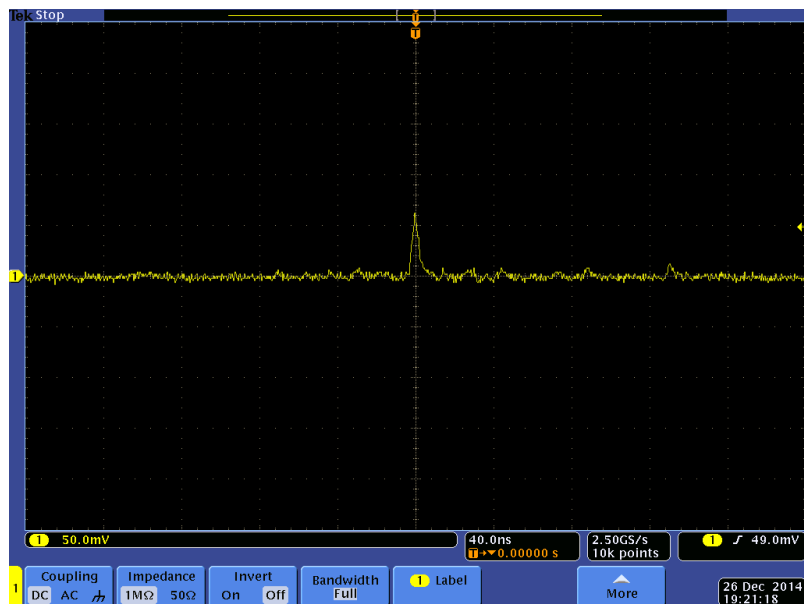

Figure 9.14: Signal from single straw using the BARC (Bhabha Atomic Research Center) preamp and source.

The back-end DAQ is still being worked out and would follow the description in Section 7.2.5. At present both CAMAC- and VME-based DAQ are available. In addition, a μTCA-based fast DAQ has also been setup.

Other activities are in progress. As part of the prototyping, 50 straws of 1.8 m from Lamina Dielectrics Ltd. and 1 km of 30 μm anode wire from Luma has been procured. The optical bench for the fabrication of the straws has been setup. Two pre-mixed gas bottles of Ar+CO_2 have been procured. The operational gas mixture of Xe+CO_2 will be added soon. Local industry and vendors have been identified for manufacturing nozzles, end-plugs, wire-spacers and steel balls. Local workshops are available to fabricate the mechanical structure to hold the straws in the prototype design and also to fabricate a test stand for studies of efficiency and characteristics with a radioactive source. Wire stringing, straw gluing and other tooling setups are still to be established.

The final design of the STT modules will be optimized based on the results obtained from the STT prototype and the related prototyping activities listed above. This task includes a detailed FEM analysis to assess the mechanical structure and the choice of final materials.

ECAL Detector

In the FGT, the ECAL detector will have 4π coverage outside the STT. The detailed description of this detector is given in Section 7.2.2. The ECAL prototype will be a 2 ×2-m^2 module similar to the downstream-ECAL design. The half-scale downstream ECAL prototype construction, which uses Pb as the absorber and extruded scintillator with embedded fiber as the active detector system, will involve the following steps:

- procure materials (plastic scintillator bars, WLS fibers, SiPM, Pb sheets, etc.;)

- set up mechanism to ensure the quality of the scintillator bars, fibers and Pb sheets;

- set up tools for the characterization of SiPMs;

- assemble scintillator bars in an aluminum frame for a prototype layer formation;

- undertake R&D for the coupling of the fiber to the SiPMs as well as the inserting of fiber in the scintillator;

- develop readout electronics for the prototype and set up a cosmic test stand with full DAQ; and

- complete ECAL mechanical design.

The ECAL readout system is centered on a highly sensitive/high-gain SiPM. During the R&D phase, SiPMs from Hamamatru, AdvanSiD and SiPM developed in India by SCL will be compared. Discussions have been started with all the vendors.

Optimization of the ECAL detector geometry with GEANT4 simulations has been initiated. The geometry in the current GEANT4 simulation includes 58 layers of alternating horizontal and vertical scintillator layers per 1.75 mm Pb along the z-direction. In the present configuration each scintillator layer is made of plastic scintillator bars of dimensions 4 m × 2.5 cm × 1 cm, resulting in 160 bars per layer, and 9280 scintillator bars for the downstream ECAL . Figure 9.15 shows the longitudinal view of the electromagnetic shower in the downstream ECAL by 2-GeV photons. Figure 7.4 shows the design of the Pb-scintillator assembly configuration for the ECAL.
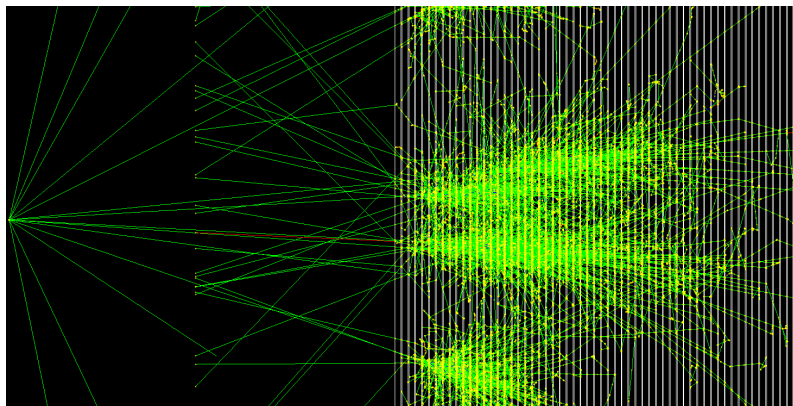

Figure 9.15: Longitudinal view of the electromagnetic shower in the downstream ECAL by 2 GeV photons.

For the construction of the prototype and for the assembly of the actual detector a space of dimension 32 m × 12 m has been identified. Construction of a class 10,000 clean room covering a laboratory space of 12 m × 12 m is under consideration. Figure 9.16 shows the schematic diagram of the laboratory refurbishment plan for the ECAL R&D and fabrication work.

Dipole Magnet Development

The massive dipole magnet (see Section 7.2.3) for the FGT is critical for the particle-momentum measurements, will provide space for the MuID–RPC installation in the magnet steel and will provide structural support for the FGT. The planned magnet prototype includes the engineering development of the tooling and infrastructure that will be used to produce one C out of the total eight Cs of the 8.0-m long dipole. The same C will be utilized in the final magnet assembly. In a similar way, one of the four coils will be assembled to establish the coil winding procedure and measure the operating characteristics. Field simulation work is very advanced (see Figure 7.5) and the mechanical designs are being produced. (Steel dimensions are being optimized to house the muon identification detectors.) Since it will be a closed system, access to the inner detector systems is under extensive study.

MuID–RPC Detector

Muon identification is accomplished via Bakelite Resistive Plate Chamber (RPC) detectors. The RPC mounting structure will be provided by the magnet steel (on sides and ends). Extensive
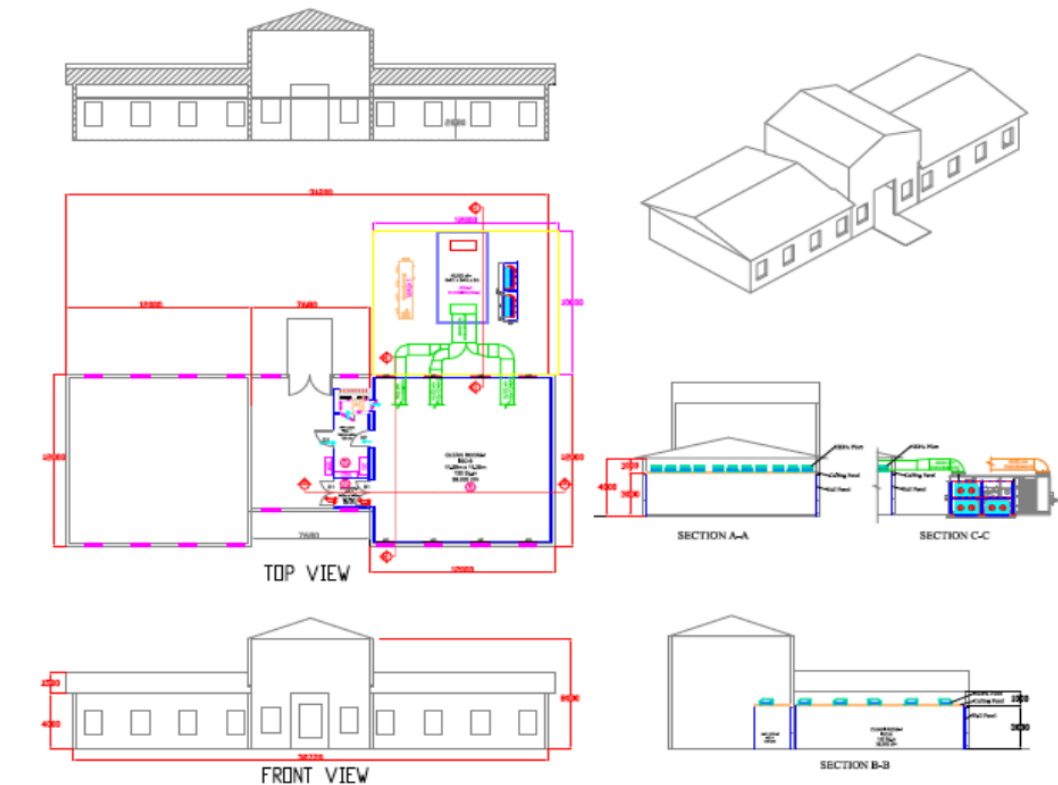
Figure 9.16: Laboratory refurbishment plan for the ECAL R&D and assembly work.

R&D for RPCs is being applied to the prototyping of the muon identifiers. The size of the FGT RPCs makes it challenging to procure the raw material from industry; however, an Indian company has been identified and a large 2.4-m × 1.2 m RPC prototype has been assembled (see Section 7.2.4). The I-V characteristics obtained for these RPCs are very encouraging. More RPCs will be fabricated during the prototyping phase and will be tested for sustained efficiency with variation in ambient parameters, as the Bakelite is sensitive to such changes. Some of the measured quantities are shown in Figure 9.17.

The readout electronics are being developed with input from INO-ICAL detector [87] R&D. The standard RPC gases will need to be replaced with safer ones for underground operation. An initiative in this direction will be taken up during the prototyping phase.

9.5.2 Beamline Measurement Detectors Prototyping Plan

This Section describes recent and ongoing prototyping efforts for the detectors described in Section 7.5.
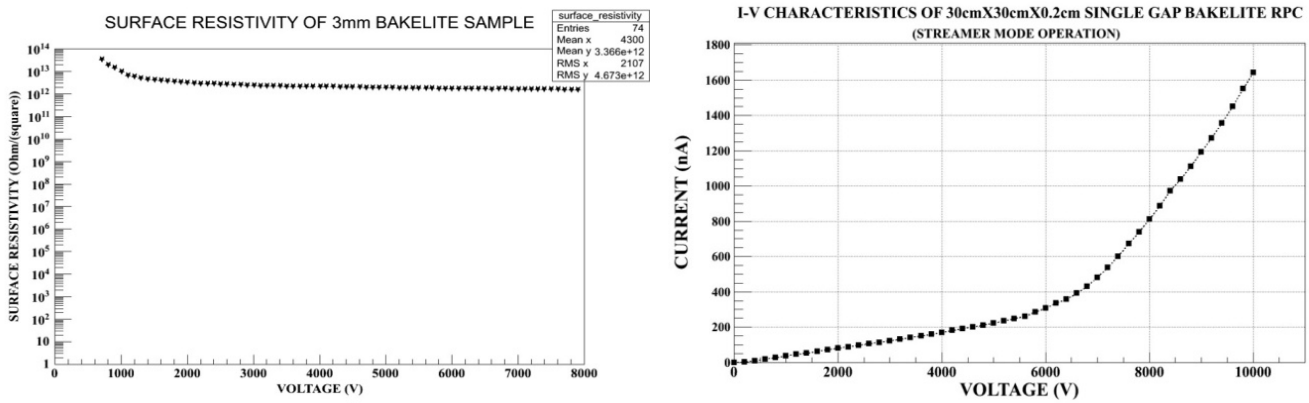
Figure 9.17: RPC characteristics measured during the prototype development.

Prototype Development for the Cherenkov and Ionization Detectors

A prototype Cherenkov counter, along with associated fully automated gas systems, HV systems, and a data acquisition system has been constructed and is undergoing testing in the NuMI neutrino beam's Muon Alcove 2. In addition, three diamond detectors [88] (from CERN) for ionization measurements have been installed in the alcove. Figure 9.18 shows the prototype detectors in the NuMI Alcove 2.

The counter has an automated gas system with an adjustable pressure that ranges from vacuum to 20 atm, corresponding to muon Cherenkov thresholds of 200 GeV/c and 1 GeV/c, respectively. When operated at vacuum, a photomultiplier tube (PMT) registers all background light unrelated to the gas, e.g., transition radiation and light from particles hitting the window and PMT glass. These contributions are observed to be very small relative to the coherent, directional Cherenkov light.

The counter is constructed with a 1-m long radiator section as shown in Figure 9.19 . A 20-foot extension allows the reflected Cherenkov light to travel to a sapphire pressure window viewed by a PMT.

The prototype has been fully integrated into NuMI operations and real-time waveforms can be viewed online as shown in Figure 9.20.

The top panel shows the waveform from the Cherenkov counter at 2 atm gas pressure, which corresponds to a muon momentum threshold of 3 GeV/c. The second panel shows the waveform from a 9 mm × 9 mm diamond detector mounted to the front flange of the Cherenkov radiator section, as shown in the inset of Figure 9.18.

The extracted NuMI proton beam produces a signal in the Resistive Wall Monitor (RWM) that is recorded with an identical digitizer. This allows a direct, bucket-by-bucket (individual proton pulses) comparison of the proton current onto the NuMI primary proton target. The muons are measured after the absorber with a 400-ps time resolution.
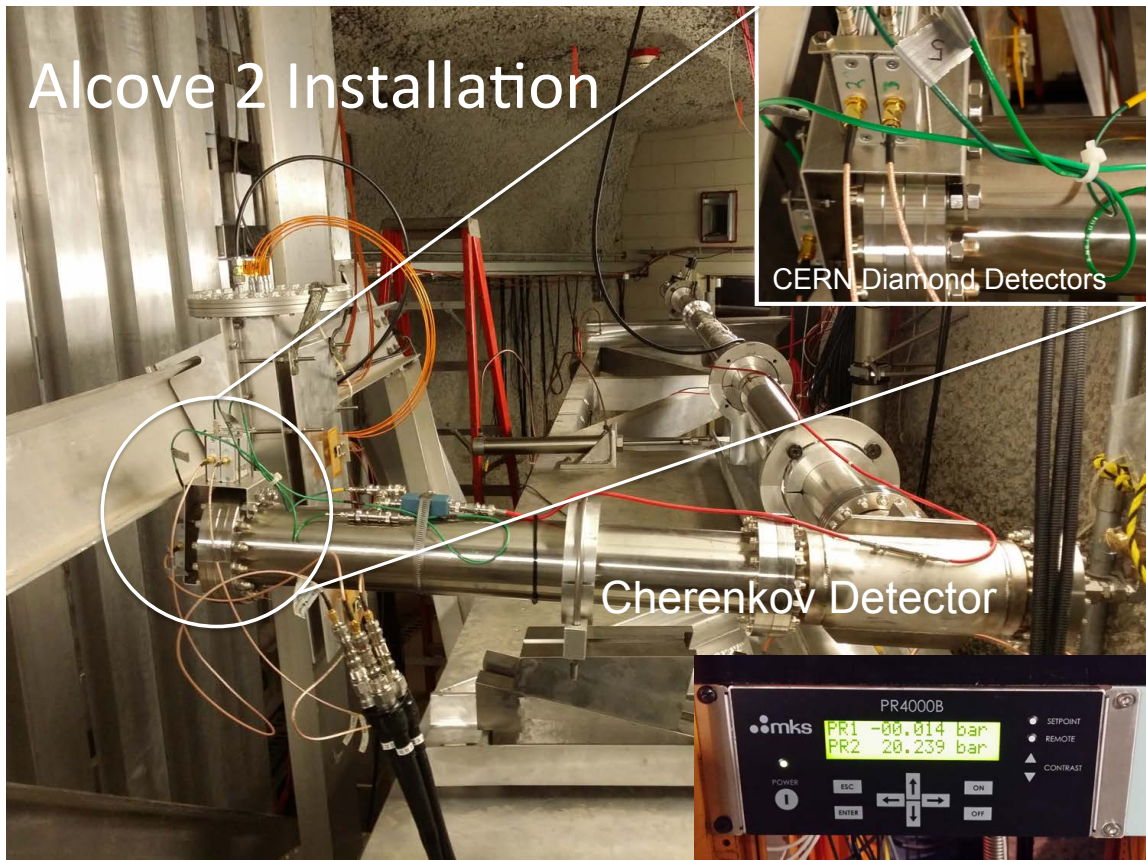
Figure 9.18: A prototype muon gas Cherenkov detector for DUNE. Muons travel through an L-shaped 4-inch Conflat pipe filled with a pressurized gas. A flat mirror mirrors directs the optical photons to a photo multiplier. The lower right inset shows the 20 bar MKS pressure reading achieved by the Cherenkov gas system, and the inset on the upper right shows the CERN/Cividec diamond detectors mounted to the Cherenkov housing.
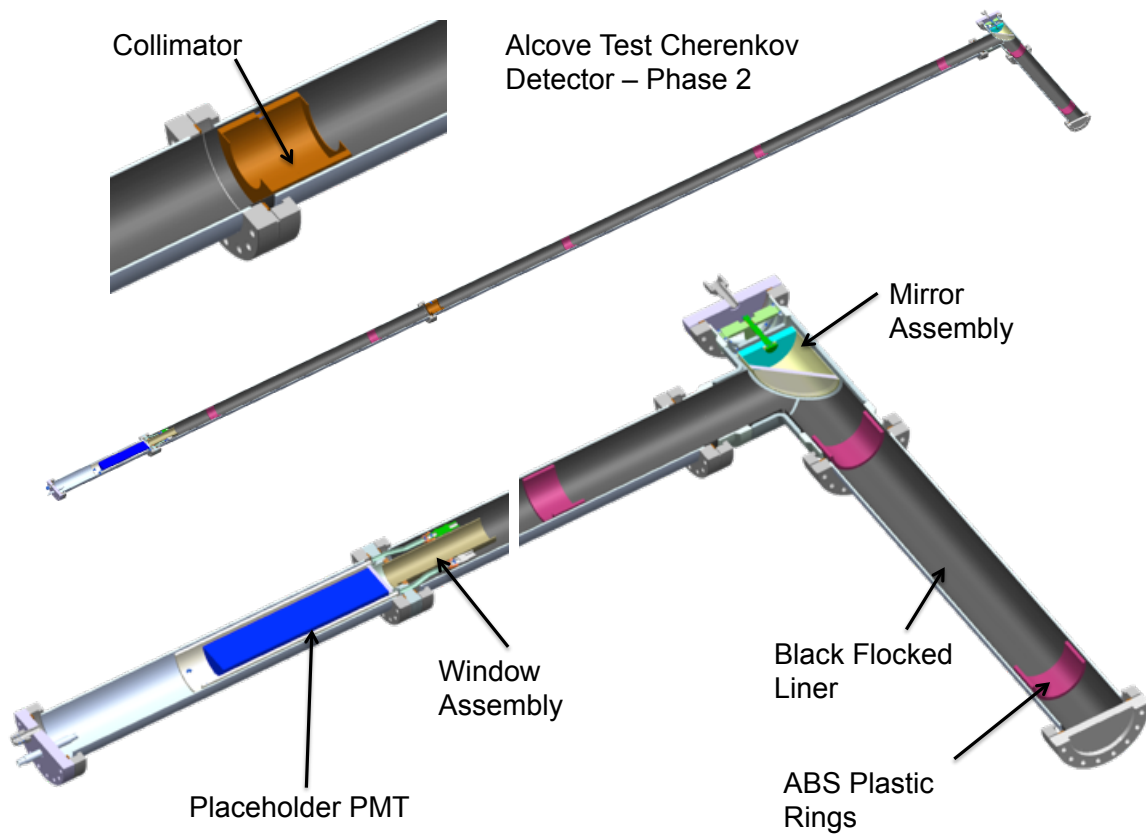
Figure 9.19: A prototype muon gas Cherenkov detector for DUNE.
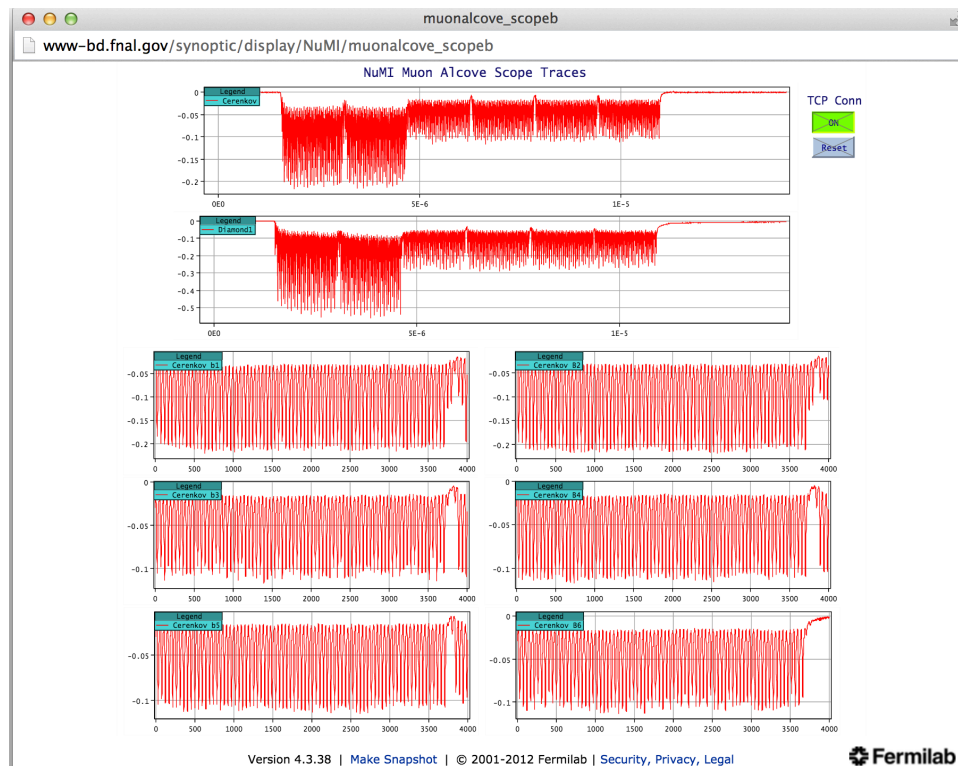
Figure 9.20: The real-time display of the muon detector prototypes in operation on the NuMI beam line. The top two panels are the Cherenkov counter and CERN diamond detector. The signals are transmitted through low-loss heliax cable, then the waveform is digitized at 2.5 GHz with a 12-bit dynamic range, and is recorded onto disk storage for analysis. The signal from the muons is contained in the short beam pulse "buckets" created by the accelerator RF structure. The fast timing allows the prompt muon signal to be easily separated from potential backgrounds such as stopped-muon decays, beta decays, and neutrons.

Prototype Development of the Stopped-Muon Counters

Prototype development activity for the Michel-electron detectors will be divided into studies of (1) the rate of particles and the radiation environment where the detectors will be located, and (2) development of the counters themselves.

The radiation environment will be studied with Monte Carlo simulation and measurement from initial prototype detectors in the NuMI muon alcoves [89]. The prototypes will be installed in the alcoves in 2016 and 2017. Studies will be performed to determine if the photon sensors can survive the radiation environment at the location of the Michel detector. If the sensors can survive, they can be attached directly to the Cherenkov medium; if not, optical guides will have to bring the light to a lower-radiation area, to the side of the beam. Potential radiation damage to the Cherenkov radiator itself will also be studied.

The detector design will focus on selecting radiator and shielding material, photon-detection technology and control/readout hardware. Possible radiators include ones that use aerogel (these may be designed to be replaced periodically) and ones that use flowing liquids such as H_2O or mineral oil. Long-timescale saturation from the very high-rate environment of the beam spill could affect the photon-counting devices [90]. Thus, it will likely be necessary to design fast-switching, high-voltage circuits that turn on the photon counters in the first few microseconds after the spill is over. A similar system was developed in the 1990s for the Brookhaven Muon (g-2) Experiment [91].

A second set of muon detectors, the final DUNE design, are being constructed at this time (2015). They are being installed directly behind the NuMI proton beam dump (Muon Alcove 1), mounted on a movable stand which has undergone an engineering review at Fermilab. The entire setup, detectors and stand, will be suitable for use in the LBNF beam. The higher-radiation environment of Alcove 1 is more representative than Alcove 2 of the conditions in the eventual DUNE installation, and will allow a more accurate calibration in the NuMI beam. The setup will be eventually transferred to the DUNE Absorber Hall.

9.6   Connections to the Short-Baseline Program at Fermilab

DUNE will benefit from a range of past and ongoing efforts at Fermilab. Some have been evolving in tandem with the former LBNE and present DUNE efforts. The strategy behind MicroBooNE — to incorporate some detector development aspects in an experiment with goals to investigate short-baseline neutrino physics — expanded to include detectors upstream and downstream. The Fermilab Short-Baseline Program on the Booster Neutrino Beamline now consists of the Short-Baseline Near Detector (SBND), MicroBooNE, and the ICARUS T-600; the program is fully described in a recent proposal [92]. There is significant overlap in the collaboration membership of DUNE and the three short-baseline detectors.

Each of the short-baseline detectors shares some technical elements with each other and/or with the DUNE far detector prototypes e.g., cryogenic system design, argon purification techniques and

cold electronics.

In other aspects, e.g., the design details of the anode wire planes, the detectors are very different. The SBND is most similar to the DUNE single-phase detector design, having adopted the 35-t APA-CPA-field cage design, while the MicroBooNE TPC field cage follows the ICARUS design. The cold electronics installed on the MicroBooNE TPC represent an initial step in an ongoing program; the 35-t and the SBND implement subsequent outgrowths of cold electronics development. While commissioning its cryogenics system, MicroBooNE conducted investigations of the voltage breakdown in high-purity argon; the results prompted some design adjustments to the field cage adopted by the 35-t Phase-2 and the SBND, demonstrating the sharing and feedback of technical developments.

Coordinated development of reconstruction software for LArTPC detectors is a major outcome of the 2009 *Integrated Plan*. LArSoft is fully supported by the Fermilab Scientific Computing Division and has contributors from all of the operating and planned LArTPC experiments at Fermilab. Track and shower reconstruction methods, and particle identification techniques , are already shared between ArgoNeuT, MicroBooNE, LArIAT and the 35-t. Real data from these detectors is assisting DUNE simulation efforts. The Short-Baseline experiments, starting with MicroBooNE, will develop neutrino interaction classification techniques based on the details revealed by their fine-grained tracking capabilities, and are likely to exert a strong influence on DUNE oscillation analyses.

Chapter 10

Summary of DUNE Detectors

The DUNE experiment is a world-leading, international physics experiment, bringing together a global neutrino community as well as leading experts in nucleon decay and particle astrophysics to explore key questions at the forefront of particle physics and astrophysics. The massive, high-reolution near and far detectors will enable an extensive suite of new physics measurements that are expected to result in groundbreaking discoveries.

The far detector will be located deep underground at the 4850L of SURF. Its 40-kt fiducial mass of LAr will enable sensitive studies of long-baseline oscillations with a 1,300 km baseline, as well as a rich program in astroparticle physics and nucleon decay searches. The far detector configuration consists of four LArTPCs. They provide excellent tracking and calorimetry performance, high signal efficiency and effective background discrimination, all of which converge to provide an overall excellent capability to precisely measure neutrino events and reconstruct kinematical properties with high resolution. The full imaging of events will enable study of neutrino interactions and other rare events to unprecedented levels.

The magnetized, high-resolution near detector will measure the spectrum and flavor composition of the neutrino beam extremely precisely. It is able to discriminate neutrino flavor through particle identification and separate neutrino and antineutrino fluxes through charge discrimination of electrons and muons produced in the neutrino charged current-interactions. These capabilities enable DUNE to reach unprecedented sensitivity in long-baseline neutrino oscillation studies. This is the primary role of the near detector, however, its exposure to an intense flux of neutrinos will provide an opportunity to collect unprecedentedly high neutrino interaction statistics, making possible a wealth of fundamental neutrino interaction measurements, an important component of the DUNE Collaboration's ancillary scientific goals.

References

[1] Particle Physics Project Prioritization Panel, "US Particle Physics: Scientific Opportunities; A Strategic Plan for the Next Ten Years," 2008. `http://science.energy.gov/~/media/hep/pdf/files/pdfs/p5_report_06022008.pdf`.

[2] `http://espp2012.ifj.edu.pl/index.php`.

[3] The DUNE Collaboration, "CDR Volume 1: The LBNF and DUNE Projects," tech. rep., 2015. `http://lbne2-docdb.fnal.gov/cgi-bin/ShowDocument?docid=10687`.

[4] The DUNE Collaboration, "CDR Volume 2: The Physics Program for DUNE at LBNF," tech. rep., 2015. `http://arxiv.org/abs/1512.06148`.

[5] The DUNE Collaboration, "CDR Volume 3: The Long-Baseline Neutrino Facility for DUNE," tech. rep., 2015. `http://lbne2-docdb.fnal.gov/cgi-bin/ShowDocument?docid=10689`.

[6] The LBNE Collaboration, "CDR Annex 4A: The LBNE Design for a Deep Underground Single-Phase Liquid Argon TPC," tech. rep., 2015. `http://lbne2-docdb.fnal.gov/cgi-bin/ShowDocument?docid=10685`.

[7] S. Amerio *et al.*, "Design, construction and tests of the ICARUS T600 detector," *Nucl.Instrum.Meth.*, vol. A527, pp. 329–410, 2004.

[8] C. Anderson, M. Antonello, B. Baller, T. Bolton, C. Bromberg, *et al.*, "The ArgoNeuT Detector in the NuMI Low-Energy beam line at Fermilab," *JINST*, vol. 7, p. P10019, 2012.

[9] L. Jiang, K. Hasbrouck, A. Svenson, J. Kim, X. Tian, and S. Mishra, "Scan and Analysis of LAr Events: NuE and NuEBar Sensitivity STudy," tech. rep., University of South Carolina, 2013. LBNE DocDB 6954-v3.

[10] The DUNE Collaboration, "CDR Annex 4C: Simulation and Reconstruction," tech. rep., 2015. `http://lbne2-docdb.fnal.gov/cgi-bin/ShowDocument?docid=10790`.

[11] M. Antonello, P. Aprili, B. Baibussinov, F. Boffelli, A. Bubak, *et al.*, "Operation and performance of the ICARUS-T600 cryogenic plant at Gran Sasso underground Laboratory." arXiv:1504.01556 [physics.ins-det], 2015.

[12] M. Antonello, B. Baibussinov, P. Benetti, F. Boffelli, A. Bubak, *et al.*, "Experimental observation of an extremely high electron lifetime with the ICARUS-T600 LAr-TPC," *JINST*, vol. 9, no. 12, p. P12006, 2014.

[13] J. Marshall and M. Thomson, "Pandora Particle Flow Algorithm," in *Proceedings, International Conference on Calorimetry for the High Energy Frontier (CHEF 2013)*, pp. 305–315, 2013.

[14] J. Marshall and M. Thomson, "The Pandora software development kit for particle flow calorimetry," *J.Phys.Conf.Ser.*, vol. 396, p. 022034, 2012.

[15] D. Gibin, "Software Tools and Data Analysis," tech. rep., FNAL, 2013. LBNE Doc 7460.

[16] A. Ankowski *et al.*, "Measurement of through-going particle momentum by means of multiple scattering with the ICARUS T600 TPC," *Eur.Phys.J.*, vol. C48, pp. 667–676, 2006.

[17] A. Ankowski *et al.*, "Energy reconstruction of electromagnetic showers from pi0 decays with the icarus t600 liquid argon tpc," *Acta Physica Polonica*, vol. B41, p. 103, 2010.

[18] C. Bromberg, B. Carls, D. Edmunds, A. Hahn, W. Jaskierny, *et al.*, "Design and operation of LongBo: a 2 m long drift liquid argon TPC." arXiv:1504.00398 [physics.ins-det], submitted to JINST, 2015.

[19] The DUNE Collaboration, "CDR Annex 4B: Expected Data Rates for the DUNE Detectors," tech. rep., 2015. `http://lbne2-docdb.fnal.gov/cgi-bin/ShowDocument?docid=10720`.

[20] MicroBooNE Collaboration, "The MicroBooNE Technical Design Report." `http://microboone-docdb.fnal.gov/cgi-bin/ShowDocument?docid=1821`, 2012.

[21] R. Rucinski and C. Thorn, "LBNE LAr Technical Board Meeting Feb. 15 2011," tech. rep., Fermilab, BNL, 2011. LBNE DocDB 3407-v6.

[22] B. Baller *et al.* tech. rep. LBNE-doc-266-v1, LBNE-doc-3414-v2.

[23] B. Baller, "TPC Wire Angle Optimization," tech. rep., 2010. LBNE Doc 2836.

[24] R. Rucinski, "FD Tecnical Board meeting on wire angle change from 45 to 36 degrees," tech. rep., Fermilab, 2014. LBNE DocDB 8981-v4.

[25] R. Abbasi *et al.*, "The IceCube Data Acquisition System: Signal Capture, Digitization, and Timestamping," *Nucl.Instrum.Meth.*, vol. A601, pp. 294–316, 2009.

[26] C. Thorn, G. D. Geronimo, A. DAndragora, S. Li, N. Nambiar, S. Rescia, E. Vernon, H. Chen, F. Lanni, D. Makowiecki, V. Radeka, and B. Yu, "Cold Electronics Development for the LBNE LAr TPC," *Phys.Procedia*, vol. 37, p. 1295, 2012.

[27] S. Li, J. Ma, G. D. Geronimo, H. Chen, and V. Radeka, "LAr TPC electronics CMOS lifetime

at 300 K and 77 K," *IEEE Trans. Nuclear Science*, vol. 60, p. 4737, 2013.

[28] I. N. *et al.*, "Attenuation length measurements of scintillation light in liquid rare gases and their mixtures using an improved reflection suppresser," *Nulcl. Inst. and Meth. in Phys. Resrch Sec. A.*, vol. 384, pp. 380–386, 1997.

[29] The LAGUNA-LBNO Consortium, "CDR Annex 4E: LAGUNA-LBNO: Part 2 - LAr Detectors - 20 kt, 50 kt and PILOT projects," tech. rep., 2014. `http://laguna.ethz.ch:8080/Plone/deliverables/laguna-lbno-284518-deliverables/part-2-liquid-argon-detectors-20-kton-50-kton-and-pilot-projects/view/`.

[30] "Final report of the LAGUNA-LBNO design of a pan-European infrastructure for large apparatus studying Grand Unification, Neutrino Astrophysics and Long Baseline Neutrino Oscillations (Funded by European Commission FP7 Research Infrastructures, grant agreement number: 284518)," *Annex.*

[31] A. Badertscher, A. Curioni, U. Degunda, L. Epprecht, A. Gendotti, *et al.*, "First operation and performance of a 200 lt double phase LAr LEM-TPC with a 40×76 cm^2 readout," *JINST*, vol. 8, p. P04012, 2013.

[32] A. Badertscher, A. Curioni, U. Degunda, L. Epprecht, A. Gendotti, *et al.*, "First operation and drift field performance of a large area double phase LAr Electron Multiplier Time Projection Chamber with an immersed Greinacher high-voltage multiplier," *JINST*, vol. 7, p. P08026, 2012.

[33] A. Badertscher, A. Curioni, L. Knecht, D. Lussi, A. Marchionni, *et al.*, "First operation of a double phase LAr Large Electron Multiplier Time Projection Chamber with a two-dimensional projective readout anode," *Nucl.Instrum.Meth.*, vol. A641, pp. 48–57, 2011.

[34] A. Bondar, A. Buzulutskov, A. Grebenuk, D. Pavlyuchenko, Y. Tikhonov, and A. Breskin, "Thick gem versus thin gem in two-phase argon avalanche detectors," *JINST*, vol. 3, no. 07, p. P07001, 2008.

[35] L. Agostino *et al.*, "LBNO-DEMO: Large-scale neutrino detector demonstrators for phased performance assessment in view of a long-baseline oscillation experiment, The LBNO-DEMO - WA105 - Collaboration." CERN-SPSC-2014-013; SPSC-TDR-004, 2014.

[36] C. Cantini, L. Epprecht, A. Gendotti, S. Horikawa, S. Murphy, *et al.*, "Long-term operation of a double phase lar lem time projection chamber with a simplified anode and extraction-grid design," *JINST*, vol. 9, p. P03017, 2014.

[37] A. Badertscher, L. Knecht, M. Laffranchi, A. Marchionni, G. Natterer, *et al.*, "Construction and operation of a Double Phase LAr Large Electron Multiplier Time Projection Chamber." arXiv:0811.3384 [physics.ins-det], 2008.

[38] A. Badertscher *et al.*, "Stable operation with gain of a double phase Liquid Argon LEM-TPC with a 1 mm thick segmented LEM," *J. Phys. Conf. Ser.*, 2011.

[39] C. Cantini, L. Epprecht, A. Gendotti, S. Horikawa, L. Periale, *et al.*, "Performance study of the effective gain of the double phase liquid Argon LEM Time Projection Chamber." arXiv:1412.4402 [physics.ins-det], accepted for publication in JINST, 2014, 2014.

[40] `https://edms.cern.ch/document/1459884/1`.

[41] "Progress report on LBNO-DEMO/WA105 (2015), G. Balik *et al.*, CERN-SPSC-2015-013/SPSC-SR-158".

[42] `https://www.picmg.org/openstandards/microtca/`.

[43] `http://www.ohwr.org/projects/white-rabbit`.

[44] PICMG, "PICMG Advanced Mezzanine Card AMC.0 Specification R2.0," 2006. `http://www.picmg.org/pdf/AMC.0_R2.0_Short_Form.pdf`.

[45] A. Badertscher *et al.*, "ArDM: first results from underground commissioning," *JINST*, vol. 8, p. C09005, 2013.

[46] "UNICOS," 2015. `http://unicos.web.cern.ch/`.

[47] J. Campagne *et al.*, "PMm**2: triggerless acquisition for next generation neutrino experiments," *JINST*, vol. 6, p. C01081, 2011.

[48] B. Genolini *et al.*, "PMm**2: Large photomultipliers and innovative electronics for the next-generation neutrino experiments," *NIM*, vol. A610, p. 249, 2009.

[49] S. D. Lorenzo *et al.*, "PARISROC, a Photomultiplier Array Integrated Read Out Chip." arXiv:0912.1269 [physics.ins-det], 2009.

[50] R. Andrews *et al.*, "A system to test the effects of materials on the electron drift lifetime in liquid argon and observations on the effect of water," *Nucl. Instrum. Meth.*, vol. A608, p. 251, 2009.

[51] The DUNE Collaboration, "CDR Annex 4G: Near Detector Reference Design," tech. rep., 2015. `http://lbne2-docdb.fnal.gov/cgi-bin/ShowDocument?docid=10684`.

[52] B.Chowdhary. R.Gandhi, C.S.Mishra, S.R.Mishra, J.Strait, "Detailed Project Report. Proposal submitted to DAE/DST.," tech. rep., 2012. LBNE DocDB 6704.

[53] J.Dolph, M.Diwan, R.Gandhi, S.R.Mishra, R.Petti, "Near Detector Systems Requirements Working Files.," tech. rep., 2014. LBNE DocDB 8806.

[54] S.R.Mishra, R.Petti, "Thoughts on the LBNE Near Detector Physics and Specifications.," tech. rep., Univ. of South Carolina, 2014. LBNE DocDB 8850.

[55] C. Adams *et al.*, "The Long-Baseline Neutrino Experiment: Exploring Fundamental Symme-

tries of the Universe." arXiv:1307.7335 [hep-ex], 2013.

[56] Diwan, M. and others, "Draft LBNF/DUNE requirements spreadsheet," tech. rep., 2015. DUNE DocDB 112.

[57] C. Andreopoulos *et al.*, "The GENIE Neutrino Monte Carlo Generator," *Nucl. Instrum. Methods*, vol. A, no. 614, pp. 87–104, 2010.

[58] S. Agostinelli *et al.*, "GEANT4 — A Simulation Toolkit," *Nucl. Instrum. Methods*, vol. A, no. 506, pp. 250–303, 2003.

[59] J. Allison *et al.*, "GEANT4 developments and applications," *IEEE Trans. Nucl. Sci.*, vol. 53, no. 1, pp. 270–278, 2006.

[60] E. D. Church, "LArSoft: A Software Package for Liquid Argon Time Projection Drift Chambers." arXiv:1311.6774 [physics.ins-det], 2013.

[61] C. Green, J. Kowalkowski, M. Paterno, M. Fischler, L. Garren, *et al.*, "The art framework," *J.Phys.Conf.Ser.*, vol. 396, p. 022020, 2012.

[62] C. Anderson *et al.*, "Analysis of a Large Sample of Neutrino-Induced Muons with the ArgoNeuT Detector," *JINST*, vol. 7, p. P10020, 2012.

[63] P. Adamson *et al.*, "LArIAT: Liquid Argon TPC in a Test Beam." FERMILAB-PROPOSAL-1034, 2013.

[64] F. Cavanna, M. Kordosky, J. Raaf, and B. Rebel, "LArIAT: Liquid Argon In A Testbeam." arXiv:1406.5560, 2014.

[65] H. Chen *et al.*, "Proposal for a New Experiment Using the Booster and NuMI Neutrino Beamlines: MicroBooNE." FERMILAB-PROPOSAL-0974, 2007.

[66] B. J. P. Jones, "The Status of the MicroBooNE Experiment," *PoS*, vol. EPS-HEP2011, p. 436, 2011.

[67] MicroBooNE Collaboration, "The MicroBooNE Conceptual Design Report." `http://microboone-docdb.fnal.gov/cgi-bin/ShowDocument?docid=1821`, 2010.

[68] D. Lussi, *Study of the response of the novel LAr LEM-TPC detector exposed to cosmic rays and a charged particle beam.* PhD thesis, ETH Zürich, 2013.

[69] C. Hagmann, D. Lange, J. Verbeke, and D. Wright, "Cosmic-ray Shower Library (CRY)," tech. rep., Lawrence Livermore National Laboratory, 2012. UCRL-TM-229453.

[70] C. Hagmann, D. Lange, J. Verbeke, and D. Wright, "Monte Carlo Simulation of Proton-induced Cosmic-ray Cascades in the Atmosphere," tech. rep., Lawrence Livermore National Laboratory, 2012. UCRL-TM-229452.

[71] C. Hagmann, D. Lange, J. Verbeke, and D. Wright. `http://nuclear.llnl.gov/simulation/main.html`.

[72] V. Gehman, "Intrinsic Radioactive Backgrounds in the LBNE Far Detector," tech. rep., LBNL, 2014. LBNE DocDB 8797-v2.

[73] `http://icarus.lngs.infn.it/`.

[74] M. Antonello, B. Baibussinov, P. Benetti, E. Calligarich, N. Canci, *et al.*, "Precise 3D track reconstruction algorithm for the ICARUS T600 liquid argon time projection chamber detector," *Adv.High Energy Phys.*, vol. 2013, p. 260820, 2013.

[75] `http://t962.fnal.gov/`.

[76] R. Acciarri *et al.*, "A study of electron recombination using highly ionizing particles in the ArgoNeuT Liquid Argon TPC," *JINST*, vol. 8, p. P08005, 2013.

[77] `http://www-microboone.fnal.gov/`.

[78] R. Kalman, "A New Approach to Linear Filtering and Prediction Problems," *J. Fluids Eng.*, vol. 82, pp. 35–45, 1960.

[79] J. Back, G. Barker, S. Boyd, J. Einbeck, M. Haigh, *et al.*, "Implementation of a local principal curves algorithm for neutrino interaction reconstruction in a liquid argon volume," *Eur.Phys.J.*, vol. C74, p. 2832, 2014.

[80] J. Thomas and D. Imel, "Recombination of electron-ion pairs in liquid argon and liquid xenon," *Phys.Rev.*, vol. A36, pp. 614–616, 1987.

[81] J. B. Birks, *The Theory and practice of scintillation counting.* Pergamon Press, 1964.

[82] "Expression of Interest for a very long baseline neutrino oscillation experiment (LBNO): CERN-SPSC-2012-021," 2012. `http://cds.cern.ch/record/1457543/files/SPSC-EOI-007.pdf`.

[83] The DUNE Collaboration, "CDR Annex 4J: CERN Single-phase Prototype Detector Proposal," tech. rep., 2015. `http://lbne2-docdb.fnal.gov/cgi-bin/ShowDocument?docid=10715`.

[84] D. Montanari *et al.*, "First scientific application of the membrane cryostat technology," *AIP Conf.Proc.*, vol. 1573, p. 1664, 2014.

[85] M. Adamowski *et al.*, "The liquid argon purity demonstrator," *JINST*, vol. 9, p. P07005, 2014.

[86] C. Adams *et al.*, "LAr1-ND: Testing Neutrino Anomalies with Multiple LArTPC Detectors at Fermilab." arXiv:1309.7987 [physics.ins-det], 2013.

[87] K. K. Meghna, A. Banerjee, S. Biswas, S. Bhattacharya, S. Bose, S. Chattopadhyay, G. Das, C. Marick, S. Saha, and Y. P. Viyogi, "Measurement of electrical properties of electrode materials for the bakelite resistive plate chambers," *Journal of Instrumentation*, vol. 7, no. 10, p. P10003, 2012.

[88] "Cividec Diamond Detector," 2014. `http://cividec.at/Diamond_Detectors_B10_Cryogenic_Diamond_Detector.html`.

[89] S. Kopp *et al.*, "Secondary beam monitors for the NuMI facility at FNAL," *Nucl. Instrum. Meth.*, vol. A568, pp. 503–519, 2006.

[90] Y. Semertzidis and F. Farley, "Effect of light flash on photocathodes," *Nucl. Instrum. Meth.*, vol. A394, p. 7, 1997.

[91] J. Ouyang and W. Earle, "Muon g-2 note no. 202," tech. rep., BNL, 1994.

[92] M. Antonello *et al.*, "A Proposal for a Three Detector Short-Baseline Neutrino Oscillation Program in the Fermilab Booster Neutrino Beam." 2015.